Evaluating Liquefaction Triggering Potential from Induced Seismicity in Oklahoma, Texas, and Kansas

Tyler J. Quick

Dissertation submitted to the faculty of the Virginia Polytechnic Institute and State University in partial fulfillment of the requirements for the degree of

Doctor of Philosophy
In
Civil Engineering

Russell A. Green, Co-Chair
James K. Mitchell, Co-Chair
Ellen M. Rathje
Adrian Rodriguez-Marek

May 28, 2021
Blacksburg, VA

Keywords: earthquakes, induced seismicity, liquefaction, probabilistic liquefaction hazard analysis

Evaluating Liquefaction Triggering Potential from Induced Seismicity in Oklahoma, Texas, and Kansas

Tyler J. Quick

ABSTRACT (Academic)

Deep wastewater injection-induced seismicity has led to over a thousand magnitude (M_w) > 3 earthquakes and four M_w>5 earthquakes in Oklahoma, Texas, and Kansas (OTK) over the last ten years. Liquefaction observed following the 3 September 2016, M_w5.8 Pawnee, OK, induced earthquake raises concerns regarding the liquefaction risk posed by future induced earthquakes. The stress-based simplified liquefaction evaluation procedure is widely used to evaluate liquefaction potential. However, empirical aspects of this procedure were primarily developed for tectonic earthquakes in active shallow-crustal tectonic regimes (e.g., California). Consequently, due to differences in ground motion characteristics and regional geology, the depth-stress reduction factor (r_d) and Magnitude Scaling Factor (MSF) relationships used in these variants may be unsuitable for use with induced earthquakes in OTK. This is because both r_d, which accounts for the non-rigid soil profile response, and MSF, which accounts for shaking duration, are affected by ground motion and soil profile characteristics.

The objective of this research is to develop and test a new liquefaction triggering model for use in assessing the regional liquefaction hazard in OTK from injection-induced earthquakes. This model incorporates induced seismicity-specific r_d and MSF relationships. To assess model efficacy, the liquefaction potential is evaluated for several sites impacted by the 2016 Pawnee earthquake using the model developed herein, as well as several models commonly used to evaluate liquefaction potential for tectonic earthquakes. Estimates are then compared with field observations of liquefaction made following the Pawnee event. This analysis shows that, at most sites, the induced seismicity-specific model more accurately predicts liquefaction severity than do models developed for tectonic earthquakes, which tend to over-predict liquefaction severity.

The liquefaction triggering model developed herein is also used to assess the minimum magnitude (M_{min}) of induced earthquakes capable of triggering liquefaction. For sites capable of supporting structures, it is shown that M_{min} = 5.0 is sufficient to fully capture liquefaction hazard

from induced events in OTK. However, for extremely liquefaction-susceptible soil profiles that are potentially relevant to other infrastructure (e.g., pipelines and levees), consideration of M_{min} as low as 4.0 may be required.

Evaluating Liquefaction Triggering Potential from Induced Seismicity in Oklahoma, Texas, and Kansas

Tyler J. Quick

ABSTRACT (General Audience)

Seismic activity caused by deep wastewater injection has caused over a thousand magnitude (M_w) > 3 earthquakes and four M_w>5 earthquakes in Oklahoma, Texas, and Kansas (OTK) over the last ten years. These events are referred to as induced earthquakes. Liquefaction observed following the 3 September 2016, M_w5.8 Pawnee, OK, induced earthquake raises concerns regarding the liquefaction risk posed by future induced earthquakes. The stress-based simplified liquefaction evaluation procedure is widely used to evaluate liquefaction potential. However, to date, variants of this procedure were developed primarily for natural, tectonic earthquakes in active seismic areas such as California. Due to differences between induced and tectonic earthquakes as well as regional geology, existing variants of the simplified procedure may be unsuitable for use with induced earthquakes in OTK.

The objective of this research is to develop and test a new liquefaction triggering model for use in assessing the regional liquefaction hazard in OTK from injection-induced earthquakes. The model was developed using regional induced earthquake ground motion recordings and soil profiles. To assess model accuracy, liquefaction potential is assessed at several sites impacted by the 2016 Pawnee earthquake using the new model, as well as several models commonly used to evaluate liquefaction potential for tectonic earthquakes. Estimates are then compared with field observations of liquefaction made following the Pawnee event. This analysis shows that, at most sites, the induced seismicity-specific model more accurately predicts liquefaction severity than do models developed for tectonic earthquakes, which tend to over-predict liquefaction severity.

The liquefaction triggering model developed herein is used to assess the minimum magnitude (M_{min}) of induced earthquakes capable of triggering liquefaction. For sites capable of supporting structures, it is shown that M_{min} = 5.0 is sufficient to fully capture liquefaction hazard from induced events in OTK. However, for extremely liquefaction-susceptible soil profiles potentially relevant to other infrastructure (e.g., pipelines and levees), M_{min} as low as 4.0 may be required.

ACKNOWLEDGEMENTS

I would like to express my sincere thanks to my advisors Dr. Russell Green and Dr. Jim Mitchell for their support, guidance, and encouragement throughout my time here at Virginia Tech. I am so grateful for the many hours they have spent working with and mentoring me through this process and for making my experience at Virginia Tech so meaningful. I will forever be grateful for their examples. I would also like to thank my other committee members, Drs. Ellen Rathje and Adrian Rodriguez-Marek, for their insight and assistance throughout this process. I am also grateful to Drs. Brett Maurer and Julian Bommer for their feedback.

I would like to thank others that have helped make this research possible including Dr. Clint Wood and Salman Rahimi for their invaluable guidance on geophysical testing and for allowing us to borrow their equipment. I am also grateful for the property owners in Pawnee, Oklahoma for meeting with us and for allowing us to perform field tests on their properties.

I am so grateful for the many friends and colleagues I have worked with here at Virginia Tech. I would like to offer special thanks to Kristin Ulmer, Mahdi Bahrampouri, Alex Osuchowski, Sneha Upadhyaya, and Caleb Shockley for providing training and assistance with field and laboratory testing, data processing, and numerous other tasks. The support of so many other friends including Julie Paprocki, Dennis Kiptoo, Kaleigh Yost, Luis Zambrano Cruzatty, Grace Huang, Hwanik Ju, Reem Jaber, Nick Brilli, Abdel Alsardi, and others throughout the years has truly helped to shape me and has made my experience at Virginia Tech a wonderful one.

I would also like to express my endless appreciation for my wonderful wife, Lisa, and my amazing children, Kylee, Caleb, Brayden, Lexi, and Jace, for standing by me and helping me smile, even during hard times. They have been a huge support and never fail to keep life exciting. I look forward to watching them find and conquer their own challenges. I also want to thank my parents and siblings for their constant encouragement, support, and love.

Finally, I want to thank my Savior, Jesus Christ, in whose strength, I can do all things.

Table of Contents

List of Figures

List of Tables

1. Introduction

1.1 Problem Statement

Deep wastewater injection has led to over a thousand earthquakes having a moment magnitude (M_w) greater than or equal to 3 in Oklahoma, Texas, and Kansas (OTK) in the last ten years, to include over nine $M_w \geq 4.8$ events. While regulations enacted to limit wastewater injection volumes in Oklahoma have led to reductions in regional seismicity, over 60 earthquakes with $M_w \geq 3$ occurred in 2019, which is still 60 times the natural tectonic rate of about one $M_w \geq 3$ earthquake per year in the state (Langenbruch and Zoback 2016; U.S. Geologic Survey 2020). Additionally, although the number of $M_w \geq 3$ earthquakes has been decreasing since 2015 when wastewater injection began to be scaled back, some of the largest events have occurred since that time. This includes the 2016, M_w5.8 Pawnee, OK earthquake, which was the strongest recorded earthquake in Oklahoma history and is one of the largest recorded earthquakes in the CEUS in the last 70 years (Tiwari and Rathje 2018).

This dramatic increase in seismicity is of particular concern because it is occurring primarily in historically aseismic areas where building codes and construction methods have not traditionally accounted for higher levels of seismicity. This means that infrastructure in these areas may be more susceptible to damage caused by ground shaking. Although most earthquakes induced by deep wastewater injection in OTK are small, larger induced events have resulted in structural damage and, of particular interest to this study, liquefaction (Clayton et al. 2016; Kolawole et al. 2017). The 2016, M_w5.8 Pawnee, OK earthquake was the first induced earthquake worldwide, that the author is aware of, where liquefaction was documented. However, extensive liquefaction was also observed during the subsequent 2017 M_w5.5 Pohang, South Korea earthquake, which resulted from enhanced geothermal activities (Choi et al. 2019). Observations of liquefaction during these events raise concerns regarding potential liquefaction during future events.

Although the stress-based simplified liquefaction evaluation procedure (Whitman 1971; Seed and Idriss 1971) is the most widely used approach for evaluating liquefaction potential worldwide, the procedure is semi-empirical, with the empirical aspects of it derived from data from moderate-sized tectonic earthquakes in active shallow-crustal tectonic regimes (e.g., California, Japan, and New Zealand). Several studies have shown that ground motions from induced earthquakes may have different characteristics than those from tectonic earthquakes (e.g., Hough 2014; Bommer et al. 2016; Novakovic et al. 2018; Zalachoris and Rathje 2019). Examples include induced events in OTK tending to exhibit higher near-source amplitudes, more rapid attenuation with distance near the source, and richer high-frequency content than tectonic events in the central and eastern United States (CEUS) or western United States (WUS). These and other differences are discussed in more detail Section 2.2. Additionally, the geologic profiles and soil deposits in areas in the US experiencing the highest rate of induced seismicity (e.g., OTK) differ from those used to develop the empirical aspects of the most widely used variants of the simplified procedure. Differences in ground motion characteristics and regional geology, in combination with the generally smaller magnitudes of induced earthquakes, raise questions about whether the depth-stress reduction factor (r_d) and Magnitude Scaling Factor (MSF) relationships used in existing variants of the simplified liquefaction evaluation models are suitable for use with induced earthquakes. This is because both r_d, which accounts for the non-rigid response of soil profiles to shaking, and MSF, which accounts for shaking duration on liquefaction triggering, are affected by ground motion and soil profile characteristics. Because existing variants of the simplified procedure may be unsuitable for use with induced earthquakes in OTK, it is important to develop a suitable framework for accurately assessing the liquefaction risk associated with induced seismicity in OTK.

Because induced events in OTK are occurring in historically aseismic areas, increased attention is being given to earthquakes that are smaller (M_w ~3 to 5.5) than would be normally considered in conventional liquefaction hazard analysis. These small-magnitude events dominate the seismic hazard in this region. As a result, establishing a minimum magnitude (M_{min}) threshold below which liquefaction is not expected to be triggered is an important part of assessing the regional liquefaction hazard in OTK. The establishment of an M_{min} threshold for liquefaction is also required for performing probabilistic liquefaction hazard analyses (PLHA) for both induced earthquakes and tectonic earthquakes (Green and Bommer 2019).

1.2 Research Objectives

This research focuses on two primary objectives to address the issues highlighted in the previous section. The first is to develop and test a new liquefaction triggering model for evaluating liquefaction potential of soils subjected to ground motions from induced earthquakes in OTK. To accomplish this objective, several sub-tasks were required. These included:

Task 1: Select and characterize sites impacted by the 3 September 2016, M_w5.8 Pawnee, OK, induced earthquake.

Task 2: Develop new r_d and MSF relationships for use in evaluating liquefaction potential due to deep wastewater injection-induced earthquakes in OTK within the context of the simplified liquefaction evaluation procedure.

Task 3: Evaluate the efficacy of the new liquefaction triggering model and existing liquefaction triggering models by assessing liquefaction potential at the sites selected and characterized in Task 1 and comparing with field observations of liquefaction response made following the Pawnee event.

The second objective of this research is to determine the M_{min} for induced earthquakes capable of triggering liquefaction that should be considered when assessing regional liquefaction hazard in OTK.

1.3 Dissertation Structure and Contents

The main body of this dissertation consists of three manuscripts, comprising Chapters 2 through 4. Chapter 5 presents a summary of key findings from these studies. Supplementary data, figures, code, and a related conference paper are included in the appendices. Additional data, including soil profiles used in the model regression discussed in Chapter 2, are available as an electronic supplement to this document.

Chapter 2 contains the first manuscript. The objective of the research presented in this manuscript is to develop a new liquefaction triggering model specific to deep wastewater injection-induced seismicity in OTK. This model incorporates new induced seismicity-specific r_d

and MSF relationships that can be used within the context of the stress-based “simplified” liquefaction evaluation procedure to estimate the liquefaction potential from induced earthquakes in OTK.

Chapter 3 contains the second manuscript. This paper presents the results of the liquefaction hazard analysis conducted for sites impacted by the 2016 M_w5.8 Pawnee, Oklahoma, induced earthquake. Results of the site characterization performed at these sites in support of the liquefaction hazard analysis are presented. Liquefaction potential at each site is then estimated using input parameters from the Pawnee event using the new OTK induced seismicity-specific liquefaction potential evaluation procedure presented in Chapter 2, as well as several procedures commonly used to evaluate liquefaction potential for tectonic earthquakes. Estimates are compared with field observations of liquefaction made following the Pawnee event to assess the efficacies of these models. This analysis showed that, at most sites, the model developed for induced earthquakes more accurately predicted liquefaction severity than did models developed for tectonic earthquakes. The tectonic models tended to over-predict liquefaction severity.

Chapter 4 contains the third manuscript. The objective of the research presented in this paper is to determine the M_{min} for induced earthquakes capable of triggering liquefaction. M_{min} is assessed by performing probabilistic seismic hazard analyses (PSHAs) and PLHAs using an idealized induced seismic source and two idealized soil profiles. This process is repeated while varying M_{min} to determine the largest M_{min} that can be used while still fully capturing the liquefaction hazard from induced earthquakes. For comparison, M_{min} is also evaluated using idealized tectonic sources for the central and eastern United States (CEUS) and western United States (WUS). Following this procedure, recommended M_{min} thresholds are determined for evaluating liquefaction triggering potential due to induced and tectonic earthquakes at sites capable of supporting building structures as well as extremely liquefaction-susceptible soil profiles that may be of relevance to other types of infrastructure (e.g., pipelines and levees). For sites capable of supporting building structures, it is shown that $M_{min} = 5.0$ is sufficient to fully capture the liquefaction hazard of both induced and tectonic events. For extremely liquefaction-susceptible soil profiles, $M_{min} = 4.5$ is sufficient to fully capture liquefaction hazard from tectonic sources.

However, based on the findings of this study, the use of an $M_{min} < 4.5$ may be required when evaluating liquefaction hazard from induced sources in OTK.

References

Bommer, J. J., Dost, B., Edwards, B., Stafford, P. J., van Elk, J., Doornhof, D., and Ntinalexis, M. (2016). “Developing an application-specific ground-motion model for induced seismicity.” *Bulletin of the Seismological Society of America*, 106(1), 158–173, doi.org/10.1785/0120150184.

Choi, J. H., Ko, K., Gihm, Y. S., Cho, C. S., Lee, H., Song, S. G., Bang, E. S., Lee, H. J., Bae, H. K., Kim, S. W., Choi, S. J., Lee, S. S., and Lee, S. R. (2019). “Surface deformations and rupture processes associated with the 2017 Mw 5.4 Pohang, Korea, earthquake.” *Bulletin of the Seismological Society of America*, 109(2), 756–769, doi.org/10.1785/0120180167.

Clayton, P., Zalachoris, G., Rathje, E., Bheemasetti, T., Caballero, S., Yu, X., and Bennett, S. (2016). *The geotechnical aspects of the September 3, 2016 M5.8 Pawnee, Oklahoma earthquake*. Report GEER-051, Geotechnical Extreme Events Reconnaissance Association, doi.org/10.5072/FK24B33797.

Green, R. A., and Bommer, J. J. (2019). “What is the Smallest Earthquake Magnitude that Needs to be Considered in Assessing Liquefaction Hazard?” *Earthquake Spectra*, 35(3), 1441–1464, doi.org/10.1193/032218eqs064m.

Hough, S. E. (2014). “Shaking from injection-induced Earthquakes in the central and eastern United States.” *Bulletin of the Seismological Society of America*, 104(5), 2619–2626, doi.org/10.1785/0120140099.

Kolawole, F., Atekwana, E. A., and Ismail, A. (2017). “Near-surface electrical resistivity investigation of coseismic liquefaction-induced ground deformation associated with the 2016 Mw 5.8 Pawnee, Oklahoma, earthquake.” *Seismological Research Letters*, 88(4), 1017–1023, doi.org/10.1785/0220170004.

Langenbruch, C., and Zoback, M. D. (2016). “How will induced seismicity in Oklahoma respond to decreased saltwater injection rates?” *Science Advances*, 2(e1601542), 1–9, doi.org/10.1126/sciadv.1601542.

Novakovic, M., Atkinson, G. M., and Assatourians, K. (2018). “Empirically Calibrated Ground-Motion Prediction Equation for Oklahoma.” *Bulletin of the Seismological Society of America*, 108(5A), 2444–2461, doi.org/10.1785/0120170331.

Seed, H. B., and Idriss, I. M. (1971). “Simplified procedure for evaluating soil liquefaction potential.” *Journal of Geotechnical Engineering*, 97(9), 1249–1273.

Tiwari, A., and Rathje, E. M. (2018). “Engineering characteristics of earthquake motions from the Pawnee and Cushing Earthquakes in Oklahoma.” *Proceedings of Geotechnical Earthquake Engineering and Soil Dynamics V (GEESD V): Seismic Hazard Analysis, Earthquake Ground Motions, and Regional-Scale Assessment*, GSP 291, American Society of Civil Engineers, Reston, VA, 378–386.

U.S. Geologic Survey. (2020). “Oklahoma Has Had a Surge of Earthquakes since 2009. Are They Due to fracking?” <https://www.usgs.gov/faqs/oklahoma-has-had-a-surge-earthquakes-2009-are-they-due-fracking?qt-news_science_products=0#qt-news_science_products>.

Whitman, R. V. (1971). “Resistance of Soil to Liquefaction and Settlement.” *Soils and Foundations*, 11(4), 59–68.

Zalachoris, G., and Rathje, E. M. (2019). “Ground Motion Model for Small-to-Moderate Earthquakes in Texas, Oklahoma, and Kansas.” *Earthquake Spectra*, 35(1), 1–20, doi.org/10.1193/022618EQS047M.

2 Manuscript #1: A Framework for Assessing Liquefaction Triggering Potential due to Deep Wastewater Injection-Induced Seismic Events in Oklahoma, Texas, and Kansas

The following manuscript will be submitted to ASCE's Journal of Geotechnical and Geoenvironmental Engineering.

Tyler Quick made the following contributions:

- Developed regional site profiles
- Conducted numerical site response
- Regressed new r_d and MSF relationships
- Prepared figures and tables
- Wrote first draft of the manuscript and incorporated subsequent edits

Dr. Russell Green made the following contributions:

- Developed project idea and scope
- Formulated the approach used to develop the new framework

Dr. Ellen Rathje made the following contributions:

- Developed the induced ground motion database used in this study
- Developed one of the ground motion prediction equations used in this study

Drs. Russell Green, Ellen Rathje, and Jim Mitchell made the following contributions:

- Provided valuable feedback throughout the study

Manuscript #1: A Framework for Assessing Liquefaction Triggering Potential due to Deep Wastewater Injection-Induced Seismic Events in Oklahoma, Texas, and Kansas

Tyler J. Quick[1], Russell A. Green[2], Ellen M. Rathje[3], and James K. Mitchell[4]

[1]Graduate Student, Department of Civil and Environmental Engineering, Virginia Tech, Blacksburg, VA; tylerjaq@vt.edu

[2]Professor, Department of Civil and Environmental Engineering, Virginia Tech, Blacksburg, VA; rugreen@vt.edu

[3]Janet S. Cockrell Centennial Chair, Department of Civil, Architectural, and Environmental Engineering, University of Texas at Austin, Austin, TX; e.rathje@mail.utexas.edu

[4]University Distinguished Professor, Emeritus, Department of Civil and Environmental Engineering, Virginia Tech, Blacksburg, VA; jkm@vt.edu

Keywords: liquefaction, liquefaction triggering, induced seismicity

Abstract

Deep Wastewater injection-induced seismicity has led to over a thousand magnitude (M_w) 3 or greater earthquakes and nine $M_w \geq 4.8$ earthquakes in Oklahoma over the last ten years. The 2016, M_w5.8 Pawnee, Oklahoma, earthquake was the first induced seismic event worldwide, that the authors are aware of, in which liquefaction was documented, raising concerns regarding liquefaction during future induced earthquakes. Due to differences in ground motion characteristics and regional geology, commonly used liquefaction evaluation procedures developed for tectonic earthquakes in active shallow-crustal tectonic regimes (e.g., California) may be unsuitable for use with induced earthquakes in Oklahoma, Texas, and Kansas (OTK). To address these issues, a new liquefaction triggering model specific to deep wastewater injection-induced seismicity in OTK is developed. The new model incorporates regional induced seismicity-specific stress reduction factor (r_d) and magnitude scaling factor (MSF) relationships

that can be used within the context of the stress-based "simplified" liquefaction evaluation procedure to estimate the liquefaction potential from induced earthquakes in OTK. Model validation performed using liquefaction/no-liquefaction case histories from the Pawnee event suggest that the model developed herein provides more accurate predictions of liquefaction severity for induced earthquakes in OTK than do existing models developed for tectonic earthquakes.

2.1 Introduction

Deep wastewater injection has led to over a thousand earthquakes having a moment magnitude (M_w) greater than or equal to 3 and over nine $M_w \geq 4.8$ events in Oklahoma, Texas, and Kansas (OTK) in the last ten years. This includes the 2016, M_w5.8 Pawnee, OK earthquake, which was the strongest recorded earthquake in Oklahoma history and is one of the largest recorded earthquakes in the CEUS in the last 70 years (Tiwari and Rathje 2018). Although most earthquakes induced by deep wastewater injection in OTK are small, larger induced events have resulted in structural damage and, of particular interest to this study, liquefaction (Clayton et al. 2016; Kolawole et al. 2017). The 2016, Pawnee, OK earthquake was the first induced earthquake worldwide, that the authors are aware of, where liquefaction was documented. However, extensive liquefaction was also observed during the subsequent 2017 M_w5.5 Pohang, South Korea earthquake, which resulted from enhanced geothermal activities (Choi et al. 2019). Observations of liquefaction during these events highlight the need to develop a suitable framework for accurately assessing the liquefaction risk associated with induced seismicity.

Although the stress-based "simplified" liquefaction evaluation procedure (Whitman 1971; Seed and Idriss 1971) is the most widely used approach for evaluating liquefaction potential worldwide, the procedure is semi-empirical, with the empirical aspects of it derived from data from moderate-sized tectonic earthquakes in active shallow-crustal tectonic regimes (e.g., California, Japan, and New Zealand). As a result, the suitability of this procedure to evaluate the liquefaction hazard due to induced seismicity in stable continental tectonic regimes is uncertain. Several studies have shown that ground motions from induced earthquakes may have different characteristics than those from tectonic earthquakes (e.g., Hough 2014; Bommer et al. 2016; Novakovic et al. 2018; Zalachoris and Rathje 2019). Additionally, the geologic profiles and soil deposits in areas in the US experiencing the highest rate of induced seismicity (e.g., Oklahoma) differ from those used to develop the empirical aspects of the most widely used variants of the simplified procedure. This, in combination with the generally smaller magnitudes of induced earthquakes, raises questions about whether the depth-stress reduction factor (r_d) and Magnitude Scaling Factor (MSF) relationships used in existing simplified liquefaction evaluation procedures for estimating normalized Cyclic Stress Ratio (CSR*) are suitable for use with induced earthquakes. This is because both r_d, which accounts for the non-rigid response of soil profiles to shaking, and MSF, which accounts for shaking duration on liquefaction triggering, are affected by ground motion and soil profile characteristics.

To address these issues, a new liquefaction triggering model is developed for evaluating liquefaction potential of soils subjected to ground motions from induced earthquakes in OTK. This model is developed following methods used in Green et al. (2017, 2020) to develop analogous models for evaluating liquefaction potential due to tectonic earthquakes in the central and eastern United States (CEUS) and due to induced earthquakes resulting from natural gas extraction in the Groningen region of the Netherlands. This approach involves developing regional induced seismicity-specific r_d and MSF relationships for calculating CSR* within the context of existing stress-based liquefaction evaluation procedures. These relationships are developed based on numerical site response analyses performed using induced ground motion recordings from OTK and representative soil profiles from liquefaction-susceptible sites in the region. Site response analyses are used to generate profiles of r_d and number of equivalent cycles (n_{eq}) for each motion/profile combination. Generated data are then used to regress new r_d and MSF relationships for injection-induced seismic ground motions in OTK.

The following sections discuss differences between induced and tectonic ground motions and the suitability of existing liquefaction triggering models for use with induced earthquakes. Regression of the new liquefaction triggering model is then discussed, and the proposed model is presented. Model validation results and conclusions drawn from this study are then presented.

2.2 Differences Between Induced and Tectonic Ground Motion Characteristics

Several studies have noted differences between the ground motion characteristics of tectonic and induced earthquakes (e.g., Hough 2014; Bommer et al. 2016; Novakovic et al. 2018; Zalachoris and Rathje 2019). However, there is some debate over the underlying mechanisms for these differences. Several studies found that stress drops associated with induced events are lower than those of similarly-sized tectonic earthquakes (e.g., Hough 2014; Boyd et al. 2017; Sumy et al. 2017). Other studies have found that there is no significant difference in the observed stress drops for induced versus tectonic events once rupture depth, faulting mechanism, and other factors are taken into account (e.g., Zhang et al. 2016; Cramer 2017; Huang et al. 2017; Kaski and Atkinson 2017; Yenier et al. 2017; Wu et al. 2018). Although stress drops may be similar for induced and tectonic earthquakes with the same focal depth and focal mechanism, induced earthquakes in OTK generally have shallower focal depths than tectonic earthquakes in the CEUS (e.g., Huang et al. 2017; Zalachoris and Rathje 2019). As a result, induced events in OTK tend to have lower stress drops, on average, than tectonic events in the CEUS. Additionally, the predominantly strike-slip earthquakes in areas of the central US, such as in OTK, tend to have smaller stress drops than predominantly reverse fault earthquakes in the eastern US (Huang et al. 2017). As a result, induced events in OTK will tend to have smaller stress drops on average compared to ground motion catalogs that include ground motions from both the central and eastern US. For a given magnitude, smaller stress drops generally result in smaller high-frequency spectral accelerations. However, several studies (e.g., Novakovic et al. 2018; Zalachoris and Rathje 2019) have noted that, for some M_w, hypocentral distances (R_{hyp}), and frequencies, induced events in OTK can result in larger spectral accelerations than would be expected for similarly-sized tectonic earthquakes in the CEUS.

Zalachoris and Rathje (2019) and Novakovic et al. (2018) both developed ground motion prediction equations (GMPEs) specific to induced seismicity in OTK, hereafter referred to as the ZR19 and Nea18 GMPEs, respectively. Novakovic et al. (2018) found that for small events ($M_w \approx 4$) and high frequencies (> 3 Hz), 5% damped pseudo-spectral accelerations (PSA) for induced events in OTK were similar to those predicted by the Yenier and Atkinson (2015) GMPE for tectonic events in the central and eastern North America (CENA). However, for low frequencies, induced events were found to have higher PSAs for these smaller events. This was attributed to amplification effects associated with regional geology. For larger events ($M_w \geq 5$), Novakovic et al. (2018) found that PSA of induced ground motions were consistently larger than those predicted for tectonic events, especially at high frequencies. They attribute this to differences in magnitude and depth dependence of the stress parameter, which exhibits weak scaling with depth but exhibits much stronger scaling with magnitude. Novakovic et al. (2018) note that this is the result of the large high-frequency spectral accelerations of the largest OTK events. In comparing the Nea18 GMPE to the Atkinson (2015) GMPE for small-to-moderate tectonic events in the WUS, Atkinson (2020) found that peak ground accelerations (a_{max}) for larger induced events in OTK ($M_w > 4$) were higher than for similarly sized tectonic events in the WUS. Based on this observation, Atkinson (2020) concluded that, to the extent that it may be influenced by a_{max}, damage potential may be higher for induced events in OTK than for tectonic events in the WUS.

Zalachoris and Rathje (2019) also found that for small magnitudes, PSA amplitudes for induced events are similar or slightly larger than predicted by the Hassani and Atkinson (2015) [HA15] GMPE for tectonic events in the CENA, which was used as the reference GMPE for their study. However, for larger magnitudes ($M_w > 4.5$), they observed that induced earthquakes tended to exhibit smaller ground motions than predicted by the HA15 GMPE. They note that this may relate to differences in stress drop or other source parameters such as faulting mechanism. Although the ZR19 GMPE generally results in smaller predicted PSA than the HA15 GMPE, Zalachoris and Rathje (2019) note that for $R_{hyp} < 20$ km, PSA for induced ground motions were larger than those predicted by the HA15 GMPE. Larger PSA at small R_{hyp} was observed at all periods but was most pronounced for $T \leq 0.1$ s. Zalachoris and Rathje (2019) attribute this to the close proximity of these events to the ground surface, offsetting the smaller stress drops. Zalachoris and Rathje (2019) also found that linear-elastic site amplification for time-averaged small-strain shear wave velocity of the upper 30 m (V_{s30}) values less than 600 m/s is lower in OTK than predicted by the Hassani and Atkinson (2015) GMPE. They attribute this to the generally moderate soil depths at sites in OTK, which leads to weaker scaling with V_{s30}, even at sites with low V_{s30}.

Example spectra for the ZR19 and Nea18 GMPEs are shown in Figure 2.1. This figure shows 5% damped PSA for the ZR19 and Nea18 GMPEs for induced earthquakes in OTK, the HA15

GMPE for tectonic events in the CEUS, and the Boore et al. (2014) [Bea14] GMPE for tectonic events in the WUS. Spectra are shown for M_w4.5, 5.0, and 5.8, R_{hyp} = 5 and 30 km, V_{s30} = 760 m/s, and depth of 5 km. As shown in this figure, for small R_{hyp} and M_w4.5 and M_w5.0, spectral accelerations are higher for induced earthquakes than for tectonic earthquakes across all periods. However, for R_{hyp} = 30 km, induced earthquake ground motions tend to exhibit similar or smaller spectral accelerations than tectonic earthquakes in the CEUS for T < ~0.1-0.2 s. For both R_{hyp}, spectral accelerations for both induced and tectonic ground motions in the CEUS tend to exceed prediction for the WUS, particularly for shorter R_{hyp}, smaller M_w, and shorter periods (T < ~0.2 s).

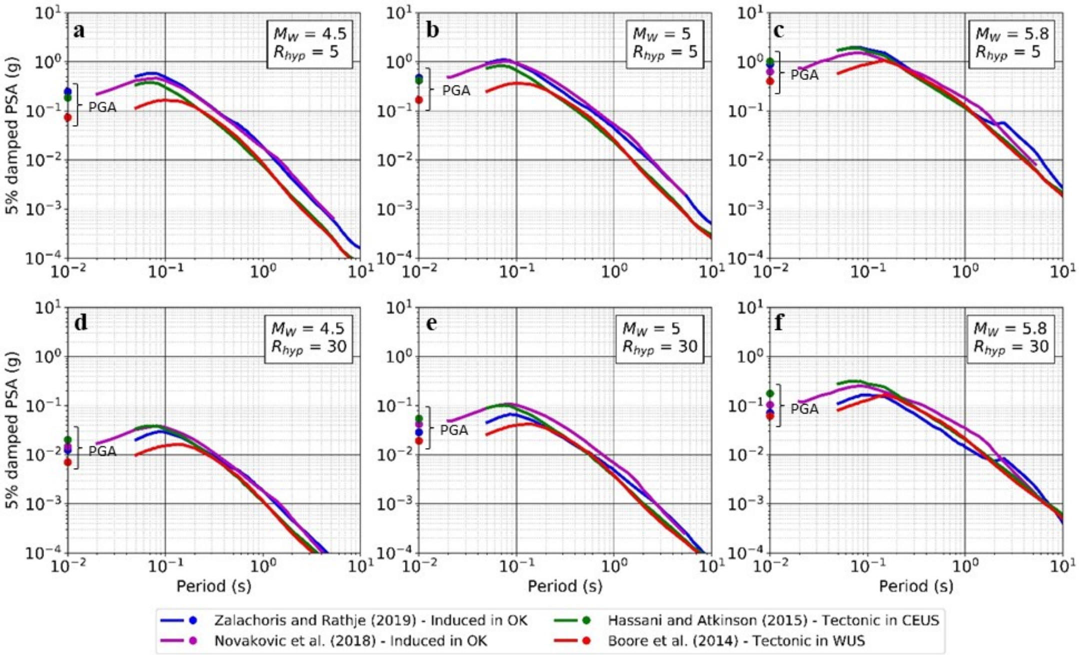

Figure 2.1. 5% damped PSA for M_w 4.5 (a, d), 5.0 (b, e), and 5.8 (c, f), R_{hyp} = 5 (a-c) and 30 (d-f) km, V_{s30} = 760 m/s, and focal depth of 5 km based on the Zalachoris and Rathje (2019) and Novakovic et al. (2018) GMPEs for induced earthquakes in OTK, Hassani and Atkinson (2015) GMPE for tectonic events in the CEUS, and Boore et al. (2014) GMPE for tectonic events in the WUS.

Potential differences in the duration of shaking of induced versus tectonic events may also impact liquefaction triggering. While OTK and the CEUS are considered stable continental tectonic regimes, the WUS is considered an active shallow-crustal regime. As noted, most liquefaction evaluation methods were developed for active shallow-crustal earthquakes. Boore and Thompson (2015) found ground motion duration increases with distance at a much faster rate in stable continental regions than in active crustal regions. This is illustrated in Figure 2.2, which presents path duration models for western North America (WNA) (Boore and Thompson 2014) and eastern North America (ENA) (Boore and Thompson 2015). In the Boore and Thompson (2014, 2015) ground motion duration models, 5% to 95% significant duration ($t_{5\text{-}95}$) is computed by adding this path duration, determined from the relationships plotted Figure 2.2, to source duration, which is a function of corner frequency. Although there are differences in source duration between ENA and WNA, for the small magnitude events relevant to induced events in OTK, the path duration term is much longer than the source duration term (Boore and Thompson 2015). As a result, the trends shown in Figure 2.2 likely reflect the overall trends between $t_{5\text{-}95}$ and site-to-source distance for events in the ENA and WNA.

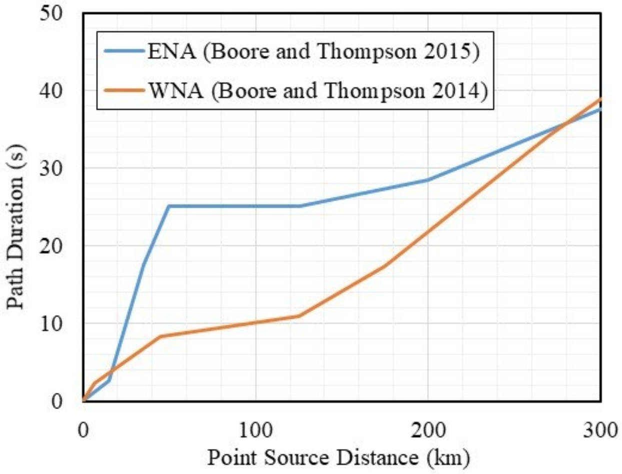

Figure 2.2. Path duration vs. point source distance for ENA (Boore and Thompson 2015) and WNA (Boore and Thompson 2014) ground motions.

2.3 Applicability of Existing Liquefaction Triggering Models to Induced Seismicity

Several methods exist for evaluating liquefaction triggering in soils due to tectonic ground motions. As noted, the most commonly used approach is the stress-based "simplified" liquefaction evaluation procedure (Whitman 1971; Seed and Idriss 1971). In this approach, factor of safety against liquefaction (FS_{liq}) can be computed as:

$$FS_{liq} = \frac{CRR_{M7.5}}{CSR^*} \tag{1}$$

where CSR*is the normalized cyclic stress ratio representing seismic demand, and $CRR_{M7.5}$ is the normalized cyclic resistance ratio representing liquefaction resistance of the soil. CSR* is the average cyclic shear stress (τ_{avg}) imposed on the soil at a given depth normalized by the initial vertical effective stress at that depth, the motion duration of a $M_w7.5$ event, 1 atm initial effective overburden stress, and level ground surface conditions. CSR* is calculated as:

$$CSR^* = CSR\frac{1}{MSF \cdot K_\sigma \cdot K_\alpha} = 0.65\frac{a_{max}}{g}\frac{\sigma_v}{\sigma'_{v0}}r_d\frac{1}{MSF \cdot K_\sigma \cdot K_\alpha} \tag{2}$$

where CSR is cyclic stress ratio, a_{max} is the peak ground acceleration at the ground surface, g is the acceleration of gravity in the same units as a_{max}, σ_v and σ'_{vo} are the total and initial vertical effective stresses at a given depth in a soil profile, and r_d is a dimensionless stress reduction factor that accounts for the non-rigid response of the soil column. MSF is a magnitude scaling factor that adjusts CSR* for shaking duration based on a reference $M_w7.5$ event, K_σ is a correction factor for initial vertical effective overburden stress using a reference initial effective overburden stress of 1 atm, and K_α is a correction factor for initial horizontal static shear stress using a reference initial static shear stress of zero (e.g., level ground conditions). The value 0.65 is an arbitrary value defining the ratio of τ_{avg} to τ_{max}, the maximum shear stress imposed by the cyclic loading, (i.e., $\tau_{avg} = 0.65 \cdot \tau_{max}$).

$CRR_{M7.5}$ represents the resistance of the soil to liquefaction triggering during an $M_w7.5$ event under level ground surface conditions and an initial vertical effective stress of 1 atm. $CRR_{M7.5}$ is typically correlated to a normalized in-situ test metric, such as normalized blow count ($N_{1,60cs}$) from standard penetration tests (SPTs); normalized tip resistance (q_{c1Ncs}) from cone penetration tests (CPTs); or normalized small-strain shear wave velocity (V_{s1}) from shear wave velocity (V_s) tests.

Within the framework of the simplified procedure, $CRR_{M7.5}$ is assumed to be an inherent property of the soil and state, and independent of shaking characteristics. For this reason,

$CRR_{M7.5}$ curves developed using case histories from tectonic earthquakes are suitable for use when estimating FS_{liq} for induced events, absent of the need for consideration of aging effects, etc. In contrast, CSR* is a function of ground response, which is a function of both the bedrock motions and the dynamic response characteristics of the soil. As a result, relationships developed for use in calculating CSR* for tectonic events may not be suitable for use in calculating FS_{liq} for induced events. Specifically, r_d and MSF are both affected by ground motion and soil profile characteristics. As a result, relationships used to estimate r_d and MSF in existing variants of the simplified procedure may be unsuitable for use in estimating profile response and ground motion duration for induced events in OTK

Several relationships for estimating r_d are commonly used in practice (e.g., Idriss 1999; Lasley et al. 2016). However, these relationships may not be applicable for induced events in OTK due to differences in ground motion characteristics between induced and tectonic events, including those discussed in the previous section. Soil profiles tend to exhibit more rigid response if the characteristic wavelength of the earthquake loading is significantly longer than the height of the profile (Green et al. 2020). For this reason, the frequency content of the ground motions has a strong influence on r_d. Larger magnitude events tend to have longer characteristic periods and, hence, longer wavelengths (e.g., Green et al. 2019). Green et al. (2020) note that, for this reason, the commonly used Idriss (1999) r_d relationship, which was developed for moderate to major tectonic events with $5 < M_w < 8$ may be inappropriate for use with evaluating the liquefaction potential for induced earthquakes, which tend to have much smaller magnitudes (e.g., $M_w \leq 5.8$ in OTK). Further, as discussed previously, frequency content and amplitudes for induced events are different than those of tectonic events in the CEUS or WUS. As a result, r_d will tend to be different for induced events. Additionally, Lasley et al. (2016) note that differences in regional geology, such as differences in impedance contrast, can affect r_d. Consequently, r_d relationships developed for the WUS are likely not be suitable for use with induced earthquakes in the CEUS.

As noted, MSF account for the influence of shaking duration on liquefaction triggering. MSF is typically computed as the ratio of the number of equivalent cycles (n_{eq}) for an $M_w7.5$ ($n_{eqM7.5}$) event to that of an event with a given M_w (n_{eqM}), raised to the power *b* [i.e., MSF = $(n_{eqM7.5}/n_{eqM})^b$], where *b* is the negative slope of the CSR vs. number of cycles to trigger liquefaction curve, both in log scale. The equivalent cycles concept converts a given earthquake loading to an equivalently damaging number of uniform cycles (e.g., Lasley et al. 2017). In this study, n_{eq} relationships are based on the approach proposed by Green and Terri (2005), which uses dissipated energy as the damage metric. Using this approach, Lasley et al. (2017) developed n_{eq} relationships for use with tectonic events in the WUS and CEUS, and Green et al. (2020) developed n_{eq} and MSF relationships for use with induced events in the Groningen region of the Netherlands. These studies found n_{eq}, and by extension MSF, to be a function of M_w, a_{max}, and, for Green et al. (2020), V_{s12}, which is the time-weighted average V_s of the upper 12 m of the profile. Green et al. (2017) developed MSF relationships for the CEUS and WUS based on the Lasley et al. (2017) n_{eq} relationships. Although the Green et al. (2017) CEUS, Green et al. (2017) WUS, and Green et al. (2020) Groningen MSF relationships were developed using the same approach, the resulting MSF relationships are different, consistent with findings from previous studies showing that ground motion duration characteristics are very different among these regions (e.g., Lee and Green 2014; Bahrampouri et al. 2021). Lasley et al. (2017) also note that impedance contrast differences between regions lead to differences in n_{eq} and MSF. Differences in these MSF relationships demonstrate the effect that regional geology and tectonic setting have on MSF (Lasley et al. 2017; Green et al. 2019, 2020). For this reason, MSF relationships developed for tectonic events in the CEUS or WUS are likely unsuitable for use with induced events in OTK.

As discussed above, due to differences in ground motion characteristics and regional geology, it is doubtful that r_d and MSF relationships used in existing simplified liquefaction triggering models are suitable for estimating CSR* for induced earthquakes in OTK. For this reason, r_d and MSF relationships specific to induced seismicity in OTK are needed. Development of these new relationships is discussed in the following section.

2.4 Model Development

An induced seismicity-specific liquefaction triggering model, incorporating r_d and MSF relationships specific to induced events in OTK, is developed. Towards this end, we follow the methods used by Green et al. (2017, 2020) to develop analogous models for evaluating the liquefaction potential from tectonic earthquakes in the CEUS and from induced earthquakes in the Groningen region of the Netherlands. Accordingly, equivalent-linear site response analyses are performed using induced ground motion recordings and representative regional soil profiles from OTK. The resulting r_d and n_{eq} values from the site response analyses are then regressed to develop new r_d and MSF relationships. The following sections describe the ground motion database, soil profiles, and site response analysis procedures used in model development.

2.4.1 Induced Ground Motion Database

Motions are selected from the induced ground motion database for OTK compiled and processed by the Center for Integrated Seismic Research (CISR) at the University of Texas at Austin (Zalachoris et al. 2020). All motions in the database were consistently processed as described in Zalachoris and Rathje (2019). For the purpose of this research, the selected motions had $M_w > 3.5$ and $R_{hyp} < 70$ km. Although the range of magnitudes of interest to liquefaction hazard evaluations is generally higher than M_w4.5 (Green and Bommer 2019), lower magnitude events are included to constrain the lower end of the regressed r_d and MSF relationships. Induced earthquakes are generally small magnitude events with shallow focal depths. As a result, induced ground motions may exhibit large amplitudes near the source but attenuate quickly with distance (Zalachoris and Rathje 2019; Atkinson 2020). Accordingly, R_{hyp} of the selected motions is limited to 70 km because induced motions at greater distances are not expected to be damaging.

Ground motion recordings from sites with $V_{s30} \geq 650$ m/s are preferred for this study. However, due to the scarcity of motions having $M_w > 5.1$ and $R_{hyp} < 70$ at sites with $V_{s30} \geq 650$ m/s, ground motions from softer sites ($500 \leq V_{s30} \leq 650$) are selected and spectrally matched to reference rock site conditions using the approach developed by Al Atik and Abrahamson (2010) and implemented in the program RSPMatch09. Recorded ground motions are matched to spectra developed using the ZR19 and spectra developed using the Nea18 GMPEs.

The spectral matching process scales ground motions based on amplitude while preserving duration characteristics such as $t_{5\text{-}95}$ (Al Atik and Abrahamson 2010). As a result, scaling ground motions for an event of a given magnitude to the response spectrum of a larger magnitude event will reflect the increased amplitude but not necessarily the increased duration expected for a larger magnitude event. This can lead to errors when trying to model the relationship between

M_w, a_{max}, and n_{eq} because n_{eq} is directly related to ground motion duration. Similar issues occur when spectrally matching ground motions with a given R_{hyp} to a spectrum developed using a different R_{hyp}, because the influence of R_{hyp} on duration and n_{eq} may not be properly maintained during the spectral matching process. To avoid these errors and to preserve the relationships among M_w, a_{max}, R_{hyp}, duration, and n_{eq}, ground motions are only spectrally matched to spectra for events having the same M_w and R_{hyp}. This allows ground motions from softer sites ($500 \leq V_{s30} \leq 600$) to be scaled to stiffer site conditions for use in site response analyses while maintaining the effects of M_w and R_{hyp} on ground motion duration. These constraints limit the available motions for use in site responses analyses, but still provide several additional ground motions with $M_w \geq 4.7$ and $R_{hyp} < 50$ km, while limiting any issues in modelling n_{eq}. Ground motions are scaled to spectra for site conditions at the National Earthquake Hazards Reduction Program B/C site class boundary ($V_{s30} = 760$ m/s) (American Society of Civil Engineers 2017). A sensitivity analysis on the effect of the target V_{s30} on site response was performed, and it was found that site response results are fairly insensitive to the selected target V_{s30} for 760 m/s $\leq V_{s30} \leq$ 1100 m/s. This corresponds to the range of V_{s30} values for the majority of recording stations used as sources for this study. A comparison of response spectra for recorded and matched ground motions for the range where these motions overlap ($4.7 \leq M_w \leq 5.0$, $R_{hyp} < 30$ km) is provided in Figure B.2 in Appendix B. As shown in this figure, there is good agreement between recorded and matched spectra within this region.

The resulting R_{hyp}-M_w distribution of the ground motions used in the site response analyses is shown in Figure 2.3. To account for potential differences in the spectra generated using the ZR19 and Nea18 GMPEs, two ground motion databases are developed. The first is comprised of the recorded ground motions and motions matched to spectra developed using the ZR19 GMPE, and the second is comprised of the recorded ground motions and motions matched to spectra developed using the Nea18 GMPE. Site response and regression analyses are carried out using both databases. Although the ground motion database used in this study is mostly comprised of recorded motions, it is still considered useful to regress models for databases based on each GMPE. This is done to evaluate the effect of GMPE selection on the r_d and MSF relationships and to allow for consideration of epistemic uncertainty related to GMPE selection. Additionally, the matched motions account for many of the largest M_w motions used in the analysis, particularly large M_w events with $R_{hyp} < 50$ km. These events tend to have the greatest engineering impact as they result in large a_{max}. As a result, it is important to assess the effect that GMPE selection has on the regressed r_d and MSF relationships.

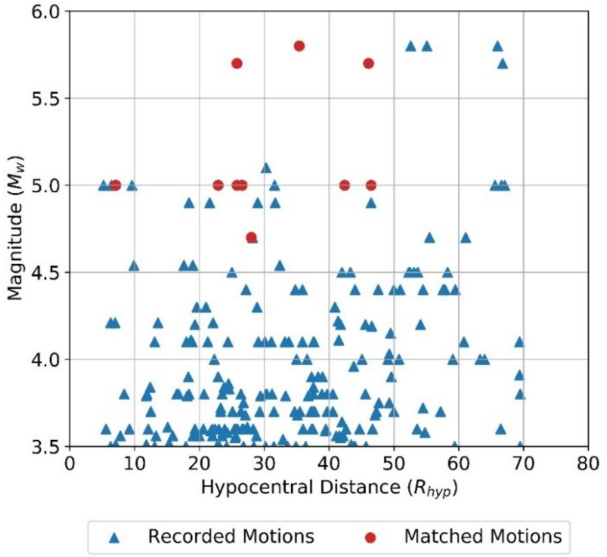

Figure 2.3. Ground motion magnitude-distance distribution.

2.4.2 Representative Soil Profiles

Representative soil profiles for the region are developed based on soil profile information from several sites across OTK. A map of these sites is presented in Figure B.1 in Appendix B. Soil profile data at these sites were provided by contractors and government agencies and included a mix of CPT, SPT, and lab test data. Soil parameters required for equivalent-linear site response analysis include V_s, total unit weight of the soil, and depth to the groundwater table. Additional soil parameters used during site response analyses include PI, over-consolidation ratio, and strength parameters such as friction angle, $(N_1)_{60}$, and undrained shear strength. V_s values are estimated using correlations with CPT (Robertson and Cabal 2015; Ulmer et al. 2020) and SPT (Wair et al. 2012; Ulmer et al. 2020). Additional soil parameters are obtained from lab test data when available. At sites where lab test information was not available, soil parameters are estimated using CPT correlations (Robertson and Cabal 2015) or randomly assigned using soil type-specific distributions developed at sites where lab test data were available.

Although the data provided for these sites allowed for reasonable characterization of the soil profiles, information about the bedrock layers (e.g., V_s, weathered rock thickness) was generally not available. To address this issue, bedrock V_s data from Stephenson et al. (2021) were used to estimate bedrock layering and V_s values at each site. Stephenson et al. (2021) developed V_s profiles at 28 seismograph stations located in central and northern Oklahoma. The developed V_s profiles consisted of 3-4 layers generally intended to reflect a soil/weathered rock/rock profile. Weathered rock and bedrock information from these profiles was used to develop statistical distributions for V_s of the bedrock ($V_{s\text{-bed}}$) and thickness of the weathered rock zone between soil and bedrock layers. These distributions are used to randomly assign $V_{s\text{-bed}}$ and weathered rock thickness for the developed site profiles. $V_{s\text{-bed}}$ for the Stephenson et al. (2021) ranged from 800 to 3500 m/s and roughly followed a log-normal distribution with a mean ($\mu_{\ln(Vs\text{-bed})}$) of 7.26 (1508.5 m/s) and standard deviation ($\sigma_{\ln(Vs\text{-bed})}$) of 0.32. This range is consistent with $V_{s\text{-bed}}$ values for CEUS site profiles used by Lasley et al. (2016, 2017) in developing r_d and n_{eq} relationships for the CEUS.

The thickness of the weathered rock transition zone between the soil profile and bedrock layers ranged from 0 to 28 m and approximately exhibited a normal distribution with mean of 16 m and standard deviation of 7.5 m. This weathered rock transition was also added to the developed profiles using a randomly assigned thickness based on the Stephenson et al. (2021) distribution. For the purposes of developing the profiles, the transition zone was divided into four sublayers with V_s values linearly increasing from the V_s at the base of the soil profile to $V_{s\text{-bed}}$. The resulting weathered rock transitions are consistent with weathered rock transitions observed in the Lasley et al. (2016, 2017) CEUS profiles.

In order to account for the effect of the random distributions used to develop the site profiles, three iterations of each profile are created using different realizations of each randomly assigned soil or rock parameter. Site response analysis results for all iterations are included in the regression database. Figure B.3 in Appendix B provides a comparison of the resulting OTK V_s profiles with the Lasley et al. (2016, 2017) CEUS V_s profiles. The OTK V_s profiles are similar to several of the Lasley et al. (2016, 2016) V_s profiles, but exhibit shallower depths to bedrock than most of the Lasley et al. (2016, 2017) V_s profiles. This is consistent with the moderate soil depths in OTK noted by Zalachoris et al. (2017). The ShakeVT2 profiles used in the site response analysis are included as an electronic supplement to this document.

2.4.3 Equivalent-Linear Site Response Analysis

Equivalent-linear site response analyses are performed using ShakeVT2 (Lasley et al. 2014; Thum et al. 2019), a rewrite of SHAKE and SHAKE91 (Schnabel et al. 1972; Idriss and Sun 1992). Site response analyses are used to compute r_d and n_{eq} data for each liquefiable soil layer as a function of depth for each ground motion-site profile combination. Separate analyses are performed using both the Darendeli and Stokoe (2001) and Ishibashi and Zhang (1993) shear modulus reduction and damping degradation (MRD) curves. These curves are used in site response analysis to model nonlinear response of the soil. These analyses are repeated for both ground motion databases discussed previously, resulting in four site response analysis datasets. These are the datasets developed using: (1) the Zalachoris and Rathje (2019) ground motion database with Ishibashi and Zhang (1993) MRD curves (hereafter referred to as the ZR19_IZ dataset), (2) the Zalachoris and Rathje (2019) ground motion database with Darendeli and Stokoe (2001) MRD curves (ZR19_DS dataset), (3) the Novakovic et al. (2018) ground motion database with Ishibashi and Zhang (1993) MRD curves (Nea18_IZ dataset), and (4) the Novakovic et al. (2018) ground motion database with Darendeli and Stokoe (2001) MRD curves (Nea18_DS dataset). Separate r_d and MSF relationships are developed for each dataset to account for the effects of MRD and GMPE selection on the regressed relationships.

2.5 Proposed r_d Relationship

Figure 2.4 presents the r_d from site response analyses as a function of the predictor variables used in the Green et al. (2020) model. These include depth, M_w, $\ln(a_{max})$, and V_{s12}. For clarity, plots for M_w, $\ln(a_{max})$, and V_{s12} are shown for depths from 5 to 10 m, but similar trends are observed at other depths. Other variables were considered for inclusion in the model, but none were shown to be significant predictors of r_d. Plots are shown for the ZR19_IZ dataset, but the observed trends are similar for all datasets. The trend of r_d with depth follows a sigmoidal shape with r_d decreasing with depth, similar to the trend observed by Green et al. (2020). Positive correlations are observed between r_d and both M_w and V_{s12}, while a negative correlation is observed between

r_d and a_{max}. The observed trend between M_w and r_d is consistent with previous studies and the expectation that larger magnitude events with longer wavelengths will lead to more rigid profile response (higher r_d). The observed positive trend between V_{s12} and r_d is also consistent with the findings of Green et al. (2020) and Lasley et al. (2016). Stiffer soil profiles (higher V_{s12}) are expected to respond more rigidly, as is demonstrated by the data shown in Figure 2.4. The negative correlation between a_{max} and r_d is consistent with the findings of Green et al. (2020). Lasley et al. (2016) also noted that a strong correlation between r_d and shaking intensity as measured by a_{max} would be expected, but they did not find significant correlation between a_{max} and r_d for their dataset. Based on the observed trends in the r_d datasets, as well as observations from previous studies, it was decided that M_w, a_{max}, and V_{s12} would be included in the r_d regression.

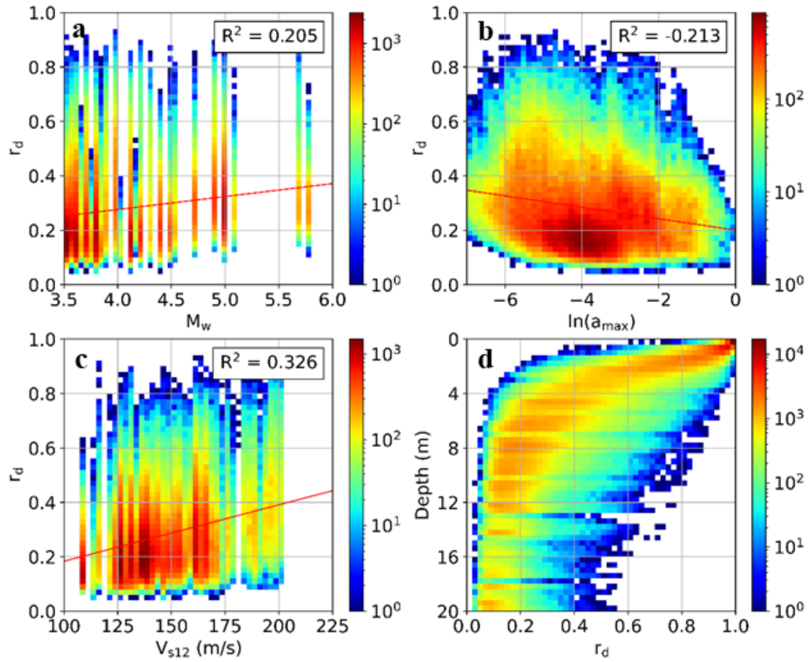

Figure 2.4. Heat map of r_d versus potential predictor variables: (a) M_w, (b) $\ln(a_{max})$, (c) V_{s12}, and (d) depth. Plots for M_w, $\ln(a_{max})$, and V_{s12} are for depths of 5 to 10 m. Values shown are for the ZR19_IZ dataset.

Statistical regressions are performed using the program *R* (R Core Team 2018) with the *lme4* package (Bates et al. 2015). The *lme4* package implements mixed effects regression, which is used to avoid potential biases from earthquakes or profiles that have a relatively large number of data points. Random effects terms are included during both the r_d and n_{eq} regressions. These include an earthquake event term and a soil profile term as shown in the r_d and n_{eq} relationships presented in this and the following section.

Several functional forms for r_d were considered, including those used by Lasley et al. (2016) and Green et al. (2020). The final function form is a slightly modified version of the r_d functional form from Green et al. (2020), which is based on a sigmoid shape with a main variable of logarithmic depth, and location and scale parameters that are functions of M_w, a_{max}, and V_{s12}. The proposed r_d relationship is:

$$r_{d-OK} = 1 - \frac{\alpha_{rd}}{1 + \exp\left[-\frac{\ln(z) - \beta_{rd}}{\gamma_{rd}}\right]} + \theta_{rd} + \delta_{\text{event\_rd}} + \delta_{\text{profile\_rd}} + \delta_{\text{0\_rd}};\ 0 \le r_d \le 1 \tag{3}$$

where z is depth in m, α_{rd}, β_{rd}, and γ_{rd} are functions of M_w, a_{max}, and V_{s12}; θ_{rd} is a regression coefficient; δ_{event_rd} and $\delta_{profile\_rd}$ are random effect terms for the earthquake events and soil profiles, respectively; and δ_{0_rd} is the residual. The random effect terms and residual terms are assumed to be zero-mean normally distributed random variables with standard deviations of τ_{event_rd}, $\tau_{profile\_rd}$, and σ_{0_rd} for the event, profile, and residual terms, respectively. As with the Green et al. (2020) study, an apparent scaling break for relatively large values of a_{max} (> 0.25g for this study) was observed and is included in the regression. Functional forms with random effect terms included in the α_{rd} term, providing for depth-dependent random effects, were considered. However, analysis of the residuals of a mixed effect regression that did not include the profile random effect showed no significant trends in depth-dependence as a function of profile. Similarly, an analysis of the residuals of a mixed effect regression that did not include the event random effect showed no significant trends in depth-dependence as a function of earthquake event. As a result, depth-independent random effect terms are used as shown in Equation 3.

To allow this model to be used for varying levels of site characterization, α_{rd}, β_{rd}, and λ_{rd} are regressed for two cases: one where V_{s12} is available (referred to as r_d Model 1) and one where

V_{s12} is not available (referred to as r_d Model 2). The resulting functional forms for α_{rd}, β_{rd}, and γ_{rd} are:

Model 1 (with V_{s12}):

$$\alpha_{rd} = a_1 + a_4 \cdot M_w + a_5 \cdot \ln(a_{max}) + a_9 \cdot V_{s12};\ \text{for } a_{max} \le 0.25\text{g} \tag{4a}$$

$$= a_1 + a_4 \cdot M_w + a_5 \cdot \ln(a_{max}) + a_8 \cdot \ln\left(\frac{a_{max}}{0.25}\right) + a_9 \cdot V_{s12};\ \text{for } a_{max} > 0.25\text{g} \tag{4b}$$

$$\beta_{rd} = a_2 + a_6 \cdot M_w + a_{10} \cdot \ln(a_{max}) + a_{14} \cdot V_{s12};\ \text{for } a_{max} \le 0.25\text{g} \tag{5a}$$

$$= a_2 + a_6 \cdot M_w + a_{10} \cdot \ln(a_{max}) + a_{12} \cdot \ln\left(\frac{a_{max}}{0.25}\right) + a_{14} \cdot V_{s12};\ \text{for } a_{max} > 0.25\text{g} \tag{5b}$$

$$\gamma_{rd} = a_3 + a_7 \cdot M_w + a_{11} \cdot \ln(a_{max});\ \text{for } a_{max} \le 0.25\text{g} \tag{6a}$$

$$= a_3 + a_7 \cdot M_w + a_{11} \cdot \ln(a_{max}) + a_{13} \cdot \ln\left(\frac{a_{max}}{0.25}\right);\ \text{for } a_{max} > 0.25\text{g} \tag{6b}$$

Model 2 (without V_{s12}):

$$\alpha_{rd} = b_1 + b_4 \cdot M_w + b_5 \cdot \ln(a_{max});\ \text{for } a_{max} \le 0.25\text{g} \tag{7a}$$

$$= b_1 + b_4 \cdot M_w + b_5 \cdot \ln(a_{max}) + b_8 \cdot \ln\left(\frac{a_{max}}{0.25}\right);\ \text{for } a_{max} > 0.25\text{g} \tag{7b}$$

$$\beta_{rd} = b_2 + b_6 \cdot M_w + b_9 \cdot \ln(a_{max});\ \text{for } a_{max} \le 0.25\text{g} \tag{8a}$$

$$= b_2 + b_6 \cdot M_w + b_9 \cdot \ln(a_{max}) + b_{11} \cdot \ln\left(\frac{a_{max}}{0.25}\right);\ \text{for } a_{max} > 0.25\text{g} \tag{8b}$$

$$\gamma_{rd} = b_3 + b_7 \cdot M_w + b_{10} \cdot \ln(a_{max});\ \text{for } a_{max} \le 0.25\text{g} \tag{9a}$$

$$= b_3 + b_7 \cdot M_w + b_{10} \cdot \ln(a_{max}) + b_{12} \cdot \ln\left(\frac{a_{max}}{0.25}\right);\ \text{for } a_{max} > 0.25\text{g} \tag{9b}$$

where a_i and b_i are regression coefficients, a_{max} is in units of g, and V_{s12} is in units of m/s. A bootstrapping technique (Efron and Tibshirani 1994) is used during regression to obtain mean and standard deviations for all regression coefficients. The bootstrapping technique consists of the following steps:

1. 30,000 data points are randomly selected (without replacement) from the dataset.

2. Regression coefficients are obtained for the sampled 30,000 data points and the functional form of interest.
3. Steps 1 and 2 are repeated 1,000 times and the regression coefficients for each iteration are recorded.
4. The mean and standard deviation of the distribution of each regression coefficient are calculated.

The mean values and standard deviations of the regression coefficients for the r_d models are presented in Table 2.1 and Table 2.2 for r_d Model 1 and Model 2, respectively. Regressed values of τ_{event_rd} and $\tau_{profile\_rd}$ are also included. Standard deviation of the regressed coefficients can be used as a measure of whether the coefficients are well-constrained by the data. Based on the low observed standard deviations relative to the mean values, coefficients associated with M_w, a_{max}, and V_{s12} appear well-constrained by the data. Standard deviations are somewhat higher for terms in α_{rd} than for terms in β_{rd} and γ_{rd}. This appears to reflect the relatively small variation in r_d at larger depths, which is governed in the model by α_{rd}. The α_{rd} terms are kept because model residuals at depth increased for models where these terms are removed.

Evaluating the uncertainty in these coefficients provides some insight into the effects of model extrapolation on r_d prediction. As noted, small coefficient standard deviations relative to mean values indicate the model is well-constrained within the range of available data. However, when extrapolating beyond this range, coefficient uncertainty is likely to propagate into greater uncertainty in r_d predictions. This is of particular concern when extrapolating the model to the large M_w, low R_{hyp} range, which is critical to consider when evaluating seismic hazard, but where little data is available.

Table 2.1. Regression coefficients for r_d Model 1.

Dataset:	**ZR19_DS**	**Nea18_DS**	**ZR19_IZ**	**Nea18_IZ**
a_1	0.9504	0.9843	0.9514	0.9693
σ_{a1}	0.02106	0.02286	0.02085	0.02281
a_2	-1.1204	-1.2094	-0.9855	-1.0643
σ_{a2}	0.05544	0.05976	0.05682	0.05977
a_3	0.05063	0.00191	0.03472	-0.03643
σ_{a3}	0.03463	0.03781	0.03344	0.03706
a_4	-0.01387	-0.02252	-0.00614	-0.01079
σ_{a4}	0.003986	0.004450	0.003882	0.004339
a_5	-0.01211	-0.01133	-0.00957	-0.00911
σ_{a5}	0.0014337	0.0014482	0.0013634	0.0013855
a_6	0.2283	0.2536	0.2261	0.2480
σ_{a6}	0.008446	0.009438	0.008375	0.009193
a_7	0.09263	0.1090	0.09936	0.1210
σ_{a7}	0.00718	0.00788	0.00694	0.00789
a_8	0.1148	0.1365	0.0672	0.0981
σ_{a8}	0.02984	0.03208	0.01700	0.01862
a_9	$-2.179\text{x}10^{-4}$	$-1.848\text{x}10^{-4}$	$-3.672\text{x}10^{-4}$	$-3.404\text{x}10^{-4}$
σ_{a9}	$8.383\text{x}10^{-6}$	$8.515\text{x}10^{-6}$	$8.361\text{x}10^{-6}$	$8.582\text{x}10^{-6}$
a_{10}	-0.1470	-0.1452	-0.1237	-0.1228
σ_{a10}	0.004163	0.004199	0.003993	0.004088
a_{11}	-0.050288	-0.04787	-0.047108	-0.04516
σ_{a11}	0.002943	0.002915	0.002723	0.002719
a_{12}	-1.0824	-1.1500	-0.5747	-0.5665
σ_{a12}	0.09958	0.09958	0.05256	0.05083
a_{13}	0.7333	0.7687	0.3977	0.4480
σ_{a13}	0.1298	0.1314	0.0574	0.0625
a_{14}	0.004663	0.004664	0.004568	0.004556
σ_{a14}	0.0002191	0.0002247	0.0002289	0.0002346
θ_{rd}	0.01109	0.01421	0.00990	0.01367
$\sigma_{\theta rd}$	0.002086	0.002215	0.001998	0.002105
τ_{event_rd}	0.0547	0.0570	0.0550	0.0574
$\tau_{profile\_rd}$	0.0380	0.0379	0.0360	0.0355

Table 2.2. Regression coefficients for r_d Model 2.

Dataset:	ZR19_DS	Nea18_DS	ZR19_IZ	Nea18_IZ
b_1	0.9147	0.9545	0.8939	0.9172
σ_{b1}	0.01842	0.02133	0.01842	0.01989
b_2	-0.4313	-0.5251	-0.3243	-0.4058
σ_{b2}	0.04749	0.04971	0.04541	0.04927
b_3	0.04963	0.00539	0.02729	-0.03972
σ_{b3}	0.03562	0.03883	0.03341	0.03740
b_4	-0.01573	-0.02466	-0.00802	-0.01321
σ_{b4}	0.004114	0.004746	0.004148	0.004545
b_5	-0.01027	-0.00944	-0.00838	-0.00806
σ_{b5}	0.001406	0.001452	0.001364	0.001320
b_6	0.2242	0.2502	0.2240	0.2462
σ_{b6}	0.008863	0.009666	0.008755	0.009936
b_7	0.09009	0.1052	0.09814	0.1185
σ_{b7}	0.00736	0.00816	0.00702	0.00796
b_8	0.1507	0.1757	0.0853	0.1148
σ_{b8}	0.03222	0.03564	0.01713	0.01837
b_9	-0.1435	-0.1421	-0.1218	-0.1210
σ_{b9}	0.004378	0.004236	0.004075	0.003851
b_{10}	-0.04905	-0.04675	-0.04671	-0.04499
σ_{b10}	0.002899	0.003002	0.002757	0.002778
b_{11}	-1.0219	-1.0755	-0.5377	-0.5309
σ_{b11}	0.10696	0.10234	0.05543	0.05019
b_{12}	0.7772	0.8222	0.4162	0.4628
σ_{b12}	0.1385	0.1446	0.0605	0.0610
θ_{rd}	0.00856	0.01145	0.00855	0.01209
$\sigma_{\theta rd}$	0.002188	0.002227	0.002181	0.002203
τ_{event_rd}	0.0548	0.0570	0.0551	0.0574
$\tau_{profile\_rd}$	0.0456	0.0449	0.0445	0.0437

Plots of model residuals as a function of predictor variables for r_d Models 1 and 2 for the ZR19_IZ dataset are shown in Figure 2.5 and Figure 2.6, respectively. This includes M_w, a_{max}, V_{s12}, and depth. Both loess and linear fits to the residuals are presented to show overall trends in the residual. Error bars showing σ_{0_rd} of the binned residuals are also presented. Although there is some variation, binned residuals tend to be mean-zero and normally distributed for both models. This suggests that both models provide acceptable fits to the r_d data for the range of M_w, a_{max}, V_{s12}, and depth considered. Although both models provide acceptable fits of the data, the inclusion of V_{s12} in Model 1 significantly reduced $\tau_{profile}$, indicating a better fit. Model 1 also provided better fits for larger values of a_{max}, which is significant for liquefaction hazard analyses.

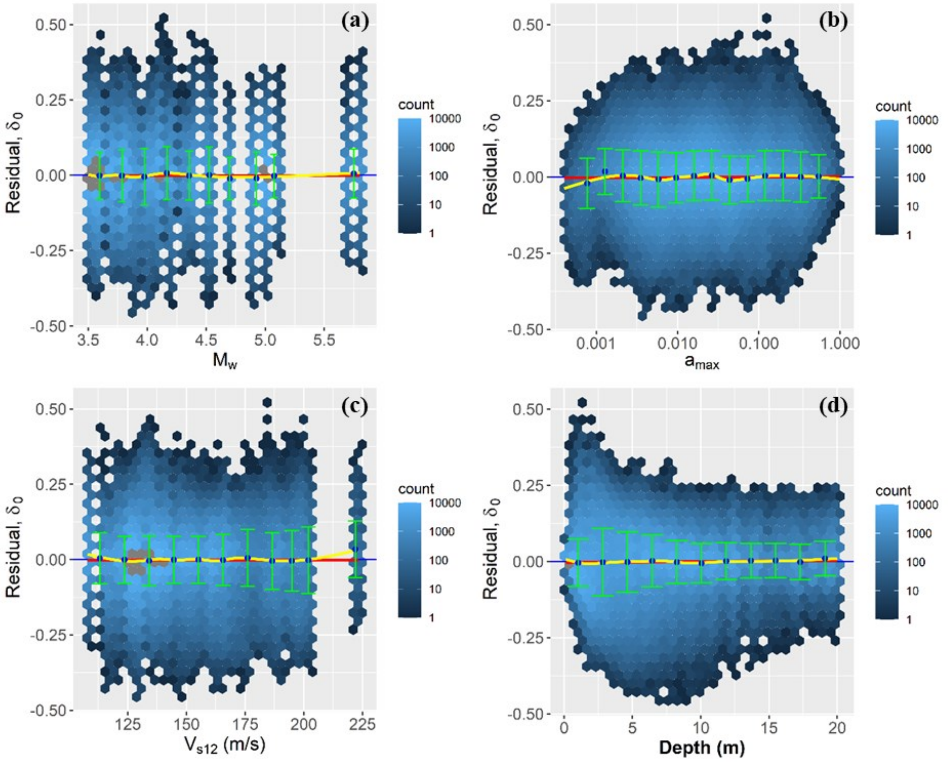

Figure 2.5. Heat map of r_d Model 1 residuals versus (a) M_w, (b) a_{max}, (c) V_{s12}, and (d) depth. Yellow lines show loess fits to the residuals, red lines show linear trends fitted to the residuals, and the green error bars show the means and standard deviations of the binned residuals. Results shown for ZR19_IZ dataset.

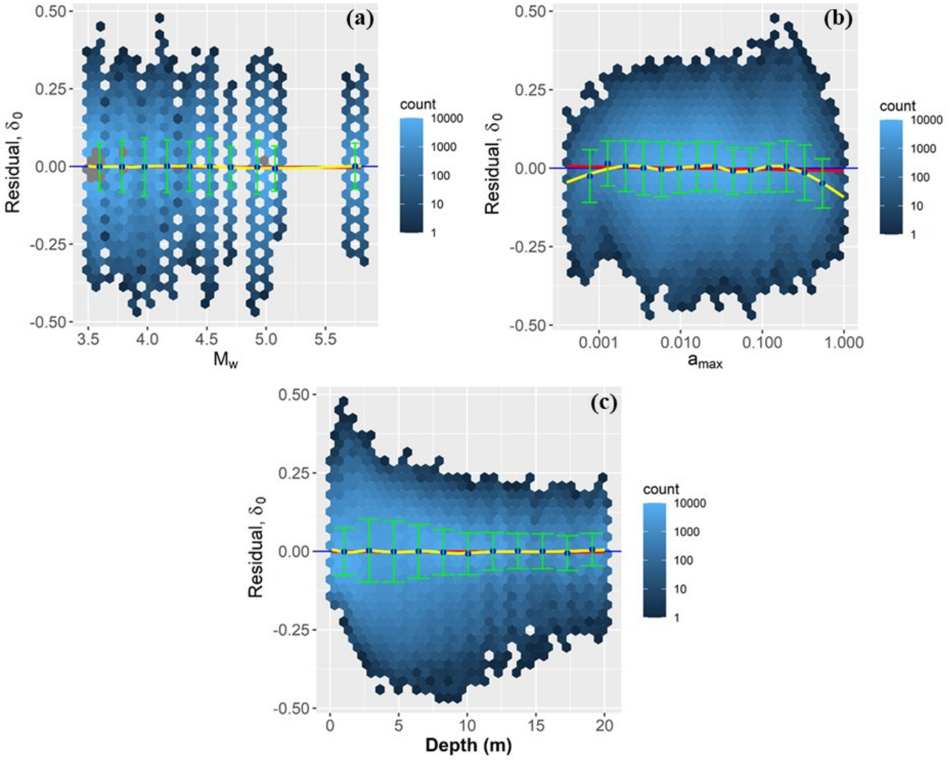

Figure 2.6. Heat map of r_d Model 2 residuals versus (a) M_w, (b) a_{max}, and (c) depth. Yellow lines show loess fits to the residuals, red lines show linear trends fitted to the residuals, and the green error bars show the means and standard deviations of the binned residuals. Results shown for ZR19_IZ dataset.

Assuming model random effect terms are uncorrelated, the total standard deviation (σ_{total_rd}) can be estimated as:

$$\sigma_{Total\_rd} = \sqrt{\tau^2_{event\_rd} + \tau^2_{profile\_rd} + \sigma^2_{0\_rd}} \tag{10}$$

As shown in Figure 2.5 and Figure 2.6, δ_{0_rd} exhibits a heteroscedastic standard deviation (σ_{0_rd}) with respect to depth, meaning that σ_{0_rd} is not constant with depth. Rather, σ_{0_rd} increases with depth for z ≤ 3.5 m and decreases with depth for z > 3.5 m. This behavior was modeled as:

$$\sigma_{0_{rd}}(z) = \frac{c_5}{\{1+\exp[-c_7(\ln(z)-c_6)]\}} \cdot \left[\frac{c_3}{\{1+\exp[-c_4(3.5-c_2)]\}} + c_1\right]; \quad \text{for z} \leq 3.5 \text{ m} \tag{11a}$$

$$= \frac{c_3}{\{1+\exp[-c_4(z-c_2)]\}} + c_1 \text{ ; for z } > 3.5 \text{ m} \tag{11b}$$

A logistic scaling term, the first term in Equation 11a, is used for depths less than 3.5 m because it provides a good fit to the data and ensures σ_0 is be zero at the ground surface. This constraint on σ_0 is used to maintain the constraint of $r_d \leq 1$ near the ground surface. The same functional form is used for σ_{0_rd} both r$_d$ Models 1 and 2. Regression coefficients for Equation 11 are determined through non-linear least squares regression. The regressed coefficients for σ_{0_rd} are shown in Table 2.3.

Table 2.3. Regression coefficients for the σ0_rd model.

Model	Dataset	*c1*	*c2*	*c3*	*c4*	*c5*	*c6*	*c7*
1	ZR19_DS	0.0537	6.0516	0.0647	-0.3607	1.0243	-0.9984	1.6515
1	Nea18_DS	0.0528	5.8068	0.0682	-0.3412	1.0225	-0.9988	1.6857
1	ZR19_IZ	0.0493	6.2395	0.0702	-0.3217	1.0324	-0.9536	1.5548
1	Nea18_IZ	0.0498	6.0594	0.0720	-0.3126	1.0316	-0.9598	1.5610
2	ZR19_DS	0.0521	5.8598	0.0702	-0.3411	1.0268	-1.1561	1.5023
2	Nea18_DS	0.0529	5.7001	0.0716	-0.3322	1.0261	-1.1574	1.5126
2	ZR19_IZ	0.0498	6.4478	0.0687	-0.3390	1.0366	-1.1536	1.3749
2	Nea18_IZ	0.0504	6.2425	0.0714	-0.3207	1.0364	-1.1525	1.3777

Although the random effect terms used in Equation 3 are considered depth-independent, it is still desirable to scale them to zero at the ground surface to ensure σ_{Total_rd} = 0 and r$_d$ ≤ 1 near the ground surface. To this end, the logistic scaling term from Equation 11a is applied to τ_{event} and $\tau_{profile}$ at depths less than 3.5 m. The resulting equations for $\tau_{event\_rd}(z)$ and $\tau_{profile}(z)$ are:

$$\tau_{event\_rd}(z) = \frac{c_5}{\{1+\exp[-c_7(\ln(z)-c_6)]\}} \cdot \tau_{event\_rd_0}; \text{ for z } \leq 3.5 \text{ m} \tag{12a}$$

$$= \tau_{event\_rd_0}; \text{ for z } > 3.5 \text{ m} \tag{12b}$$

and

$$\tau_{profile\_rd}(z) = \frac{c_5}{\{1+\exp[-c_7(\ln(z)-c_6)]\}} \cdot \tau_{profile\_rd_0}; \text{ for z } \leq 3.5 \text{ m} \tag{13a}$$

$$= \tau_{profile\_rd_0}; \text{ for z } > 3.5 \text{ m} \tag{13b}$$

where $\tau_{event\_rd_0}$ and $\tau_{profile\_rd_0}$ are the depth-independent event and profile random effect standard deviations output during regression (equivalent to τ_{event_rd} and $\tau_{profile\_rd}$ in Table 2.1 and Table 2.2). Regression coefficients c_5 through c_7 in Equations 12 and 13 are the same as those in Equation 11. These are listed in Table 2.3. Total standard deviation as a function of depth is then estimated as:

$$\sigma_{Total\_rd}(z) = \sqrt{\left(\tau_{event\_rd}(z)\right)^2 + \left(\tau_{profile\_rd}(z)\right)^2 + \left(\sigma_{0\_rd}(z)\right)^2} \tag{14}$$

Figure 2.7 shows a comparison of r_d Models 1 and 2 developed for OTK (ZR19_IZ dataset) and the r_d relationships proposed by Lasley et al. (2016) for the CEUS and WUS and by Idriss (1999) for the WUS. Estimates are shown for $M_w = 4.5$, 5.0, and 5.8, representative of the valid magnitude range overlap for the models, and for V_{s12} values 120 m/s and 180 m/s to illustrate the effect of V_{s12} on the predicted r_d. As may be observed from this figure, the r_d estimates for the OTK model tend to be lower than for the Idriss (1999) or Lasley et al. (2016) models for the range of M_w and V_{s12} shown. For $M_w \leq 5$, $V_{s12} = 120$ m/s, and depths greater than approximately 12 m, the difference between the OTK models and Lasley et al. (2016) models is not large. However, for shallower depths, larger M_w, and/or higher V_{s12}, the Lasley et al. (2016) models predict similar r_d values to the OTK models. The OTK r_d models exhibit weaker scaling with both M_w and V_{s12} than the tectonic models. As a result, the difference between r_d estimated by the models becomes significantly more pronounced with increases in M_w or V_{s12}, particularly for depths between 2 and 10 m. The Idriss (1999) model leads to larger over-predictions than Lasley et al. (2016) for all values of M_w, a_{max}, and V_{s12} considered. As expected, the OTK models are closer to the Lasley et al. (2016) CEUS model than to either of the WUS models. Ground motion and site profile characteristics, particularly impedance contrast, for induced events in OTK are expected to be more consistent with tectonic events in the CEUS than with tectonic events in the WUS. However, the Lasley et al. (2016) CEUS model still tends to significantly over-predict r_d for $M_w > 5$ and larger V_{s12} values. These trends are consistent with the observations of Novakovic et al. (2018) that induced ground motions are similar to tectonic motions for low M_w

but exhibit larger spectral accelerations for higher M_w, particularly at high frequencies. Greater high frequency content is expected to lead to less rigid response of the soil column and, thus, lower r_d, as observed for the OTK r_d model. Model 1 for OTK, which includes V_{s12}, exhibits a trend of increasing r_d with increasing V_{s12}. This is consistent with expectations that stiffer soil profiles will exhibit more rigid soil response and larger values of r_d. However, the scaling of r_d with V_{s12} is not as pronounced for the OTK models as it is for either of the Lasley et al. (2016) models.

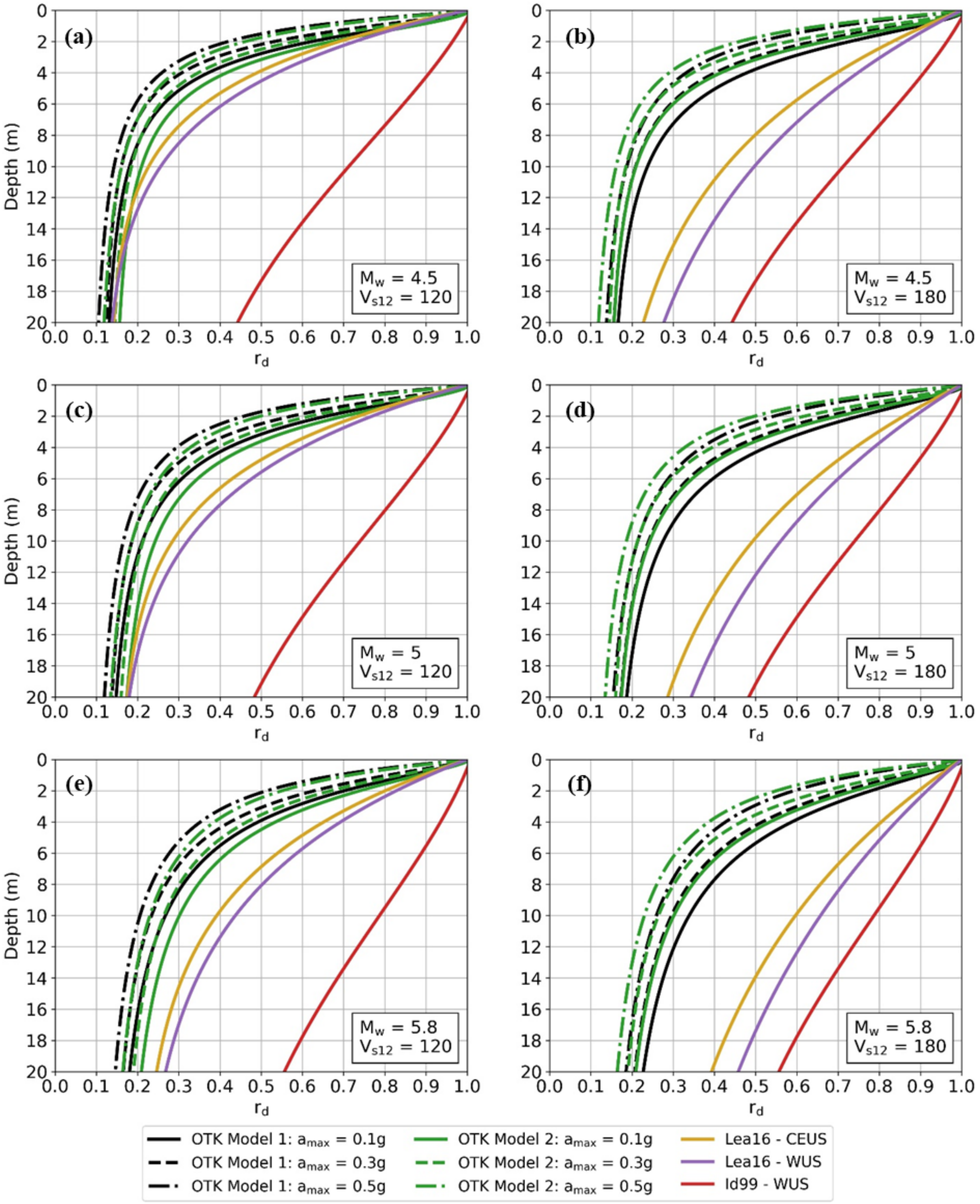

Figure 2.7. Comparison of OTK r_d Models 1 and 2 (ZR19_IZ dataset) to relationships proposed by Lasley et al. (2016) [Lea16] for the CEUS and WUS and by Idriss (1999) [Id99] primarily for the WUS for M_w = 4.5 (a-b), 5.0 (c-d), and 5.8 (e-f) and V_{s12} = 120 m/s (a, c, e) and 180 m/s (b, d, f). OTK r_d are presented for a_{max} = 0.1g, 0.3g, and 0.5g.

To investigate the effects of ground motion characteristics and site profile characteristics on r_d separately, r_d relationships were developed based on site response analyses performed using OTK ground motion datasets and the Lasley et al. (2016, 2017) site profiles. The resulting r_d model as well as OTK r_d Models 1 and 2 and the Lasley et al. (2016) CEUS r_d relationship are provided in Figure B.4 in Appendix B. A comparison of the OTK r_d models with the r_d models developed using the same ground motions but using the Lasley et al. (2016) CEUS profiles shows that site profile characteristics have a significant effect on r_d. This is consistent with previous studies (e.g., Lasley et al. 2016, Green et al. 2020), which have found that site characteristics such as impedance contrast can influence r_d.

Comparing the Lasley et al. (2016) CEUS r_d relationship with the r_d relationships developed using the Lasley et al. (2016) site profiles but the OTK motions illustrates the effect of ground motion characteristics on r_d. Similar to the trends observed in Figure 2.7, Figure B.4 shows that r_d relationships based on the OTK motions are similar to those based on the Lasley et al. (2016, 2017) CEUS motions for small M_w ($< \sim 5.0$) but diverge for larger M_w. This is consistent with the findings of Novakovic et al. (2018) and Zalachoris and Rathje (2019) regarding frequency content and magnitude scaling for larger induced events in OTK. Figure 2.8 presents a comparison of response spectra for OTK ground motions and Lasley et al. (2016, 2017) CEUS ground motions within the range of overlap for the two ground motion databases (i.e., $5.0 \leq M_w \leq 5.2$ and $R_{hyp} < 35$ km). As shown in this figure, while the spectra are similar for the induced and tectonic ground motions within this range, there are some differences at certain frequencies. Similar, direct comparisons of spectra for larger M_w were not possible due to the sparseness of the OTK and Lasley et al. (2016, 2017) ground motion catalogs for $5.2 \leq M_w \leq 6.0$.

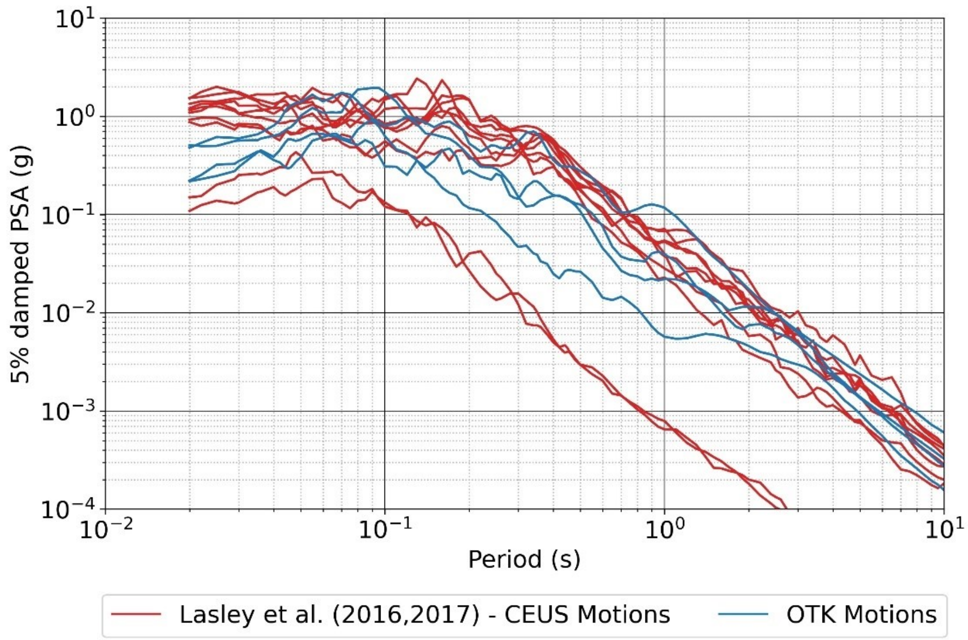

Figure 2.8. Comparison of response spectra for the Lasley et al. (2016, 2017) CEUS ground motions and recorded OTK induced ground motions. Spectra are shown for ground motions with $5.0 \leq M_w \leq 5.2$ and $R_{hyp} < 35$ km.

All else being equal, the smaller r_d for OTK result in smaller calculated CSR* and higher FS_{liq} than for the tectonic models. Figure B.5 in Appendix B provides a comparison of standard deviations for the OTK and Lasley et al. (2016) models.

As noted, the OTK r_d curves in Figure 2.7 are for the ZR19_IZ dataset. Results are similar for all four datasets. However, r_d for the ZR19 datasets (i.e., ZR19_IZ and ZR19_DS datasets) tends to be slightly higher than for the Nea18 datasets (i.e., Nea18_IZ and Nea18_DS datasets). Figure C.1 in Appendix C provides a comparison of r_d for the four datasets. While the r_d relationships for the four datasets are generally similar, the effect of GMPE and MRD selection on predicted r_d should be considered during liquefaction hazard analysis. Results for the different r_d relationships can be averaged for cases where ground motions are known or assumed. In cases where ground motions are estimated using the ZR19 or Nea18 GMPEs, the corresponding r_d models should be used.

A sensitivity analysis was conducted to determine the effect of the $V_{s\text{-bed}}$ model used to develop the representative regional soil profiles, as discussed in Section 2.4.2, on the regressed r_d relationship. An additional site response analysis was performed with site profiles developed using a depth-dependent $V_{s\text{-bed}}$ model based on the Stephenson et al. (2021) V_s profiles. The resulting data were regressed to develop new r_d models, which were compared to the OTK r_d relationships discussed above. This analysis showed that the use of the depth-dependent $V_{s\text{-bed}}$ model had negligible effect on the regressed r_d relationship. Similarly, the use of the depth-dependent $V_{s\text{-bed}}$ had negligible effect on the regressed n_{eq} relationships. This may be due to the weak variation in the $V_{s\text{-bed}}$ distribution for the Stephenson et al. (2021) profiles. Based on these results, regression of the r_d and n_{eq} models presented herein was completed using the depth-independent model discussed in Section 2.4.2.

2.6 Proposed n_{eq} and MSF Relationships

As noted, MSF is a function of n_{eq}. For this reason, n_{eq} relationships are regressed first and used to develop MSF relationships. Figure 2.9 and Figure 2.10 present n_{eq} from site response analysis as a function of several predictor variables used in previous n_{eq} models including M_w, $\ln(a_{max})$, R_{hyp}, and V_{s12} (e.g., Liu et al. 2001; Green et al. 2017, 2020). Plots of n_{eq} versus $V_{s\text{-bed}}$ and depth are also shown. As shown in these figures, the most significant predictor variables for n_{eq} are $\ln(a_{max})$ and R_{hyp}, with $\ln(a_{max})$ being negatively correlated to n_{eq} and R_{hyp} being positively correlated to n_{eq}. No significant correlation is observed between n_{eq} and either M_w or V_{s12}, and only very weak correlation is observed between n_{eq} and $V_{s\text{-bed}}$ or depth. Although 5% to 75% significant duration ($t_{5\text{-}75}$) is not used in n_{eq} modelling, Figure 2.11 shows $\ln(n_{eq})$ as a function of the $\ln(t_{5\text{-}75})$ to illustrate the relationship between n_{eq} and ground motion duration. As shown in this figure, there is a strong correlation between n_{eq} and $t_{5\text{-}75}$, consistent with the use of n_{eq} as a means of accounting for duration in liquefaction triggering modelling. Because n_{eq} and is correlated to significant duration, factors that increase significant duration, specifically $t_{5\text{-}75}$, are expected to increase n_{eq}.

The negative correlation between a_{max} and n_{eq} is consistent with trends observed by both Lasley et al. (2017) and Green et al. (2020). The positive correlation between R_{hyp} and n_{eq} is consistent with the expectation that ground motion duration increases with R_{hyp} (e.g., Boore and Thompson

2015). Similar trends were observed by Liu et al. (2001), Lee (2009), and Lasley et al. (2017) who developed n_{eq} models that included site-to-source distance (R) as a predictor variable. The shape of the observed n_{eq}-R_{hyp} curve (Figure 2.9c) is similar to the path duration-point source distance model for the CEUS developed by Boore and Thompson (2015) and shown in Figure 2.2. The Boore and Thompson (2015) model shows path duration increases rapidly with distance up to a point-source distance of ~45 km, at which distance path duration plateaus out to a distance of 125 km. Similarly, as shown in Figure 2.9, n_{eq} increases rapidly with R_{hyp} up to R_{hyp} ≈ 35 km at which distance n_{eq} does not increase significantly with further increases in R_{hyp}. The lack of significant depth-dependency for n_{eq} is also consistent with previous studies.

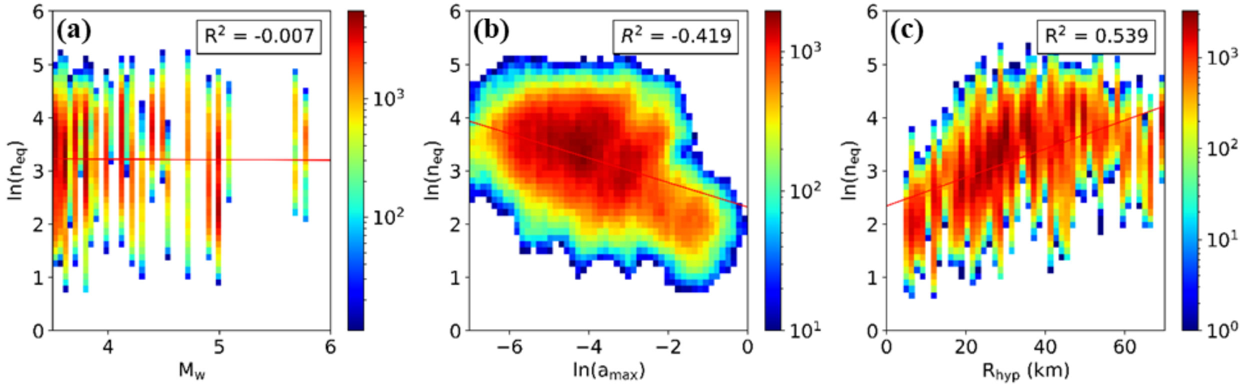

Figure 2.9. Heat map of $\ln(n_{eq})$ versus (a) M_w, (b) $\ln(a_{max})$, and (c) R_{hyp}. Values shown are for the ZR19_IZ dataset.

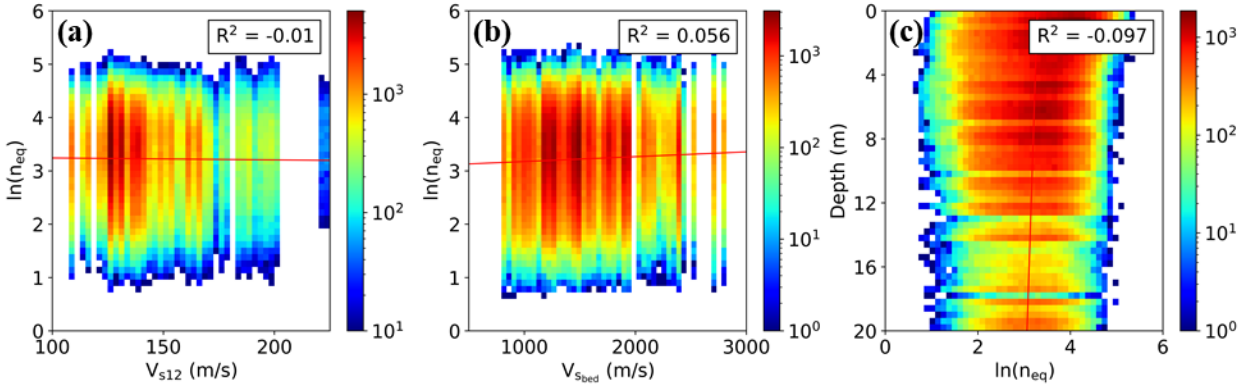

Figure 2.10. Heat map of $\ln(n_{eq})$ versus (a) R_{hyp}, (b) V_{sbed}, and (c) depth. Values shown are for the ZR19_IZ dataset.

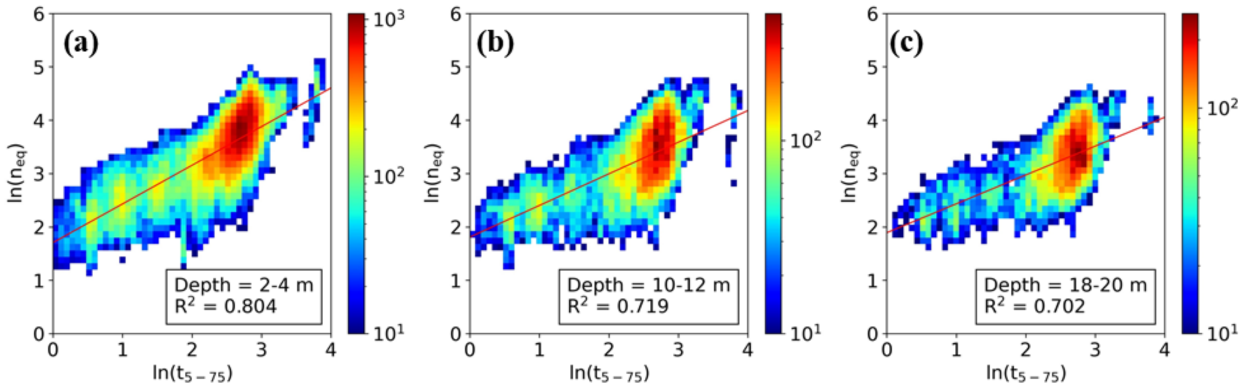

Figure 2.11. Heat map of ln(n_{eq}) versus ln($t_{5\text{-}75}$) for depths of (a) 2-4 m, (b) 10-12 m, and (c) 18-20 m. Values shown are for the ZR19_IZ dataset.

The lack of a strong correlation with M_w was surprising given the tendency for ground motion duration to increase with increasing earthquake magnitude (e.g., Lasley et al. 2017; Green et al. 2020). The relationship between n_{eq} and M_w was investigated further by partitioning the n_{eq} results by a_{max} and then plotting the partitioned n_{eq} values as a function of M_w (Figure 2.12). As shown in this figure, there is a strong positive correlation between the partitioned n_{eq} values and M_w, consistent with previous studies. No significant correlation was observed between n_{eq} and V_{s12} or $V_{s\text{-}bed}$, even after partitioning the data by a_{max} or R_{hyp}. Based on the observed trends in the data, it was determined that the n_{eq} model would be regressed using M_w, a_{max}, and R_{hyp} as predictors. The regressions are performed using n_{eq} computed from individual horizontal components of motion similar to the approach used by Green et al. (2020) and Approach 1 from Lasley et al. (2017). This approach was used to accommodate the single-component spectrally matched ground motions included in ground motion database.

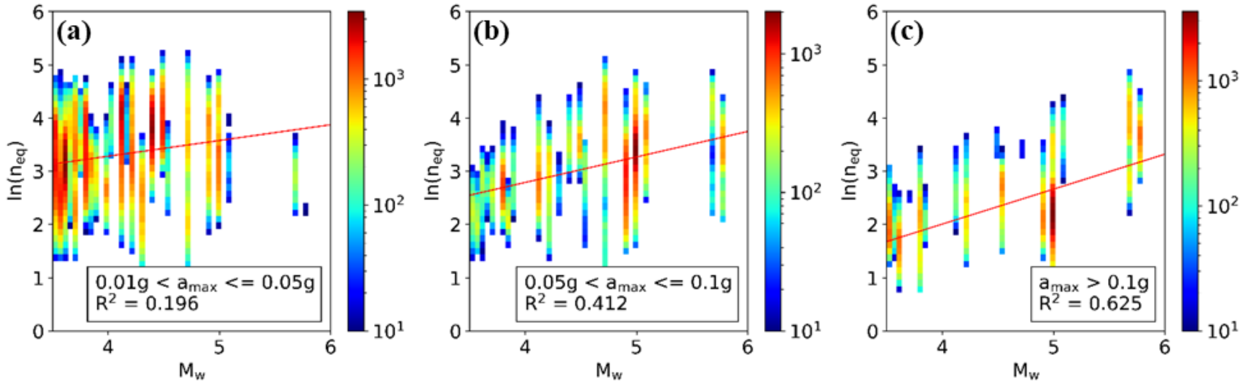

Figure 2.12. ln(n_{eq}) vs. M_w for (a) 0.01g < $a_{max} \leq$ 0.05g, (b) 0.05g < $a_{max} \leq$ 0.1g, and (c) a_{max} > 0.1g. Values shown are for the ZR19_IZ dataset and for all depths.

The proposed functional forms for the n_{eq} relationship are based on the n_{eq} models developed by Lasley et al. (2017) and Green et al. (2020). Two models are proposed: n_{eq} Model 1, which includes M_w, a_{max}, and R_{hyp} as predictors, and n_{eq} Model 2, which includes M_w and a_{max} as predictors. Both models include a break in scaling for $a_{max} \geq 0.25$g, similar to the scaling break used for the r_d model. The scaling break observed in Figure 2.9 for $R_{hyp} \geq 35$ km is also included in the Model 1. The functional forms for n_{eq} Model 1 and n_{eq} Model 2 are:

Model 1:

$$\ln\left[n_{eq-OK}\left(M_w, a_{max}, R_{hyp}\right)\right] = d_1 + d_2 \cdot M_w + d_3 \cdot \ln\left(a_{max}\right) + d_5 \cdot R_{hyp} + \delta_{\text{event\_neq}} + \delta_{\text{profile\_neq}} + \delta_{\text{0\_neq}};\ \text{for } a_{max} \leq 0.25\text{g},\ R_{hyp} \leq 35\text{ km} \quad (15a)$$

$$= d_1 + d_2 \cdot M_w + d_3 \cdot \ln(a_{max}) + d_4 \cdot \ln\left(\frac{a_{max}}{0.25}\right) + d_5 \cdot R_{hyp} + \delta_{\text{event\_neq}} + \delta_{\text{profile\_neq}} + \delta_{\text{0\_neq}};\ \text{for } a_{max} > 0.25\text{g},\ R_{hyp} \leq 35\text{ km} \quad (15b)$$

$$= d_1 + d_2 \cdot M_w + d_3 \cdot \ln(a_{max}) + d_5 \cdot R_{hyp} + d_6 \cdot \left(R_{hyp} - 35\text{ km}\right) + \delta_{\text{event\_neq}} + \delta_{\text{profile\_neq}} + \delta_{\text{0\_neq}};\ \text{for } a_{max} \leq 0.25\text{g},\ R_{hyp} > 35\text{ km} \quad (15c)$$

$$= d_1 + d_2 \cdot M_w + d_3 \cdot \ln(a_{max}) + d_4 \cdot \ln\left(\frac{a_{max}}{0.25}\right) + d_5 \cdot R_{hyp} + d_6 \cdot \left(R_{hyp} - 35\text{ km}\right) + \delta_{\text{event\_neq}} + \delta_{\text{profile\_neq}} + \delta_{\text{0\_neq}};\ \text{for } a_{max} > 0.25\text{g},\ R_{hyp} > 35\text{ km} \quad (15d)$$

and Model 2:

$$\ln\left[n_{eq-OK}(M_w, a_{max})\right] = e_1 + e_2 \cdot M_w + e_3 \cdot \ln(a_{max}) + \delta_{\mathrm{event}_{\mathrm{neq}}} + \delta_{\mathrm{profile}_{\mathrm{neq}}} + \delta_{0_{\mathrm{neq}}}; \quad \text{for } a_{max} \leq 0.25\mathrm{g} \tag{16a}$$

$$= e_1 + e_2 \cdot M_w + e_3 \cdot \ln(a_{max}) + e_4 \cdot \ln\left(\frac{a_{max}}{0.25}\right) + \delta_{\mathrm{event\_neq}} + \delta_{\mathrm{profile\_neq}} + \delta_{\mathrm{0\_neq}}; \quad \text{for } a_{max} > 0.25\mathrm{g} \tag{16b}$$

The mean values and standard deviations of the regression coefficients for the n_{eq} Models 1 and 2 are presented in Table 2.4 and Table 2.5, respectively. The low values of standard deviation relative to mean values for the regressed parameters indicate that they are well-constrained by the data.

Table 2.4. Regression coefficients for the n_{eq} Model 1.

Dataset:	**ZR19_DS**	**Nea18_DS**	**ZR19_IZ**	**Nea18_IZ**
d_1	-1.0483	-0.7663	-1.1128	-0.8634
σ_{d1}	0.0430	0.0465	0.0431	0.0458
d_2	0.4905	0.4207	0.5209	0.4590
σ_{d2}	0.00793	0.00882	0.00813	0.00890
d_3	-0.3044	-0.2995	-0.3065	-0.3021
σ_{d3}	0.00517	0.00523	0.00516	0.00508
d_4	0.3504	0.4023	0.2467	0.3019
σ_{d4}	0.0307	0.0269	0.0236	0.0204
d_5	0.03094	0.03146	0.02952	0.03009
σ_{d5}	0.000578	0.000574	0.000584	0.000574
d_6	-0.0217	-0.0222	-0.0203	-0.0209
σ_{d6}	0.000754	0.000749	0.000752	0.000742
τ_{event_neq}	0.5404	0.5238	0.543	0.5243
$\tau_{profile\_neq}$	0.1048	0.1025	0.1087	0.1066
σ_{0_neq}	0.3717	0.3725	0.3682	0.3691
$\sigma_{\ln(neq-OK)}$	0.6642	0.6508	0.665	0.65

Table 2.5. Regression coefficients for the n_{eq} Model 2.

Dataset:	**ZR19_DS**	**Nea18_DS**	**ZR19_IZ**	**Nea18_IZ**
e_1	-2.1040	-1.9571	-2.1180	-2.0142
σ_{e1}	0.03901	0.04135	0.03892	0.04077
e_2	0.7658	0.7330	0.7895	0.7672
σ_{e2}	0.00616	0.00675	0.00623	0.00676
e_3	-0.511	-0.509	-0.5003	-0.4991
σ_{e3}	0.00352	0.00354	0.00346	0.00342
e_4	0.4642	0.5327	0.3059	0.3771
σ_{e4}	0.03037	0.02712	0.02273	0.02020
τ_{event_neq}	0.5789	0.5715	0.5781	0.5669
$\tau_{profile\_neq}$	0.1389	0.1368	0.1384	0.1364
σ_{0_neq}	0.3865	0.3877	0.3819	0.3832
$\sigma_{\ln(neq\text{-}OK)}$	0.7098	0.704	0.7065	0.6978

Figure 2.13 and Figure 2.14 are plots of model residuals versus predictor variables for n_{eq} Models 1 and 2, respectively. Plots of residuals versus depth are also shown. Both loess and linear fits to the residuals are presented to show the overall trends in the residuals. Error bars showing σ_{0_neq} of the binned residuals are also presented. The binned residuals for both models are generally mean-zero and normally distributed, suggesting the models are suitable fits of the n_{eq} data for the range of M_w, a_{max}, R_{hyp}, and depth considered. Although both models fit the data well, the inclusion of R_{hyp} in Model 1 significantly reduced τ_{event_neq}, $\tau_{profile\_neq}$, and σ_{0_neq}, indicating a significantly improved fit of the data. Both models exhibited a tendency to slightly over-predict $\ln(n_{eq})$ for very small a_{max} values ($a_{max} \lesssim 0.003g$). However, a_{max} values in this range do not pose a threat of liquefaction (e.g., Rodriguez-Arriaga and Green 2018). Plots are shown for the ZR19_IZ dataset but similar trends are observed for the other datasets.

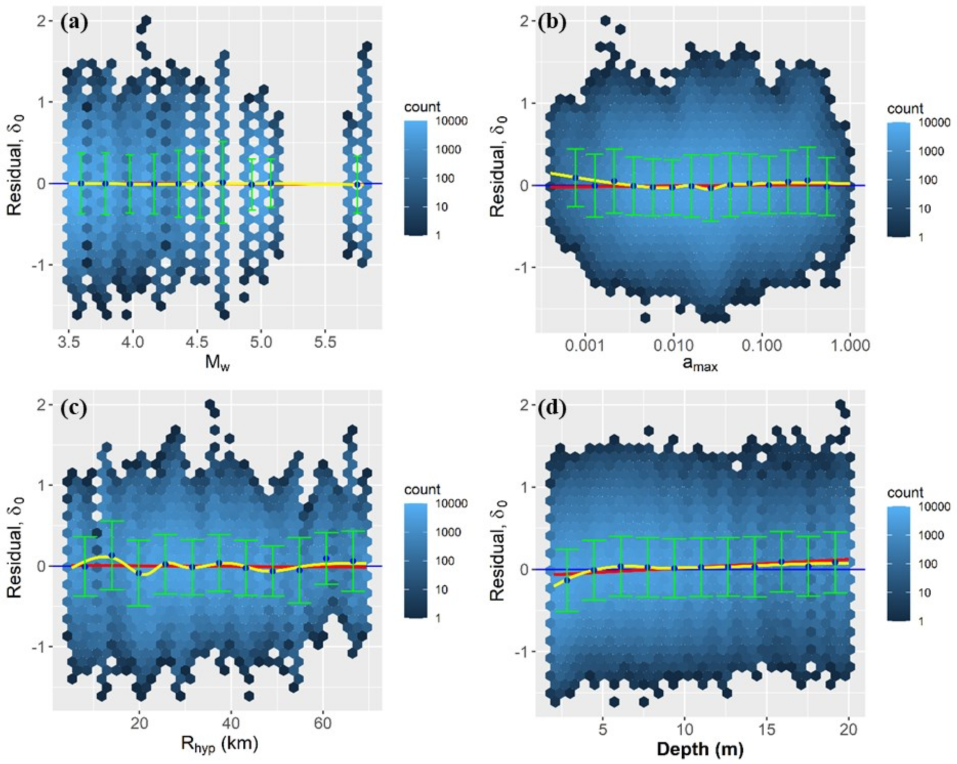

Figure 2.13. Heat map of n_{eq} Model 1 residuals versus predictor variables (Equation 15). Residuals versus depth are also shown. Yellow lines show loess fits to the residuals, red lines show linear trends fitted to the residuals, and the green error bars show the means and standard deviations of the binned residuals. Results shown for ZR19_IZ dataset.

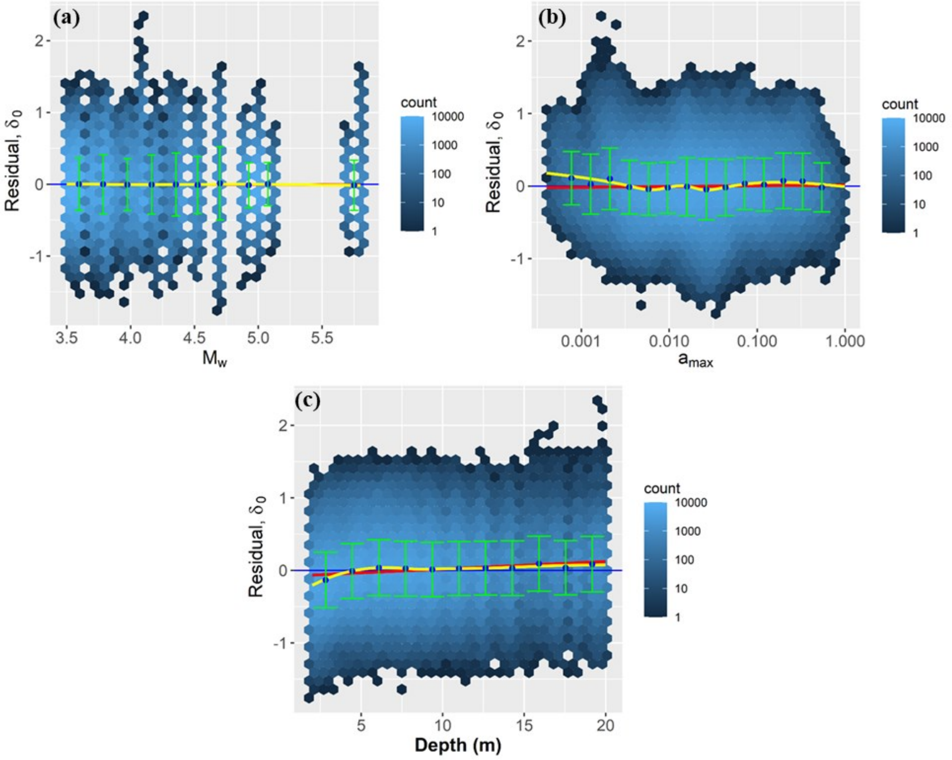

Figure 2.14. Heat map of n_{eq} Model 2 residuals versus predictor variables (Equation 16). Residuals versus depth are also shown. Yellow lines show loess fits to the residuals, red lines show linear trends fitted to the residuals, and the green error bars show the means and standard deviations of the binned residuals. Results shown for ZR19_IZ dataset.

Similar to the observations made by Green et al. (2020), there is no compelling evidence of a depth-dependency in σ_{0_neq} for the OTK dataset. Accordingly, a depth-independent model was used for $\sigma_{\ln(n_{eq-OK})}$ given by:

$$\sigma_{\ln(n_{eq-OK})} = \sqrt{\tau^2_{event\_neq} + \tau^2_{profile\_neq} + \sigma^2_{0\_neq}} \tag{17}$$

where τ_{event_neq}, $\tau_{profile\_neq}$, and σ_{0_neq} are the random effect terms and residual standard deviation from the model regression. These values, as well as the estimates for $\sigma_{\ln(n_{eq-OK})}$, are presented in Table 2.4 and Table 2.5 for n_{eq} Model 1 and n_{eq} Model 2, respectively.

As noted previously, the OTK n_{eq} models are developed using individual horizontal components of ground motion. As a result, MSF for the new model (MSF_{OK}) is computed using $n_{eq\ M7.5}$ = 7.25, similar to the MSF relationship from Green et al. (2020). Accordingly, the OTK-specific MSF Model 1 and Model 2 for n_{eq} Models 1 and 2 are:

MSF Model 1 (based on n_{eq} Model 1):

$$MSF_{OK}(M_w, a_{max}, R_{hyp}) = \left(\frac{7.25}{n_{eqM-OK}(M_w, a_{max}, R_{hyp})}\right)^{0.34} \leq 2.04 \qquad (18)$$

and MSF Model 2 (based on n_{eq} Model 2):

$$MSF_{OK}(M_w, a_{max}) = \left(\frac{7.25}{n_{eqM-OK}(M_w, a_{max})}\right)^{0.34} \leq 2.04 \qquad (19)$$

The standard deviation of these models, $\sigma_{\ln(MSF_{OK})}$, can be estimated as:

$$\sigma_{\ln(MSF_{OK})} = 0.34 \cdot \sigma_{\ln(n_{eq-OK})} \leq 2.04 \qquad (20)$$

where $\sigma_{\ln(n_{eq-OK})}$ is the standard deviation of the n_{eq} model being used.

Figure 2.15 provides a comparison of MSF models developed herein and MSF models proposed by Boulanger and Idriss (2014) and Green et al. (2017). As may be observed from this figure, MSF for OTK tend to be lower than MSF for either the Boulanger and Idriss (2014) or Green et al. (2017) models for ~M_w 4.5 to 6, the magnitude range for which all models are valid. These differences are more pronounced for larger R_{hyp}. However, for R_{hyp} = 5 km and a_{max} = 0.1g, MSF from OTK Model 1 is actually higher than the Green et al. (2017) CEUS model for M_w < 5.3 but is lower for larger M_w. Additionally, the OTK models exhibited weaker scaling with a_{max} than the Green et al. (2017) models, particularly for $a_{max} \geq 0.25$g. MSF for the current study tend to be higher for Model 1 than Model 2 at small R_{hyp} (R_{hyp} < ~30 km), but this trend is reversed for larger R_{hyp}.

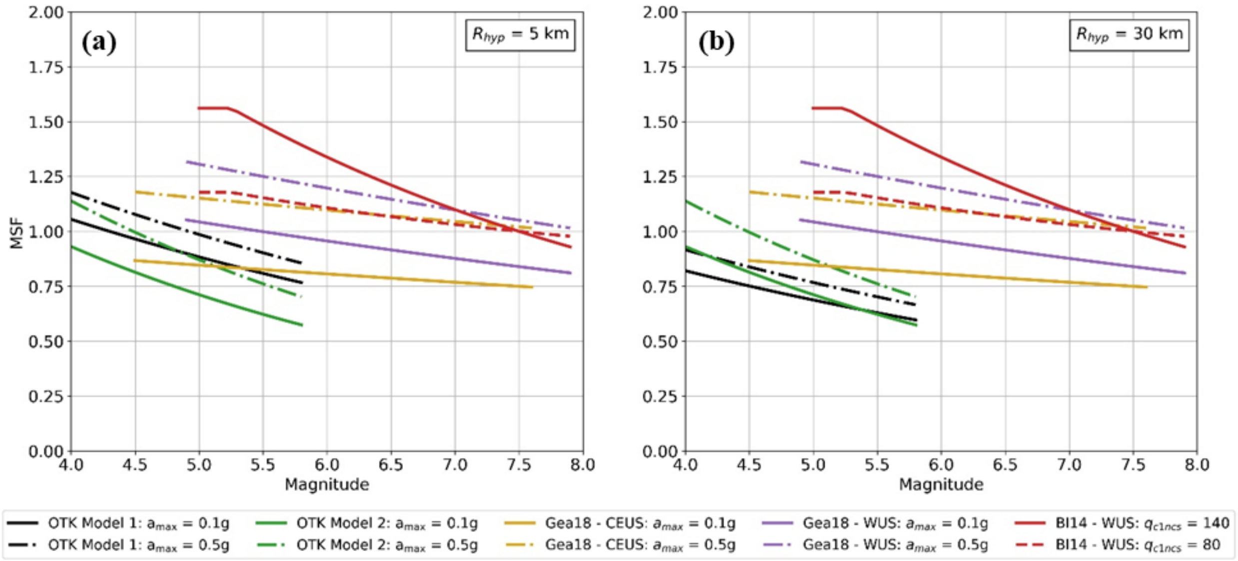

Figure 2.15. Comparison of MSF Models 1 and 2 developed herein and models proposed by Green et al. (2017) for the CEUS (Gea17 – CEUS) and WUS (Gea17 – WUS) and by Boulanger and Idriss (2014) primarily for the WUS (BI14 – WUS). OTK and Gea17 MSF estimates are shown for a_{max} = 0.1g and 0.5g. The BI14 model is shown for q_{c1ncs} = 80 and 140 atm. OTK MSF Model 1 is a function of R_{hyp}. As a result, MSF for OTK Model 1 are plotted for (a) R_{hyp} = 5 km and (b) R_{hyp} = 30 km.

The significant differences observed between MSF for induced ground motions in OTK and MSF for the WUS are consistent with the observations about path duration made by Boore and Thompson (2015): ground motion durations in the CEUS increase much faster with R_{hyp} than they do in the WUS. Additionally, these differences reflect noted difference in $t_{5\text{-}75}$ durations across the different regions (e.g., Lee and Green 2014; Bahrampouri et al. 2020). Differences in regional geology between OTK and the WUS, particularly impedance contrast, may also influence these MSF relationships (Lasley et al. 2017). The OTK MSF are closer to the Green et al. (2017) CEUS MSF but are still lower than CEUS MSF for larger M_w. The majority of the ground motions used to develop the Green et al. (2017) CEUS model were scaled from WUS ground motions using state-of-the-art methods (McGuire et al. 2001). However, the scaling procedures used were likely focused on scaling for spectral amplitude as opposed to duration. This may explain why the durations of the Green et al. (2017) CEUS ground motions are more in line with those of the Green et al. (2017) WUS model than the OTK models. All else being equal, the smaller MSF for OTK result in larger calculated CSR* and lower FS_{liq} than for the tectonic models. Figure B.6 in Appendix B provides a comparison of standard deviations for the OTK and Green et al. (2017) models.

Although the MSF curves shown in Figure 2.15 are for the ZR19_IZ dataset, observed trends are similar for the other datasets. A comparison of MSF for the four datasets is provided in Figure C.2 in Appendix C. The effect of MRD and GMPE selection on MSF is smaller than for r_d (i.e., differences in MSF up to 7% between the ZR19_IZ to Nea18_DS datasets). However, uncertainties related to MRD and GMPE selection should still be considered when using these relationships. As discussed previously, MSF for the four relationships can be averaged in cases where ground motions are known or assumed. Or, in cases where ground motions are estimated using the ZR19 or Nea18 GMPEs, the corresponding MSF relationships should be used.

2.7 Correlation of r_d across Depth and Correlation between OTK r_d and $\ln(n_{eq})$ Relationships

It was found that $r_{d\text{-}OK}$ values are correlated across depth. The functional form used by Green et al. (2020) to model correlation of r_d across depths for induced events in the Groningen region of the Netherlands was found to provide a good fit for the correlation for $r_{d\text{-}OK}$ across depths. Using this functional form, the correlation coefficient of $r_{d\text{-}OK}$ between depths z_i and z_j is given by:

$$\rho\left[\epsilon_{r_d}(z_i), \epsilon_{r_d}(z_i)\right] = 1 + \eta_{r_d} \cdot \left|z_i - z_j\right| \tag{21}$$

where $\epsilon_{r_d}(z_i)$ and $\epsilon_{r_d}(z_i)$ are the residuals of r_d at depths z_i and z_j normalized by $\sigma_0(z_i)$ and $\sigma_0(z_j)$, respectively, and η_{r_d} is a regression coefficient. It was also found that $\ln(n_{eq\text{-}OK})$ and $r_{d\text{-}OK}$ are negatively correlated at a given depth. Regressed values of η_{r_d}, as well as correlation coefficients between $\ln(n_{eq\text{-}OK})$ and $r_{d\text{-}OK}$ (i.e., $\rho_{\ln(neq-OK),rd-OK}$), are presented in Table 2.6. The observed correlations are similar to those observed between $\ln(n_{eq})$ and r_d and those of r_d across depths observed by Green et al. (2020) for induced events in the Groningen region of the Netherlands, except the cross-depth correlation was somewhat stronger for the OTK r_d model.

Table 2.6. Correlation coefficients for $r_{d\text{-}OK}$ and $\ln(n_{eq\text{-}OK})$ models.

Dataset	r_d Model	n_{eq} Model	η_{rd}	$\rho_{\ln(neq),rd}$
ZR19_DS	1	1	-0.05778	-0.33605
Nea18_DS	1	1	-0.05702	-0.33676
ZR19_IZ	1	1	-0.05842	-0.33520
Nea18_IZ	1	1	-0.05724	-0.33605
ZR19_DS	1	2	-0.05778	-0.33103
Nea18_DS	1	2	-0.05702	-0.33290
ZR19_IZ	1	2	-0.05842	-0.32849
Nea18_IZ	1	2	-0.05724	-0.33084
ZR19_DS	2	1	-0.05662	-0.33110
Nea18_DS	2	1	-0.05751	-0.33146
ZR19_IZ	2	1	-0.05538	-0.33125
Nea18_IZ	2	1	-0.05509	-0.33227
ZR19_DS	2	2	-0.05662	-0.32634
Nea18_DS	2	2	-0.05751	-0.32792
ZR19_IZ	2	2	-0.05538	-0.32465
Nea18_IZ	2	2	-0.05509	-0.32666

2.8 Implementation of $r_{d\text{-}OK}$ and MSF_{OK} for Assessing Liquefaction Hazard for Induced Ground Motions in Oklahoma, Texas, and Kansas

The r_d and MSF relationships developed herein are intended for use in calculating CSR* within the context of the stress-based simplified liquefaction triggering evaluation procedure. The resulting CSR* can be used in conjunction with the Green et al. (2019) $CRR_{M7.5}$ curve to assess liquefaction triggering potential (e.g., FS_{liq}) for induced ground motions in OTK. The Green et al. (2019) $CRR_{M7.5}$ curve was developed by reanalyzing the CPT liquefaction case history database compiled by Boulanger and Idriss (2014) using MSF relationships based on Lasley et al. (2017) and the r_d relationship developed by Lasley et al. (2016) while using other parameters and relationships as specified by Boulanger and Idriss (2014). The case histories were then used to regress an "unbiased" deterministic liquefaction curve (i.e., $CRR_{M7.5}$) given by:

$$CRR_{M7.5} = exp\left[\frac{q_{c1Ncs}}{113} + \left(\frac{q_{c1Ncs}}{1000}\right)^2 - \left(\frac{q_{c1Ncs}}{140}\right)^3 + \left(\frac{q_{c1Ncs}}{137}\right)^4 - 2.8119\right] \leq 0.6 \qquad (22)$$

where q_{c1Ncs} is computed using the procedure outlined by Boulanger and Idriss (2014). This curve corresponds to a probability of liquefaction (P_{liq}) of approximately 35% based on total uncertainty and approximately corresponds to P_{liq} = 15% for the Boulanger and Idriss (2014) $CRR_{M7.5}$ curve, which considers only model uncertainty.

In general, r_d and MSF relationships developed from one study should not be used in conjunction with $CRR_{M7.5}$ relationships developed from other studies (NRC 2016). However, the r_d and MSF relationships used to develop the Green et al. (2019) $CRR_{M7.5}$ and those developed herein were developed using identical approaches. As a result, it is reasonable to use the r_d and MSF relationships developed herein in conjunction with the Green et al. (2019) $CRR_{M7.5}$ curves to evaluate liquefaction potential at sites in OTK subjected to induced ground motions.

2.9 Model Validation

To evaluate the efficacy of the new liquefaction triggering model, detailed geotechnical site characterizations were performed at sites that experienced significant shaking during the 3 September 2016, M_w5.8 Pawnee, OK, earthquake. Liquefaction potential is assessed at each test location using the OTK model developed herein as well as the Green et al. (2017) CEUS and WUS and Boulanger and Idriss (2014) liquefaction triggering models developed for tectonic earthquakes. The severity of surficial liquefaction manifestations is predicted using the Ishihara-inspired liquefaction potential index (LPI_{ish}) framework (Maurer et al. 2015) based on input parameters for the Pawnee event. Predicted surficial liquefaction manifestation severities based on LPI_{ish} are compared to the documented observations of liquefaction manifestations made following the Pawnee event to evaluate the efficacy of the selected models. Detailed results of the site characterization and liquefaction hazard assessment are presented in Quick et al. (2021) [Chapter 3 of this document], but are summarized herein.

As a result of trends in r_d and MSF, the induced seismicity-specific liquefaction triggering model generally resulted in higher FS_{liq} and less severe predictions of liquefaction than predicted by tectonic models. At most locations evaluated, the less-severe predictions made by the induced seismicity-specific triggering model were more consistent with field observations than were predictions made by existing models for tectonic earthquakes. The tectonic models tended to over-predict liquefaction severity, particularly at sites where no liquefaction was observed. The new model slightly under-predicted liquefaction severity at some sites where minor severity was reported. These under-predictions may result from difficulties in matching post-event damage surveys with field test locations, particularly for minor liquefaction features. Model validation results suggest that the new model developed herein provides more accurate assessments of liquefaction potential from induced earthquakes in OTK than do existing models developed for use with tectonic earthquakes in either the CEUS or WUS.

2.10 Summary and Conclusions

Although several models are commonly used in practice for assessing liquefaction triggering potential due to tectonic earthquakes, these models are semi-empirical, with the empirical aspects being derived from data primarily taken from moderate-sized tectonic earthquakes in active shallow-crustal tectonic regimes. Due to differences in ground motion characteristics and regional geology, the suitability of these models for evaluating liquefaction triggering for induced earthquakes in Oklahoma, Texas, and Kansas (OTK) is uncertain. To address this, a new liquefaction triggering model specific to deep wastewater injection-induced earthquakes in OTK was developed. This liquefaction triggering model was developed based on the approach used in Green et al. (2017) and Green et al. (2020) to develop analogous models for evaluating liquefaction triggering in the central and eastern United States (CEUS) and the Groningen region of the Netherlands. This approach involved using numerical site response analyses performed using a catalog of induced ground motions and representative soil profiles from the region to develop new depth-stress reduction factor (r_d) and Magnitude Scaling Factor (MSF) relationships specific to induced events in OTK. The new r_d and MSF relationships can be used to compute normalized cyclic stress ratio (CSR*) in the context of the stress-based simplified procedure. The resulting CSR* can be used in conjunction with the normalized cyclic resistance ratio ($CRR_{M7.5}$) curves from Green et al. (2019) to estimate liquefaction potential for induced earthquakes in OTK.

The r_d relationship developed herein tends to predict lower values of r_d than the models developed for tectonic earthquakes. This is consistent with observations by Novakovic et al.

(2018) that, for larger earthquakes, induced earthquake ground motions tend to be richer in high-frequency content than tectonic earthquakes. These high frequency motions lead to less rigid soil column response and, hence, lower r_d. Magnitude (M_w), time-weighted average small-strain shear wave velocity of the upper 12 m (V_{s12}), and peak ground acceleration (a_{max}) were found to be significant predictors of r_d. However, r_d did not scale as strongly with M_w or V_{s12} for the new model as it did for the Lasley et al. (2016) models for the CEUS and western United States (WUS).

MSF for OTK was found to increase with increasing a_{max} and decrease with increasing M_w and hypocentral distance (R_{hyp}). MSF in OTK exhibits scaling breaks for relatively large values of a_{max} (> 0.25g) and for relatively large values of R_{hyp} (> 35 km). MSF for the model developed herein tend to be lower than MSF for existing models for most M_w and R_{hyp}. This is consistent with the observations of Boore and Thompson (2015) that path duration tends to increase much more rapidly with distance in the CEUS than in the WUS.

Accounting for the observed differences in liquefaction triggering potential for induced and tectonic earthquakes is important when considering seismic design and policy in areas subject to induced seismicity. The findings of this study show that existing methods used to assess the liquefaction triggering potential of tectonic earthquakes tend to over-predict the liquefaction potential for a given induced earthquake. As a result, use of traditional liquefaction triggering models in design may lead to over-conservatism in design and increased costs. It is important to note, however, that while the findings of this study show that the liquefaction potential from induced earthquakes is less than from tectonic earthquakes, the overall risk of liquefaction in areas currently experiencing liquefaction may still be higher than historic levels due to the increased rate of induced seismicity in these areas. Additionally, the current study considers liquefaction potential from induced earthquakes in a single case study area (i.e., OTK). As confirmed in this study, relationships for r_d and MSF vary by region and seismic source. As a result, research into liquefaction potential from induced earthquakes in other regions is also needed.

References

American Society of Civil Engineers. (2017). *Minimum Design Loads and Associated Criteria for Buildings and Other Structures*. American Society of Civil Engineers, Reston, VA, doi.org/10.1061/9780784414248.

Al Atik, L., and Abrahamson, N. (2010). "An Improved Method for Nonstationary Spectral Matching." *Earthquake Spectra*, 26(3), 601–617, doi.org/10.1193/1.3459159.

Atkinson, G. M. (2015). "Ground-motion prediction equation for small-to-moderate events at short hypocentral distances, with application to induced-seismicity hazards." *Bulletin of the Seismological Society of America*, 105(2), 981–992, doi.org/10.1785/0120140142.

Atkinson, G. M. (2020). "The Intensity of Ground Motions from Induced Earthquakes with Implications for Damage Potential." *Bulletin of the Seismological Society of America*, 110(5), 2366–2379, doi.org/10.1785/0120190166.

Bahrampouri, M., Rodriguez-Marek, A., and Green, R. A. (2021). "Ground motion prediction equations for significant duration using the KiK-net database." *Earthquake Spectra*, 37(2), 903–920, doi.org/10.1177/8755293020970971.

Bates, D., Mächler, M., Bolker, B., and Walker, S. (2015). "Fitting Linear Mixed-Effects Models Using lme4." *Journal of Statistical Software*, 67(1), 1–48, doi.org/10.18637/jss.v067.i01.

Bommer, J. J., Dost, B., Edwards, B., Stafford, P. J., van Elk, J., Doornhof, D., and Ntinalexis, M. (2016). "Developing an application-specific ground-motion model for induced seismicity." *Bulletin of the Seismological Society of America*, 106(1), 158–173, doi.org/10.1785/0120150184.

Boore, D. M. (2010). "Orientation-Independent, Nongeometric-Mean Measures of Seismic Intensity from Two Horizontal Components of Motion." *Bulletin of the Seismological Society of America*, 100(4), 1830–1835, doi.org/10.1785/0120090400.

Boore, D. M., Stewart, J. P., Seyhan, E., and Atkinson, G. M. (2014). "NGA-West2 Equations for Predicting PGA, PGV, and 5% Damped PSA for Shallow Crustal Earthquakes." *Earthquake Spectra*, 30(3), 1057–1085, doi.org/10.1193/070113EQS184M.

Boore, D. M., and Thompson, E. M. (2014). "Path durations for use in the stochastic-method simulation of ground motions." *Bulletin of the Seismological Society of America*, 104(5), 2541–2552, doi.org/10.1785/0120140058.

Boore, D. M., and Thompson, E. M. (2015). "Revisions to some parameters used in stochastic-method simulations of ground motion." *Bulletin of the Seismological Society of America*, 105(2), 1029–1041, doi.org/10.1785/0120140281.

Boulanger, R. W., and Idriss, I. M. (2014). *CPT and SPT based liquefaction triggering procedures*. Report No. UCD/CGM-14/01, University of California at Davis, Davis, CA, doi.org/10.1061/(ASCE)GT.1943-5606.0001388.

Boyd, O. S., McNamara, D. E., Hartzell, S., and Choy, G. (2017). "Influence of lithostatic stress on earthquake stress drops in North America." *Bulletin of the Seismological Society of America*, 107(2), 856–868, doi.org/10.1785/0120160219.

Choi, J. H., Ko, K., Gihm, Y. S., Cho, C. S., Lee, H., Song, S. G., Bang, E. S., Lee, H. J., Bae, H. K., Kim, S. W., Choi, S. J., Lee, S. S., and Lee, S. R. (2019). "Surface deformations and rupture processes associated with the 2017 Mw 5.4 Pohang, Korea, earthquake." *Bulletin of the Seismological Society of America*, 109(2), 756–769, doi.org/10.1785/0120180167.

Clayton, P., Zalachoris, G., Rathje, E., Bheemasetti, T., Caballero, S., Yu, X., and Bennett, S. (2016). *The geotechnical aspects of the September 3, 2016 M5.8 Pawnee, Oklahoma earthquake*. Report GEER-051, Geotechnical Extreme Events Reconnaissance Association, doi.org/10.5072/FK24B33797.

Cramer, C. H. (2017). "Brune stress parameter estimates for the 2016 Mw 5.8 pawnee and other Oklahoma earthquakes." *Seismological Research Letters*, 88(4), 1005–1016, doi.org/10.1785/0220160224.

Darendeli, M. B., and Stokoe, K. H. (2001). *Development of a new family of normalized modulus reduction and material damping curves*. Geotechnical Engineering Report GD01-1, Univ. of Texas at Austin, Austin, TX.

Efron, B., and Tibshirani, R. J. (1994). *An Introduction to Bootstrap*. Vol. 57, CRC Press, Chicago, IL.

Green, R. A., and Bommer, J. J. (2019). "What is the Smallest Earthquake Magnitude that Needs to be Considered in Assessing Liquefaction Hazard?" *Earthquake Spectra*, 35(3), 1441–1464, doi.org/10.1193/032218eqs064m.

Green, R. A., Bommer, J. J., Rodriguez-Marek, A., Maurer, B. W., Stafford, P. J., Edwards, B., Kruiver, P. P., de Lange, G., and van Elk, J. (2019). "Addressing limitations in existing 'simplified' liquefaction triggering evaluation procedures: application to induced seismicity in the Groningen gas field." *Bulletin of Earthquake Engineering*, Springer Netherlands, 17(8), 4539–4557, doi.org/10.1007/s10518-018-0489-3.

Green, R. A., Bommer, J. J., Stafford, P. J., Maurer, B. W., Kruiver, P. P., Edwards, B., Rodriguez-Marek, A., de Lange, G., Oates, S. J., Storck, T., Omidi, P., Bourne, S. J., and van Elk, J. (2020). “Liquefaction Hazard in the Groningen Region of the Netherlands due to Induced Seismicity.” *Journal of Geotechnical and Geoenvironmental Engineering*, 146(8), 04020068, doi.org/10.1061/(asce)gt.1943-5606.0002286.

Green, R. A., Maurer, B. W., and Haskell, A. (2017). *Development of Probabilistic Magnitude-Bound Curves for the New Madrid Seismic Zone (NMSZ) for Paleoliquefaction Studies*. U.S. Geological Society Technical Report G14AP00046, U.S. Geological Survey, Reston, VA.

Green, R. A., and Terri, G. A. (2005). “Number of Equivalent Cycles Concept for Liquefaction Evaluations—Revisited.” *Journal of Geotechnical and Geoenvironmental Engineering*, 131(4), 477–488, doi.org/10.1061/(ASCE)1090-0241(2005)131:4(477).

Hassani, B., and Atkinson, G. M. (2015). “Referenced Empirical Ground-Motion Model for Eastern North America.” *Seismological Research Letters*, 86(2A), 477–491, doi.org/10.1785/0220140156.

Hough, S. E. (2014). “Shaking from injection-induced Earthquakes in the central and eastern United States.” *Bulletin of the Seismological Society of America*, 104(5), 2619–2626, doi.org/10.1785/0120140099.

Huang, Y., Ellsworth, W. L., and Beroza, G. C. (2017). “Stress drops of induced and tectonic earthquakes in the central United States are indistinguishable.” *Science Advances*, 3(8), 1–7, doi.org/10.1126/sciadv.1700772.

Idriss, I. M. (1999). “An update to the Seed-Idriss simplified procedure for evaluating liquefaction potential.” *Proceedings of TRB Workshop on New Approaches to Liquefaction, Publication No. FHWA-RD-99-165*, Federal Highway Administration, Washington, DC.

Idriss, I. M., and Sun, J. I. (1992). *User’s manual for SHAKE91: A computer program for conducting equivalent linear seismic response analyses of horizontally layered soil deposits*. Center for Geotechnical Modeling, Dept. of Civil and Environmental Engineering, Univ. of California, Davis, CA.

Ishibashi, I., and Zhang, X. (1993). “Unified dynamic shear moduli and damping ratios of sand and clay.” *Soils and Foundations*, 33(1), 182–191, doi.org/10.3208/sandf1972.33.182.

Jeong, S., Stump, B. W., and DeShon, H. R. (2020). "Spectral Characteristics of Ground Motion from Induced Earthquakes in the Fort Worth Basin, Texas, Using the Generalized Inversion Technique." *Bulletin of the Seismological Society of America*, 110(5), 2058–2076, doi.org/10.1785/0120200097.

Kaski, K. M., and Atkinson, G. M. (2017). "A Comparison of Ground-Motion Characteristics from Induced Seismic Events in Alberta with Those in Oklahoma." *Seismological Research Letters*, 88(6), 1570–1585, doi.org/10.1785/0220170064.

Kolawole, F., Atekwana, E. A., and Ismail, A. (2017). "Near-surface electrical resistivity investigation of coseismic liquefaction-induced ground deformation associated with the 2016 Mw 5.8 Pawnee, Oklahoma, earthquake." *Seismological Research Letters*, 88(4), 1017–1023, doi.org/10.1785/0220170004.

Lasley, S. J., Green, R. A., and Rodriguez-Marek, A. (2014). "Comparison of Equivalent-Linear Site Response Analysis Software." *Proceedings of 10th National Conference in Earthquake Engineering*, Earthquake Engineering Research Institute, Oakland, CA, 1–11, doi.org/10.4231/D3P26Q42R.

Lasley, S. J., Green, R. A., and Rodriguez-Marek, A. (2016). "New Stress Reduction Coefficient Relationship for Liquefaction Triggering Analyses." *Journal of Geotechnical and Geoenvironmental Engineering*, 142(11), 06016013, doi.org/10.1061/(ASCE)GT.1943-5606.0001530.

Lasley, S. J., Green, R. A., and Rodriguez-Marek, A. (2017). "Number of Equivalent Stress Cycles for Liquefaction Evaluations in Active Tectonic and Stable Continental Regimes." *Journal of Geotechnical and Geoenvironmental Engineering*, 143(4), 04016116, doi.org/10.1061/(ASCE)GT.1943-5606.0001629.

Lee, J. (2009). "Engineering Characterization of Earthquake Ground Motions." Ph.D. Dissertation, University of Michigan, Ann Arbor, MI., doi.org/10.1017/CBO9781107415324.004.

Lee, J., and Green, R. A. (2014). "An empirical significant duration relationship for stable continental regions." *Bulletin of Earthquake Engineering*, 12(1), 217–235, doi.org/10.1007/s10518-013-9570-0.

Liu, A. H., Stewart, J. P., Abrahamson, N. A., and Moriwaki, Y. (2001). "Equivalent Number of Uniform Stress Cycles for Soil Liquefaction Analysis." *Journal of Geotechnical and*

Geoenvironmental Engineering, 127(12), 1017–1026, doi.org/10.1061/(ASCE)1090-0241(2001)127:12(1017).

Maurer, B. W., Green, R. A., and Taylor, O. D. S. (2015). "Moving towards an improved index for assessing liquefaction hazard: Lessons from historical data." *Soils and Foundations*, 55(4), 778–787, doi.org/10.1016/j.sandf.2015.06.010.

McGuire, R. K., Silva, W. J., and Costantino, C. J. (2001). *Technical basis for revision of regulatory guidance on design ground motions: Hazard- and risk-consistent ground motion spectra guidelines*. Division of Engineering Technology, Office of Nuclear Regulatory Research, U.S. Nuclear Regulatory Commission, Washington, DC.

Novakovic, M., Atkinson, G. M., and Assatourians, K. (2018). "Empirically Calibrated Ground-Motion Prediction Equation for Oklahoma." *Bulletin of the Seismological Society of America*, 108(5A), 2444–2461, doi.org/10.1785/0120170331.

NRC. (2016). *State of the Art and Practice in the Assessment of Earthquake-Induced Soil Liquefaction and Its Consequences*. *State of the Art and Practice in the Assessment of Earthquake-Induced Soil Liquefaction and Its Consequences*, National Research Council, The National Academies Press, Washington, DC, doi.org/10.17226/23474.

R Core Team. (2018). *R: A language and environment for statistical computing*. R Foundation for Statistical Computing, Vienna, Austria. Available online at https://www.R-project.org/.

Robertson, P. K., and Cabal, K. L. (2015). *Guide to Cone Penetration Testing for Geotechnical Engineering*. Gregg Drilling & Testing, Inc., Signal Hill, CA.

Rodriguez-Arriaga, E., and Green, R. A. (2018). "Assessment of the cyclic strain approach for evaluating liquefaction triggering." *Soil Dynamics and Earthquake Engineering*, Elsevier Ltd, 113(May), 202–214, doi.org/10.1016/j.soildyn.2018.05.033.

Schnabel, P., Seed, H. B., and Lysmer, J. (1972). "Modification of seismograph records for effects of local soil conditions." *Bulletin of the Seismological Society of America*, 62(6), 1649–1664.

Seed, H. B., and Idriss, I. M. (1971). "Simplified procedure for evaluating soil liquefaction potential." *Journal of Geotechnical Engineering*, 97(9), 1249–1273.

Stephenson, W. J., Odum, J. K., Hartzell, S. H., Leeds, A. L., and Williams, R. A. (2021). "Shear-Wave Velocity Site Characterization in Oklahoma from Joint Inversion of Multimethod Surface Seismic Measurements: Implications for Central U.S. Ground-Motion

Prediction." *Bulletin of the Seismological Society of America*, (xx), doi.org/10.1785/0120200348.

Sumy, D. F., Neighbors, C. J., Cochran, E. S., and Keranen, K. M. (2017). "Low stress drops observed for aftershocks of the 2011 Mw5.7 Prague, Oklahoma, earthquake." *Journal of Geophysical Research: Solid Earth*, 122(5), 3813–3834, doi.org/10.1002/2016JB013153.

Thum, T. S., Lasley, S., Green, R. A., and Rodriguez-Marek, A. (2019). *ShakeVT2: A computer program for equivalent linear site response analysis, CGPR #98*. Center for Geotechnical Practice and Research, Virginia Tech, Blacksburg, VA.

Tiwari, A., and Rathje, E. M. (2018). "Engineering characteristics of earthquake motions from the Pawnee and Cushing Earthquakes in Oklahoma." *Proceedings of Geotechnical Earthquake Engineering and Soil Dynamics V (GEESD V): Seismic Hazard Analysis, Earthquake Ground Motions, and Regional-Scale Assessment*, GSP 291, American Society of Civil Engineers, Reston, VA, 378–386.

Ulmer, K. J., Green, R. A., and Rodriguez-Marek, A. (2020). "A Consistent Correlation between V s , SPT, and CPT Metrics for Use in Liquefaction Evaluation Procedures." *Proceedings of Geo-Congress 2020*, American Society of Civil Engineers, Reston, VA, 132–140, doi.org/10.1061/9780784482810.015.

Wair, B. R., Dejong, J. T., and Shantz, T. (2012). *Guidelines for Estimation of Shear Wave Velocity Profiles*. *PEER Report 2012/08*, Pacific Earthquake Engineering Research Center, University of California, Berkeley, CA.

Whitman, R. V. (1971). "Resistance of Soil to Liquefaction and Settlement." *Soils and Foundations*, 11(4), 59–68.

Wu, Q., Chapman, M., and Chen, X. (2018). "Stress-drop variations of induced earthquakes in Oklahoma." *Bulletin of the Seismological Society of America*, 108(3), 1107–1123, doi.org/10.1785/0120170335.

Yenier, E., and Atkinson, G. M. (2015). "Regionally adjustable generic ground-motion prediction equation based on equivalent point-source simulations: Application to central and eastern North America." *Bulletin of the Seismological Society of America*, 105(4), 1989–2009, doi.org/10.1785/0120140332.

Yenier, E., Atkinson, G. M., and Sumy, D. F. (2017). "Ground motions for induced earthquakes in Oklahoma." *Bulletin of the Seismological Society of America*, 107(1), 198–215, doi.org/10.1785/0120160114.

Zalachoris, G., He, J., and Rathje, E. (2020). “Earthquake Time Series from Events in Texas, Oklahoma, and Kansas.” DesignSafe-CI, doi.org/10.17603/ds2-v310-qc53.

Zalachoris, G., and Rathje, E. M. (2019). “Ground Motion Model for Small-to-Moderate Earthquakes in Texas, Oklahoma, and Kansas.” *Earthquake Spectra*, 35(1), 1–20, doi.org/10.1193/022618EQS047M.

Zalachoris, G., Rathje, E. M., and Paine, J. G. (2017). “VS30 characterization of Texas, Oklahoma, and Kansas using the p-wave seismogram method.” *Earthquake Spectra*, 33(3), 943–961, doi.org/10.1193/102416EQS179M.

Zhang, X., Jeffrey, R. G., Wu, B., and Zhang, G. (2016). “Modeling of Injection Induced Seismic Events.” *Proceedings of SPE Asia Pacific Hydraulic Fracturing Conference*, Society of Petroleum Engineers, Richardson, Texas, 1–25, doi.org/10.2118/181793-MS.

3 Manuscript #2: Evaluating Liquefaction Triggering Potential at Sites Impacted by the 2016 M_w5.8 Pawnee, Oklahoma, Induced Earthquake

The following manuscript will be submitted to ASCE’s Journal of Geotechnical and Geoenvironmental Engineering.

Tyler Quick made the following contributions:

- Coordinated with property owners to coordinate testing
- Oversaw CPT testing and conducted MASW and HVSR tests
- Developed the liquefaction triggering model for induced earthquakes
- Performed liquefaction analyses for the Pawnee test sites
- Prepared figures and tables
- Wrote first draft of the manuscript and incorporated subsequent edits

Dr. Russell Green made the following contributions:

- Set up CPT testing contracts and assisted with test coordination
- Assisted with HVSR testing and initial site investigation

Dr. Ellen Rathje made the following contributions:

- Developed the ground motion prediction equation used in this study
- Assisted with characterizing ground motions for the Pawnee earthquake

Drs. Russell Green, Ellen Rathje, and Jim Mitchell made the following contributions:

- Contributed to the development of the liquefaction triggering model for induced earthquakes
- Provide valuable feedback throughout the study

Manuscript #2: Evaluating Liquefaction Triggering Potential at Sites Impacted by the 2016 M_w5.8 Pawnee, Oklahoma, Induced Earthquake

Tyler J. Quick[1], Russell A. Green[2], Ellen M. Rathje[3], and James K. Mitchell[4]

[1]Graduate Student, Department of Civil and Environmental Engineering, Virginia Tech, Blacksburg, VA; tylerjaq@vt.edu

[2]Professor, Department of Civil and Environmental Engineering, Virginia Tech, Blacksburg, VA; rugreen@vt.edu

[3]Janet S. Cockrell Centennial Chair, Department of Civil, Architectural, and Environmental Engineering, University of Texas at Austin, Austin, TX; e.rathje@mail.utexas.edu

[4]University Distinguished Professor, Emeritus, Department of Civil and Environmental Engineering, Virginia Tech, Blacksburg, VA; jkm@vt.edu

Keywords: liquefaction, liquefaction triggering, induced seismicity

Abstract

Deep wastewater injection-induced seismicity in Oklahoma has led to over a thousand $M_w>3$ earthquakes over the last ten years, four of which had $M_w > 5$. Furthermore, the 3 Sep 2016, M_w5.8 Pawnee, Oklahoma, earthquake was the first induced event worldwide, that the authors are aware of, that triggered liquefaction, which raises concerns regarding liquefaction risk posed by induced earthquakes. To address them, Quick et al. (2021) developed a new framework for evaluating the regional liquefaction hazard in Oklahoma, Texas, and Kansas (OTK) from induced earthquakes. This framework incorporates new stress reduction factor (r_d) and Magnitude Scaling Factor (MSF) relationships that can be used within the stress-based simplified liquefaction evaluation procedure to assess liquefaction potential from induced earthquakes. MSF and r_d relationships were developed based on site response analyses performed using regional soil profiles and recorded ground motions and scaled motions representative of induced

earthquakes in OTK. To this end, sites were characterized where liquefaction was and was not observed following the Pawnee earthquake. Liquefaction potential at each site was estimated using input parameters from the Pawnee event using the new OTK induced seismicity-specific liquefaction potential evaluation procedure, as well as several procedures commonly used to evaluate liquefaction potential for tectonic earthquakes. Estimates were compared with field observations following the Pawnee event to assess the efficacies of these models. This analysis showed that at most sites the induced seismicity-specific model more accurately predicted liquefaction severity than did models developed for tectonic earthquakes, which tended to over-predict liquefaction severity.

3.1 Introduction

Deep wastewater disposal into injection wells has led to a significant increase in seismicity in areas where oil and gas production are prevalent, such as Oklahoma, Texas, and Kansas (OTK). Although recent regulations enacted to limit wastewater injection volumes in Oklahoma have led to reductions in regional seismicity, over 60 earthquakes with moment magnitudes (M_w) of three or greater occurred in 2019, which is still 60 times the natural tectonic rate of about one $M_w \geq 3$ earthquake per year in the state (Langenbruch and Zoback 2016; U.S. Geologic Survey 2020). Additionally, although the number of $M_w \geq 3$ earthquakes has been decreasing since 2015 when wastewater injection was scaled back, some of the largest events, including the 2016, M_w5.8 Pawnee, OK earthquake, have occurred since that time. This dramatic increase in seismicity is of particular concern because it is occurring primarily in historically aseismic areas where building codes and construction methods have not traditionally accounted for higher levels of seismicity. This means that infrastructure in these areas may be more susceptible to damage caused by ground shaking. Although most earthquakes triggered by deep wastewater injection in Oklahoma have been small, larger events have resulted in structural damage and, of particular interest to this study, liquefaction (Clayton et al. 2016; Kolawole et al. 2017). In addition to damages caused by induced earthquakes in Oklahoma, induced events worldwide such as the 2017, M_w5.5 Pohang, South Korea, earthquake and the 25 February 2019, M_L4.9 Sichuan, China earthquake have led to injuries, structural damage, liquefaction, and significant economic losses (Choi et al. 2019; Yang et al. 2020). Observations of liquefaction during the 2016, Pawnee, OK earthquake and other induced events highlight the need to develop a suitable framework for accurately assessing the risk due to liquefaction associated with induced seismicity.

Although the stress-based "simplified" liquefaction evaluation procedure (Whitman 1971; Seed and Idriss 1971) is the most widely used approach for evaluating liquefaction triggering worldwide, the procedure is semi-empirical, with the empirical aspects of it derived from data from moderate-sized tectonic earthquakes in active shallow-crustal tectonic regimes (e.g., California, Japan, and New Zealand). As a result, the suitability of this procedure to evaluate the liquefaction hazard due to induced seismicity in stable continental tectonic regimes is uncertain. To address this issue, Quick et al. (2021) [Chapter 2 of this document] developed a new liquefaction triggering model for evaluating the liquefaction triggering potential of soils subjected to ground motions from induced earthquakes in OTK. The Quick et al. (2021) [Qea21] model was developed following the approach used by Green et al. (2017, 2020) to develop analogous liquefaction triggering models for evaluating liquefaction triggering due to tectonic earthquakes in the central and eastern United States (CEUS) and due to induced earthquakes resulting from natural gas extraction in the Groningen region of the Netherlands. This approach involved developing new regional, induced seismicity-specific depth-stress reduction factor (r_d) and Magnitude Scaling Factor (MSF) relationships for calculating normalized Cyclic Stress Ratio (CSR*) within the context of existing simplified liquefaction evaluation procedures.

As part of model development and validation, detailed geotechnical site characterizations were performed at sites where evidence of liquefaction was and was not observed following the during the 3 September 2016, M_w5.8 Pawnee, OK event. Site characterization included seismic Cone Penetration Tests (sCPT), Multichannel Spectral Analysis of Surface Waves (MASW) tests, and Horizontal-to-Vertical Spectral Ratio (HVSR) tests. Site profiles developed during the site characterization were used in development and validation of the Qea21 model. To assess the efficacy of the Qea21 model, liquefaction potential at the Pawnee test sites is evaluated using the new OTK induced seismicity-specific liquefaction triggering model as well as several existing models developed for tectonic events. These included the Boulanger and Idriss (2014) and Green et al. (2017) variants of the stress-based simplified procedure. Liquefaction potential at these sites is also evaluated using the global geospatial liquefaction model presented in Baise and

Rashidian (2018). Predictions of liquefaction severity based on the selected models are compared to field observations of liquefaction response made following the Pawnee event to evaluate the Qea21 model and the utility of existing models for assessing liquefaction triggering potential from induced earthquakes in OTK.

The following sections provide an overview of test site selection and detail the site characterization efforts. Results of site characterization are then presented. Finally, the results of the liquefaction hazard evaluation and model evaluation are presented, and conclusions drawn from this study are discussed.

3.2 Test Site Selection and Preliminary Site Characterization

The epicenter of the 3 September 2016, M_w5.8 Pawnee, OK, earthquake, was located about 15 km northwest of Pawnee, OK. This event was the strongest recorded earthquake in Oklahoma history and is one of the largest recorded earthquakes in the CEUS in the last 70 years (Tiwari and Rathje 2018). Contours of peak ground acceleration (a_{max}) from the U.S. Geological Survey (USGS) ShakeMap for the Pawnee event are shown in Figure 3.1 (U.S. Geologic Survey 2016a). Inferred a_{max} values were as high as 0.36g within 5 km of the earthquake epicenter, decreasing to less than 0.06g at a distance of approximately 40 km.

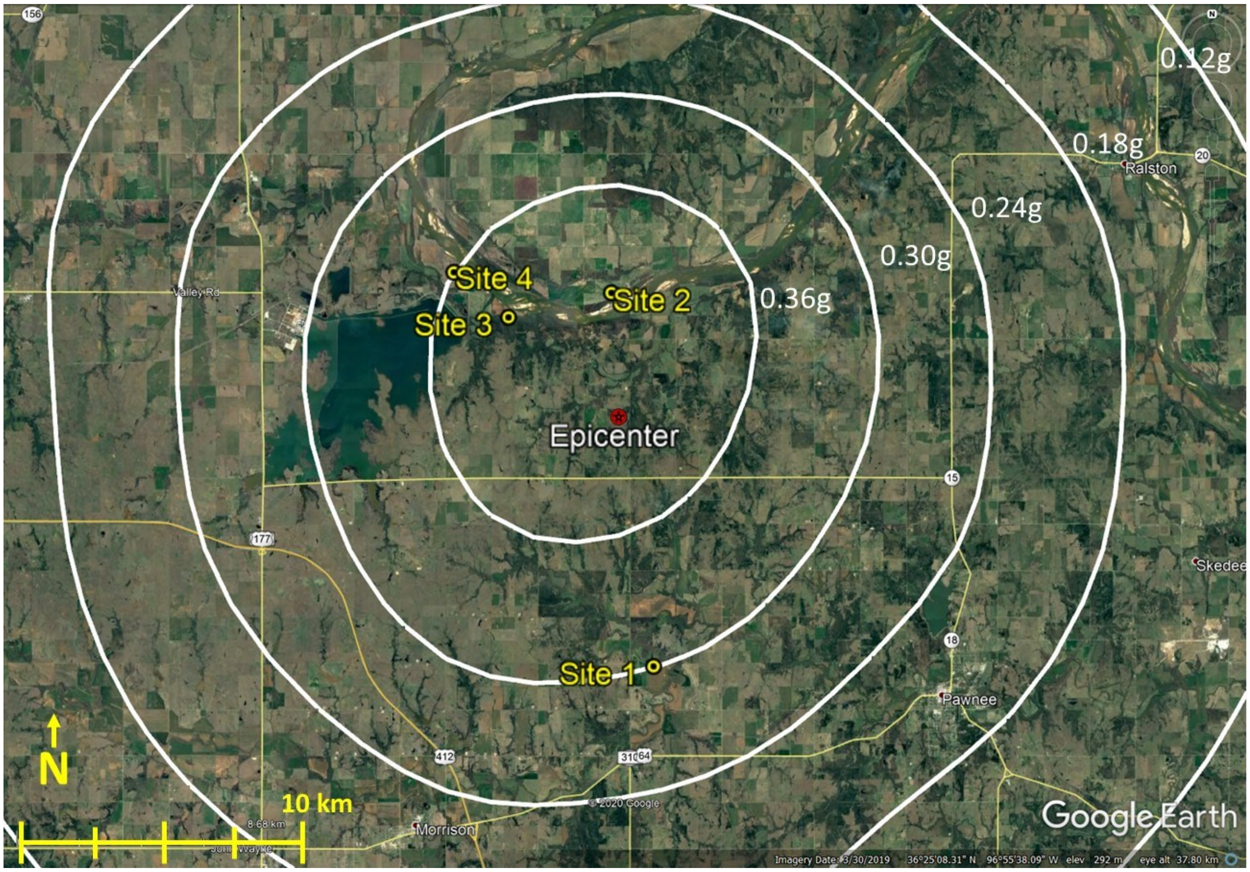

Figure 3.1. USGS ShakeMap for 2016 M_W5.8 Pawnee, OK earthquake showing contours of inferred peak ground acceleration. Liquefaction Sites 1, 2, 3, and 4, identified by Clayton et al. (2016) and Kolawole et al. (2017), are also indicated. Aerial imagery source: Google Earth, imagery date 3/30/2019, date accessed 10/7/2020.

To provide additional site profiles for use in developing the Qea21 model and to provide liquefaction and non-liquefaction case histories for use in model validation, several sites that experienced significant shaking during the Pawnee event were selected for characterization. Post-earthquake reconnaissance performed by Clayton et al. (2016) and Kolawole et al. (2017) following the 2016, Pawnee, Oklahoma earthquake identified four sites where potential liquefaction manifestations were observed and documented. These sites are labeled in Figure 3.1 as Sites 1 through 4. Site 1 lies along Black Bear Creek, a tributary of the Arkansas River, while Sites 2 through 4 are located within the floodway of the Arkansas River. Examples of the liquefaction manifestations observed at each site are shown in Figure 3.2 through Figure 3.5.

Figure 3.2. Photos of liquefaction manifestations at Test Site 1 (Photos courtesy of Dan Ripley).

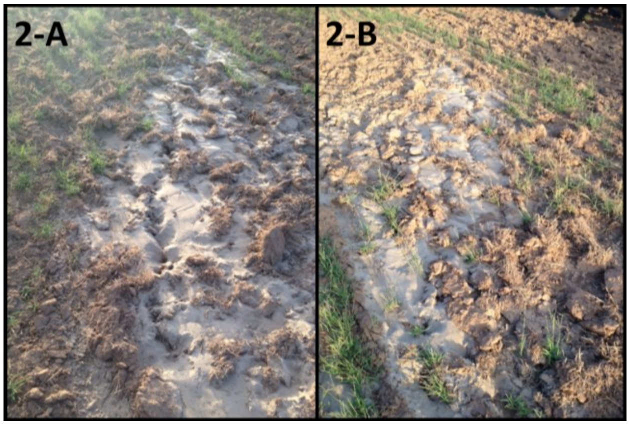

Figure 3.3. Photos of liquefaction manifestations at Test Site 2 (Photos courtesy of Rick Rice).

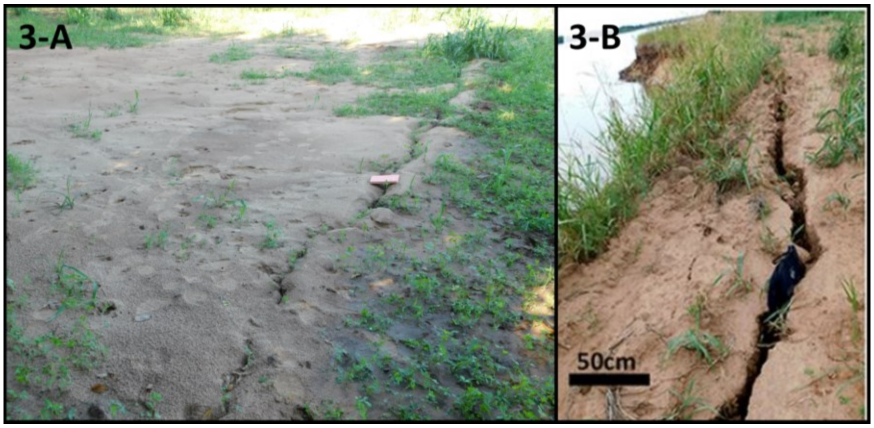

Figure 3.4. Photos of liquefaction manifestations at Test Site 3 (Kolawole et al. 2017).

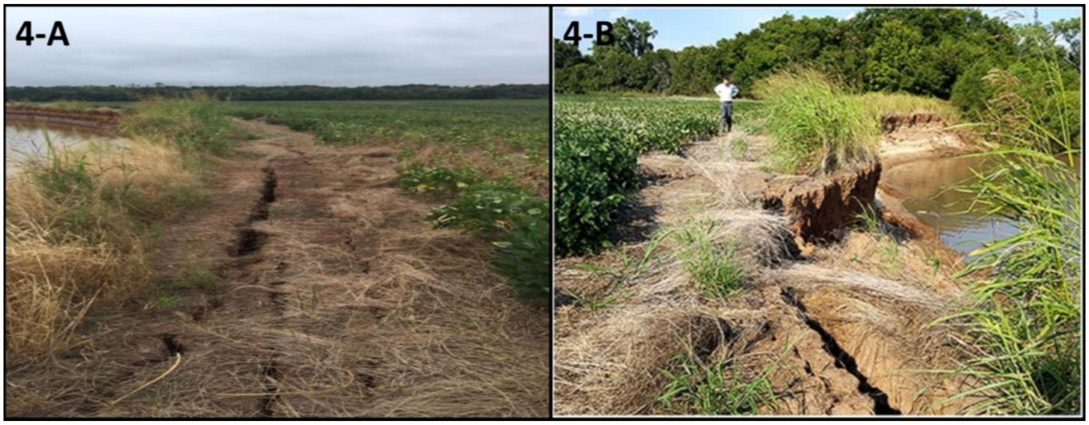

Figure 3.5. Photos of cracking at Test Site 4 (Photos courtesy of Martin Williams).

Liquefaction features at Site 1 included sand boils ranging from a few inches to a few feet in diameter in several locations at the site. Sand boils in the eastern part of the site were aligned and oriented NNE (Clayton et al. 2016). Site 2 included cracks approximately 2 to 5 m long with small amounts of ejecta. Deep cracks extending meters deep near the river at this site and the adjacent property were also observed (Jefferson Chang, Personal Communication, 13 July 2018). Manifestations at Site 3 included cracking and ejecta. Cracks were reported with lengths ranging from 4 to 42 m and widths ranging from 0.5 to 8 cm. Sand ejecta associated with two of the largest cracks covered approximately 145 and 56 m^2, respectively (Kolawole et al. 2017). Large fractures measuring 0.5-34 cm wide were also observed along the riverbank, possibly associated with lateral spreading (Kolawole et al. 2017). Site 4 was described as potential lateral spreading due to large cracks subparallel to the riverbank. However, Clayton et al. (2016) noted that it could not be confirmed from post-earthquake communication with the property owner whether the cracking and sliding of the riverbank was associated with lateral spreading or a simple slump failure of the riverbank. Conversations with landowners near the selected sites indicated that there were additional locations where liquefaction was observed but not documented. This included the property directly to the west of Site 2, which experienced cracking near the riverbank and sand boils about 1000 m from the riverbank. While these additional sites were not included in the present study, they are evidence that liquefaction was more widespread than documented during the initial post-earthquake reconnaissance.

Preliminary site investigations were performed at the identified sites in January 2019. The primary purpose of these investigations was to gather existing information and accurately determine areas at each site where liquefaction features were and were not observed. USGS geologic maps for the four Pawnee liquefaction sites (Stanley and Chang 2016) are shown in Figure E.1 in Appendix E. All four sites are located in alluvial zones (Stanley and Chang 2016), which the USGS describes as consisting of sand, silt, clay, and gravel with maximum thicknesses along major streams ranging from 9 to 24 m and along minor streams ranging from 0 to 18 m (U.S. Geologic Survey 2019). These descriptions are consistent with the results from the detailed site characterization discussed in later sections. Groundwater depth during the January 2019 site investigation was visually estimated as 1 m at Site 1, 2 m at Sites 2 and 4, and 1 to 2 m at Site 3 based on river/stream levels adjacent to the sites.

Findings from Clayton et al. (2016) and Kolawole et al. (2017) in conjunction with GPS-tagged photos and anecdotal evidence provided during interviews with the property owners were used to estimate the extent of areas where liquefaction was observed at each site. Based on this information, test locations were selected at each site. Test locations were selected both in areas where liquefaction manifestations were and were not observed. The no-liquefaction sites were selected so as to be near to the observed liquefaction sites and in areas where conditions are favorable for liquefaction to occur (e.g., profiles with liquefiable materials, locations inside river bends, areas of low elevation, etc.), while remaining in areas where it was determined that no liquefaction manifestations were reported.

Based on field observations from site visits in January 2019 and further discussion with the owner and others that visited the site following the earthquake, it was determined that the cracking reported at Site 4 was likely related to a seismic slope failure and not the result of liquefaction as initially reported. As such, Site 4 was excluded from further site investigation. It should also be noted that, while Kolawole et al. (2017) provided detailed mapping of cracking and ejecta in some areas at Site 3, at Sites 1 and 2, as well as in some areas of Site 3, only approximate locations were available for liquefaction features. As a result, the identified zones of liquefaction may not represent the exact extent of liquefaction manifestations that occurred at each site, and liquefaction manifestations may have occurred outside these areas. Difficulties in observing the full extent of liquefaction features following the earthquake due to crops, plowed fields, and other vegetation may also have led to under-reporting and underestimations of the extent of liquefaction at these sites. However, test locations were selected using the best available information. Figure 3.6 shows the estimated zones of liquefaction at each site as well as the locations of the photos provided in Figure 3.2 through Figure 3.5.

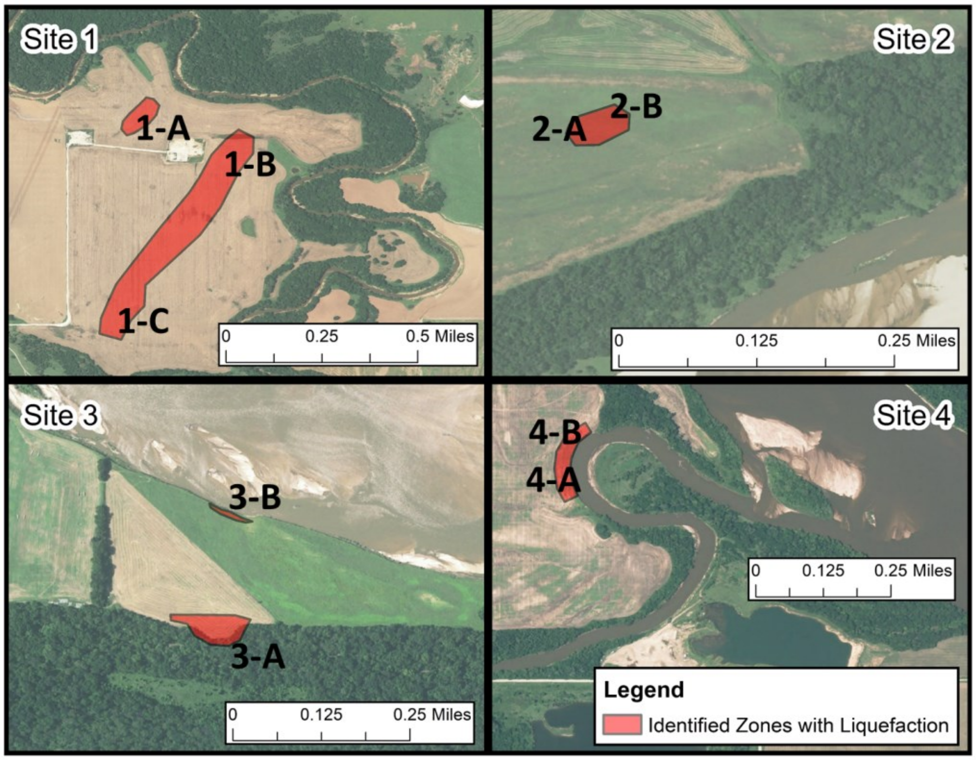

Figure 3.6. Identified liquefaction areas at the Pawnee sites. Locations of the photos presented in Figure 3.2 through Figure 3.5 are also indicated.

HVSR tests were also performed at each site as part of the preliminary site characterization. HVSR tests were performed following the guidelines provided by the SESAME project (Bard and SESAME-team 2004) using ambient vibrations recorded using a three-component broadband seismometer. HVSR test results provided information on fundamental site frequency and were used to constrain the V_s models determined from MASW tests (Yust et al. 2018) performed as part of the full site characterization. The results of the HVSR tests are presented in the following section in context of the results from the detailed site characterization.

Initial estimates of the liquefaction hazard at the test sites based on ground motions from the Pawnee earthquake were made as part of the preliminary site characterization using the global geospatial liquefaction model presented by Baise and Rashidian (2018). This model provides estimates of probability of liquefaction (P_{liq}) as well as liquefaction spatial extent (LSE), the percent of a given area covered by surface manifestations of liquefaction. Baise and Rashidian (2018) note that this model was developed for regional prediction of liquefaction spatial extent rather than site-specific assessment. However, the model was used during the preliminary investigation to provide preliminary insight into the liquefaction hazard at these sites prior to detailed site characterization.

P_{liq} and LSE were estimated based on peak ground velocity (PGV), time-averaged small-strain shear wave velocity of the upper 30 m (V_{s30}), mean annual precipitation, closest distance to water, and water table depth. PGV was estimated based on the USGS ShakeMap (U.S. Geologic Survey 2016a), and precipitation data were taken from National Oceanic and Atmospheric Administration (NOAA) Station USC00346940 (NOAA 2019). Shear wave velocity information was not available during the preliminary investigation, but, as discussed in the following section, V_{s30} values for Sites 1 through 3 were determined during the full site characterization. V_s testing was not performed at Site 4. However, V_{s30} values reported by Zalachoris et al. (2017) for other alluvial sites in the region ranged from 362 m/s to 580 m/s. Based on this information, a V_{s30} of 360 m/s was used for Site 4. Average water table depths at Sites 1 through 3 during the Pawnee event were estimated based on water table depths observed during CPT, adjusted as described in Section 3.5.1. Water table depth for Site 4 was estimated based on river levels adjacent to the site during the preliminary investigation, adjusted in similar fashion as done for Sites 1 through 3. Inputs and results for each site are shown in Table 3.1.

Table 3.1. Liquefaction Hazard Estimates for the Pawnee Earthquake Test Sites based on Baise and Rashidian (2008).

Site	Peak Ground Velocity (cm/s)	V_{s30} (m/s)	Mean Annual Precipitation (mm)	Closest Distance to Water (km)	Water Table Depth (m)	Probability of Liquefaction	Liquefaction Spatial Extent (%)
1	20	270.2	1021	0.15	2.9	0.375	8.8
2	25	273.6	1021	0.3	2.8	0.380	9.3
3	20	285.7	1021	0.11	2.2	0.357	7.2
4	20	360	1021	0	2.5	0.265	2.2

Given the fairly small areal extent report liquefaction at these sites, LSEs of 8.8% and 9.3% for Sites 1 and 2, respectively, appear high. However, LSE of 7.2% may be reasonable for Site 3 where liquefaction was more extensive. LSE for Site 4 (2.2%) was lower than for the other sites but still appears to overestimate the liquefaction hazard given the lack of documented liquefaction manifestations at the site. The Baise and Rashidian (2008) approach was developed for tectonic earthquakes and may not be entirely suitable for use with induced earthquakes. Additionally, as noted previously, the model was developed for regional hazard assessment as opposed to site-specific assessments. However, this analysis does provide some insight as to what the liquefaction hazard was in the area due to ground motions from the Pawnee event. Similar estimates of P_{liq} and LSE are expected for comparable, nearby sites. This agrees with observations made by local landowners that liquefaction was more widespread and occurred at more sites than those formally documented in Clayton et al. (2016) and Kolawole et al. (2017).

3.3 Detailed Site Characterization

Detailed characterization of the selected sites, including cone penetration (CPT) and MASW tests, were performed in November 2019 and March 2020. CPT soundings were performed at both liquefaction and no-liquefaction test locations identified at Sites 1, 2, and 3. sCPT tests were performed at two liquefaction locations and two no-liquefaction locations at Site 2 and at all test locations at Site 3. CPT soundings extended to refusal. Table 3.2 provides a summary of the CPT tests performed at each site.

Table 3.2. Summary of CPT Soundings at Pawnee, OK Test Sites.

Sounding	Site	Max Depth of CPT (m)	Seismic CPT Test	MASW	Liquefaction Reported
CPT-01	1	17	N	N	N
CPT-02	1	16	N	Y	Y
CPT-03	1	15	N	Y	Y
CPT-04	2	14	Y	Y	Y
CPT-05	2	14	Y	Y	Y
CPT-06	2	13	N	N	N
CPT-07	2	14	N	N	N
CPT-08	2	13	Y	N	N
CPT-09	2	13	Y	N	N
CPT-10	3	15	Y	Y	Y
CPT-11	3	14	Y	Y	Y
CPT-12	3	16	Y	N	Y
CPT-13	3	15	Y	N	N
CPT-14	3	15	Y	N	N
CPT-15	3	15	Y	N	N

MASW tests were also performed in identified areas of liquefaction at Sites 1 through 3, as listed in Table 3.2. One MASW test was performed each at Site 2 and Site 3. Two MASW tests were performed at Site 1 using perpendicular geophone arrays. MASW tests were performed using a 2-m geophone spacing and source offsets of 5, 10, 20, and 40 m. A sledge hammer that impacted a Plexiglas strike-plate was used as the active source for the MASW testing. Hand auger samples were taken near CPT-03 at Site 1 and CPT-05 at Site 2. Sampling depth was limited to 4.5 m at CPT-03 due to unsafe weather conditions and 4 m at CPT-05 due to borehole collapse. Locations for CPT, MASW tests, HVSR, and auger sampling are shown in Figure 3.7 through Figure 3.9 for Sites 1 through 3, respectively. As discussed previously, no additional testing (CPT or MASW) was performed at Site 4 because the features noted at this site following the Pawnee event were likely the result of seismic slope stability and unrelated to liquefaction. Raw data from CPT, MASW, and HVSR testing are provided as an electronic supplement to this document.

Several originally planned test locations had to be adjusted due to site conditions at the time of testing. In particular, at Site 1, testing was limited to the northwest portion of the site due to wet ground conditions and ponding in other areas of the site. CPT-02 was relocated farther from the center of the identified liquefaction area due to soft ground conditions that made the original test location inaccessible to the CPT rig. Flooding of the Arkansas River in May 2019 eroded a large portion of Site 3, including one area that had potentially liquefied, which resulted in the relocation of CPT-15. The riverbank alignment at the time of CPT testing in March 2020 is shown in Figure 3.9. CPT-13 at Site 3 was also moved from its planned location due to ponding at the site during testing.

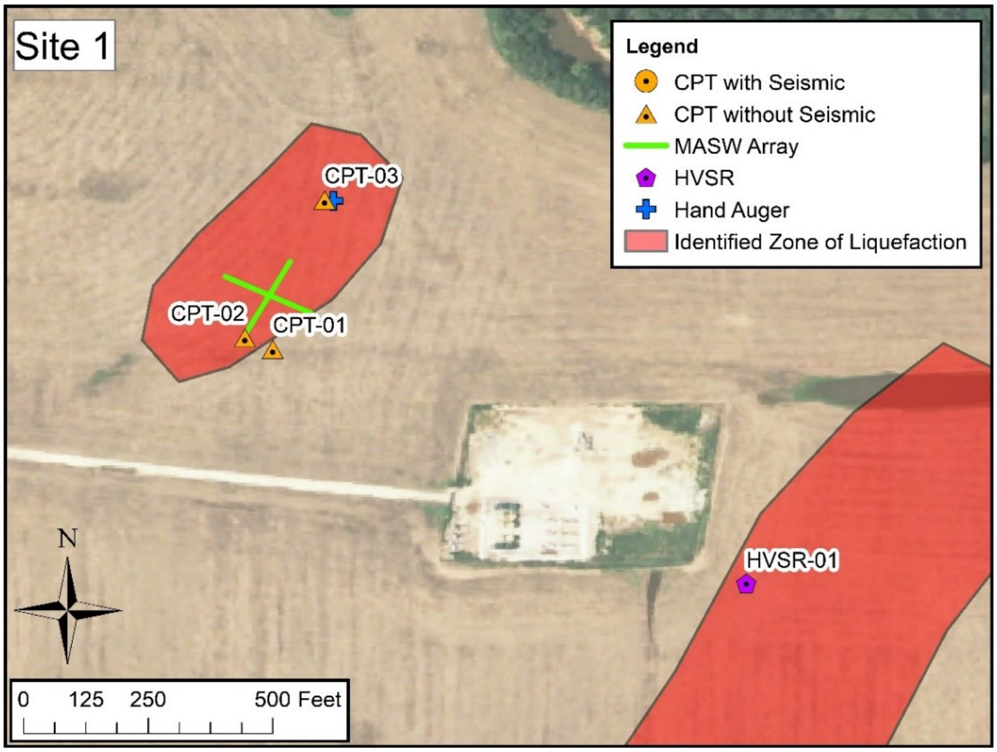

Figure 3.7. CPT, MASW, HVSR, and Hand Auger test locations at Site 1.

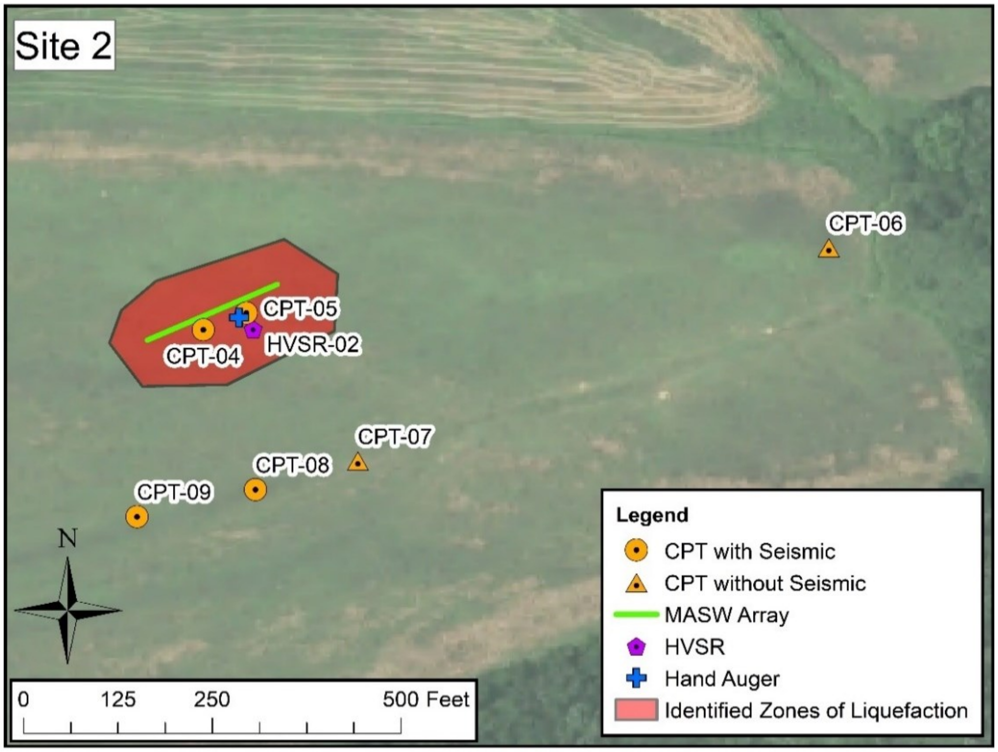

Figure 3.8. CPT, MASW, HVSR, and Hand Auger test locations at Site 2.

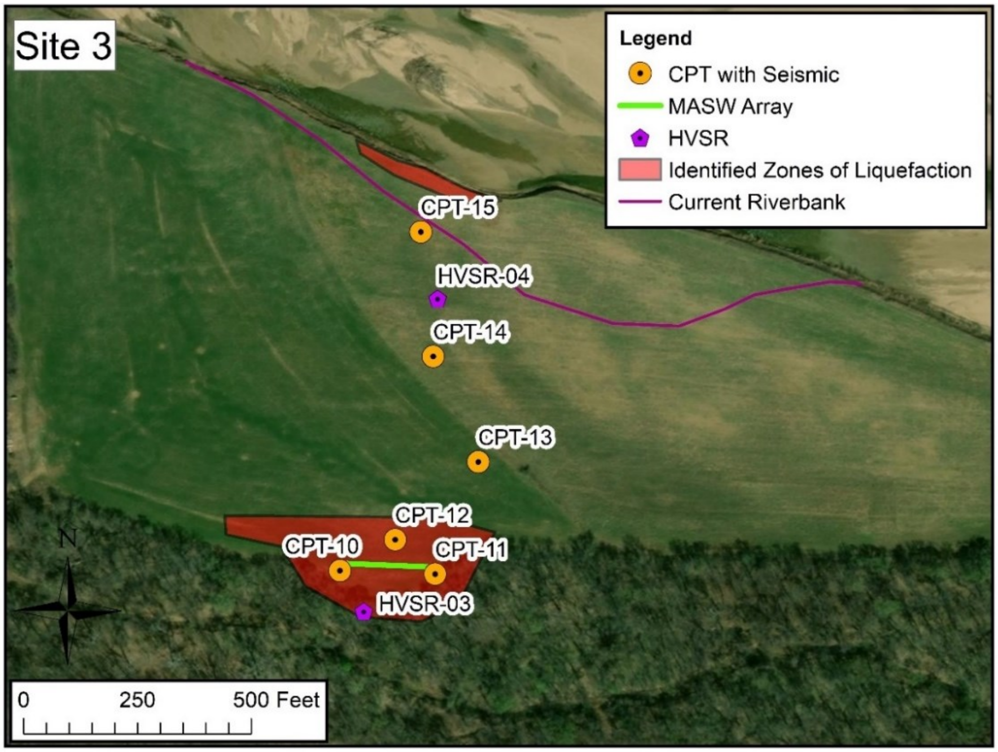

Figure 3.9. CPT, MASW, and HVSR test locations at Site 3.

3.4 Site Characterization Results

Profiles of CPT tip resistance (q_t), friction ratio (F_r), and soil behavior type index (I_c) were developed at each sounding location. CPT data were processed based on recommendations in Robertson and Cabal (2015). I_c values and listed soil behavior types are based off the normalized CPT soil behavior type (SBT_n) chart developed by Robertson (2010) as presented in Robertson and Cabal (2015). Ground water depth at the time of CPT testing was estimated from CPT pore water pressure measurements. As an example, q_t, F_r, and I_c profiles for CPT-07 at Site 2 are shown in Figure 3.10. Profiles for all test locations are presented in Figure F.1 through Figure F.15 in Appendix F. As noted previously, CPT soundings extended to refusal.

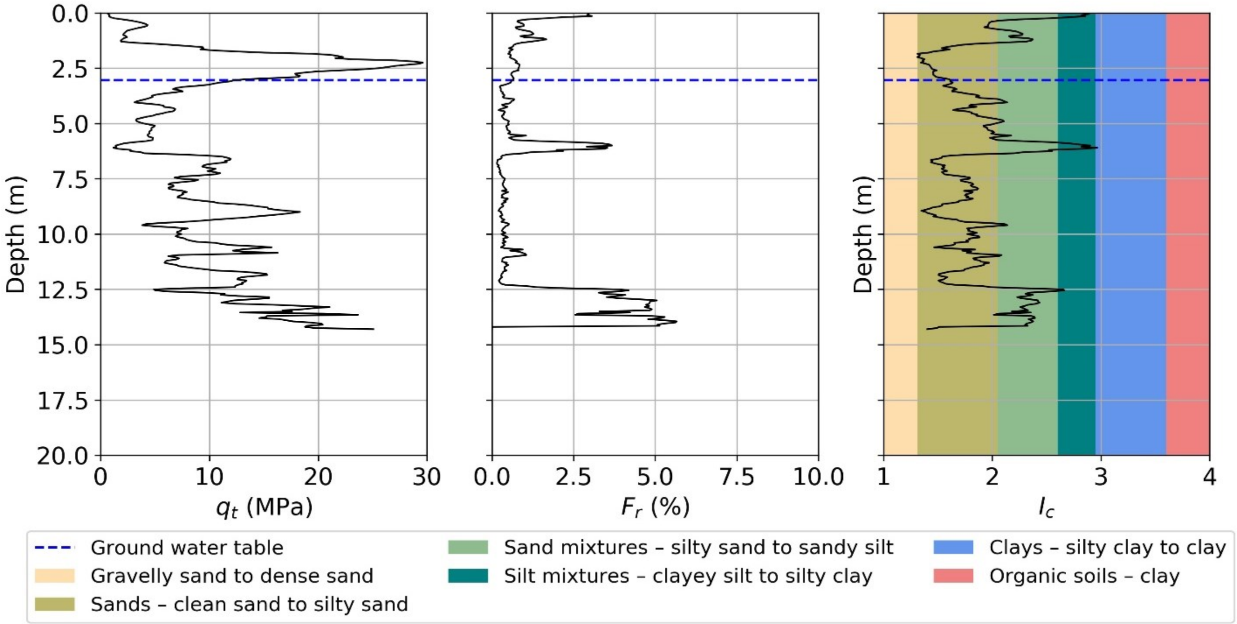

Figure 3.10. CPT test results for CPT-07, Site 2.

An I_c value of 2.6, the boundary between "sandy silt" and "clayey silt mixtures" based on SBT_n, is often used to screen out clay-like soils from liquefaction analyses because they are likely not susceptible to liquefaction triggering (Robertson and Wride 1998). However, Boulanger and Idriss (2014) note that other cutoff values as high as 2.8 or as low as 2.4 may be justified based on site-specific sampling and testing (e.g., Maurer et al. 2019). For this reason, lab tests, including particle-size analysis and Atterberg limit tests, were performed on hand auger samples taken near CPT-03 at Site 1 and CPT-05 at Site 2. Samples were taken at depths where I_c values were close to 2.6 to better assess the properties of these soils. Lab tests at Site 1 confirmed I_c = 2.6 was an appropriate cutoff for liquefaction susceptibility based on plasticity of the tested soils (i.e., plasticity index, PI $\geq$ 24 for soils having $I_c > 2.6$). Lab test results at Site 2 suggested that soils with I_c as low as 2.4 may not be susceptible to liquefaction due to the plasticity (PI $\geq$ 9) of these soils. However, a sensitivity analysis was performed during liquefaction hazard assessment to test the effect of I_c cutoff on estimated liquefaction potential. This analysis found that, due to the scarcity of soil having $2.4 \leq I_c < 2.6$, the choice of I_c threshold between 2.4 to 2.6 had negligible impact on estimated risk of liquefaction at Site 2. Similar results were found during sensitivity analysis for Site 3. For this reason, an I_c cutoff of 2.6 was used at all sites to be consistent with general implementation of the selected liquefaction triggering models. Additional detail on lab testing and I_c threshold selection is available in Appendix F.

HVSR analysis was performed using the Geopsy software package. Ambient vibrations were recorded at each site using a three-component Nanometrics Trillium Compact Broadband Seismometer. Seismometer data was recorded using a Centaur Digitizer with a sampling rate of 100 Hz. Ambient motion recordings from each site were divided up into smaller time windows, and Fourier spectra were computed for each time window for each of the recorded components of motion (N-S, E-W, Vertical). A cosine taper was applied and the spectra were smoothed using a Konno-Ohmachi (Konno and Ohmachi 1998) smoothing filter, with the parameter, *b*, set to 20. The ratio of the vertical spectrum to geometric mean of the two horizontal spectra was plotted for each window and the mean horizontal-to-vertical (H/V) curve was calculated. H/V curves for the individual time windows, as well as the mean H/V curve, were plotted for each site. Once plotted, the frequency corresponding to the maximum point of the mean H/V curve is identified. This peak frequency corresponds to the fundamental frequency of a given site (e.g., Rahpeyma et al. 2016). HVSR plots for Sites 1 through 3 are shown in Figure 3.11. The fundamental frequency at the three sites along the Arkansas River (i.e., Sites 2, 3, and 4) was approximately 3 Hz, while it was 0.86 Hz at Site 1, located along Black Bear Creek. This may be an indication of differences in alluvium thickness along the Arkansas River versus that along Black Bear Creek, where less alluvium would lead to a stiffer site and higher fundamental frequency and vice-versa.

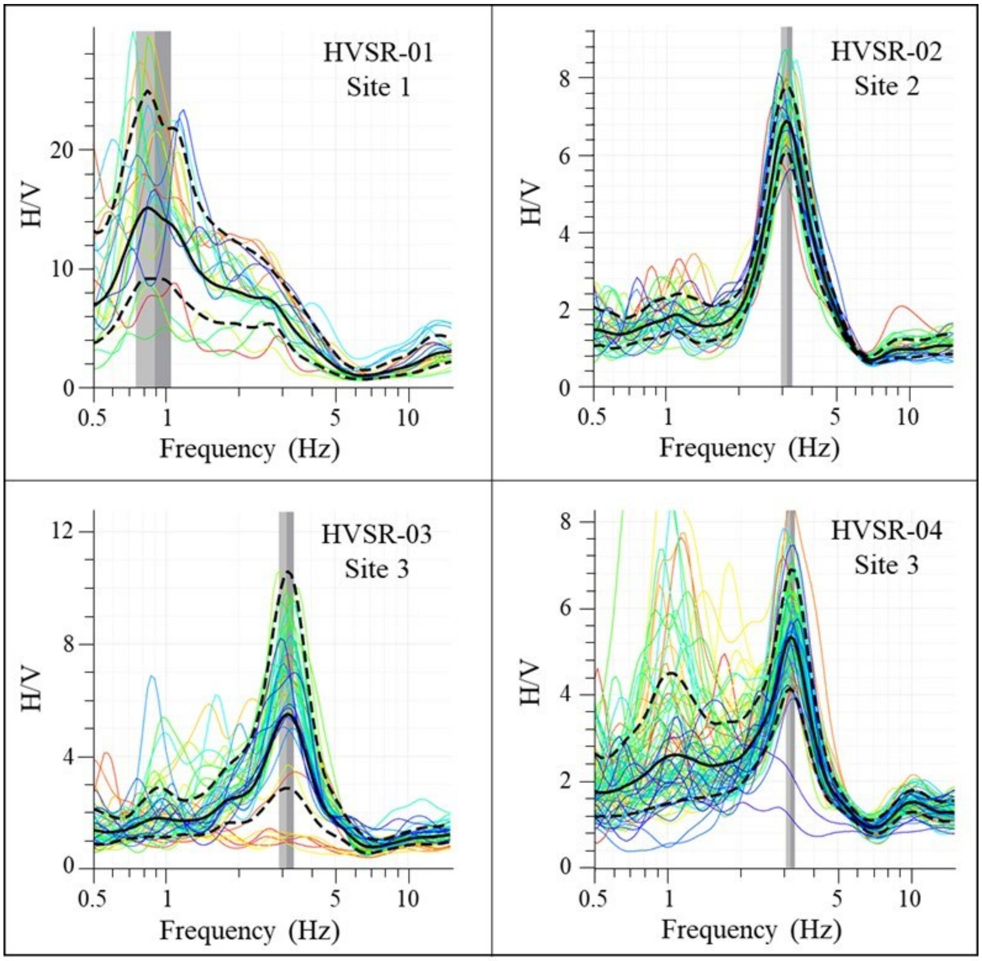

Figure 3.11. HVSR results for Sites 1-3. H/V vs. frequency is shown for individual time windows from the recorded ambient ground motions. Average H/V curves +/- standard deviation are indicated by the solid and dashed black lines and the corresponding peak frequency +/- one standard deviation is indicated by the gray bands.

V_s profiles were developed at each CPT sounding location using a combination of CPT, sCPT, and MASW data. V_s profiles based on sCPT data were developed using the interval and slope methods presented by Hallal and Cox (2019). V_s profiles from MASW data were developed using the program Dinver (Wathelet et al. 2020) following the Layering Ratio method proposed by Cox and Teague (2016). HVSR data were used to constrain bedrock depth during V_s profile inversion (Yust et al. 2018). However, due to limitations of the source used during MASW testing, the V_s values below a depth of approximately 30 m could not reliably be resolved. As such, the developed MASW V_s profiles do not extend below this depth. V_s profiles were also developed using correlations with CPT data. Profiles were developed using both the Robertson and Cabal (2015) and Ulmer et al. (2020) correlations. Combined correlation-based V_s profiles were also developed by using the Robertson and Cabal (2015) correlation to estimate V_s for non-liquefiable soils and the Ulmer et al. (2020) correlation to estimate V_s for liquefiable soils. The resulting V_s profiles are plotted in Figure F.16 through Figure F.30 in Appendix F.

Time-averaged small-strain shear wave velocity of the upper 12 m (V_{s12}) was estimated at each sounding location based on tests performed at that location. These results are provided in Table 3.3. MASW geophone arrays were laid out between two CPT sounding locations at each site (i.e., CPT-02 and CPT-03 at Site 1, CPT-04 and CPT-05 at Site 2, and CPT-10 and CPT-11 at Sites 3). As a result, the same V_{s12} from the MASW tests is presented for both sounding locations. Estimated V_{s12} values were used to compute r_d and MSF for the liquefaction hazard assessment. As shown in this table, there is fairly good agreement in V_{s12} values estimated using the sCPT slope method, MASW, and Robertson and Cabal (2014) correlations. In contrast, the Ulmer et al. (2020) CPT correlation, and consequently the combined CPT correlation, resulted in consistently lower V_{s12} values. The sCPT interval method led to more erratic V_s profiles than other methods, resulting in V_{s12} at some locations that are very different than those predicted by the other methods. This agrees with the observations of Hallal and Cox (2019) that the sCPT slope method provides more reliable velocities than the interval method. Where available, V_{s12} measurements from sCPT tests (slope method) were used in the analysis. MASW results were used if sCPT data were not available, and combined CPT correlations results were used if sCPT and MASW data were not available.

Table 3.3. Estimated V_{s12} Based on sCPT, CPT, and MASW Tests.

Sounding	Site	V_{s12} (m/s)						
		sCPT - Interval Method	sCPT - Slope Method	CPT - Robertson and Cabal (2014)	CPT - Ulmer et al. (2020)	CPT - Combined by Soil Type	MASW	
CPT-01	1	-	-	162.65	119.95	162.65	-	
CPT-02	1	-	-	143.73	117.13	140.28	175.51	177.07
CPT-03	1	-	-	144.72	118.13	135.68	175.51	177.07
CPT-04	2	177.40	169.02	181.30	139.05	141.58	171.60	
CPT-05	2	204.21	172.04	177.83	133.56	134.67	171.60	
CPT-06	2	-	-	171.91	127.51	140.19	-	
CPT-07	2	-	-	177.61	134.94	140.98	-	
CPT-08	2	161.26	158.96	177.39	133.95	141.12	-	
CPT-09	2	195.87	173.28	182.05	138.98	143.97	-	
CPT-10	3	157.54	148.28	152.34	117.25	116.67	157.80	
CPT-11	3	147.96	142.91	126.29	77.92	77.89	157.80	
CPT-12	3	78.31	150.18	144.98	101.96	102.04	-	
CPT-13	3	179.41	156.54	144.39	99.41	99.71	-	
CPT-14	3	165.65	156.89	157.34	124.37	125.99	-	
CPT-15	3	274.14	174.91	162.27	113.79	113.77	-	

CPT test results and V_s profiles were used to create representative site profiles that could be used in site response analyses as part of the Qea21 model development. Site characterization results are also used, in conjunction with observations of liquefaction made following the Pawnee event, to validate the Qea21 liquefaction triggering model.

3.5 Liquefaction Hazard Assessment and Validation of the Quick et al. (2021) OTK Induced Seismicity Liquefaction Triggering Model

To evaluate the efficacy of the Qea21 OTK induced seismicity-specific liquefaction triggering model, liquefaction potential is evaluated at each CPT sounding location using the Qea21 model as well as three existing tectonic models: the Green et al. (2017) models for the CEUS [Gea17-CEUS] and western US (WUS) [Gea17-WUS] and the Boulanger and Idriss (2014) [BI14] model for the WUS. Liquefaction potential is assessed using input parameters for the Pawnee event. The predicted liquefaction response is compared to field observations following the

Pawnee event to assess the efficacy of these models for evaluating liquefaction triggering potential during induced earthquakes in Oklahoma.

3.5.1 Ground Motion Characteristics and Other Inputs for Liquefaction Hazard Assessment

For the liquefaction assessment, required ground motion parameters include M_w, a_{max}, and R_{hyp} for each site evaluated. Values for a_{max} at each site during the Pawnee event are estimated using the USGS ShakeMap (USGS 2016). While the ShakeMap provides peak a_{max} (largest a_{max} for the two recorded horizontal components of motion) at each location, the geometric mean a_{max} is needed for liquefaction evaluation. Boore and Kishida (2017) found that the typical ratio of peak a_{max} to geometric mean a_{max} was 1.117. Accordingly, geometric mean a_{max} for the Pawnee event are calculated by dividing peak a_{max} from the ShakeMap by a factor of 1.117. The resulting geometric mean a_{max} at each test location are provided in Table 3.4. A map of geometric mean a_{max} for the Pawnee earthquake based on the USGS ShakeMap is shown in Figure E.2 in Appendix E. For comparison, a_{max} was also estimated using the Zalachoris and Rathje (2019) ground motion prediction equation (GMPE). These a_{max} are also provided in Table 3.4. Estimated a_{max} from the Zalachoris and Rathje (2019) GMPE are similar to geometric mean values from the ShakeMap (USGS 2016), particularly at Site 1, which is slightly farther from the epicenter. The Zalachoris and Rathje (2019) GMPE predicts a_{max} values at Sites 2 and 3 that are approximately 13% higher than a_{max} estimates from the USGS ShakeMap. Estimates of a_{max} from the ShakeMap are used for assessing liquefaction hazard and model validation.

Table 3.4. Ground motion and site characteristics for liquefaction hazard analysis at the Pawnee Earthquake test sites.

Sounding	Site	ShakeMap Geometric Mean PGA (g)	ShakeMap Standard Deviation of ln(PGA) (ln units)	PGA from ZR19 GMPE (g)	Epicentral Distance (km)	Hypocentral Distance (km)	Estimated Groundwater Depth (m)	V_{s12} (m/s)	V_{s30} (m/s)
CPT-01	1	0.2606	0.4938	0.2543	8.64	10.30	2.29	162.65	270.16
CPT-02	1	0.2606	0.4938	0.2546	8.63	10.29	2.90	176.29	270.16
CPT-03	1	0.2606	0.4938	0.2571	8.55	10.22	3.51	176.29	270.16
CPT-04	2	0.3874	0.5865	0.4337	4.36	7.10	3.05	170.20	273.56
CPT-05	2	0.3874	0.5865	0.4337	4.36	7.10	3.05	172.04	273.56
CPT-06	2	0.3874	0.5865	0.4328	4.38	7.11	2.74	140.19	273.56
CPT-07	2	0.3874	0.5865	0.4354	4.34	7.08	2.59	140.98	273.56
CPT-08	2	0.3874	0.5865	0.4381	4.29	7.05	2.59	158.96	273.56
CPT-09	2	0.3874	0.5865	0.4381	4.28	7.05	2.90	173.28	273.56
CPT-10	3	0.3519	0.5890	0.4003	5.18	7.63	3.36	148.28	285.66
CPT-11	3	0.3519	0.5890	0.4026	5.14	7.60	1.51	142.91	285.66
CPT-12	3	0.3519	0.5890	0.4011	5.17	7.62	2.16	150.18	285.66
CPT-13	3	0.3519	0.5890	0.4003	5.18	7.63	1.36	156.54	285.66
CPT-14	3	0.3519	0.5890	0.3973	5.24	7.67	2.96	156.89	285.66
CPT-15	3	0.3519	0.5890	0.3944	5.3	7.71	4.76	174.91	285.66

CPT profiles and V_{s12} from the site investigation are used for the liquefaction analysis. Although groundwater depths during CPT testing are available, water table depth at these sites during the Pawnee event are not available. As a result, groundwater depths during the 2016 Pawnee event are estimated by comparing river gage heights during the earthquake to gage heights during CPT testing for rivers/creeks adjacent to the test sites. River gage data do not provide a direct measure of water table depth, but may provide a rough indication of overall groundwater fluctuation at these sites. Accordingly, the differential in gage height is used to adjust the groundwater depth observed during CPT testing either up or down to provide an estimate of groundwater depth during the Pawnee earthquake. Gage data for Black Bear Creek at Pawnee, OK are used for Site 1, and gage data for the Arkansas River at Ralston, OK are used for Sites 2 and 3 (U.S. Geologic Survey 2016b; c). USGS gage data plots are provided in Figure E.3 through Figure E.5 in Appendix E. Estimated water table depths are provided in Table 3.4.

Unfortunately, no river gages are located in close proximity to the test sites. As a result, the gages used were located 15-30 km downstream of the test sites. These gages provide only a rough estimate of differences in water level (and rougher estimates of water table depth) at the test sites themselves. However, these data provide the best available estimate of water table depths during the Pawnee event, and the resulting water table depths are used in the liquefaction hazard analysis. To assess the effect of these assumptions on the analysis results, a sensitivity analysis was performed by assessing liquefaction potential using water table depths 0.5 m higher and lower than the best estimate depths. Results are discussed in Section 4.5.3.

3.5.2 Assessment of Liquefaction Potential at the Pawnee Earthquake Test Sites

As noted previously, liquefaction potential at the selected test sites is evaluated using the Gea17-CEUS, Gea17-WUS, and BI14 models for tectonic earthquakes in addition to the Qea21 model for induced earthquakes in OTK. The BI14 model was developed for earthquakes in active shallow-crustal tectonic regions (e.g., WUS) but is commonly used in other areas, while the Gea17-CEUS model is specific to the CEUS. The Gea17-WUS model is included as an example of an updated model for active shallow-crustal tectonic regimes. These models, particularly the BI14 and Gea17-CEUS models, represent the standard of practice for liquefaction evaluation for tectonic earthquakes in OTK. As such, these models are used as benchmarks against which comparisons can be made with the results from the new induced seismicity-specific liquefaction hazard model developed herein.

The Qea21 model incorporates new r_d and MSF relationships specific to induced seismicity in OTK. These relationships can be used within the context of the stress-based simplified liquefaction evaluation procedure to assess the liquefaction potential from induced earthquakes in OTK. As discussed in Quick et al. (2021) [Chapter 2 in this document], both r_d and MSF tend to be lower for induced earthquakes in OTK than for tectonic earthquakes in WUS and CEUS. Quick et al. (2021) suggest that differences in r_d and MSF between induced and tectonic ground motions are related to the greater high frequency content of induced ground motions, the longer durations of ground motions in OTK as compared to the WUS, and other factors. The net effect of these differences is that factor of safety against liquefaction (FS_{liq}) for a given ground motion and soil profile tends to be higher for the Qea21 model than for the Gea17 or BI14 models. However, the Qea21 model can result in lower FS_{liq} at shallow depths (< ~2-3 m).

The four selected liquefaction triggering models were used to calculate FS_{liq} as a function of depth at each CPT test location. Based on the computed FS_{liq} profiles, surficial liquefaction manifestation severity at each location is predicted using the Ishihara-inspired Liquefaction Potential Index (LPI_{ish}) framework (Maurer et al. 2015b). LPI_{ish} is a dimensionless index that represents the cumulative liquefaction response of a soil profile from the ground surface to a depth of 20 m and has been shown to correlate well to surficial liquefaction manifestation severity (Maurer et al. 2015b). Similar to the liquefaction potential index (LPI) proposed by Iwasaki et al. (1978), LPI_{ish} is proportional to the cumulative thickness of liquefied layers in the upper 20 m, the depth to these layers, and the degree to which FS_{liq} for these layers is less than 1.0. However, LPI_{ish} also accounts for the effect of the thickness of the non-liquefied crust (H_1) relative to the cumulative thickness of the underlying liquefied materials (H_2) on the severity of liquefaction manifestations by incorporating concepts from the H_1-H_2 chart developed by Ishihara (1985). LPI_{ish} is defined as (Maurer et al. 2015b):

$$LPI_{ish} = \int_{H_1}^{20\,m} F_{LPI_{ish}}\left(FS_{liq}\right) \cdot \frac{25.56}{z}\,dz \tag{23a}$$

$$F_{LPI_{ish}}\left(FS_{liq}\right) = 1 - FS_{liq}; \quad \text{if } FS_{liq} \leq 1 \text{ and } H_1 \cdot m(FS) \leq 3 \tag{23b}$$

$$= 0; \quad \text{if } FS_{liq} > 1 \text{ or } H_1 \cdot m(FS) > 3 \tag{23c}$$

$$m\left(FS_{liq}\right) = \exp\left\{\frac{5}{25.56 \cdot \left(1 - FS_{liq}\right)}\right\} - 1; \quad \text{if } FS_{liq} \leq 0.95 \tag{23d}$$

$$= 100; \quad \text{if } FS_{liq} > 0.95 \tag{23e}$$

where H_1 is the shallowest depth where $FS_{liq} < 1$. As noted, LPI_{ish} is used to predict surficial liquefaction manifestation severity. The optimal LPI_{ish} thresholds corresponding to the different surficial liquefaction manifestation severities will be dependent on the procedure used to estimate FS_{liq} as well as profile characteristics (Maurer et al. 2015a). However, because of limited liquefaction case history for induced earthquakes in OTK, the thresholds presented by

Maurer et al. (2014) for LPI were adapted for use with LPI_{ish} in this study. Accordingly, the LPI_{ish} thresholds used were:

$LPI_{ish} < 4$:	No Surficial Liquefaction Manifestations;
$4 \leq LPI_{ish} < 8$:	Minor Surficial Liquefaction Manifestations;
$8 \leq LPI_{ish} < 15$:	Moderate Surficial Liquefaction Manifestations;
$LPI_{ish} \geq 15$:	Severe Surficial Liquefaction Manifestations.

Using these thresholds, surficial liquefaction manifestation severity is predicted at each test location using the four liquefaction triggering models. The predicted severities were then compared to the severity of liquefaction manifestations observed at each site following the Pawnee earthquake to evaluate the efficacy of these models.

3.5.3 Liquefaction Hazard Analysis and Model Evaluation Results – FS_{liq} and LPI_{ish}

Reported liquefaction manifestation severity at each sounding location is classified as “no liquefaction,” “minor liquefaction,” “moderate liquefaction,” or “severe liquefaction” based on criteria developed by Green et al. (2014) and shown in Table 3.5. Green et al. (2014) provide example photos of these damage classifications. Documented observations of liquefaction at each sounding location and assigned liquefaction severity classifications are shown in Table 3.6.

Table 3.5. Liquefaction severity classification criteria (Green et al. 2014).

Classification	Criteria
No Liquefaction	No surficial liquefaction manifestation or lateral spread cracking
Minor Liquefaction	Small, isolated liquefaction features; streets had traces of ejecta or wet patches less than a vehicle width; < 5% of ground surface covered by ejecta
Moderate Liquefaction	Groups of liquefaction features; streets had ejecta patches greater than a vehicle width but were still passable; 5-40% of ground surface covered by ejecta
Severe Liquefaction	Large masses of adjoining liquefaction features, streets impassible due to liquefaction, >40% of ground surface covered by ejecta

Table 3.6. Liquefaction severity classifications at CPT sounding locations.

Sounding	Site	Documented Liquefaction Manifestations	Severity Classification (Green et al. 2014)
CPT-01	1	None	No Liquefaction
CPT-02	1	Small cluster of sand boils with small amount of ejecta	Minor
CPT-03	1	Small cluster of sand boils with small amount of ejecta	Minor
CPT-04	2	Cracks approximately 2 to 5 m long with small amount of ejecta	Minor
CPT-05	2	Cracks approximately 2 to 5 m long with small amount of ejecta	Minor
CPT-06	2	None	No Liquefaction
CPT-07	2	None	No Liquefaction
CPT-08	2	None	No Liquefaction
CPT-09	2	None	No Liquefaction
CPT-10	3	Cracks from 0.5 to 5 cm wide and over 4 m long with small amount of ejecta.	Minor
CPT-11	3	Cracks up to 8 cm wide and up to 42 m long. Sand blow with ejecta covering a 146 m^2 area and associated ground settlement.	Severe
CPT-12	3	Cracks from 0.5 to 5 cm wide and over 4 m long with small amount of ejecta.	Minor
CPT-13	3	None	No Liquefaction
CPT-14	3	None	No Liquefaction
CPT-15	3	None	No Liquefaction

As an example of liquefaction hazard analysis results, Figure 3.12 shows profiles of normalized CPT tip resistance (q_{c1Ncs}), I_c, FS_{liq}, and FS_{liq} normalized by FS_{liq} from the Gea17-CEUS model (FS_{Gea17_CEUS}) for CPT-07 at Site 2. Plots for all CPT location are shown in Figure G.1 through Figure G.15 in Appendix G. Figure headings indicate the severity of observed liquefaction manifestations at each location based on the Green et al. (2014) criteria. FS_{Gea17_CEUS} is used for FS_{liq} comparisons since it was developed specifically for liquefaction hazard analysis in the CEUS and is thus considered most suitable for evaluating liquefaction potential for tectonic earthquakes in the region. Comparisons of FS_{liq} provide fairly direct comparisons of r_d/MSF for each model because the remaining inputs to CSR* are the same for each method. Normalized cyclic resistance ratio ($CRR_{M7.5}$) curves for the three models differ slightly, but the observed differences in FS_{liq} are primarily due to differences in r_d and MSF.

The Qea21 model provides two forms of r_d and MSF relationships that can be used based on available information. These are referred to in Quick et al. (2021) as r_d Models 1 and 2 and MSF Models 1 and 2. The preferred implementation is to use r_d Model 1, which is a function of M_w, a_{max}, and V_{s12}, and MSF Model 1, which is a function of M_w, a_{max}, and R_{hyp}. However, r_d Model 2 and/or MSF Model 2 may be used if V_{s12} and/or R_{hyp} are not available. Figure 3.12 includes FS_{liq} profiles for the possible combinations of the Qea21 r_d and MSF relationships. As shown in this figure, MSF Model 1 results in higher computed FS_{liq} than MSF Model 2. This is a result of the short R_{hyp} ($R_{hyp} \leq 11$ km) at Site 2. The choice of r_d model has less of an impact than choice of MSF model, with r_d Model 1 resulting in slightly lower computed FS_{liq} at most of the sites. Quick et al. (2021) regressed r_d and MSF relationships for four different site response analysis result datasets developed using two different shear modulus and damping degradation (MRD) curves and induced ground motion catalogs that included some motions that were scaled to two different GMPEs. Additional detail on these datasets are provided in Quick et al. (2021). Results for the Qea21 model presented herein are for the ZR19_IZ dataset, which was developed using the Ishibashi and Zhang (1993) MRD curves and the ground motion catalog including motions scaled based on the Zalachoris and Rathje (2019) GMPE. However, calculated FS_{liq} and LPI_{ish} at the Pawnee test sites are similar for all four datasets. A comparison of LPI_{ish} results for the four datasets is presented in Appendix H.

As shown in Figure 3.12 for CPT-07 and also observed for the other CPT test locations, $FS_{liq} <$ 1.0 is predicted over much of the depth of the soil profiles using all the liquefaction triggering models. However, for depths greater than approximately 3 m, the Qea21 model tends to result in substantially higher estimates of FS_{liq} than the tectonic models. This is reflective of trends in r_d/MSF for the various models. As noted previously, the Qea21 model results in lower MSF estimates than the BI14 or Gea17 models. All else equal, lower MSF results in a decrease in FS_{liq}. However, r_d estimates for the Qea21 model are also lower than r_d estimates for the other models, which, all else equal, leads to increases in FS_{liq}. For depths greater than 3 m, the effect of the lower r_d for the Qea21 model outweighs the effect of the lower MSF. As a result, FS_{liq} at these depths tends to be higher for the OTK induced-seismicity triggering model. At shallower depths, r_d for the Qea21 model is closer to r_d for the other models but MSF is still lower. As a result, FS_{liq} for the Qea21 model is similar to or, in some cases, lower than FS_{liq} for the other models at these depths.

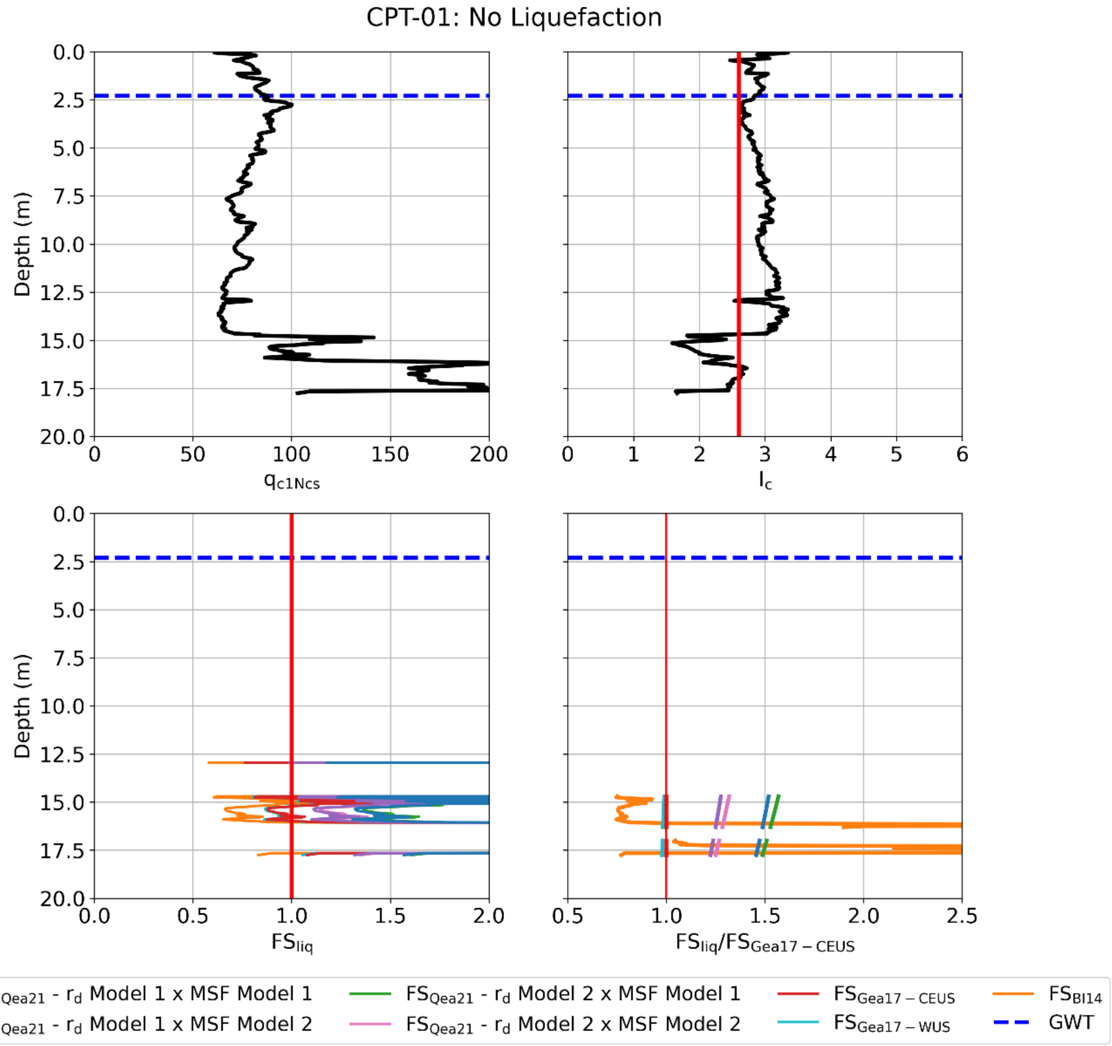

Figure 3.12. Profiles of q_{c1Ncs}, I_c, FS_{liq}, and FS_{liq} normalized by FS_{liq} for the Green et al. (2017) CEUS model ($FS_{Gea17\text{-}CEUS}$) for CPT-07, Site 2 (no post-event liquefaction manifestations observed). FS_{liq} for the Qea21 model (FS_{Qea21}) is shown for the ZR19_IZ database.

As noted previously, FS_{liq} for each of the liquefaction triggering models is used to compute LPI_{ish} profiles at each test location. As an example, Figure 3.13 shows the resulting LPI_{ish} profile for CPT-07, Site 2. The FS_{liq} profile for CPT-07, shown in Figure 3.12, is included for reference.

The Maurer et al. (2014) thresholds for "No," "Minor," "Moderate," and "Severe" liquefaction are also indicated. LPI_{ish} for the Qea21 model is shown based on r_d Model 1 and MSF Model 1. A comparison of LPI_{ish} based on the different Qea21 r_d and MSF relationships is presented in Table H.2 in Appendix H. Profiles for the other CPT soundings are shown in Figure G.16 through Figure G.30 of Appendix G. Figure titles indicate the observed severity of liquefaction at each sounding location. As shown in this figure, for CPT-07, Site 2, $FS_{liq} < 1.0$ at most depths for all four liquefaction triggering models. However, the predicted FS_{liq} for the Qea21 model is consistently higher than for the tectonic models. As a result, the computed LPI_{ish}, and thus the predicted liquefaction surficial manifestation severity, tends to be lowest for the Qea21 model. This trend of higher FS_{liq} and lower LPI_{ish} for the Qea21 model is consistent across most CPT soundings. In contrast, FS_{liq} tended to be lowest for the BI14 liquefaction triggering model. Consequently, LPI_{ish} and predicted liquefaction severity tended to be highest for the BI14 model. LPI_{ish} for the Gea17 models tended to lie between LPI_{ish} for the BI14 and Qea21 models, with the Gea17-WUS model tending to predict slightly lower LPI_{ish} values than Gea17-CEUS model.

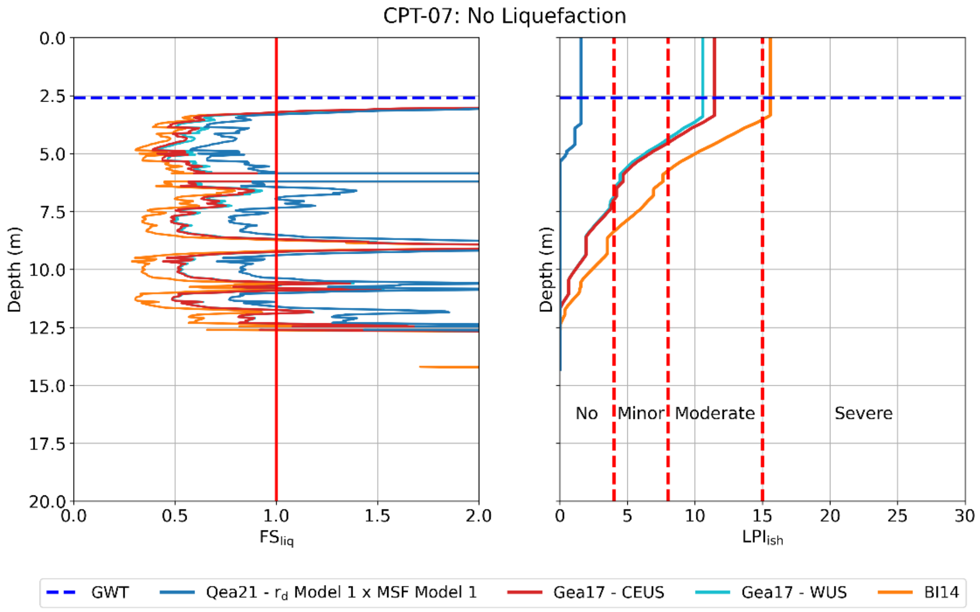

Figure 3.13. FS_{liq} and LPI_{ish} profiles for CPT-07, Site 2. Qea21 results are shown for r_d Model 1, MSF Model 1, and the ZR19_IZ dataset. LPI_{ish} liquefaction surficial manifestation severity thresholds are also indicated.

Table 3.7 presents documented liquefaction severity, computed LPI$_{ish}$ values, predicted surficial liquefaction manifestation severity category at each CPT sounding location based on the Qea21, Gea17, and BI14 triggering models. As noted previously, the Qea21 model tends to result in lower LPI$_{ish}$ than the Gea17 and BI14 models. Based on initial comparisons, the lower LPI$_{ish}$ values for the Qea21 model tend to more accurately predict the severity of liquefaction observed following the Pawnee event. While this comparison provides a quick assessment of model efficacy, a more detailed assessment of model efficacy is performed based on methods used by Maurer et al. (2014) for evaluating LPI model accuracy.

Table 3.7. Observed liquefaction severity, LPI$_{ish}$, and predicted liquefaction surficial manifestation category for the Pawnee test sites. Results are shown for the Quick et al. (2021) OTK induced seismicity-specific [Qea21], Green et al. (2017) [Gea17] CEUS and WUS, and Boulanger and Idriss (2014) [BI14] liquefaction triggering models. Qea21 model results are shown for r_d Model 1 and MSF Model 1. Shaded cells correspond to correct predictions of liquefaction severity.

Sounding	Site	Observed Liquefaction Severity	Qea21		Gea17-CEUS		Gea17-WUS		BI14	
			LPI$_{ish}$	Predicted Severity	LPI$_{ish}$	Predicted Severity	LPI$_{ish}$	Predicted Severity	LPI$_{ish}$	Predicted Severity
CPT-01	1	None	0.0	None	0.0	None	0.0	None	0.0	None
CPT-02	1	Minor	0.0	None	0.1	None	0.1	None	0.4	None
CPT-03	1	Minor	0.0	None	0.0	None	0.0	None	0.0	None
CPT-04	2	Minor	0.2	None	7.4	Minor	6.7	Minor	8.8	Moderate
CPT-05	2	Minor	1.0	None	8.7	Moderate	7.5	Minor	11.2	Moderate
CPT-06	2	None	2.4	None	9.8	Moderate	9.1	Moderate	13.0	Moderate
CPT-07	2	None	1.6	None	11.5	Moderate	10.6	Moderate	15.6	Severe
CPT-08	2	None	2.7	None	10.0	Moderate	8.6	Moderate	12.0	Moderate
CPT-09	2	None	0.1	None	9.5	Moderate	8.2	Moderate	10.7	Moderate
CPT-10	3	Minor	1.0	None	9.2	Moderate	7.7	Minor	13.0	Moderate
CPT-11	3	Severe	20.5	Severe	27.1	Severe	25.9	Severe	30.7	Severe
CPT-12	3	Minor	3.1	None	11.5	Moderate	10.4	Moderate	14.8	Moderate
CPT-13	3	None	7.8	Minor	15.7	Severe	14.0	Moderate	17.3	Severe
CPT-14	3	None	0.0	None	2.1	None	1.8	None	3.5	None
CPT-15	3	None	0.0	None	0.6	None	0.6	None	1.8	None

Following this approach, model prediction error (E) for each sounding is computed based on the expected LPI_{ish} ranges corresponding to the observed liquefaction severity at each test location. Model error is computed as $E = LPI_{ish} -$ (min *or* max LPI_{ish}) of the relevant range. For example, if LPI_{ish} at a site is computed to be 12 for a site with minor liquefaction, $E = 12 - 8 = 4$ (where 8 is the maximum LPI_{ish} for the minor liquefaction range). In contrast, if LPI_{ish} is computed to be 5 for a site with moderate liquefaction, $E = 5 - 8 = -3$ (where 8 is the minimum LPI_{ish} for the moderate liquefaction range). Accordingly, positive values of E indicate over-prediction of liquefaction severity while negative values of E indicate under-prediction of liquefaction severity. Based on magnitude of the error, errors were assigned one of nine classifications as shown in Table 3.8 (Maurer et al. 2014).

Table 3.8. LPI_{ish} prediction error classifications (after Maurer et al. 2014).

Error (E) classification	**E (LPI_{ish} units)**
Excessive under-prediction	$E < -15$
Severe to excessive under-prediction	$-15 \leq E < -10$
Moderate to severe under-prediction	$-10 \leq E < -5$
Slight to moderate under-prediction	$-5 \leq E < -1$
Accurate prediction	$-1 \leq E \leq 1$
Slight to moderate over-prediction	$1 < E \leq 5$
Moderate to severe over-prediction	$5 < E \leq 10$
Severe to excessive over-prediction	$10 < E \leq 15$
Excessive over-prediction	$E > 15$

The computed prediction errors for each of the four liquefaction triggering models are shown in Figure 3.14 for each CPT sounding location. Results for the Qea21 model are shown for r_d Model 1, MSF Model 1, and the ZR19_IZ dataset. As shown in this figure, the Qea21 model resulted in accurate predictions ($-1 \leq E \leq 1$) at 9 of the 15 sounding locations, while it resulted in slight under-prediction at 5 locations and slight over-prediction at one location. The slight under-predictions occurred at sites where "minor" liquefaction occurred (e.g., CPT-04, CPT-05, and CPT-10), but estimated LPI_{ish} was between 0 and 4 (i.e., "No Surficial Liquefaction Manifestations" predicted). Although these predictions fall below the Maurer et al. (2014)

"Minor" severity liquefaction range, they do fall into the "None to Minor Liquefaction" severity category recommended by Iwasaki et al. (1978) and commonly used in practice. In contrast, the Gea17 and BI14 triggering models tended to over-predict the severity of liquefaction, particularly at sites where no liquefaction was observed. These models slightly to excessively over-predict the severity at 7 locations (*E* as high as 13) and slightly under-predict severity at 2 locations. However, they accurately predict the severity at 6 locations including the minor liquefaction at CPT-04, Site 2, which is slightly under-predicted by the OTK model.

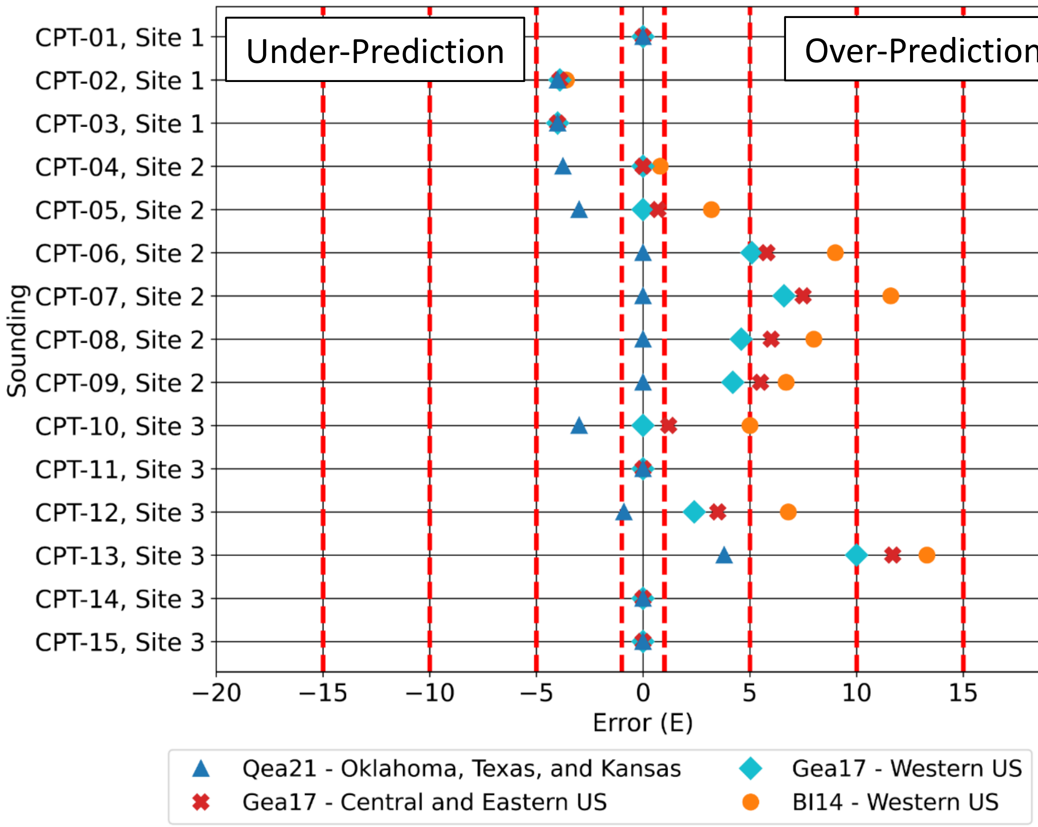

Figure 3.14. LPI$_{ish}$ prediction error (*E*) for the Pawnee test sites. Results are shown for the Quick et al. (2021) [Qea21] OTK induced seismicity-specific model using r$_d$ Model 1, MSF Model 1, and the ZR19_IZ dataset; the Green et al. (2017) CEUS [Gea17 – CEUS] and WUS [Gea17 – WUS] models; and the Boulanger and Idriss (2014) [BI14] model. Error classification thresholds from Table 3.8 are also indicated.

There were two locations at Site 1 (CPT-02 and CPT-03) where minor liquefaction features were reported but all models resulted in $LPI_{ish} \approx 0$. Both the CPT-02 and CPT-03 profiles include a thin, liquefiable sand layer at a depth of approximately 7.5 m. While this layer was thin enough at CPT-02 and CPT-03 that surficial manifestations were not predicted at those locations, the thickness of this layer may vary laterally and may be thicker in nearby areas. This could account for the isolated clusters of sand boils observed in the general area while the models predict no liquefaction would occur at the sounding locations. Observed sand boil locations were estimated using GPS-tagged photos, which due to the site being an open field with flat topography provide only approximate location information. Additionally, the sounding locations had to be adjusted slightly due to ponding at the site during CPT testing. For these reasons, it is possible that the CPT sounding locations were not located at the exact locations where liquefaction manifested. This could also explain why LPI_{ish} were lower than expected at these locations. In general, the predicted LPI_{ish} for the induced seismicity and tectonic seismicity models were very similar, being at or near zero for both CPT-02 and CPT-03. All models correctly predicted no surficial liquefaction manifestations would occur at CPT-01.

At Site 2, minor liquefaction was documented at CPT-04 and CPT-05 consisting of cracks 2 to 5 m long with small amounts of sand ejecta. The observed liquefaction severity at these locations was slightly under-predicted by the Qea21 model (LPI_{ish} = 0.3 and 1.0). The Gea17-WUS model predictions (LPI_{ish} = 6.7 and 7.5) fell within the range of minor liquefaction while the Gea17-CEUS model (LPI_{ish} = 7.4 and 8.7) and BI14 model (LPI_{ish} = 8.8 and 11.2) over-predicted liquefaction severity at these locations, particularly CPT-05. As with Site 1, locations of surficial liquefaction manifestations were roughly estimated using GPS-tagged photos. As a result, locations may not coincide exactly with observed liquefaction locations. This may have led to the under-prediction of liquefaction severity by the Qea21 model.

No liquefaction was documented at CPT-06 through CPT-09 at Site 2. This is consistent with LPI_{ish} predictions for the Qea21 triggering model (LPI_{ish} = 0.1 to 2.7), which fell within the no liquefaction range. However, the other models predicted moderate to severe liquefaction at these locations (LPI_{ish} = 8.2 and 15.6). This is classified as a moderate to excessive over-prediction. The site owner indicated that, as far as he could remember, the cracking and ejecta at Site 2 were limited to the area around CPT-04 and CPT-05. However, given that the property is a large, plowed field, it is possible that liquefaction did occur at the other sounding locations but was not observed or photographed. However, it is unlikely that if moderate to severe liquefaction occurred at these locations, as predicted by these models, that it would have gone unnoticed or undocumented. As a result, the Qea21 model appears to more accurately reflect liquefaction manifestation severity at these locations.

At Site 3, liquefaction manifestations were documented at CPT-10, CPT-11, and CPT-12. Detailed mapping of fractures and ejecta was performed across most of the site by Kolawole et al. (2017). As a result, the areal extent of liquefaction was better known at Site 3 than at Sites 1 and 2. Manifestations at CPT-10 and CPT-12 consisted of cracks 0.5 to 5 cm wide with trace amounts of ejecta, which were classified as minor severity liquefaction due to the limited extent of ejecta. The Qea21 model (LPI_{ish} = 1.0) slightly under-predicted liquefaction severity at CPT-10 while the Gea17-WUS model (LPI_{ish} = 7.7) fell within the minor liquefaction range. The Gea17-CEUS and BI14 models (LPI_{ish} = 9.2 and 13.0) slightly over-predicted liquefaction at this location. The Qea21 model (LPI_{ish} = 3.1, $E \leq 1$) accurately predicted minor liquefaction severity at CPT-11, while the other models (LPI_{ish} = 10.4 and 14.8) predicted more severe liquefaction would occur.

More severe manifestations were observed at Site 3 near CPT-11 where the post-earthquake survey found cracks up to 8 cm wide and sand blows with ejecta covering an approximately 145 m^2 area. As a result, CPT-11 was classified as severe liquefaction. Both the Qea21 model (LPI_{ish} = 20.5) and the tectonic models (LPI_{ish} = 25.9 to 30.7) accurately predicted severe liquefaction manifestations at this location.

No surficial liquefaction manifestations were observed at CPT-13, CPT-14, or CPT-15. The Qea21 model resulted in LPI_{ish} = 0 at both CPT-14 and CPT-15, which accurately predicted the lack of observed liquefaction. The other models resulted in LPI_{ish} values ranging from 1.8 to 3.5 for CPT-14 and 0.6 to 1.8 for CPT-15. While $LPI_{ish} > 0$ for these models, estimates still lie within the “no liquefaction range.” Calculated LPI_{ish} values for all of the models at CPT-13 were not in accord with field observations. Although no liquefaction was documented at CPT-13, the

Qea21 model (LPI_{ish} = 7.8) fell within the minor liquefaction range, the Gea17-WUS model (LPI_{ish} = 14.0) fell within the moderate liquefaction range, and the Gea17-CEUS and BI14 models (LPI_{ish} = 15.7 and 17.3) fell within the severe liquefaction range. Given the low FS_{liq} and high LPI_{ish} computed at this location, it is likely that soils at CPT-13 did liquefy during the Pawnee earthquake. The location of CPT-13 was adjusted due to ponding at the site during CPT testing and was moved just outside the Kolawole et al. (2017) detailed survey area. As a result, liquefaction manifestations may have occurred at CPT-13 during the Pawnee earthquake but may not have been observed during the Kolawole et al. (2017) survey. However, similar to the apparent false-positives at Site 2, it seems more likely that the minor liquefaction predicted by the Qea21 model would not have been observed than that moderate to severe manifestations predicted by the tectonic models not being observed.

As noted previously, a sensitivity analysis was performed to observe the effect of groundwater depth assumptions on liquefaction analysis results. LPI_{ish} was computed using water table depths both 0.5 m higher and 0.5 m lower than best estimates. The resulting LPI_{ish} prediction error plots are shown in Figure G.31 and Figure G.32 in Appendix G. As expected, changes in water table depth affected the predicted severity for each of the models. In general, shallower water table depth resulted in higher LPI_{ish}, resulting in more accurate predictions by the Qea21 at one location but more severe over-prediction by the tectonic models with inaccurate predictions at more locations. The deeper water table reduced LPI_{ish}, resulted in slight under-predictions by Qea21 model at one additional site and reduced over-prediction by the tectonic models. Even for the deeper water table, the Qea21 model provided accurate predictions of severity for as many or more locations than the tectonic models, which still tended to over-predict severity for sites where no liquefaction was observed. These trends are similar to those observed for the best estimate water table depths.

Comparisons of observed and predicted surficial liquefaction manifestation severity at Sites 1, 2, and 3 indicate that the Qea21 liquefaction triggering model for induced events in OTK did a better job predicting liquefaction manifestation severity for the Pawnee earthquake than the other models evaluated. Although the induced and tectonic models yield similar LPI_{ish} values at some locations (e.g., Site 1, CPT-11), the Gea17 and BI14 models tend to over-predict the liquefaction potential and manifestation severity relative to observed liquefaction severity. Similarly, the Baise and Rashidian (2018) geospatial model developed using tectonic events overpredicted liquefaction spatial extent at both Sites 1 and 2, although the model did provide more reasonable estimates of liquefaction extent at Site 3. The OTK induced seismicity-specific triggering model results in slight under-predictions of liquefaction at some locations but accurately predicts liquefaction severity at most locations. Overall, the model validation results suggest that the Qea21 induced seismicity-specific liquefaction triggering model provides a more accurate assessment of the liquefaction hazard due to induced earthquakes in OTK than existing models developed for tectonic earthquakes.

3.6 Summary and Conclusions

Although several models are commonly used in practice for assessing liquefaction triggering due to tectonic earthquakes, these models are semi-empirical, with the empirical aspects being derived from data primarily taken from moderate-sized tectonic earthquakes in active shallow-crustal tectonic regimes. As a result, the suitability of these models for evaluating liquefaction triggering for induced earthquakes in Oklahoma, Texas, and Kansas (OTK) is uncertain, due to differences in ground motion characteristics and regional geologies. To address this, Quick et al. (2021) developed a new liquefaction triggering model (referred to herein as the Qea21 model) for assessing the liquefaction hazard due to earthquakes resulting from deep wastewater injection in OTK.

To assist with model development and validation, detailed geotechnical site characterizations were performed at several sites that experienced significant shaking during the 3 September 2016, M_w5.8 Pawnee, OK, earthquake. Cone Penetration Tests (CPT), Multichannel Analysis of Surface Waves (MASW) tests, and Horizontal-to-Vertical Spectral Ratio (HVSR) tests were performed at each site. Liquefaction potential was computed at each test location using the Qea21 OTK model as well as several existing models for tectonic earthquakes. The severity of surficial liquefaction manifestations at each test location was predicted using the Ishihara-inspired Liquefaction Potential Index (LPI_{ish}) (Maurer et al. 2015b). Computed LPI_{ish} values and the corresponding predicted liquefaction surficial manifestation severity categories were compared to the documented observations of liquefaction manifestations made following the

Pawnee event to evaluate the efficacy of the selected models. Estimates of P_{liq} and spatial extent of liquefaction were also made using the geospatial liquefaction model presented in Baise and Rashidian (2018).

At most locations evaluated, predictions from the new liquefaction triggering model were more consistent with field observations than predictions from existing models. The models developed for tectonic earthquakes tended to over-predict the severity of liquefaction for the Pawnee earthquake. While the new model slightly under-predicts liquefaction severity at some Pawnee test sites, it generally provides accurate predictions of liquefaction severity at the Pawnee test locations. There were several sites where either liquefaction is predicted by all models but was not observed or where liquefaction is not predicted by any of the models but was observed following the Pawnee event. This may be due to under-reporting of liquefaction extent, difficulties in matching post-event damage surveys with field test locations, or limitations of the simplified procedure itself. In general, this study showed that the new induced seismicity-specific triggering model provides a more accurate assessment of the liquefaction hazard for the Pawnee event.

Accounting for the observed differences in liquefaction potential for induced and tectonic earthquakes is important when considering seismic design and policy in areas subject to induced seismicity. The findings of this study show that existing methods used to assess the liquefaction potential of tectonic earthquakes tend to over-predict the liquefaction potential for a given induced earthquake. As a result, use of traditional liquefaction triggering models in design may lead to over-conservatism in design and increased costs.

References

Baise, L. G., and Rashidian, V. (2018). “A Geospatial Approach to Liquefaction Assessment for Rapid Response and Loss Estimation.” *Geotechnical Earthquake Engineering and Soil Dynamics V (GEESD V): Seismic Hazard Analysis, Earthquake Ground Motions, and Regional-Scale Assessment*, GSP 291, American Society of Civil Engineers, Reston, VA, 1–10.

Bard, P. Y., and SESAME-Team. (2004). *Guidelines for the implementation of the H/V spectral* *ratio technique on ambient vibrations-measurements, processing and interpretations*. SESAME European Research Project No. EVG1-CT-2000-00026, May. Brussels: European Commision.

Boore, D. M., and Kishida, T. (2017). "Relations between Some Horizontal-Component Ground-Motion Intensity Measures Used in Practice." *Bulletin of the Seismological Society of America*, 107(1), 334–343.

Boulanger, R. W., and Idriss, I. M. (2014). *CPT and SPT based liquefaction triggering procedures*. Report No. UCD/CGM-14/01, University of California at Davis, Davis, CA.

Choi, J. H., Ko, K., Gihm, Y. S., Cho, C. S., Lee, H., Song, S. G., Bang, E. S., Lee, H. J., Bae, H. K., Kim, S. W., Choi, S. J., Lee, S. S., and Lee, S. R. (2019). "Surface deformations and rupture processes associated with the 2017 Mw 5.4 Pohang, Korea, earthquake." *Bulletin of the Seismological Society of America*, 109(2), 756–769.

Clayton, P., Zalachoris, G., Rathje, E., Bheemasetti, T., Caballero, S., Yu, X., and Bennett, S. (2016). *The geotechnical aspects of the September 3, 2016 M5.8 Pawnee, Oklahoma earthquake*. Report GEER-051, Geotechnical Extreme Events Reconnaissance Association.

Cox, B. R., and Teague, D. P. (2016). "Layering ratios: a systematic approach to the inversion of surface wave data in the absence of a priori information." *Geophysical Journal International*, 207(1), 422–438.

Darendeli, M. B., and Stokoe, K. H. (2001). *Development of a new family of normalized modulus reduction and material damping curves*. Geotechnical Engineering Report GD01-1, Univ. of Texas at Austin, Austin, TX.

Green, R. A., Cubrinovski, M., Cox, B., Wood, C., Wotherspoon, L., Bradley, B., and Maurer, B. (2014). "Select Liquefaction Case Histories from the 2010-2011 Canterbury Earthquake Sequence." *Earthquake Spectra*, 30(1), 131–153.

Green, R. A., Maurer, B. W., and Haskell, A. (2017). *Development of Probabilistic Magnitude-Bound Curves for the New Madrid Seismic Zone (NMSZ) for Paleoliquefaction Studies*. U.S. Geological Society Technical Report G14AP00046, U.S. Geological Survey, Reston, VA.

Hallal, M. M., and Cox, B. R. (2019). "Theoretical Evaluation of the Interval Method Commonly Used for Downhole Seismic Testing." *Proceedings of Geo-Congress 2019*, American Society of Civil Engineers, Reston, VA, 376–386.

Ishibashi, I., and Zhang, X. (1993). “Unified dynamic shear moduli and damping ratios of sand and clay.” *Soils and Foundations*, 33(1), 182–191.

Ishihara, K. (1985). “Stability of natural deposits during earthquakes.” *Proceedings of 11th Intern. Conf. on Soil Mechanics and Foundation EngineeringSoil Mechanics and Foundation Engineering*, International Society of Soil Mechanics and Geotechnical Engineering, London, UK, 321–376.

Iwasaki, T., Tatsuoka, F., Tokida, K., and Yasuda, S. (1978). “A practical method for assessing soil liquefaction potential based on case studies at various sites in Japan.” *Proceedings of 2nd International Conference on Microzonation*, National Science Foundation, Washington, DC.

Kolawole, F., Atekwana, E. A., and Ismail, A. (2017). “Near-surface electrical resistivity investigation of coseismic liquefaction-induced ground deformation associated with the 2016 Mw 5.8 Pawnee, Oklahoma, earthquake.” *Seismological Research Letters*, 88(4), 1017–1023.

Konno, K., and Ohmachi, T. (1998). “Ground-motion characteristics estimated from spectral ratio between horizontal and vertical components of microtremor.” *Bulletin of the Seismological Society of America*, 88(1), 228–241.

Langenbruch, C., and Zoback, M. D. (2016). “How will induced seismicity in Oklahoma respond to decreased saltwater injection rates?” *Science Advances*, 2(e1601542), 1–9.

Maurer, B. W., Green, R. A., van Ballegooy, S., and Wotherspoon, L. (2019). “Development of region-specific soil behavior type index correlations for evaluating liquefaction hazard in Christchurch, New Zealand.” *Soil Dynamics and Earthquake Engineering*, Elsevier Ltd, 117(September 2017), 96–105.

Maurer, B. W., Green, R. A., Cubrinovski, M., and Bradley, B. A. (2014). “Evaluation of the Liquefaction Potential Index for Assessing Liquefaction Hazard in Christchurch , New Zealand.” *Journal of Geotechnical and Geoenvironmental Engineering*, 140(7), 1–11.

Maurer, B. W., Green, R. A., Cubrinovski, M., and Bradley, B. A. (2015a). “Fines-content effects on liquefaction hazard evaluation for infrastructure in Christchurch, New Zealand.” *Soil Dynamics and Earthquake Engineering*, 76, 58–68.

Maurer, B. W., Green, R. A., and Taylor, O. D. S. (2015b). “Moving towards an improved index for assessing liquefaction hazard: Lessons from historical data.” *Soils and Foundations*, 55(4), 778–787.

NOAA. (2019). “Normals Annual/Seasonal Station Details: PAWNEE, OK US, GHCND:USC00346940.” <https://www.ncdc.noaa.gov/cdo-web/datasets/normal_ann/stations/GHCND:USC00346940/detail> (Sep. 10, 2019).

Novakovic, M., Atkinson, G. M., and Assatourians, K. (2018). “Empirically Calibrated Ground-Motion Prediction Equation for Oklahoma.” *Bulletin of the Seismological Society of America*, 108(5A), 2444–2461.

Rahpeyma, S., Halldorsson, B., Olivera, C., Green, R. A., and Jónsson, S. (2016). “Detailed site effect estimation in the presence of strong velocity reversals within a small-aperture strong-motion array in Iceland.” *Soil Dynamics and Earthquake Engineering*, 89, 136–151.

Robertson, P. K. (2010). “Soil behaviour type from the CPT: an update.” *Proceedings of 2nd International Symposium on Cone Penetration Testing.*, CPT’10, Huntington Beach, CA, USA.

Robertson, P. K., and Cabal, K. L. (2015). *Guide to Cone Penetration Testing for Geotechnical Engineering*. Gregg Drilling & Testing, Inc., Signal Hill, CA.

Robertson, P. K., and Wride, C. (1998). “Evaluating cyclic liquefaction potential using the cone penetration test.” *Canadian Geotechnical Journal*, 35(3), 442–459.

Seed, H. B., and Idriss, I. M. (1971). “Simplified procedure for evaluating soil liquefaction potential.” *Journal of Geotechnical Engineering*, 97(9), 1249–1273.

U.S. Geologic Survey. (2016a). “Shake Map for M5.8 - 14km NW of Pawnee, Oklahoma.” <https://earthquake.usgs.gov/earthquakes/eventpage/us10006jxs/executive> (Jun. 19, 2019).

U.S. Geologic Survey. (2016b). “National Water Information System data available on the World Wide Web (USGS Water Data for the Nation): USGS 07153000 Black Bear Creek at Pawnee, OK.” <https://waterdata.usgs.gov/nwis/uv?site_no=07153000> (Jul. 4, 2019).

U.S. Geologic Survey. (2016c). “National Water Information System data available on the World Wide Web (USGS Water Data for the Nation): USGS 07152500 Arkansas River at Ralston, OK.” <https://waterdata.usgs.gov/ok/nwis/uv/?site_no=07152500&PARAmeter_cd=00065,00060> (Jul. 4, 2019).

U.S. Geologic Survey. (2019). “Oklahoma Alluivum.” <https://mrdata.usgs.gov/geology/state/sgmc-unit.php?unit=OKQal%3B0> (Jul. 2, 2019).

U.S. Geologic Survey. (2020). “Oklahoma Has Had a Surge of Earthquakes since 2009. Are

They Due to fracking?” <https://www.usgs.gov/faqs/oklahoma-has-had-a-surge-earthquakes-2009-are-they-due-fracking?qt-news_science_products=0#qt-news_science_products>.

Ulmer, K. J., Green, R. A., and Rodriguez-Marek, A. (2020). “A Consistent Correlation between V s , SPT, and CPT Metrics for Use in Liquefaction Evaluation Procedures.” *Proceedings of Geo-Congress 2020*, American Society of Civil Engineers, Reston, VA, 132–140.

Wathelet, M., Chatelain, J. L., Cornou, C., Giulio, G. Di, Guillier, B., Ohrnberger, M., and Savvaidis, A. (2020). “Geopsy: A user-friendly open-source tool set for ambient vibration processing.” *Seismological Research Letters*, 91(3), 1878–1889.

Whitman, R. V. (1971). “Resistance of Soil to Liquefaction and Settlement.” *Soils and Foundations*, 11(4), 59–68.

Yang, H., Zhou, P., Fang, N., Zhu, G., Xu, W., Su, J., Meng, F., and Chu, R. (2020). “A Shallow Shock: The 25 February 2019 ML 4.9 Earthquake in the Weiyuan Shale Gas Field in Sichuan, China.” *Seismological Research Letters*, 91(6), 3182–3194.

Yust, M. B. S., Cox, B. R., and Cheng, T. (2018). “Epistemic Uncertainty in Vs Profiles and Vs30 Values Derived from Joint Consideration of Surface Wave and H/V Data at the FW07 TexNet Station.” *Geotechnical Earthquake Engineering and Soil Dynamics V (GEESD V): Seismic Hazard Analysis, Earthquake Ground Motions, and Regional-Scale Assessment*, GSP 291, American Society of Civil Engineers, Reston, VA, 387–399.

Zalachoris, G., and Rathje, E. M. (2019). “Ground Motion Model for Small-to-Moderate Earthquakes in Texas, Oklahoma, and Kansas.” *Earthquake Spectra*, 35(1), 1–20.

4 Manuscript #3: Minimum Magnitude for Liquefaction Triggering during Induced Earthquakes in the Central US

The following manuscript will be submitted to ASCE's Journal of Geotechnical and Geoenvironmental Engineering.

Tyler Quick made the following contributions:

- Developed source models
- Developed the liquefaction triggering model for induced earthquakes
- Performed PSHA and PLHA
- Prepared figures and tables
- Wrote first draft of the manuscript and incorporated subsequent edits

Drs. Russell Green and Julian Bommer made the following contributions:

- Developed the site profiles used in the paper
- Conducted a thorough review of liquefaction case histories for small-magnitude events

Dr. Ellen Rathje made the following contribution:

- Developed the ground motion prediction equation used for the induced seismic source

Dr. Julian Bommer made the following contributions:

- Provided valuable feedback on the study methodology

Drs. Russell Green, Ellen Rathje, and Jim Mitchell made the following contributions:

- Contributed to the development of the liquefaction triggering model for induced earthquakes
- Provided valuable feedback throughout the study

Manuscript #3: Minimum Magnitude for Liquefaction Triggering during Induced Earthquakes in the Central US

Tyler J. Quick[1], Russell A. Green[2], Ellen M. Rathje[3], and James K. Mitchell[4]

[1]Graduate Student, Department of Civil and Environmental Engineering, Virginia Tech, Blacksburg, VA; tylerjaq@vt.edu

[2]Professor, Department of Civil and Environmental Engineering, Virginia Tech, Blacksburg, VA; rugreen@vt.edu

[3]Janet S. Cockrell Centennial Chair, Department of Civil, Architectural, and Environmental Engineering, University of Texas at Austin, Austin, TX; e.rathje@mail.utexas.edu

[4]University Distinguished Professor, Emeritus, Department of Civil and Environmental Engineering, Virginia Tech, Blacksburg, VA; jkm@vt.edu

Keywords: liquefaction, liquefaction triggering, induced seismicity, probabilistic seismic hazard analysis, probabilistic liquefaction hazard analysis

Abstract

The potential for liquefaction due to induced earthquakes has led to increased scrutiny of the liquefaction hazard associated with small magnitude events. As a result, it is important to determine the minimum magnitude (M_{min}) for induced earthquakes capable of triggering liquefaction. To address this issue, a probabilistic seismic hazard analysis and probabilistic liquefaction hazard analysis were performed using an idealized induced seismic source and two idealized soil profiles. This process was repeated while varying M_{min} to determine the largest M_{min} that can be used while fully capturing the liquefaction hazard from induced earthquakes. For comparison, M_{min} was also evaluated using idealized tectonic sources for the central and eastern United States and western United States. For sites capable of supporting building structures, it was found that M_{min} = 5.0 was sufficient to fully capture the liquefaction hazard of

both induced and tectonic events. For extremely liquefaction-susceptible soil profiles that may be of relevance to other types of infrastructure (e.g., pipelines and levees), $M_{min} = 4.5$ is required to fully capture liquefaction hazard from tectonic sources. These findings are in accord with previous recommendations regarding M_{min} for probabilistic liquefaction hazard analyses for tectonic events. Based on the findings of this study, there is some justification for the use of M_{min} as low as 4.0 when evaluating liquefaction hazard from induced earthquakes at extremely susceptible sites in Oklahoma, Texas, and Kansas. It is worthwhile to note though that there have been numerous induced events with $M_w < 4.5$ in this region with no documented cases of liquefaction. This could either be because liquefaction has not occurred during these events or because any liquefaction that did occur during these events was not observed. However, because no liquefaction has been documented during events with $M_w < 4.5$, and because the use of $M_{min} < 4.5$ results in only minor changes in the estimated liquefaction hazard, the use of $M_{min} = 4.5$ for extremely susceptible sites may still be suitable for induced events in Oklahoma, Texas, and Kansas.

4.1 Introduction

While liquefaction triggering during earthquakes generally does not result in fatalities, liquefaction poses a significant threat to the built environment and can have severe economic consequences (e.g., Bird and Bommer 2004; Choi et al. 2019). Liquefaction during small earthquakes (i.e., moment magnitude, M_w, less than ~6) has become a greater concern in the last decade due to the dramatic increase in induced earthquakes in the US and abroad. Induced earthquakes are earthquakes resulting from human activities such as wastewater injection, fracking, and carbon capture and storage (Ellsworth 2013; Foulger et al. 2018). These activities have resulted in significantly elevated seismicity in areas of large-scale oil and gas production such as Oklahoma where the current rate of $M_w \geq 3$ earthquakes is approximately 60 times the natural tectonic rate (Langenbruch and Zoback 2016; U.S. Geologic Survey 2020). This dramatic increase in seismicity is of particular concern because induced earthquakes often occur in areas of low historic seismicity where building codes and construction methods have not traditionally accounted for higher levels of seismic hazard. As a result, attention is now being given to smaller earthquakes (M_w ~3 to 5.5) than would be normally considered in conventional liquefaction hazard analysis. Induced seismicity does not generally result in large earthquakes but has led to over nine $M \geq 4.8$ events in Oklahoma, including the $M_w5.8$ 2016 Pawnee, OK earthquake. The Pawnee earthquake was the largest recorded earthquake in Oklahoma history and is one of the largest recorded earthquakes in the central and eastern US (CEUS) in the last 70 years (Tiwari and Rathje 2018). Additionally, both the Pawnee earthquake and the 2017, $M_w5.5$ Pohang, South Korea, induced earthquake, have triggered liquefaction. These events have raised concerns regarding liquefaction that might occur during future induced events. Because the seismic hazard in these regions is dominated by small-magnitude events, establishing a minimum magnitude (M_{min}) threshold below which liquefaction is not expected to be triggered is an important part of assessing the regional liquefaction hazard. The establishment of an M_{min} threshold for liquefaction is also required for performing probabilistic liquefaction hazard analyses (PLHA) for both induced earthquakes and tectonic earthquakes (Green and Bommer 2019).

An M_{min} of 5.0 has traditionally been used in PLHA for tectonic earthquakes (e.g., Atkinson et al. 1984). Green and Bommer (2019) completed a thorough review of liquefaction case histories for low-magnitude earthquakes to determine the minimum magnitude earthquake that has resulted in observed manifestations of liquefaction. They found that case history databases used in developing most liquefaction-related hazard models included one case of liquefaction during an event with $M_w = 4.83$ and all remaining events had $M_w \geq 5$. Green and Bommer (2019) reviewed additional liquefaction case histories for small magnitude events and found evidence of surface manifestations of liquefaction for events with magnitudes as small as ~4.5. However, they note that these cases correspond to extremely loose, liquefaction-susceptible sites that would be unsuitable for even light building structures. Based on these findings, Green and Bommer (2019) conclude that $M_{min} = 5$ is an appropriate lower bound for liquefaction hazard assessment for building structure sites, but $M_{min} = 4.5$ may be necessary for extremely susceptible sites where other infrastructure (e.g., pipelines, levees) may be located. This is because buried pipelines can be installed in very poor soils, and levees can be constructed on weak soils if the slope angles are sufficient to spread the load over a large area. As a result, liquefaction hazard for these types of infrastructure may need to be assessed at sites that would be unsuitable for typical construction.

Green and Bommer (2019) also discuss the 1865 magnitude ~2.5-3.5 Barrow-In-Furness, United Kingdom earthquake as the sole case history where liquefaction was reported for an event with $M_w < 4.5$ (Musson 1998). However, they note that there are serious doubts regarding the source parameters for this event as well as whether liquefaction actually occurred. Descriptions of potential liquefaction observed during this event do not resemble classical liquefaction. Further, Green and Bommer (2019) point out that it is extremely unlikely that liquefaction occurred during such a small-magnitude event when liquefaction has not been observed during any similarly sized events in the ~150 years since. For these reasons, they conclude that this case history should not be considered when assessing the required M_{min} for liquefaction triggering. Goda et al. (2011) also investigated the effect of variations in M_{min} on liquefaction hazard at several sites in Canada. They found that, for sites where smaller magnitude events contributed more to overall seismic hazard, the use of $M_{min} = 4.5$, as opposed to $M_{min} = 5$, led to non-negligible increases in liquefaction hazard. Green and Bommer (2019) state the difference between $M_{min} = 4.5$ found in the Goda et al. (2011) study and $M_{min} = 5.0$ found in their study is likely related to the r_d relationship used in the Goda et al. (2011) as well as general shortcomings of the shear wave velocity-based liquefaction evaluation procedure used in the Goda et al. (2011) study. Also, Goda et al. (2011) focused on tectonic events, while Green and Bommer (2019) considered liquefaction hazard in the Groningen region of the Netherlands due to induced seismicity in addition to tectonic events.

One major finding in Green et al. (2019, 2020) is the regionality of the liquefaction triggering models due to characteristics of the ground motions and the soil profiles. Because of differences between the ground motion characteristics of tectonic and induced earthquakes (e.g., Hough 2014; Bommer et al. 2016; Novakovic et al. 2018; Zalachoris and Rathje 2019; Quick et al. 2021), a different M_{min} threshold may be required for tectonic earthquakes in different regions, for induced earthquakes in different regions, and for induced versus tectonic earthquakes in a given region. The purpose of this study is to establish an appropriate M_{min} threshold for liquefaction hazard assessment for induced earthquakes in Oklahoma, Texas, and Kansas and to quantitatively assess the applicability of M_{min} thresholds recommended for tectonic earthquakes. To evaluate the required M_{min} for induced earthquakes, a probabilistic seismic hazard analysis (PSHA) and PLHA are performed using an idealized induced seismic source and two idealized soil profiles. The PSHA and PLHA are repeated for different values of M_{min} and the estimated liquefaction hazard for each M_{min} are compared to determine the required M_{min} for use with induced earthquakes. This process is repeated for idealized tectonic seismic sources for both the CEUS and the western US (WUS). This provides a quantitative assessment of M_{min} for tectonic events and allows a comparison to be made between M_{min} for tectonic and induced events in Oklahoma, Texas, and Kansas. The following section provides a brief summary of the PSHA and PLHA processes and the importance of M_{min} in these analyses. The seismic sources, site profiles, and liquefaction hazard evaluation models used in the PSHA and PLHA will then be discussed. Finally, results of the PSHA and PLHA will be presented, and conclusions drawn from this study will be discussed.

4.2 PSHA, PLHA, and M_{min}

In order to evaluate the liquefaction hazard at a given site, design ground motion and soil profile information is required. Once obtained, these data are used with liquefaction triggering models such as those proposed by Green et al. (2019) or Quick et al. (2021) to evaluate liquefaction hazard. Ground motions are often characterized probabilistically via a PSHA. However, in practice, a single level of ground shaking corresponding to a single, specified return period is often selected as the design ground motion for liquefaction evaluation (i.e., a "pseudo-probabilistic" analysis). While this approach is common in practice, it does not account for the reality that a given site may be subjected to a wide range of ground shaking intensities having a range of return periods and that the liquefaction triggering potential at the site will be different for each level of shaking. To account for this, a PLHA can be used. PLHA is a method for evaluating liquefaction hazard that accounts for the contributions from all hazard levels and all earthquake magnitudes (e.g., Kramer and Mayfield 2007).

A PSHA primarily integrates over three variables (i.e., magnitude, source-to-site distance, and number of standard deviations above or below the logarithmic mean value from the ground-motion prediction equation, GMPE; Bommer and Crowley 2017). This process is used to develop a curve showing mean annual frequency of exceedance (AFE) versus a specific intensity measure such as peak ground acceleration (a_{max}). As an example, for a given seismic source, the AFE of a given intensity (i.e., a_{max}) can be computed as:

$$P(a_{max} \geq a) = \nu \int_{M_{min}}^{M_{max}} \int_{R_{min}}^{R_{max}} P(a_{max} \geq a|EQK: M_w, R) f(R|m) f(M_w) dr dm \tag{24}$$

where ν is the annual recurrence rate of earthquakes for the seismic source calculated based on the Gutenberg–Richter (GR) recurrence model (Gutenberg and Richter 1956); M_{min} and M_{max} are the lower and upper bounds of integration for magnitude; R_{min} and R_{max} are the lower and upper bounds of integration for site-to-source distance (R); $P(a_{max} \geq a|EQK: M_w, R)$ is the probability of a_{max} exceeding a given value of a_{max}, a, during an earthquake with magnitude, M_w, and site-source-distance, R, based on the selected GMPE; and $f(R)$ and $f(M_w)$ are the probability density functions of R and M_w, respectively.

As shown in Equation 24 and noted by Bommer and Crowley (2017), the limits of integration must be considered for each random variable considered in the PSHA. For magnitude, the limits of integration are typically defined by two parameters, M_{min} and M_{max}. M_{max} represents the largest earthquake that is reasonably expected to occur within a defined time frame and is primarily limited by the dimensions of potential fault ruptures in the source zone (Bommer and Crowley 2017). In contrast, M_{min} is defined as "the smallest magnitude earthquake that is capable of generating potentially damaging levels of ground shaking" (Bommer and Crowley 2017). As such, Bommer and Crowley (2017) point out that M_{min}, rather than being a function of the seismic hazard, is actually an engineering parameter related to risk. In this context, the function of M_{min} is to exclude from hazard integrations ground motions that are not sufficiently energetic to cause damage to the structures for which the hazard is being estimated. Based on this definition, M_{min} will actually be scenario-dependent based on the structure type, damage metric of interest, and other factors.

Green and Bommer (2019) point out that the definition of M_{min} used in a PSHA can be directly translated to PLHA by analogy if the "risk" is now considered to be the severity or damage potential of soil liquefaction rather than structural damage, which is a more common measure in seismic risk estimation. In this scenario, fragility functions from seismic risk analysis are replaced with liquefaction susceptibility models. In this context, M_{min} can be considered the smallest earthquake magnitude sufficient to generate ground motions capable of triggering liquefaction. Liquefaction triggering is controlled by both amplitude and duration of the ground motion. For this reason, Green and Bommer (2019) note that magnitude is a potentially good indicator of the capability of an earthquake to trigger liquefaction because, over short distances, both a_{max} and duration show a dependence on magnitude (Lasley et al. 2017). As a result, they state that M_{min} is a potentially effective lower bound of integration for use in a PLHA and a convenient screening criterion when evaluating the liquefaction hazard for earthquakes.

A PLHA combines the results of a PSHA with a probabilistic evaluation of liquefaction potential in order to estimate the mean annual rate of non-exceedance of a selected factor of safety against liquefaction (FS_{liq}). Kramer and Mayfield (2007) present this concept in discretized form as:

$$\Lambda_{FS^*_{liq}} = \sum_{j=1}^{N_M} \sum_{i=1}^{N_{a_{max}}} P\left[FS_{liq} < FS^*_{liq} | a_{max_i}, m_j\right] \Delta\lambda_{a_{max_i},m_j} \tag{25}$$

where N_M and $N_{a_{max}}$ are the number of magnitude and peak ground acceleration increments into which "hazard space" is subdivided; $P\left[FS_{liq} < FS^*_{liq} | a_{max_i}, m_j\right]$ is the conditional probability that the estimated FS_{liq} will not exceed a given threshold, FS^*_{liq}, for an event with $a_{max} = a_{max_i}$ and $M_w = m_j$; and $\Delta\lambda_{a_{max},m_j}$ is the incremental mean annual rate of a_{max_i} and m_j. $\Delta\lambda_{a_{max},m_j}$ corresponds to a conditional hazard curve for a given magnitude and a_{max}. The value of $\Lambda_{FS^*_L}$ corresponds to the mean annual rate of FS_{liq} being less than FS^*_{liq}. Assuming that liquefaction occurs when $FS^*_{liq} < 1.0$, the return period (T_r) of liquefaction for a given site is equal to the reciprocal of $\Lambda_{FS^*_{liq}=1.0}$ (Kramer and Mayfield 2007).

PLHA can also be used to determine the AFE for liquefaction damage indices such liquefaction potential index (LPI) (Iwasaki et al. 1978) or the Ishihara-inspired liquefaction potential index (LPI_{ish}) (Maurer et al. 2015b). This is done by replacing the conditional probability term in Equation 25 with the conditional probability of exceeding a given value of LPI or LPI_{ish}. The AFE for a given value of LPI or LPI_{ish} can be calculated as:

$$\Lambda_{LPI^*} = \sum_{j=1}^{N_M} \sum_{i=1}^{N_{a_{max}}} P\left[LPI \geq LPI^* | a_{max_i}, m_j\right] \Delta\lambda_{a_{max_i},m_j} \tag{26}$$

$$\Lambda_{LPI_{ish}^{*}} = \sum_{j=1}^{N_M} \sum_{i=1}^{N_{a_{max}}} P\left[LPI_{ish} \geq LPI_{ish}^{*} | a_{max_i}, m_j\right] \Delta\lambda_{a_{max_{i},m_j}} \tag{27}$$

where Λ_{LPI^*} is the AFE for a given LPI, LPI^*, and $P\left[LPI \geq LPI^* | a_{max_i}, m_j\right]$ is the conditional probability of exceeding LPI^* for a given $a_{max} = a_{max_i}$ and $M_w = m_j$. Similarly, $\Lambda_{LPI_{ish}^{*}}$ is the AFE for a given LPI_{ish}, LPI_{ish}^{*}, and $P\left[LPI_{ish} \geq LPI_{ish}^{*} | a_{max_i}, m_j\right]$ is the conditional probability of exceeding LPI_{ish}^{*} for a given $a_{max} = a_{max_i}$ and $M_w = m_j$. In contrast to the probability of liquefaction computed using Equation 25, LPI and LPI_{ish} are evaluated deterministically. As a result, the conditional probability terms in Equation 26 and 27 resolve to 1 when LPI ≥ LPI^* or $LPI_{ish} \geq LPI_{ish}{*}$ for a given M_w and a_{max}, and to 0 for cases where LPI < LPI^* or $LPI_{ish} < LPI_{ish}{*}$ for a given M_w and a_{max}.

While mean annual rate of liquefaction and T_r represent the likelihood of a given soil layer to liquefy, LPI and LPI_{ish} correlate with the severity of the resulting liquefaction manifestations at the ground surface. LPI and LPI_{ish} have been shown to correlate well with liquefaction damage potential (Iwasaki et al. 1978; Maurer et al. 2015b). As such, they provide a good metric for evaluating the practical impacts of M_{min} selection in PLHA when evaluating the potential for liquefaction-related damages. For this reason, the effect of M_{min} selection on the estimation of both mean annual rate of liquefaction and AFE of LPI and LPI_{ish} is assessed as part of this study.

4.3 Source Characteristics and Ground Motion Prediction Equations

The seismic source models used in this study are based on idealized circular areal sources having a radius of 200 km. Liquefaction hazard is estimated assuming that the soil profiles being evaluated are located at the center of this idealized source. This provides a worst-case scenario with regards to smaller magnitude events, because they are generally only likely to trigger liquefaction at short site-to-source distances. Based on this geometry, three different source types are considered: one for induced earthquakes in Oklahoma, Texas, and Kansas (OTK), one for tectonic earthquakes in the CEUS, and one for tectonic earthquakes in the WUS. Earthquake recurrence rates for each source are based on annualized Gutenberg–Richter (GR) recurrence distributions. GR recurrence distribution models are expressed in terms of annual recurrence per km^2. The GR recurrence distribution parameters for the OTK source (a = 0.2018, b = 1.05) are derived from the Grigoratos et al. (2020a; b) estimates for induced earthquake rates in 2020. GR parameters for the CEUS source (a = -1.38, b = 0.937) are based on recurrence rates for the Eastern Tennessee Seismic Zone [ETSZ] (Bockholt et al. 2015). GR parameters for the WUS source (a = -1.47, b = 0.95) are based on the South Sierran Source Block Source Zone in California (U.S. Bureau of Reclamation 2002). GR parameters are for the declustered catalogs. To separate the effects of GR recurrence distributions on M_{min} from the effects of liquefaction model and GMPE, a sensitivity analysis is also conducted using the same GR parameters for all three sources. Results are discussed in Section 4.6.

An M_{max} of 7.5 was used for the CEUS source based on the M_{max} of the ETSZ (Bockholt et al. 2015). An M_{max} of 7.0 was used for the WUS source based on the South Sierran Source Block Source Zone (U.S. Bureau of Reclamation 2002). Because induced seismicity is driven by short-lived anthropogenic operations, it is difficult to determine an appropriate M_{max} for induced seismic sources. However, an M_{max} of 7.0 was used for the OTK source based on the size of faults in the region (Hornsby et al. 2020). This is consistent with M_{max} used in other studies for induced seismicity in OTK (e.g., Grigoratos et al. 2021).

Region- and source-specific GMPEs are selected for each of the three sources. The Zalachoris and Rathje (2019) [ZR19] GMPE for induced earthquakes is used for the OTK source, the Hassani and Atkinson (2015) [HA15] GMPE for tectonic earthquakes is used for the CEUS source, and the Boore et al. (2014) [Bea14] GMPE for tectonic earthquakes is used for the WUS source. The ZR19 GMPE uses hypocentral distance (R_{hyp}) as an input variable. As a result, the PSHA and PLHA for the OTK source integrate over both R_{epi} and focal depth. The seismogenic depth interval for the OTK source is set to between 2 km and 10 km (Grigoratos et al. 2021). Within this range, an empirically-based distribution of focal depths is used based on $M_w \geq 3$ events in the Zalachoris et al. (2020) induced ground motion database for Oklahoma, Texas, and Kansas. Median depth for the distribution is 5 km. The HA15 and Bea14 GMPEs use R_{jb} distance (closest distance to the surface projection of the fault rupture plane). Given that the events being considered for this PLHA are generally small, it is assumed that R_{jb} is approximately equivalent to epicentral distance (R_{epi}). As a result, the PSHA and PLHA for the CEUS and WUS sources integrate over R_{epi} but do not integrate over focal depth.

Figure 4.1 shows a comparison of a_{max} as a function of R_{epi} for the three GMPEs for a focal depth of 5 km. Curves are shown for $M_w = 3$, 5, and 7 and for time-weighted average small-strain shear wave velocity (V_s) over the upper 30 m of the soil profile (V_{s30}) values of 760 m/s and 150 m/s. The ZR19 GMPE was developed for $M_w = 3.0\text{-}5.8$, so a_{max} predictions for $M_w > 5.8$ were extrapolated while holding the magnitude scaling adjustment factor, F_m, constant for $M_w \geq 5.8$. This is consistent with the approach used in Grigoratos et al. (2021).

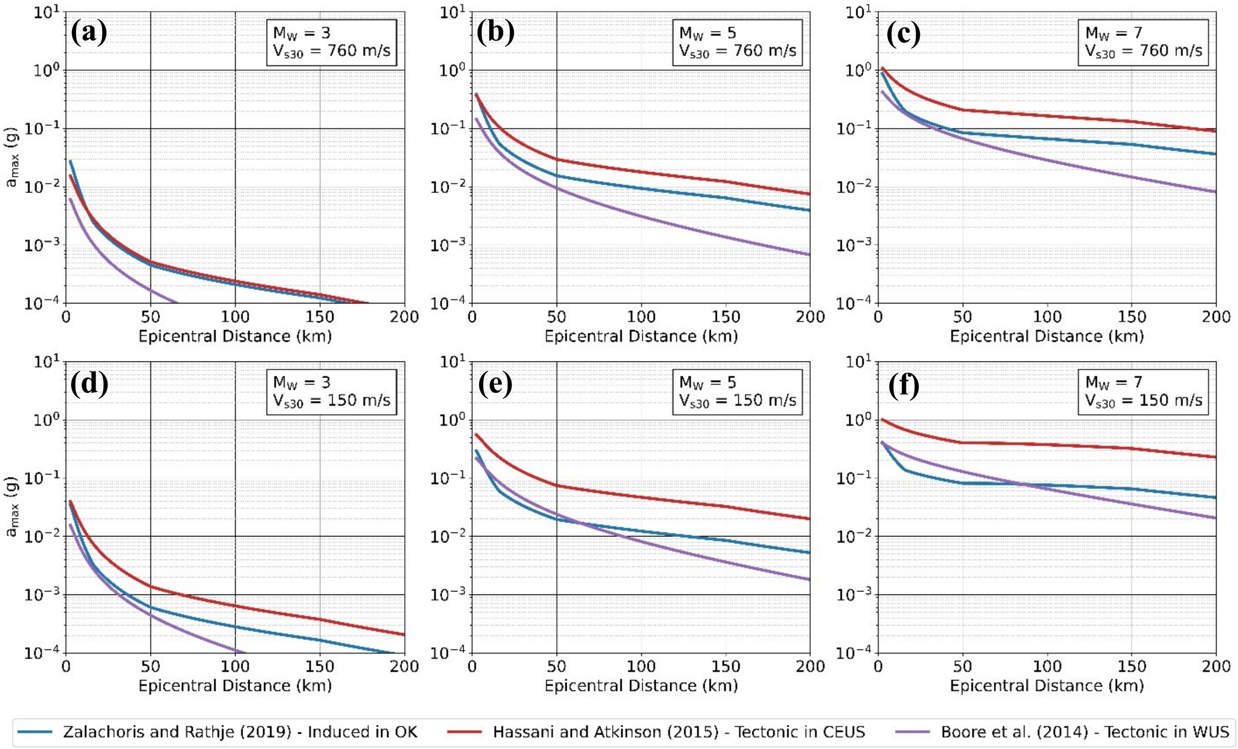

Figure 4.1. Comparison of a_{max} vs. R_{epi} for the Zalachoris and Rathje (2019) GMPE for induced earthquakes in Oklahoma, Texas, and Kansas, the Hassani and Atkinson (2015) GMPE for tectonic earthquakes in the CEUS, and the Boore et al. (2014) GMPE for tectonic earthquakes in the WUS. Curves are shown for $M_w = 3$ (a, d), 5 (b, e), and 7 (c, f) and for $V_{s30} = 760$ m/s (a-c) and 150 m/s (d-f). Focal depth for the Zalachoris and Rathje (2019) GMPE is 5 km.

As shown in this figure, a_{max} tends to be highest for tectonic earthquakes in the CEUS for most R_{epi}. For short R_{epi} and stiff sites (e.g., V_{s30} = 760 m/s in the figure), induced earthquakes in OTK can have intensities that exceed those of tectonic earthquakes in the CEUS, as reflected in higher a_{max} values. This higher near-source intensity has been attributed to the shallow focal depths of induced earthquakes, which result in ruptures very near the epicenter (i.e., short R_{hyp}). However, this effect is offset to some extent by the smaller stress drops that result from these shallow focal depths (Atkinson 2015; Zalachoris and Rathje 2019). Due to these shallow focal depths, a_{max} for induced events decreases rapidly with increasing R_{epi} near the source. However, induced ground motions exhibit similar attenuation rates to the tectonic ground motions in the CEUS at longer distances ($R_{hyp} > \sim 17$ km for the ZR19 GMPE). It should be noted that these models are poorly constrained for short R_{epi} due to the sparseness of available data. As a result, it is difficult to attribute the differences observed between the three GMPEs at small R_{epi} solely to regional differences or differences between induced and tectonic earthquakes as they may be heavily influenced by assumptions regarding site-to-source distance and other modelling parameters.

Zalachoris and Rathje (2019) found that ground motions in OTK tend to exhibit weaker scaling with magnitude than do tectonic events in the CEUS for periods less than ~1.0 s. They suggest this trend could be explained by the smaller stress drops of induced events or other source parameters such as faulting mechanism. Because of this weaker magnitude scaling, a_{max} for a given R_{epi} exhibits smaller increases with increasing magnitude for the ZR19 GMPE than for the HA15 or Bea14 GMPEs, as shown in the figure. This same trend is observed when comparing the Novakovic et al. (2018) GMPE for induced events in OTK to the Atkinson (2015) GMPE for small-to-moderate events in California as done in Atkinson (2020). At small magnitudes (M_w = 3.5-4.0), a_{max} for the Novakovic et al. (2018) GMPE is higher than for the Atkinson (2015) GMPE. However, as magnitude increases, a_{max} predicted by the Atkinson (2015) GMPE approaches and eventually exceeds a_{max} predicted by the Novakovic et al. (2018) GMPE for some R_{hyp}. As with short R_{epi}, these models are poorly constrained for $M_w > \sim 5.2$ due to the sparseness of the dataset. As a result, the observed trends may not be solely related to differences in ground motion characteristics or geology but may be influenced by modelling assumptions.

Induced ground motions in OTK also exhibit weaker linear-elastic site amplification at soft sites (e.g., V_{s30} = 150 m/s in the figure) than predicted for tectonic ground motions in the CEUS or WUS (Zalachoris and Rathje 2019). This is shown in the figure, where the increase in a_{max} from V_{s30} = 760 m/s to V_{s30} = 150 m/s is much more pronounced for the HA15 and Bea14 GMPEs than for the ZR19 GMPE. Zalachoris and Rathje (2019) attribute this to the relatively shallow depth to bedrock in OTK as compared to the WUS, even for sites with small V_{s30}. They note that the linear amplification model for the ZR19 GMPE exhibits trends similar to the linear site amplification model proposed for the CEUS by Stewart et al. (2017), but still results in smaller amplification for sites for soft sites, particularly at longer periods. The ZR19 GMPE uses the same non-linear site amplification model used in the HA15 GMPE.

4.4 Site Profile Characteristics

The soil profiles used in this study are based on the idealized profiles presented in Green and Bommer (2019). This includes both "extremely susceptible" and "very susceptible" soil profiles. The "extremely susceptible" profile consists of very loose, clean sand (normalized tip resistance from cone penetration test, q_{c1Ncs}, equal to 84 atm) down to a depth of 30 m. This correlates to a relative density of approximately 20% (Robertson and Cabal 2015). The water table for the "extremely susceptible" profile is at the ground surface. The "very susceptible" profile is the same as the "extremely susceptible" profile except that it includes a 1-m-thick dense surface crust (q_{c1Ncs} = 180 atm) and the water table depth corresponds to the base of the crust at a depth of 1 m. Green and Bommer (2019) note that the "very susceptible" profile is of more relevance to typical liquefaction hazard evaluations because it is capable of supporting a building structure, while the "extremely susceptible" profile is not suitable for even light building structures. However, they note that the "extremely susceptible" profile may have relevance to liquefaction hazard evaluations for other infrastructure, particularly levees or pipelines. V_s profiles are developed for each profile using the Ulmer et al. (2020) CPT-based V_s correlation for liquefiable soils. The Robertson and Cabal (2015) correlation for general soils is used to estimate V_s of the surface layer for the "very susceptible" profile. The resulting V_s profiles are used to compute time-weighted average V_s over the upper 12 m of the soil profile (V_{s12}) and V_{s30} for use with the GMPEs and liquefaction triggering models.

4.5 Liquefaction Hazard Evaluation

The factor of safety against liquefaction triggering (FS_{liq}) for the PLHA is calculated using liquefaction triggering models specific to each source. The model developed by Quick et al. (2021) is used to assess liquefaction hazard for the OTK source while the Green et al. (2017) CEUS and Green et al. (2017) WUS models are used to assess the liquefaction hazard for the CEUS and WUS sources, respectively. These models are variants of the "simplified" stress-based procedure (e.g., Whitman 1971; Seed and Idriss 1971). Within this framework, FS_{liq} is computed as:

$$FS_{liq} = \frac{CRR_{M7.5}}{CSR^*} \tag{28}$$

where $CRR_{M7.5}$ represents the resistance of the soil to liquefaction triggering during an M_w7.5 event under level ground surface conditions and an initial vertical effective stress of 1 atm, and CSR^* is the cyclic stress ratio normalized to the same conditions as $CRR_{M7.5}$. $CRR_{M7.5}$ is correlated to normalized *in situ* test metrics, such as normalized blow count ($N_{1,60cs}$) from standard penetration tests (SPTs); q_{c1Ncs} from cone penetration tests (CPTs); or normalized small-strain shear wave velocity (V_{s1}) from V_s tests.

CSR* is calculated as:

$$CSR^* = 0.65\frac{a_{max}}{g}\frac{\sigma_v}{\sigma'_{v0}}r_d\frac{1}{MSF \cdot K_\sigma \cdot K_\alpha} \tag{29}$$

where σ_v and σ'_{vo} are the total and initial vertical effective stresses at a given depth in a soil profile, a_{max} is the peak ground acceleration at the ground surface, *g* is the acceleration of gravity in the same units as a_{max}, and r_d is a dimensionless stress reduction factor that accounts for the non-rigid response of the soil column. MSF is the magnitude scaling factor that adjusts CSR for shaking duration based on a reference M_w7.5 event, K_σ is a correction factor for initial vertical effective overburden stress using a reference initial effective overburden stress of 1 atm, and K_α is a correction factor for initial horizontal static shear stress using a reference initial static shear stress of zero (e.g., level ground conditions). The value 0.65 is an arbitrary value defining the ratio of the "average" imposed cyclic shear stress (τ_{avg}) to the maximum imposed cyclic shear stress (τ_{max}) (i.e., $\tau_{avg} = 0.65 \cdot \tau_{max}$).

The $\mathrm{CRR}_{\mathrm{M7.5}}$ curve used in the Green et al. (2017) models is given as:

$$CRR_{M7.5} = exp\left[\frac{q_{c1Ncs}}{113} + \left(\frac{q_{c1Ncs}}{1000}\right)^2 - \left(\frac{q_{c1Ncs}}{140}\right)^3 + \left(\frac{q_{c1Ncs}}{137}\right)^4 - C_o + \sigma_T \cdot \Phi^{-1}(P_{liq})\right] \tag{30}$$

where q_{c1Ncs} is the normalized tip resistance from a cone penetration test (CPT), C_o= 2.632, σ_T is the total standard deviation equal to 0.468, Φ^{-1} is the standard cumulative normal distribution, and P_{liq} is the probability of liquefaction. By combining Equations 28 through 30 and rearranging, P_{liq} can be computed as:

$$P_{liq}(q_{c1Ncs}, CSR^*) = \Phi\left[-\frac{\frac{q_{c1Ncs}}{113} + \left(\frac{q_{c1Ncs}}{1000}\right)^2 - \left(\frac{q_{c1Ncs}}{140}\right)^3 + \left(\frac{q_{c1Ncs}}{137}\right)^4 - 2.632 - \ln(CSR^*)}{\sigma_T}\right] \tag{31}$$

This equation is used to evaluate the conditional probability term in Equation 25 when evaluating $\mathrm{T_r}$ of liquefaction. Although the Quick et al. (2021) liquefaction triggering model is intended for use the with $\mathrm{CRR}_{\mathrm{M7.5}}$ curve presented in Green et al. (2019), probabilistic versions of the Green et al. (2019) $\mathrm{CRR}_{\mathrm{M7.5}}$ curve are still under development. As a result, the Quick et al. (2021) model is implemented in this study using the Green et al. (2017) $\mathrm{CRR}_{\mathrm{M7.5}}$ curve given by Equation 30.

Although the same $\mathrm{CRR}_{\mathrm{M7.5}}$ curve is used by all three liquefaction triggering models, the relationships used to estimate CSR* differ. Specifically, different $\mathrm{r_d}$ and MSF relationships are used to compute CSR* for each model. As result, for a given $\mathrm{M_w}$ and $\mathrm{a_{max}}$, the three frameworks will result in different computed values of $\mathrm{FS_{liq}}$ and $\mathrm{P_{liq}}$. The Green et al. (2017) CEUS and WUS models use region-specific $\mathrm{r_d}$ relationships for tectonic earthquakes developed by Lasley et al. (2016) in addition to region-specific MSF relationships developed by Green et al. (2017) based on earlier work by Lasley et al. (2017). The Quick et al. (2021) model incorporates new $\mathrm{r_d}$ and MSF relationships specific to induced seismic events in Oklahoma, Texas, and Kansas. The Quick et al. (2021) model was developed using ground motions with $3.5 \leq \mathrm{M_w} \leq 5.8$ while the Green et al. (2017) model was developed using ground motions with $\mathrm{M_w} \geq 4.5$ and $\mathrm{M_w} \geq 4.9$ for the CEUS and WUS, respectively. As a result, extrapolation of the $\mathrm{r_d}$ and MSF relationships is required to cover the range of $3 \leq \mathrm{M_w} \leq 7$ considered in this study, as is the case for the ZR19 GMPE used to estimate $\mathrm{a_{max}}$. Additionally, the Quick et al. (2021) model was developed for $\mathrm{R_{hyp}}$

< 70 km and requires extrapolation with for larger R_{hyp}. It should be noted that these extrapolations introduce additional uncertainties into the liquefaction triggering evaluation. However, these models provide the best available estimates and are used for this study. Differences in r_d and MSF relationships for the Quick et al. (2021), Green et al. (2017) CEUS, and Green et al. (2017) WUS models are reflective of differences in both ground motion characteristics and regional geology (Lasley et al. 2016, 2017; Quick et al. 2021). Both the Quick et al. (2021) and Lasley et al. (2016, 2017) datasets include soil profiles extending deeper than 30 m and containing primary liquefaction-susceptible soils. This suggests that the Quick et al. (2021) and Lasley et al. (2016, 2017) models should be compatible with the profiles used in this study. V_{s12} is used in the Quick et al. (2021) and Lasley et al. (2016) r_d models as well as the Quick et al. (2021) MSF model to account for the effect of profile stiffness. However, V_{s12} for the profiles used in this study fall at the low end of the range of V_{s12} values included in the Quick et al. (2021) and Lasley et al. (2016) studies. As a result, the effect of V_{s12} on r_d and MSF may be poorly constrained for these sites. Additionally, V_{s12} for the "extremely susceptible" profile falls just below the range for the profiles in the Lasley et al. (2016, 2017) dataset. As a result, these models require extrapolation with respect to V_{s12} to assess liquefaction potential for the "extremely susceptible" profile. As noted, this extrapolation introduces additional uncertainties into the liquefaction triggering evaluation.

A comparison of the Quick et al. (2021) r_d relationship and the Lasley et al. (2016) r_d relationships used in the Green et al. (2017) models is shown in Figure 4.2. Values are shown for $M_w = 3$, 5, and 7 and $V_{s12} = 125$ m/s, which is the approximate V_{s12} of the "very susceptible" profile. The Quick et al. (2021) r_d relationship is also a function of a_{max} and is shown for $a_{max} = 0.1$ g and 0.5 g in Figure 4.2. Quick et al. (2021) r_d values are extrapolated for $M_w = 3$ and 7, and Lasley et al. (2016) r_d values are extrapolated for $M_w = 3$. As shown in this figure, r_d at shallow depths is similar for all models, but tends to be lower for the Quick et al. (2021) at deeper depths. This difference is more pronounced as M_w increases. This is reflective of the greater high frequency content of induced ground motions in OTK (Novakovic et al. 2018; Zalachoris and Rathje 2019). Greater high frequency content is expected to lead to less rigid response of the soil columns and, consequently, lower r_d. Differences in r_d also reflects differences in regional geologic characteristics such as impedance contrast between bedrock and the soil profile as well as depth to bedrock (Quick et al. 2021). All else being equal, the smaller r_d for the Quick et al. (2021) model result in higher computed FS_{liq} than computed by the Lasley et al. (2016) models.

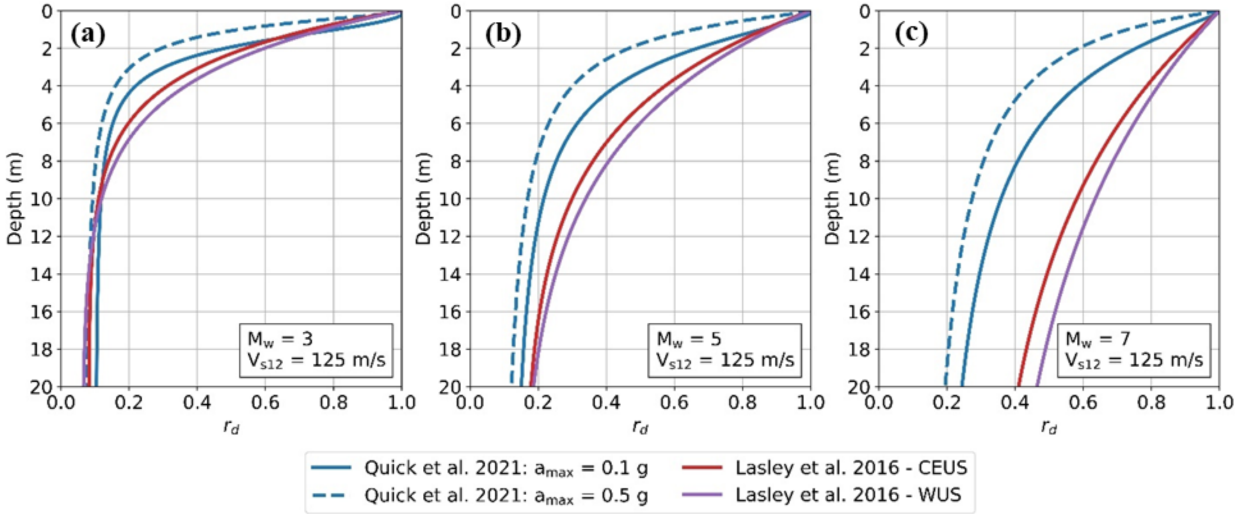

Figure 4.2. Comparison of r_d models proposed by Quick et al. (2021) for induced earthquakes in Oklahoma, Texas, and Kansas and models proposed by Lasley et al. (2016) for the CEUS and WUS. Curves are shown for M_w = 3, 5, and 7 (a-c) and V_{s12} = 125 m/s. Estimates for the Quick et al. (2021) model are presented for a_{max} = 0.1 g and 0.5 g. Quick et al. (2021) r_d values are extrapolated for M_w = 3 and 7, and Green et al. (2017) r_d values are extrapolated for M_w = 3.

A comparison of MSF relationships for the three models is shown in Figure 4.3. Values are shown for M_w = 3, 5, and 7, a_{max} = 0.1 g and 0.5 g, and V_{s12} = 125 m/s. The Quick et al. (2021) MSF relationship is also a function of R_{hyp} and MSF are shown for R_{hyp} = 10 km and 35 km in Figure 4.3. Extrapolated values are indicated by dotted lines. As shown in this figure, except for very small magnitudes and short R_{hyp}, MSF is consistently lower for the Quick et al. (2021) model than for the Green et al. (2017) models. This difference becomes more pronounced with increasing M_w, a_{max}, and R_{hyp}. Differences between MSF for the Quick et al. (2021) model and the Green et al. (2017) models are reflective of the fact that ground motion durations increase much faster with R_{hyp} in the CEUS than WUS (Boore and Thompson 2015). The ground motions used to develop the Green et al. (2017) CEUS model were scaled from WUS motions using state-of-the-art methods (McGuire et al. 2001). However, the scaling procedures used were likely focused on scaling for spectral amplitude as opposed to duration. This may explain why the durations of the Green et al. (2017) CEUS ground motions are more in line with those of the Green et al. (2017) WUS model than the Quick et al. (2021) model. Regional differences in impedance contrast between bedrock and soil profiles and differences in frequency content of the ground motions may also affect MSF (Lasley et al. 2017). All else being equal, the smaller MSF for the Quick et al. (2021) model result in lower computed FS_{liq} than computed by the Green et al. (2017) models.

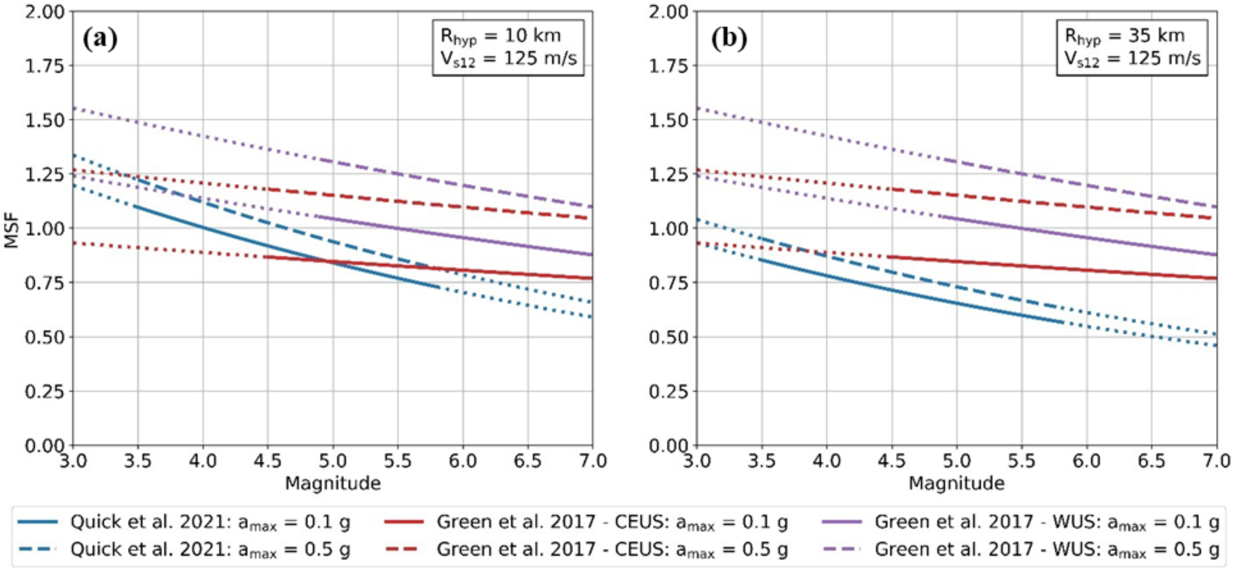

Figure 4.3. Comparison of the MSF models proposed by Quick et al. (2021) for induced earthquakes in Oklahoma, Texas, and Kansas and Green et al. (2017) for tectonic earthquakes in the CEUS and WUS. Curves are shown for a_{max} = 0.1 g and 0.3 g, V_{s12} = 125 m/s, and R_{hyp} = 15 km and 50 km. Extrapolated values are indicated by dotted lines.

Because the effects of the smaller r_d and the smaller MSF estimated by the Quick et al. (2021) model have opposing effects on FS_{liq}, it is important to consider the effect of these two parameters concurrently. Curves of r_d/MSF for the three liquefaction triggering models are shown in Figure 4.4. Because all other factors in computing CSR* are the same for these models for a given soil profile and earthquake event, the trends shown are indicative of relative trends in FS_{liq} for the three models. Values are shown for M_w = 3, 5, and 7, a_{max} = 0.1 g and 0.3 g, R_{hyp} = 10 km and 35 km, and V_{s12} = 125 m/s. Values for the Quick et al. (2021) model are extrapolated for M_w = 3 and 7, and values for the Green et al. (2017) models are extrapolated for M_w = 3. As shown in this figure, for most depths, M_w, and R_{hyp}, r_d/MSF for the Quick et al. (2021) tend to be lower than for the Green et al. (2017) models resulting in higher estimates of FS_{liq}. However, at shallow depths r_d/MSF for the Quick et al. (2021) models can be larger than for the Green et al. (2017) models. These differences become more pronounced with increasing M_w and R_{hyp}. The higher r_d/MSF values for the Quick et al. (2021) model lead to lower computed FS_{liq} and higher computed P_{liq} at shallow depths.

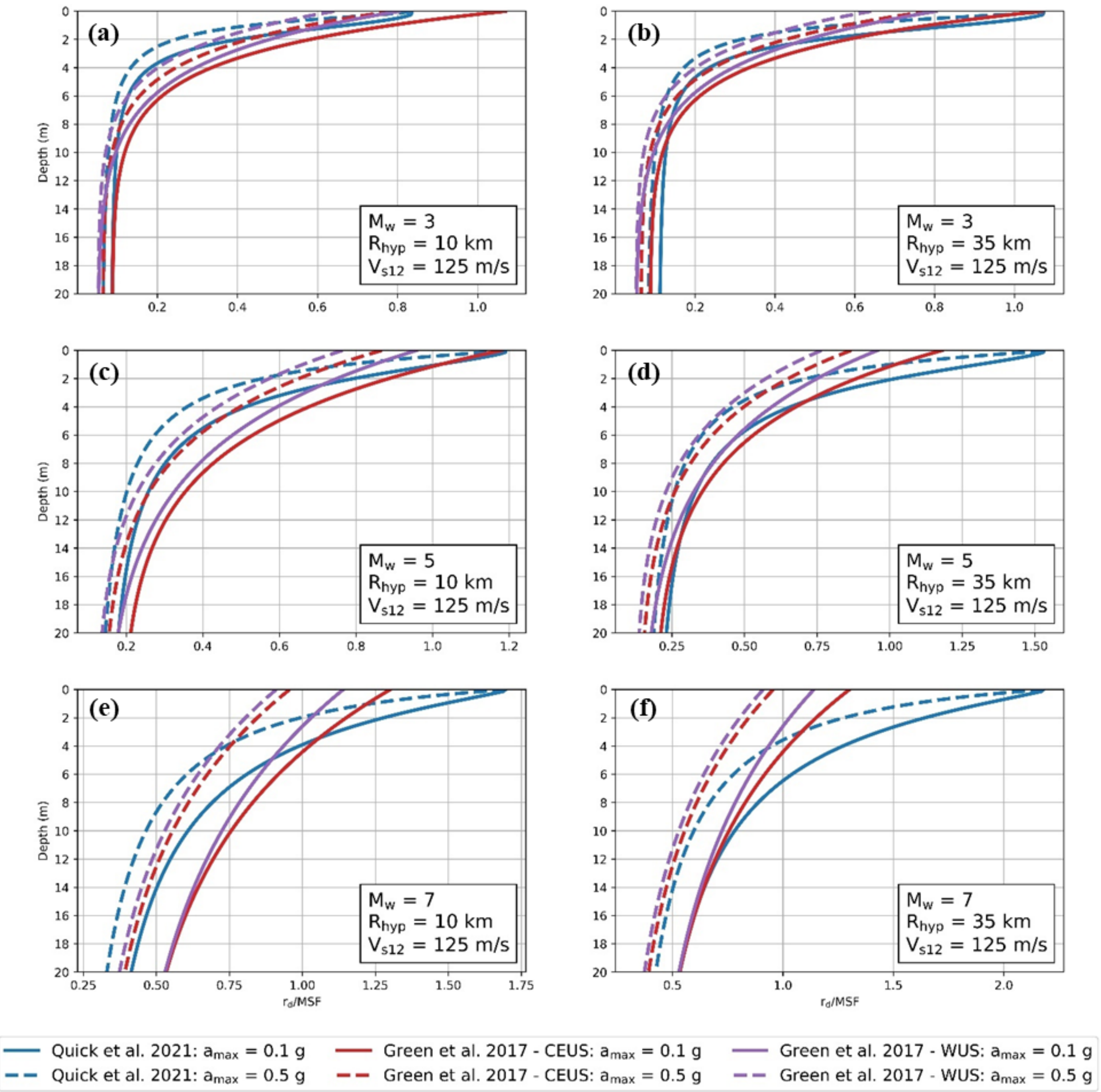

Figure 4.4. Comparison of r_d/MSF for the Quick et al. (2021) liquefaction triggering model for induced earthquakes in Oklahoma, Texas, and Kansas and Green et al. (2017) models for tectonic earthquakes in the CEUS and WUS. Curves are shown for $M_w = 3$ (a, b), 5 (c, d), and 7 (e, f), $a_{max} = 0.1$ g and 0.3 g, $R_{hyp} = 10$ km (a-c) and 35 km (d-f), and $V_{s12} = 125$ m/s. Values for the Quick et al. (2021) model are extrapolated for $M_w = 3$ and 7, and values for the Green et al. (2017) models are extrapolated for $M_w = 3$.

To constrain the computed liquefaction hazard associated with low amplitude, long duration motions, the concept of threshold strain (γ_{tv}) proposed by Dobry et al. (1982) is implemented. Dobry et al. (1982) found that for normally consolidated clean sands, excess pore pressures do not develop if the applied cyclic shear strain is less than a certain threshold strain, regardless of the number of cycles. For normally consolidated clean sands, Dobry et al. (1982) found $\gamma_{tv} \approx$ 0.01%. Rodriguez-Arriaga and Green (2018) note that, by extension, there is a threshold a_{max}, $(a_{max})_t$, corresponding to γ_{tv} for which, if the applied a_{max} is below this value, no excess pore pressures will develop and liquefaction triggering will not occur. Rodriguez-Arriaga and Green (2018) proposed the following equation for estimating $(a_{max})_t$ for a given soil layer:

$$(a_{max})_t = 0.000154 \frac{G_{max}(G/G_{max})_{\gamma_{tv}}}{\sigma_v r_d} \tag{32}$$

where $(a_{max})_t$ is in units of g, G_{max} is the small-strain shear modulus of the given soil layer in the same units as σ_v, and $(G/G_{max})_{\gamma_{tv}}$ is the normalized shear modulus reduction ratio of the layer corresponding to γ_{tv} (0.01% strain). The values of σ_v and r_d are for the depth of interest, with r_d based on the liquefaction evaluation framework being used. G_{max} is computed using V_s values computed as described earlier and assumed densities for loose sand (i.e., 17 kN/m^3 above the water table and 19.5 kN/m^3 below the water table). For the purposes of this study, $(G/G_{max})_{\gamma_{tv}}$ is estimated using the Ishibashi and Zhang (1993) modulus reduction and damping curves. Because r_d is a function of M_w in the Green et al. (2017) liquefaction triggering models, estimates of $(a_{max})_t$ are made for each magnitude evaluated in the PLHA. The r_d relationship utilized by the Quick et al. (2021) model depends on both M_w and a_{max}. As a result, $(a_{max})_t$ is estimated for each M_w-a_{max} pair evaluated in the PLHA. Regardless of the liquefaction triggering model used, P_{liq} for a given depth in the profile for given M_w or M_w-a_{max} pair is set to zero if a_{max} at is less than $(a_{max})_t$ for that depth [Note that $(a_{max})_t$ is the a_{max} at the profile surface required to induce a γ at specific depth that is greater than or equal to γ_{tv}.]. This constraint is used to ensure that ground motions with long durations (low MSF) but $a_{max} < (a_{max})_t$ do not contribute to the estimated liquefaction hazard.

As noted, the effect of M_{min} selection on estimated AFE for LPI and LPI_{ish} is also investigated. LPI and LPI_{ish} are dimensionless indices used to predict the severity of surficial liquefaction manifestations and reflect the cumulative liquefaction response of a soil profile from the ground surface to a depth of 20 m. LPI, developed by Iwasaki et al. (1978), is proportional to the cumulative thickness of the liquefied layers, the depth to these layers, and the degree to which FS_{liq} for these layers is less than 1.0. LPI is computed as:

$$LPI = \int_{0}^{20\,m} F_{LPI}(FS_{liq}) \cdot w(z)dz \tag{33}$$

where $F_{LPI} = 1 - FS_{liq}$ for $FS_{liq} < 1.0$, $F_{LPI} = 0$ for $FS_{liq} \geq 1.0$; and w(z) is a depth weighting function given by $w(z) = 10 - 0.5z$, where z is the depth below the ground surface in meters. LPI assumes that each liquefied layer shallower than 20 m contributes to the severity of surficial liquefaction manifestations. The relative contribution of each liquefied layer increases with both layer thickness and proximity to the ground surface. LPI can range from 0 for a site having $FS_{liq} > 1.0$ for the entire upper 20 m of the site to a maximum of 100 for a site where $FS_{liq} = 0$ for the entire upper 20 m.

LPI_{ish} builds on the LPI concept but also accounts for the effect of the thickness of the non-liquefied crust (H_1) relative to the cumulative thickness of the underlying liquefied materials (H_2) on the severity of liquefaction manifestations. LPI_{ish} is defined as (Maurer et al. 2015b):

$$LPI_{ish} = \int_{H_1}^{20\,m} F_{LPI_{ish}}(FS_{liq}) \cdot \frac{25.56}{z} dz \tag{34a}$$

$$F_{LPI_{ish}}(FS_{liq}) = 1 - FS_{liq}; \quad \text{if } FS_{liq} \leq 1 \text{ and } H_1 \cdot m(FS) \leq 3 \tag{34b}$$

$$= 0; \quad \text{if } FS_{liq} > 1 \text{ or } H_1 \cdot m(FS) > 3 \tag{34c}$$

$$m(FS_{liq}) = \exp\left\{\frac{5}{25.56 \cdot (1 - FS_{liq})}\right\} - 1; \quad \text{if } FS_{liq} \leq 0.95 \tag{34d}$$

$$= 100; \quad \text{if } FS_{liq} > 0.95 \tag{34e}$$

where H_1 is the shallowest depth where $FS_{liq} < 1$. FS_{liq} in Equations 33 and 34 is computed using the deterministic Green et al. (2017) $CRR_{M7.5}$ curve. The deterministic implementation of the Green et al. (2017) $CRR_{M7.5}$ curve corresponds to a P_{liq} of approximately 35% based on total uncertainty. This is computed as:

$$CRR_{M7.5} = exp\left[\frac{q_{c1Ncs}}{113} + \left(\frac{q_{c1Ncs}}{1000}\right)^2 - \left(\frac{q_{c1Ncs}}{140}\right)^3 + \left(\frac{q_{c1Ncs}}{137}\right)^4 - 2.8119\right] \leq 0.6 \qquad (35)$$

The optimal LPI and LPI_{ish} thresholds corresponding to the different surficial liquefaction manifestation severities will depend on the procedure used to compute FS_{liq}, as well the profile characteristics (Maurer et al. 2015a). The following severity criteria are commonly used in practice (Iwasaki et al. 1978): LPI or $LPI_{ish} < 5$ corresponds to "no to minor" liquefaction, $5 \leq$ (LPI or LPI_{ish}) ≤ 15 corresponds to moderate severity liquefaction manifestations, and LPI or $LPI_{ish} > 15$ corresponds to severe surficial manifestations.

As noted previously, $M_{max} = 7.0$ is used for the OTK and WUS sources, and $M_{max} = 7.5$ is used for the CEUS source. These M_{max} are used as the upper bound for the integration in the PLHA and PSHA. M_{min} values ranging from 3.0 to 5.5 were considered as part of this study.

4.6 Results and Discussion

Results of the PSHA are shown in Figure 4.5. These include AFE vs. a_{max} curves for each of the three seismic sources, computed for M_{min} = 3.0, 3.5, 4.0, 4.5, 5.0, and 5.5. As shown in this figure, for the OTK source, there is a significant difference in AFE calculated using $M_{min} = 5.5$ and 5.0 across the range of a_{max} values shown. There are also differences in AFE calculated using $M_{min} = 5.5$ and 5.0 for the CEUS and WUS sources, but these differences diminish with increasing a_{max} and are limited to the range of $a_{max} < \sim 0.2$ g and $a_{max} < \sim 0.3$ g for the CEUS, and WUS sources, respectively. When comparing AFE for $M_{min} = 5.0$ and $M_{min} = 4.5$, differences are evident for the OTK source for all a_{max} shown, although these differences are smaller than between $M_{min} = 5.5$ and $M_{min} = 5.0$. For $a_{max} > \sim 0.1$ g, which is the range of a_{max} values most likely to trigger liquefaction, there is no observable difference in AFE for the CEUS and WUS for $M_{min} = 5.0$ and $M_{min} = 4.5$. However, for smaller a_{max}, the CEUS source exhibits significant differences for $M_{min} = 5.0$ and $M_{min} = 4.5$ and the WUS source exhibits some, smaller differences. There is no significant difference in AFE of a_{max} for the CEUS and WUS sources for $M_{min} < 4.5$ for any a_{max} considered. In contrast, for the OTK source, small differences in the AFE of $a_{max} < \sim 0.3$ g are observed for $M_{min} < 4.5$, but these differences are generally small and decrease rapidly with increasing a_{max}.

The contribution of events with $M_{min} < 4.5$ to the AFE of $a_{max} > 0.1$ g is consistent with large near-source intensities predicted for induced events at small magnitudes (Zalachoris and Rathje 2019). Although the effect is offset to some extent by reductions in stress drops, the shallow focal depths of induced earthquakes in Oklahoma, Texas, and Kansas can result in significant ground motion intensities, even for small magnitude events (Atkinson 2015; Zalachoris and Rathje 2019). Atkinson (2020) notes that induced events with M_w as low as 3.5 to 4.0 are sufficient to generate potentially damaging ground motions for small R_{hyp}. The increased influence of smaller magnitude events for the OTK source as compared to the CEUS and WUS is reflective of the predominance of smaller magnitude events in this region (i.e., $b = 1.05$ for the OTK source whereas $b = 0.94$ and 0.95 for the CEUS and WUS sources, respectively, based on the declustered catalogs). Additionally, the weaker magnitude scaling observed by Zalachoris and Rathje (2019) for induced events and included in the ZR19 GMPE may also contribute to the increased influence of these smaller events. The weaker scaling of the ZR19 GMPE means that an increase in magnitude for an induced event results in a smaller increase in expected a_{max} than would be expected for the same increase in magnitude for a tectonic event. This serves to increase the overall percent contribution of more frequent, smaller magnitude events to AFE of a_{max}, even for larger values of a_{max}. This increases the potential contribution of these smaller events to the liquefaction hazard.

The observed trends may also be influenced to some extent by the extrapolation of the ZR19 GMPE for $M \geq 5.8$. The extrapolation method used (i.e., holding F_m constant for $M \geq 5.8$) is unlikely to decrease the relative contribution of $M \geq 5.8$ events to the computed hazard. As a result, model extrapolation likely does not explain the increased influence of smaller magnitude events on seismic hazard for the OTK source relative to the tectonic sources. As noted though, due to the limited number of induced events with $M_w >$ ~5.0, magnitude scaling effects for $M_w >$ ~5.2 are poorly constrained. This adds additional uncertainty, particularly when extrapolating the model to larger magnitudes.

Although events with $M_w < 5$ contribute to AFE of a_{max} for all three sources, this does not necessarily indicate that use of an $M_{min} < 5$ is necessary in a PLHA for any of the three sources. In fact, if M_{min} did not have an impact on hazard estimates, it would not be needed. The use of $M_{min} \geq 5.0$ may still be acceptable for a PLHA as long as the selected M_{min} excludes all motions that may result in liquefaction-related damage (Green and Bommer 2019). Therefore, to establish the required M_{min}, mean annual rate of liquefaction, and AFE of LPI and LPI_{ish} must be considered.

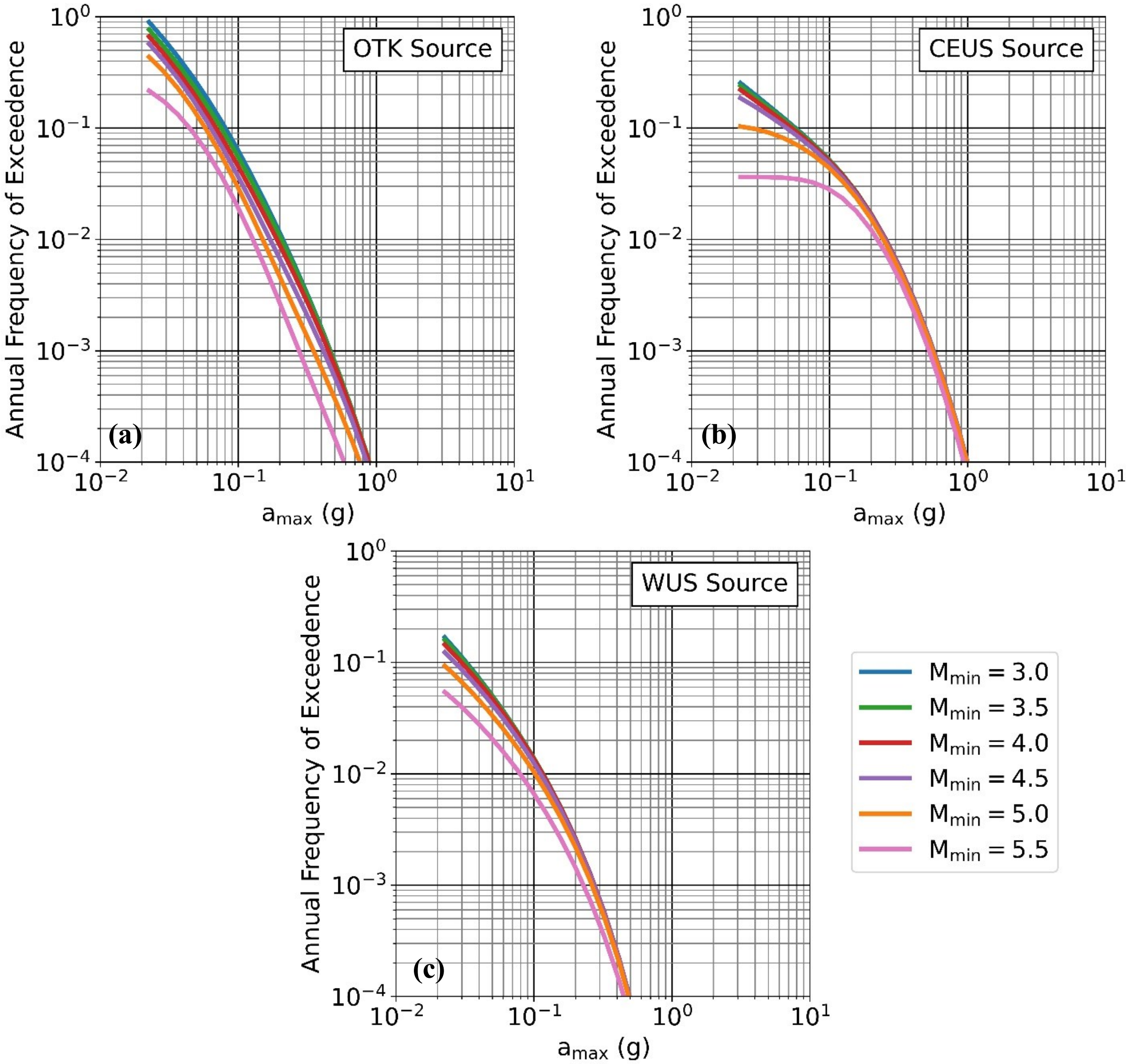

Figure 4.5. AFE vs. a_{max} curves for the OTK (a), CEUS (b), and WUS (c) sources. Curves are shown for M_{min} = 3.0 to 5.5.

Figure 4.6 shows mean annual rate of liquefaction vs. depth for the “very susceptible” and “extremely susceptible” profiles for the OTK, CEUS, and WUS sources. As shown in this figure, estimated mean rate of liquefaction increases from $M_{min} = 5.5$ to $M_{min} = 5.0$ for all three sources and both profiles. The observed differences are most pronounced at depths less than approximately 10 m. Similarly, mean annual rate of liquefaction for $M_{min} = 4.5$ is higher than for $M_{min} = 5.0$ for all sources and for both profiles. However, for the “very susceptible” profile, the observed difference is generally small and observable over only a small range of depths, although the difference appears more pronounced for the WUS source. No differences are noted in mean annual rate of liquefaction for $M_{min} < 4.5$.

For the “extremely susceptible” profile, the difference in mean annual rate of liquefaction for $M_{min} = 5.0$ and $M_{min} = 4.5$ is more pronounced and evident over a wider range of depths than observed for the “very susceptible” profile. There are minimal differences in mean annual rate of liquefaction for the CEUS source for $M_{min} < 4.5$ and only slightly larger differences for the WUS for $M_{min} < 4.5$. In contrast, for the OTK source, there is an observable difference in mean annual rate of liquefaction for $M_{min} < 4.5$. However, this difference is small and limited to depths of 1-2 m.

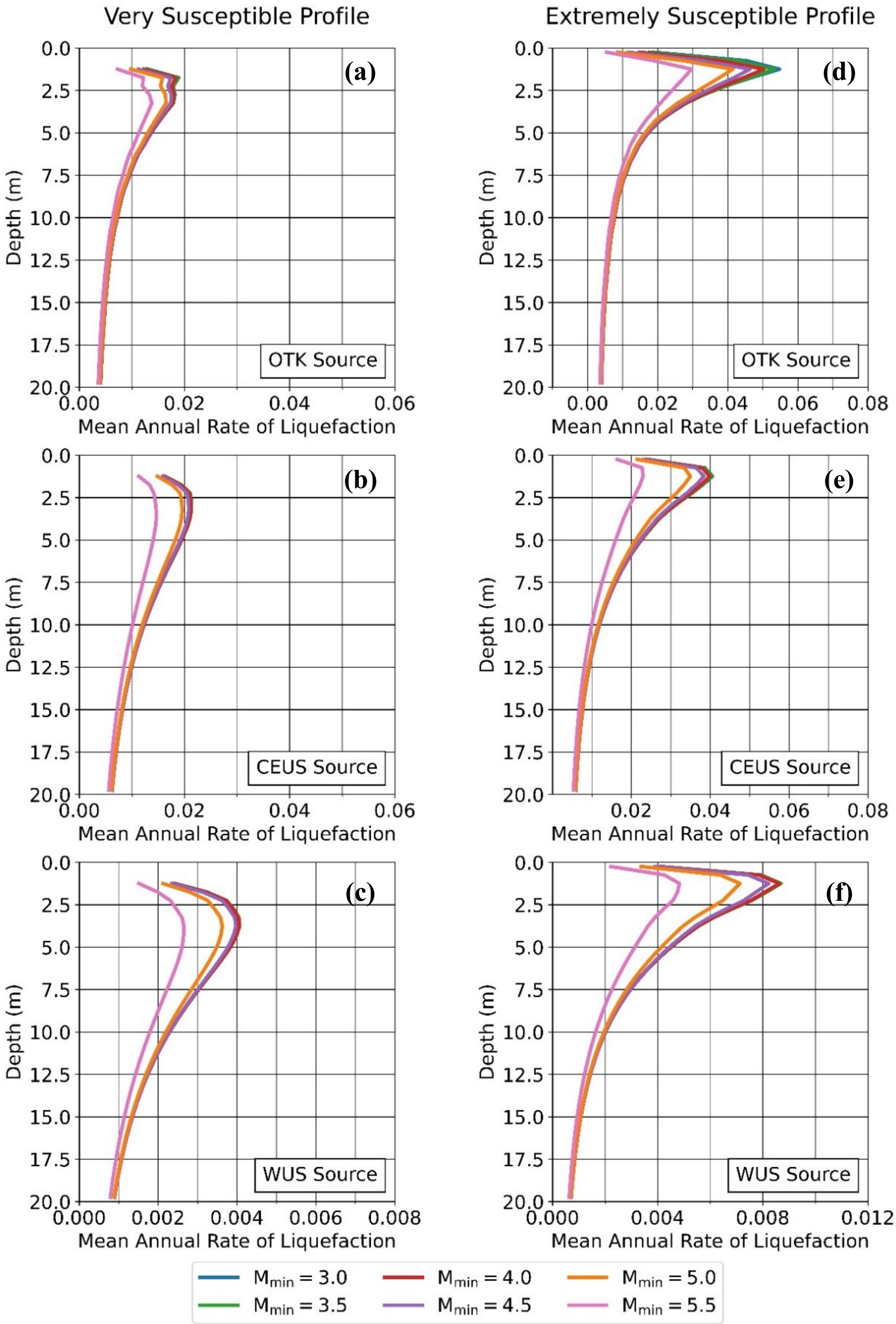

Figure 4.6. Profiles of mean annual rate of liquefaction for the "very susceptible" profile (a-c) and "extremely susceptible" profile (d-f) based on the OTK (a, d), CEUS (b, e), and WUS (c, f) sources. Curves are shown for M_{min} = 3.0 to 5.5.

To quantify the effect of M_{min} on mean annual rate of liquefaction, mean annual rate of liquefaction was deaggregated based on M_w. Deaggregation curves were developed for a depth of 2.75 m for the “very susceptible” profile and at a depth of 1.75 m for the “extremely susceptible” profile. The selected depths are where M_{min} appeared to have the greatest effect on estimated liquefaction hazard for each profile based on Figure 4.6. Results of the deaggregation are shown in Figure 4.7. The cumulative percent contribution as M_w increases from 3.0 to 7.0 is indicated by the black line in this figure. As shown in this figure, the use of $M_{min} = 5$ for the “very susceptible” profile would exclude 10-12% of total computed liquefaction hazard at a depth of 2.75 m, while $M_{min} = 5$ would exclude 15-20 % of the computed at a depth of 1.75 m for the “extremely susceptible” profile. As a result, $M_{min} = 5.0$ underestimates the liquefaction potential of these layers. In general, $M_{min} = 4.5$ was sufficient to exclude less than 5% of the computed hazard for the “very susceptible” profile for all sources and for the “extremely susceptible” profile and CEUS and WUS sources. However, for the OTK source and “extremely susceptible” profile, $M_{min} = 4.5$ excludes more than 5% of the computed hazard at a depth of 1.75 m and a lower M_{min} would be required to fully capture liquefaction potential for this specific layer. It is important to note that although $M_{min} < 5$ was shown to affect liquefaction potential at specific depths in both profiles, this does not confirm that an $M_{min} < 5$ is required for a PLHA. This is because soil layers can liquefy without resulting in any observed surficial liquefaction manifestations or damage, particularly when the liquefied layers are thin or deep. As a result, it is more useful to consider LPI and LPI_{ish} when determining M_{min} for a PLHA.

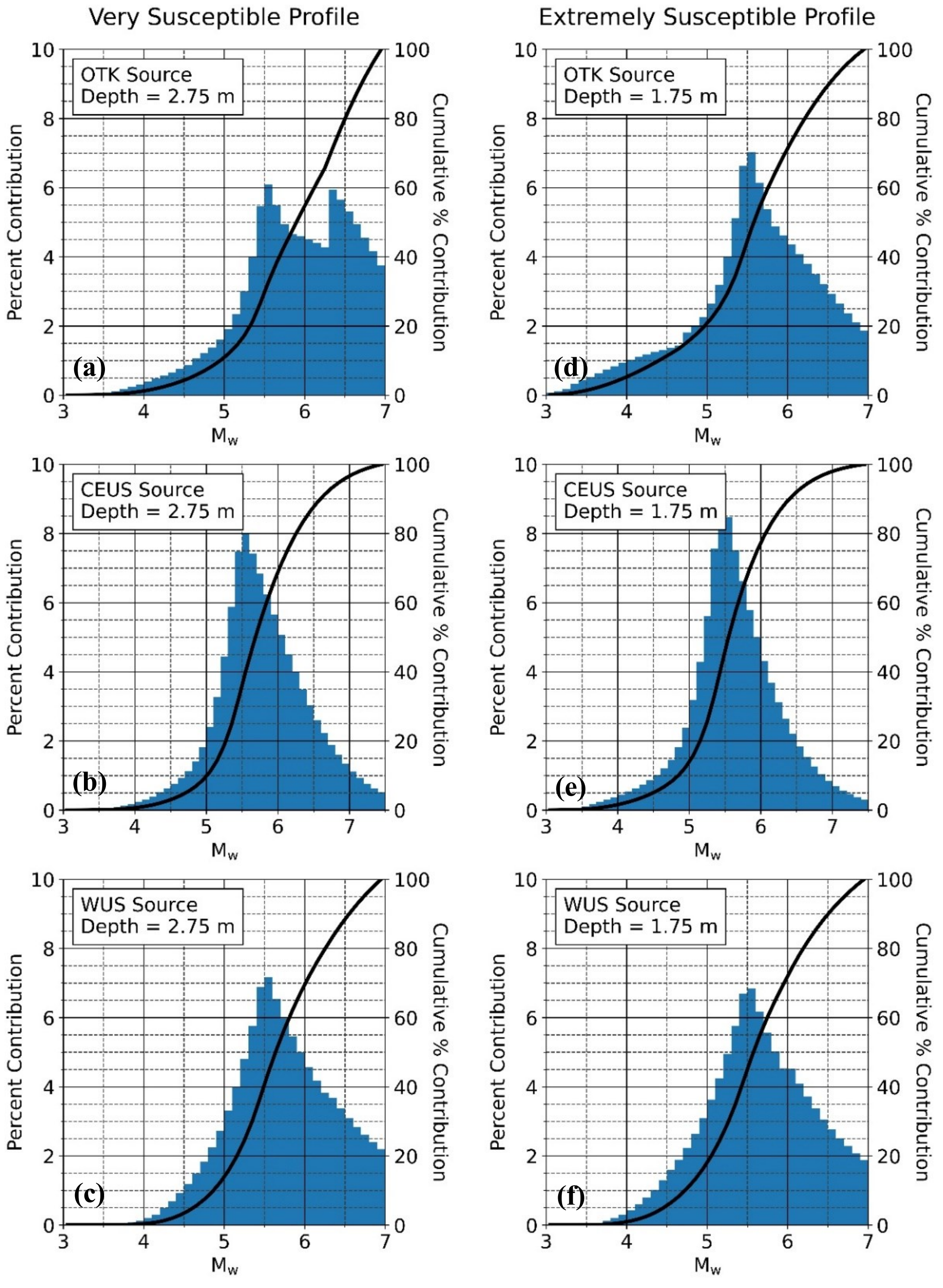

Figure 4.7. Contributions to mean annual rate of liquefaction for the “very susceptible” profile (a-c) at a depth of 2.75 m and for the “extremely susceptible” profile (d-f) at a depth of 1.75 m, deaggregated by M_w. Results are shown for the OTK (a, d), CEUS (b, e), and WUS (c, f) sources. Cumulative percent contribution as M_w increases from 3.0 to 7.0 is indicated by the black line.

As noted previously, LPI and $\mathrm{LPI}_{\mathrm{ish}}$ have been shown to correlate to liquefaction damage potential (e.g., Iwasaki et al. 1978; Maurer et al. 2015). As a result, LPI and $\mathrm{LPI}_{\mathrm{ish}}$ provide a better indication of the M_{min} necessary to capture liquefaction damage potential than mean annual rate of liquefaction. AFE vs. LPI and AFE vs. $\mathrm{LPI}_{\mathrm{ish}}$ curves for the "very susceptible" profile are shown in Figure 4.8. For the OTK source, there is an observable difference in AFE of LPI and $\mathrm{LPI}_{\mathrm{ish}}$ between $M_{\mathrm{min}} = 5.5$ and $M_{\mathrm{min}} = 5.0$, but the observed difference is generally small with changes in LPI or $\mathrm{LPI}_{\mathrm{ish}}$ typically less than 2 for a given AFE. For the CEUS and WUS sources, AFE of LPI and $\mathrm{LPI}_{\mathrm{ish}}$ for $M_{\mathrm{min}} = 5.0$ is higher than AFE for $M_{\mathrm{min}} = 5.5$ for all LPI or $\mathrm{LPI}_{\mathrm{ish}}$ considered with differences in LPI or $\mathrm{LPI}_{\mathrm{ish}}$ for a given AFE as high as 8. The observed differences tend to decrease with increasing LPI and $\mathrm{LPI}_{\mathrm{ish}}$. However, a difference in LPI or $\mathrm{LPI}_{\mathrm{ish}}$ of 8 can lead to significant under-predictions of liquefaction severity at low LPI or $\mathrm{LPI}_{\mathrm{ish}}$.

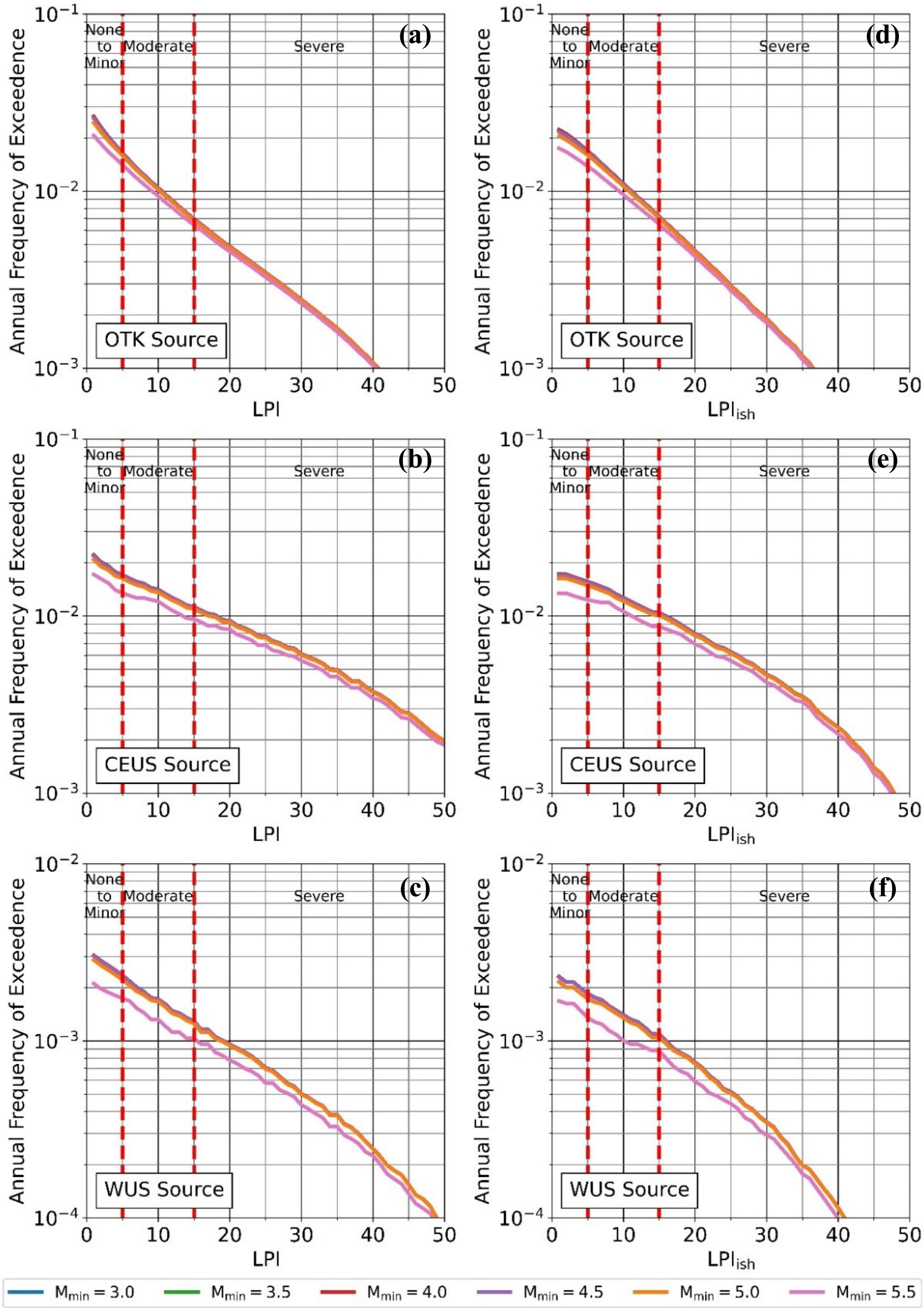

Figure 4.8. AFE vs. LPI (a-c) and AFE vs. LPI$_{ish}$ (d-f) curves for the "very susceptible" profile based on the OTK (a, d), CEUS (b, e), and WUS (c, f) sources. Curves are shown for M_{min} = 3.0 to 5.5. Iwasaki et al. (1978) surficial manifestation severity classifications are indicated.

To further quantify the effect of M_{min} on AFE of LPI and LPI_{ish} for the “very susceptible” profile, the AFE curves were deaggregated based on M_w. Results are shown in Figure 4.9. The cumulative percent contribution as M_w increases from 3.0 to 7.0 is also indicated in this figure by the black line. As shown in these curves, the total contribution to the AFE for LPI or LPI_{ish} for $M_w < 5$ is less than approximately 5% for all three sources. Thus, excluding events with $M_w < 5$ does not significantly affect the estimated liquefaction hazard for the “very susceptible” profile for either induced or tectonic sources. Based on these results, the use of $M_{min} = 5.0$ appears sufficient to exclude ground motions likely to result in surficial manifestations of liquefaction for the “very susceptible” profile. This is consistent with the recommendation of Green and Bommer (2019) of $M_{min} = 5.0$ for sites capable of supporting building structures. The recommended M_{min} of 5.0 appears applicable to tectonic earthquakes in the CEUS and WUS as well as induced earthquakes in Oklahoma, Texas, and Kansas.

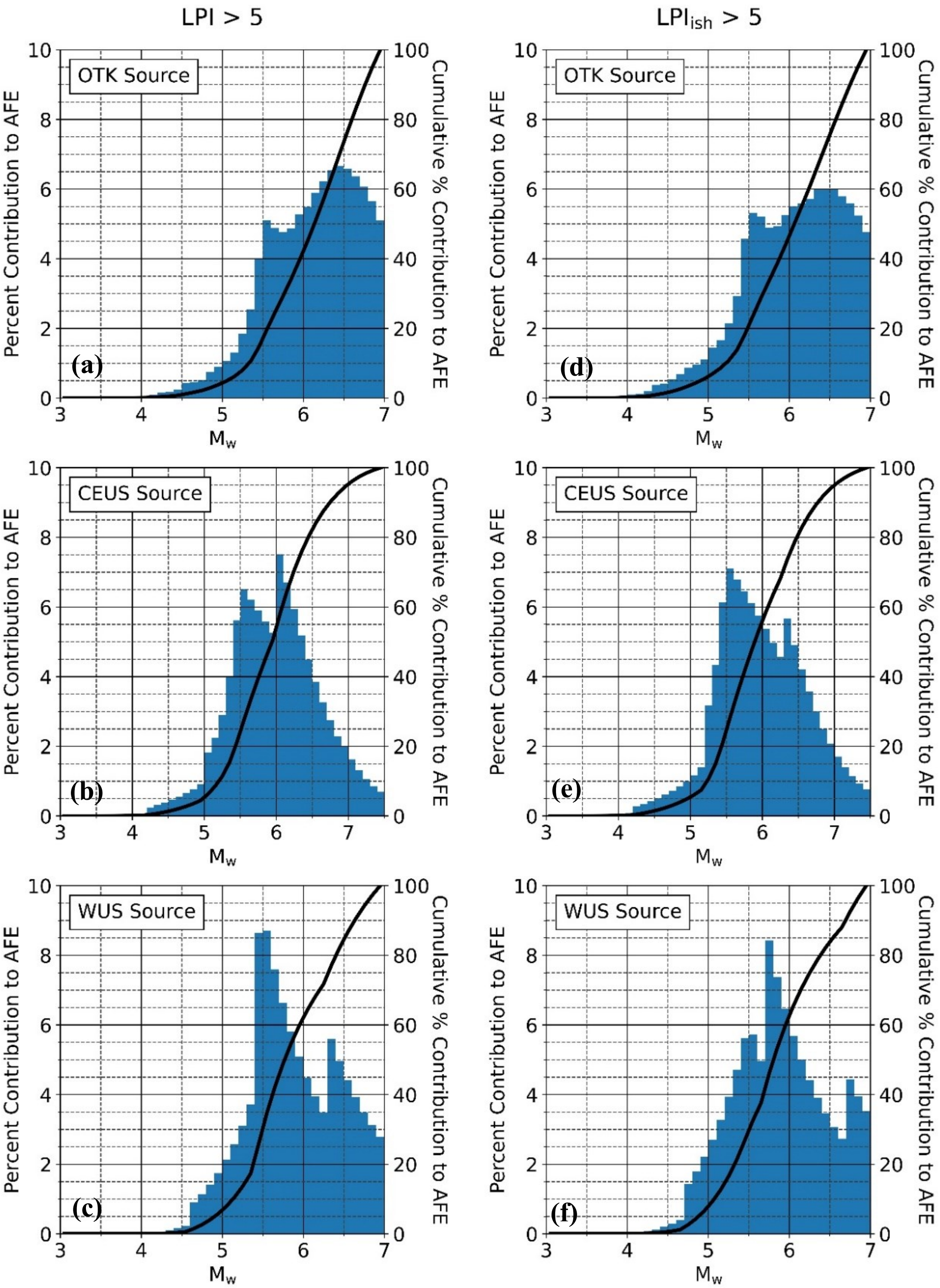

Figure 4.9. Contributions to AFE for LPI > 5 (a-c) and LPI_{ish} > 5 (d-f) deaggregated by M_w for the "very susceptible" profile. Results are shown for the OTK (a, d), CEUS (b, e), and WUS (c, f) sources. Cumulative percent contribution as M_w increases from 3.0 to 7.0 is indicated by the black line.

AFE vs. LPI and AFE vs. LPI_{ish} curves for the “extremely susceptible” profile are shown in Figure 4.10. For the OTK source, AFE of LPI was higher for $M_{min} = 5.0$ than for $M_{min} = 5.5$ for LPI < ~20 with differences in LPI for a given AFE as high as 5. The observed differences decrease with increasing LPI. For the CEUS and WUS sources, there was a significant difference in AFE of LPI and LPI_{ish} for $M_{min} = 5.5$ and $M_{min} = 5.0$ for all LPI considered. Change in LPI for a given AFE was generally less than 6 and decreased with increasing LPI. The use of $M_{min} < 5.0$ did not significantly influence AFE of LPI for the CEUS and WUS sources. In contrast, the use of $M_{min} = 4.5$ led to slight increases in AFE of LPI for the OTK source for LPI < ~10. However, the resulting differences were small and were primarily limited to the range of “none to minor” surficial liquefaction manifestation severity.

The choice of M_{min} had a more pronounced impact on AFE of LPI_{ish} for the “extremely susceptible” profile. For the CEUS and WUS sources, reducing M_{min} from 5.5 to 5.0 resulted in increases in LPI_{ish} greater than 10 for some AFE and significant increases in AFE across the across the range of LPI_{ish} values considered. Additionally, differences were noted between AFE of LPI_{ish} for $M_{min} = 5.0$ and 4.5 for these sources, although the differences in AFE were generally small. Use of $M_{min} = 4.5$ resulted in increases of LPI_{ish} as high as 5 for some AFE but generally resulted in increases of LPI_{ish} less than 3. There was no change in AFE of LPI_{ish} for $M_{min} < 4.5$ for the CEUS and WUS sources.

For the OTK source, the use of $M_{min} = 5.0$ also resulted in increases of AFE of LPI_{ish} as compared to using $M_{min} = 5.5$. This effect was observed for the full range of LPI_{ish} considered. Differences were also noted in AFE of LPI_{ish} between $M_{min} = 5.0$ and $M_{min} = 4.5$. The use of $M_{min} = 4.5$ resulted in increases of LPI_{ish} as high as 4 for a given AFE. Further increases in AFE of LPI_{ish} for $M_{min} < 4.5$ were also observed for the OTK source with events with M_w as low as 3.5 appearing to contribute to AFE of LPI_{ish} for $LPI_{ish} > 5$. However, the observed impact of these smaller events is fairly minor with changes to LPI_{ish} less than 2 for any AFE. Additionally, it should be noted that the LPI_{ish} framework was not calibrated for water table at the ground surface conditions such as those present in the “extremely susceptible” profile (Maurer et al. 2015b; Green and Bommer 2019). As a result, LPI_{ish} may be overestimated for the “extremely susceptible” profile, which could exaggerate the effect of small magnitudes on AFE of LPI_{ish}.

This may explain why AFE of LPI_{ish} curves for the OTK source changed with M_{min} as low as 3.75 or 4.0, but AFE of LPI did not change significantly for LPI < 4.5.

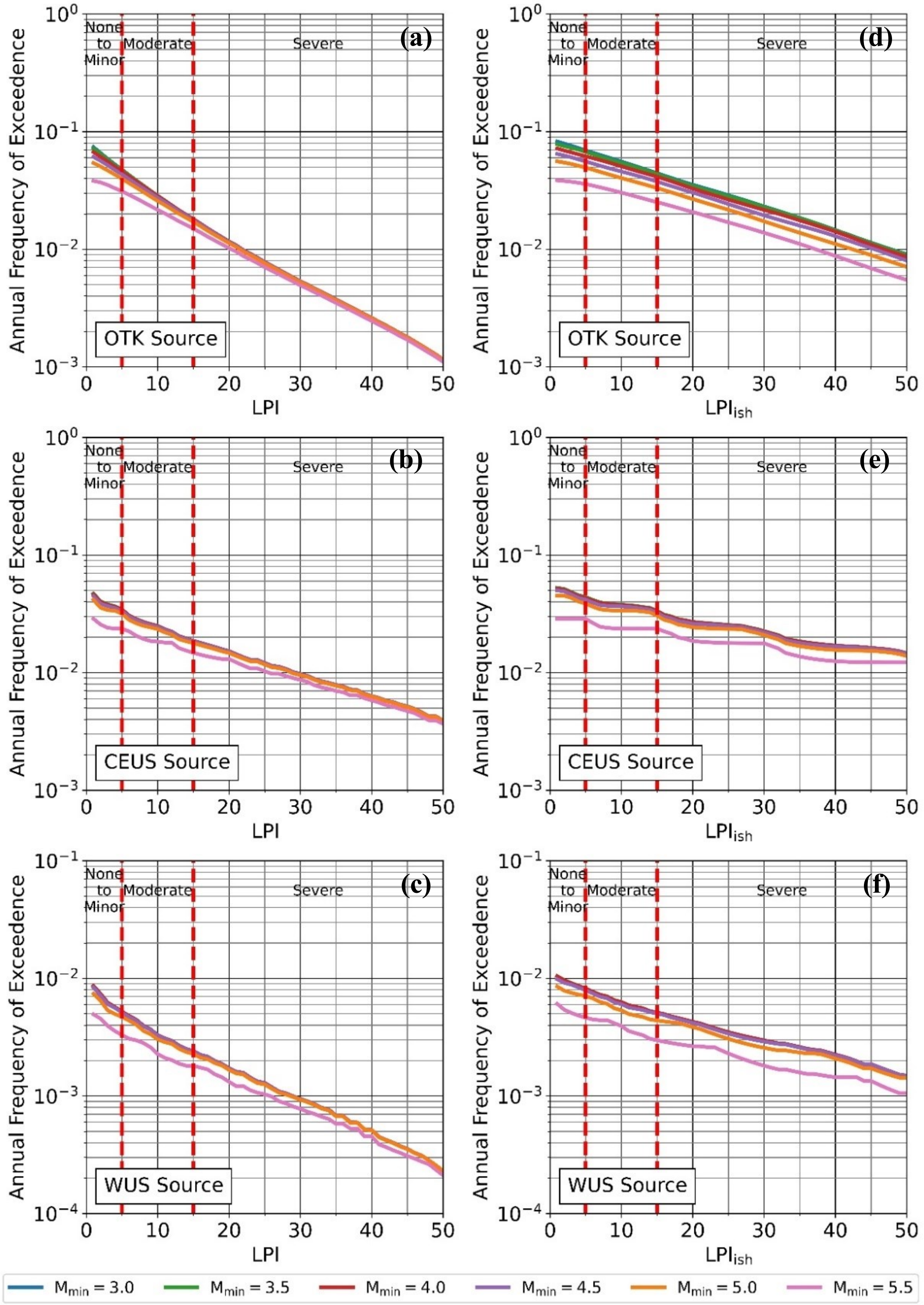

Figure 4.10. AFE vs. LPI (a-c) and AFE vs. LPI$_{ish}$ (d-f) curves for the "extremely susceptible" profile based on the OTK (a, d), CEUS (b, e), and WUS (c, f) sources. Curves are shown for M_{min} = 3.0 to 5.5. Iwasaki et al. (1978) surficial manifestation severity classifications are indicated.

Deaggregation curves for AFE of LPI and LPI_{ish} AFE for the “extremely susceptible” profile based on M_w are shown in Figure 4.11. As with the “very susceptible” profiles, AFE of LPI and $LPI_{ish} > 5$ was considered. The cumulative percent contribution as M_w increases from 3.0 to 7.0 is indicated by the black line in this figure. As shown by these curves, the total contribution to the AFE of LPI or LPI_{ish} for $M_w < 5$ is greater than 10% for all three sources and for both LPI and LPI_{ish}. Thus, excluding events with $M_w < 5$ would significantly affect the estimated liquefaction hazard for the “extremely susceptible” profile for both induced and tectonic events. As a result, smaller M_{min} are required to fully capture liquefaction hazard for the “extremely susceptible” profile.

For the CEUS and WUS sources, less than 5% of the total AFE is contributed by events with $M_w < 4.5$ for either LPI or LPI_{ish}. Based on these results and trends observed in Figure 4.11, $M_{min} = 4.5$ appears to be an acceptable threshold when considering liquefaction hazard at “extremely susceptible sites” from tectonic ground motions in the CEUS and WUS. This is consistent with the findings of Green and Bommer (2019) who recommended $M_{min} = 4.5$ for “extremely susceptible” sites.

For the OTK source, $M_{min} = 4.0$ appears necessary to exclude < 5% of the total AFE of LPI while $M_{min} = 3.75$ appears necessary to exclude < 5% of the total AFE of LPI_{ish}. These results suggest that an M_{min} as low as 3.75 may be necessary to fully capture liquefaction hazard at “extremely susceptible” sites due to induced earthquakes. However, as noted previously, the change in LPI for $M_{min} < 4.5$ was less than 2 for any AFE, which is unlikely to impact the estimated severity of liquefaction at a given site. Additionally, as noted previously, the LPI_{ish} estimates for the “extremely susceptible” may be over-estimated due to the $z_{gwt} = 0$ m conditions. As a result, the contribution of events with $M_w < 4.5$ to the AFE of LPI_{ish} for the OTK source may be exaggerated.

Based on these findings, there is some justification to use an M_{min} as low as 4.0 when evaluating liquefaction hazard at “extremely susceptible” sites due to induced earthquakes in Oklahoma, Texas, and Kansas. These findings are consistent with trends observed in the AFE vs. a_{max} curve for the OTK source, which shows that events with $M_w < 4.5$ contribute to AFE of a_{max} as < ~0.3

g for the OTK source. Additionally, sites with $z_{gwt} = 0$ and loose near-surface soils may be more susceptible to liquefaction during induced earthquakes due to the high r_d/MSF ratios at shallow depths for induced earthquakes in Oklahoma, Texas, and Kansas.

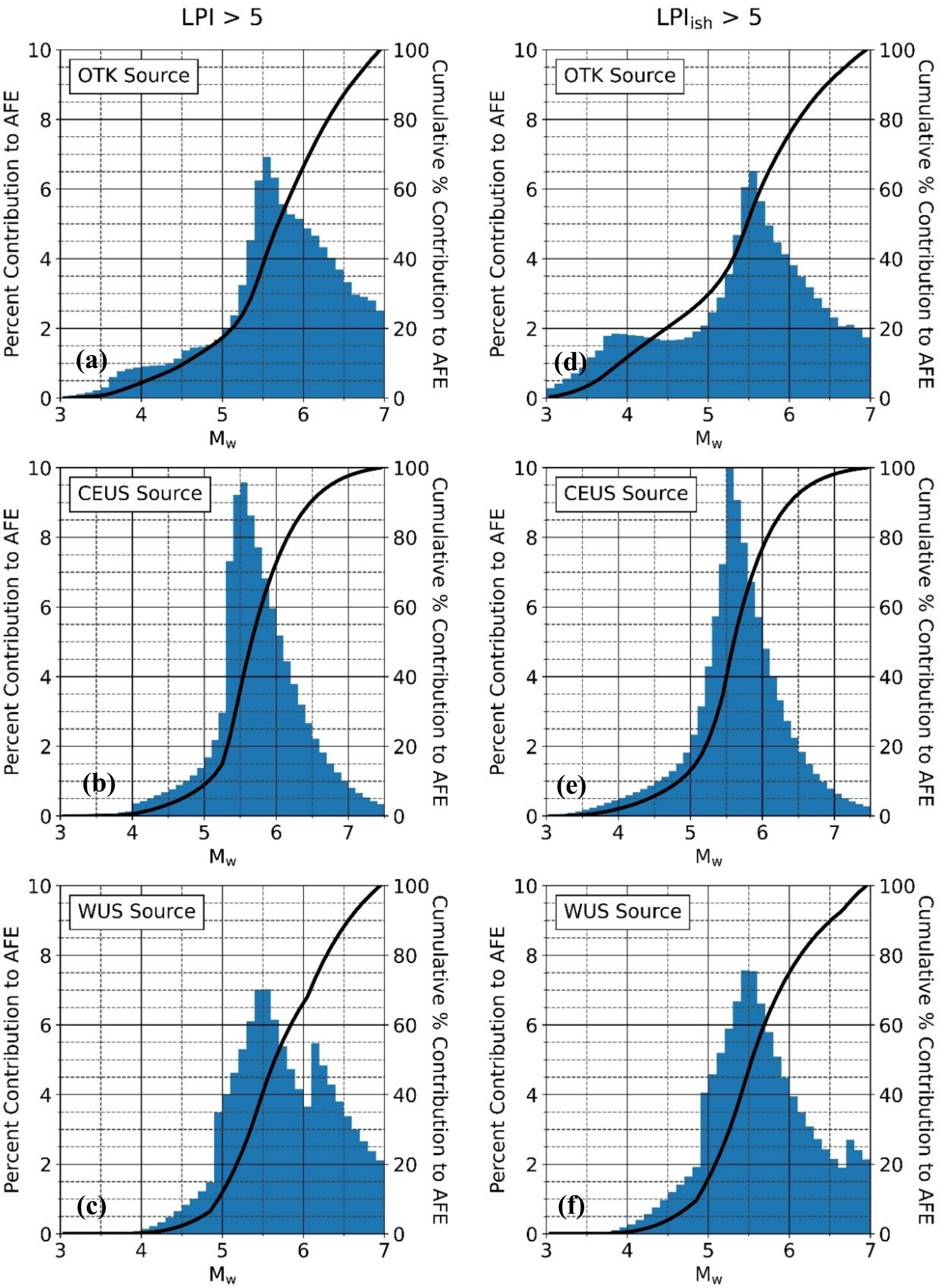

Figure 4.11. Contributions to AFE for LPI > 5 (a-c) and LPI_{ish} > 5 (d-f) deaggregated by M_w for the "extremely susceptible" profile. Results are shown for the OTK (a, d), CEUS (b, e), and WUS (c, f) sources. Cumulative percent contribution as M_w increases from 3.0 to 7.0 is indicated by the black line.

As noted previously, Green and Bommer (2019) did not identify any documented cases of liquefaction for events with $M_w < 4.5$ for either tectonic or induced events. As a result, and because the use of $M_{min} < 4.5$ results in only minor changes in estimated LPI or LPI_{ish} for the OTK source, the use of $M_{min} = 4.5$ may still be justified. However, induced seismicity on the scale presently being observed is a fairly recent phenomenon and few events with $M_w > 4$ have occurred. Additionally, as shown in this analysis, liquefaction during events with $M_w < 5$ is only expected at "extremely susceptible" sites. As a result, conditions during previous $M_w < 4.5$ earthquakes in Oklahoma, Texas, and Kansas may not have been favorable to liquefaction occurrence. Additionally, any minor liquefaction that may have occurred at "extremely susceptible" sites during previous $M_w < 4.5$ earthquakes may have gone unnoticed. Consequently, there is some possibility that liquefaction could occur during future $M_w < 4.5$ events in Oklahoma, Texas, and Kansas, and this risk should be accounted for when using PLHA to the assess the liquefaction hazard at "extremely susceptible" sites in this region

Quick et al. (2021) [Chapter 2] derived standard deviation models for the OTK r_d and MSF relationships. To observe the effect of uncertainty in r_d and MSF on M_{min}, AFE vs. LPI and AFE vs. LPI_{ish} curves were developed based on the mean r_d and MSF relationships as well as the mean relationships plus or minus one standard deviation. Although, Quick et al. (2021) found r_d and MSF were positively correlated such that the effects of uncertainty in these parameters will offset to some extent, for clarity during this analysis, uncertainty in r_d and MSF were considered separately. The resulting curves are provided in Figure I.1 through Figure I.4 of Appendix I. As shown in Figures I.1 and I.2, which present results for the "very susceptible" profile, uncertainty in r_d and MSF has minimal impact on the M_{min} needed to capture liquefaction hazard. For all profiles and for both LPI and LPI_{ish}, using $M_{min} = 5$ appears sufficient to capture liquefaction hazard for all r_d and MSF models considered. The choice of r_d relationship also did not impact required M_{min} for the "extremely susceptible profile." $M_{min} = 4.0$ appears sufficient to capture liquefaction hazard for this profile for all r_d models. The use of the mean minus sigma MSF model resulted in slight changes to AFE of LPI_{ish} for $M_{min} < 4.0$. However, these changes are small (change in $LPI_{ish} < \sim 2$) for a given AFE. Additionally, the use of the mean minus sigma MSF model did not significantly affect AFE of LPI. Based on these observations, there does not seem to sufficient justification to adjust the recommended M_{min} for the “extremely susceptible” profile.

A sensitivity analysis was also conducted to separate the effect of GR recurrence distribution on required M_{min} from the effects of the selected liquefaction models and GMPEs. To this end, AFE curves were developed for a_{max}, LPI, and LPI_{ish} for each seismic source using the GR distribution parameters from the OTK source. Source-specific GMPEs and liquefaction models were still used for the CEUS and WUS sources. The results of this analysis shown in Figure I.5 through Figure I.7 in Appendix I. The use of the OTK GR distribution parameters led to overall increases in the seismic hazard for the CEUS and WUS sources and resulted in slight increases in the relative contribution of small-magnitude events to the calculated liquefaction hazard. However, these changes were not sufficient to change the recommended M_{min} thresholds for the tectonic sources. This analysis also showed that the differences between M_{min} for induced and tectonic events, while affected by GR distribution parameters, are primarily driven by differences in GMPEs and liquefaction models.

4.7 Conclusion

Induced seismicity related to oil and gas production has led to dramatic increases in the seismic hazard of areas such as Oklahoma where the current rate of $M_w \geq 3$ earthquakes is approximately 60 times the natural tectonic rate (Oklahoma Office of the Secretary of Energy & Environment 2019). This increase in earthquakes in a historically low seismicity area has led to increased focus on events that are smaller in magnitude ($M < \sim 5.5$) than are typically considered during conventional liquefaction analysis. Liquefaction observed during the 2016 Pawnee, OK earthquake and the 2017 Pohang, South Korea earthquake has raised concerns about liquefaction during future induced events. Because the seismic hazard in these regions is dominated by small-magnitude events, establishing a minimum magnitude (M_{min}) threshold below which liquefaction is not expected to occur is an important part of assessing liquefaction hazard. The establishment of an M_{min} threshold for liquefaction is also required for performing probabilistic liquefaction hazard analyses (PLHA) for both induced and tectonic earthquakes (Green and Bommer 2019). The purpose of this study was to establish an appropriate M_{min} threshold for liquefaction hazard assessment for induced earthquakes in Oklahoma, Texas, and Kansas and to quantitatively assess the applicability of M_{min} thresholds recommended for tectonic earthquakes. A probabilistic seismic hazard analysis (PSHA) and PLHA were performed using idealized induced and tectonic sources and idealized liquefaction-susceptible soil profiles. By repeating the PSHA and PLHA process for different values of M_{min}, the largest M_{min} required to fully capture the liquefaction hazard was determined. For sites capable of supporting building structures, $M_{min} = 5.0$ was sufficient to fully capture liquefaction hazard for both tectonic and induced seismic sources. For "extremely susceptible" sites that may be of relevance to other infrastructure (e.g., pipelines or levees), $M_{min} = 4.5$ is recommended when considering tectonic sources. These findings are in accord with previous recommendations regarding M_{min} for probabilistic liquefaction hazard analyses for tectonic events. In contrast, there is some indication that $M_{min} = 4.0$ may be required to fully capture the liquefaction hazard due to induced earthquakes at extremely susceptible sites in Oklahoma, Texas, and Kansas. However, there is no evidence of liquefaction occurring during tectonic or induced events with $M_w < 4.5$ in this region, so an $M_{min} = 4.5$ may still be acceptable for induced events.

4.8 Acknowledgements

This study is based on work supported in part by the USGS grant G18AP00094 and U.S. National Science Foundation (NSF) Grants CMMI-1825189 and CMMI-1937984. The authors gratefully acknowledge this support. This study has also significantly benefited from review comments from Dr. Julian Bommer. However, any opinions, findings, and conclusions expressed in this paper are those of the authors and do not necessarily reflect the views of the USGS or NSF, nor the others acknowledged.

References

Atkinson, G. M. (2015). "Ground-motion prediction equation for small-to-moderate events at short hypocentral distances, with application to induced-seismicity hazards." *Bulletin of the Seismological Society of America*, 105(2), 981–992, doi.org/10.1785/0120140142.

Atkinson, G. M. (2020). "The Intensity of Ground Motions from Induced Earthquakes with Implications for Damage Potential." *Bulletin of the Seismological Society of America*, 110(5), 2366–2379, doi.org/10.1785/0120190166.

Atkinson, G. M., Finn, W. D. L., and Charlwood, R. G. (1984). "Simple Computation of Liquefaction Probability for Seismic Hazard Applications." *Earthquake Spectra*, 1(1), 107–123, doi.org/10.1193/1.1585259.

Bird, J. F., and Bommer, J. J. (2004). "Earthquake losses due to ground failure." *Engineering Geology*, 75(2), 147–179, doi.org/10.1016/j.enggeo.2004.05.006.

Bockholt, B. M., Langston, C. A., and Withers, M. (2015). "Local Magnitude and Anomalous Amplitude Distance Decay in the Eastern Tennessee Seismic Zone." *Seismological Research Letters*, 86(3), 1040–1050, doi.org/10.1785/0220140201.

Bommer, J. J., and Crowley, H. (2017). "The purpose and definition of the minimum magnitude limit in PSHA calculations." *Seismological Research Letters*, 88(4), 1097–1106, doi.org/10.1785/0220170015.

Bommer, J. J., Dost, B., Edwards, B., Stafford, P. J., van Elk, J., Doornhof, D., and Ntinalexis, M. (2016). "Developing an application-specific ground-motion model for induced seismicity." *Bulletin of the Seismological Society of America*, 106(1), 158–173, doi.org/10.1785/0120150184.

Boore, D. M., Stewart, J. P., Seyhan, E., and Atkinson, G. M. (2014). "NGA-West2 Equations for Predicting PGA, PGV, and 5% Damped PSA for Shallow Crustal Earthquakes." *Earthquake Spectra*, 30(3), 1057–1085, doi.org/10.1193/070113EQS184M.

Boore, D. M., and Thompson, E. M. (2015). "Revisions to some parameters used in stochastic-method simulations of ground motion." *Bulletin of the Seismological Society of America*, 105(2), 1029–1041, doi.org/10.1785/0120140281.

Choi, J. H., Ko, K., Gihm, Y. S., Cho, C. S., Lee, H., Song, S. G., Bang, E. S., Lee, H. J., Bae, H. K., Kim, S. W., Choi, S. J., Lee, S. S., and Lee, S. R. (2019). "Surface deformations and rupture processes associated with the 2017 Mw 5.4 Pohang, Korea, earthquake." *Bulletin of the Seismological Society of America*, 109(2), 756–769, doi.org/10.1785/0120180167.

Dobry, R., Ladd, R. S., Yokel, F. Y., Chung, R. M., and Powell, D. (1982). *Prediction of Pore Water Pressure Buildup and Liquefaction of Sands during Earthquakes by the Cyclic Strain Method. NBS Building Science Series 138*, National Bureau of Standards, Washington, DC.

Ellsworth, W. L. (2013). "Injection-induced earthquakes." *Science*, 341(6142), 1–8, doi.org/10.1126/science.1225942.

Foulger, G. R., Wilson, M. P., Gluyas, J. G., Julian, B. R., and Davies, R. J. (2018). "Global review of human-induced earthquakes." *Earth-Science Reviews*, 178, 438–514, doi.org/10.1016/j.earscirev.2017.07.008.

Goda, K., Atkinson, G. M., Hunter, J. A., Crow, H., and Motazedian, D. (2011). "Probabilistic Liquefaction Hazard Analysis for Four Canadian Cities." *Bulletin of the Seismological Society of America*, 101(1), 190–201, doi.org/10.1785/0120100094.

Green, R. A., and Bommer, J. J. (2019). "What is the Smallest Earthquake Magnitude that Needs to be Considered in Assessing Liquefaction Hazard?" *Earthquake Spectra*, 35(3), 1441–1464, doi.org/10.1193/032218eqs064m.

Green, R. A., Bommer, J. J., Rodriguez-Marek, A., Maurer, B. W., Stafford, P. J., Edwards, B., Kruiver, P. P., de Lange, G., and van Elk, J. (2019). "Addressing limitations in existing 'simplified' liquefaction triggering evaluation procedures: application to induced seismicity in the Groningen gas field." *Bulletin of Earthquake Engineering*, Springer Netherlands, 17(8), 4539–4557, doi.org/10.1007/s10518-018-0489-3.

Green, R. A., Bommer, J. J., Stafford, P. J., Maurer, B. W., Kruiver, P. P., Edwards, B., Rodriguez-Marek, A., de Lange, G., Oates, S. J., Storck, T., Omidi, P., Bourne, S. J., and van Elk, J. (2020). "Liquefaction Hazard in the Groningen Region of the Netherlands due to Induced Seismicity." *Journal of Geotechnical and Geoenvironmental Engineering*, 146(8), 04020068, doi.org/10.1061/(asce)gt.1943-5606.0002286.

Green, R. A., Maurer, B. W., and Haskell, A. (2017). *Development of Probabilistic Magnitude-Bound Curves for the New Madrid Seismic Zone (NMSZ) for Paleoliquefaction Studies*. U.S. Geological Society Technical Report G14AP00046, U.S. Geological Survey, Reston, VA.

Grigoratos, I., Bazzurro, P., Rathje, E., and Savvaidis, A. (2021). "Time-dependent seismic hazard and risk due to wastewater injection in Oklahoma." *Earthquake Spectra*, 875529302098802, doi.org/10.1177/8755293020988020.

Grigoratos, I., Rathje, E., Bazzurro, P., and Savvaidis, A. (2020a). "Earthquakes Induced by Wastewater Injection, Part I: Model Development and Hindcasting." *Bulletin of the Seismological Society of America*, 110(5), 2466–2482, doi.org/10.1785/0120200078.

Grigoratos, I., Rathje, E., Bazzurro, P., and Savvaidis, A. (2020b). "Earthquakes Induced by Wastewater Injection, Part II: Statistical Evaluation of Causal Factors and Seismicity Rate Forecasting." *Bulletin of the Seismological Society of America*, 110(5), 2483–2497, doi.org/10.1785/0120200079.

Gutenberg, B., and Richter, C. F. (1956). “Earthquake magnitude, intensity, energy, and acceleration: (Second paper).” *Bulletin of the Seismological Society of America*, 46(2), 105–145.

Hassani, B., and Atkinson, G. M. (2015). “Referenced Empirical Ground-Motion Model for Eastern North America.” *Seismological Research Letters*, 86(2A), 477–491, doi.org/10.1785/0220140156.

Hornsby, K. T., Streig, A. R., Bennett, S. E. K., Chang, J. C., and Mahan, S. (2020). “Neotectonic and Paleoseismic Analysis of the Northwest Extent of Holocene Surface Deformation along the Meers Fault, Oklahoma.” *Bulletin of the Seismological Society of America*, 110(1), 49–66, doi.org/10.1785/0120180148.

Hough, S. E. (2014). “Shaking from injection-induced Earthquakes in the central and eastern United States.” *Bulletin of the Seismological Society of America*, 104(5), 2619–2626, doi.org/10.1785/0120140099.

Ishibashi, I., and Zhang, X. (1993). “Unified dynamic shear moduli and damping ratios of sand and clay.” *Soils and Foundations*, 33(1), 182–191, doi.org/10.3208/sandf1972.33.182.

Iwasaki, T., Tatsuoka, F., Tokida, K., and Yasuda, S. (1978). “A practical method for assessing soil liquefaction potential based on case studies at various sites in Japan.” *Proceedings of 2nd International Conference on Microzonation*, National Science Foundation, Washington, DC.

Kramer, S. L., and Mayfield, R. T. (2007). “Return period of soil liquefaction.” *Journal of Geotechnical and Geoenvironmental Engineering*, 133(7), 802–813, doi.org/10.1061/(ASCE)1090-0241(2007)133:7(802).

Langenbruch, C., and Zoback, M. D. (2016). “How will induced seismicity in Oklahoma respond to decreased saltwater injection rates?” *Science Advances*, 2(e1601542), 1–9, doi.org/10.1126/sciadv.1601542.

Lasley, S. J., Green, R. A., and Rodriguez-Marek, A. (2016). “New Stress Reduction Coefficient Relationship for Liquefaction Triggering Analyses.” *Journal of Geotechnical and Geoenvironmental Engineering*, 142(11), 06016013, doi.org/10.1061/(ASCE)GT.1943-5606.0001530.

Lasley, S. J., Green, R. A., and Rodriguez-Marek, A. (2017). “Number of Equivalent Stress

Cycles for Liquefaction Evaluations in Active Tectonic and Stable Continental Regimes." *Journal of Geotechnical and Geoenvironmental Engineering*, 143(4), 04016116, doi.org/10.1061/(ASCE)GT.1943-5606.0001629.

Maurer, B. W., Green, R. A., Cubrinovski, M., and Bradley, B. A. (2015a). "Assessment of CPT-based methods for liquefaction evaluation in a liquefaction potential index framework." *Géotechnique*, 65(5), 328–336, doi.org/10.1680/geot.SIP.15.P.007.

Maurer, B. W., Green, R. A., and Taylor, O. D. S. (2015b). "Moving towards an improved index for assessing liquefaction hazard: Lessons from historical data." *Soils and Foundations*, 55(4), 778–787, doi.org/10.1016/j.sandf.2015.06.010.

Musson, R. M. W. (1998). "The Barrow-in-Furness Earthquake of 15 February 1865: Liquefaction from a Very Small Magnitude Event." *Pure and Applied Geophysics*, 152(4), 733–745, doi.org/10.1007/s000240050174.

Novakovic, M., Atkinson, G. M., and Assatourians, K. (2018). "Empirically Calibrated Ground-Motion Prediction Equation for Oklahoma." *Bulletin of the Seismological Society of America*, 108(5A), 2444–2461, doi.org/10.1785/0120170331.

Oklahoma Office of the Secretary of Energy & Environment. (2019). "Earthquakes in Oklahoma: What We Know." <https://earthquakes.ok.gov/what-we-know/> (Jun. 20, 2019).

Quick, T. J., Green, R. A., Rathje, E. M., and Mitchel, J, K. (2021). *Evaluating Liquefaction Triggering Potential from Induced Seismicity*. U.S. Geologic Survey Grant G18AP00094, U.S. Geologic Survey, Reston, VA.

Robertson, P. K., and Cabal, K. L. (2015). *Guide to Cone Penetration Testing for Geotechnical Engineering*. Gregg Drilling & Testing, Inc., Signal Hill, CA.

Rodriguez-Arriaga, E., and Green, R. A. (2018). "Assessment of the cyclic strain approach for evaluating liquefaction triggering." *Soil Dynamics and Earthquake Engineering*, Elsevier Ltd, 113(May), 202–214, doi.org/10.1016/j.soildyn.2018.05.033.

Seed, H. B., and Idriss, I. M. (1971). "Simplified procedure for evaluating soil liquefaction potential." *Journal of Geotechnical Engineering*, 97(9), 1249–1273.

Stewart, J. P., Parker, G. A., Harmon, J. A., Atkinson, G. M., Boore, D. M., Darragh, R. B., Silva, W. J., and Hashash, Y. M. A. (2017). *Expert Panel Recommendations for Ergodic Site Amplification in Central and Eastern North America, PEER Report 2017/04. Peer Report No. 2017/04*, Pacific Earthquake Engineering Research Center, Berkeley, CA.

Tiwari, A., and Rathje, E. M. (2018). “Engineering characteristics of earthquake motions from the Pawnee and Cushing Earthquakes in Oklahoma.” *Proceedings of Geotechnical Earthquake Engineering and Soil Dynamics V (GEESD V): Seismic Hazard Analysis, Earthquake Ground Motions, and Regional-Scale Assessment*, GSP 291, American Society of Civil Engineers, Reston, VA, 378–386.

U.S. Bureau of Reclamation. (2002). *Appraisal-Level Probabilistic Ground Motion Evaluation for the Upper San Joaquin River Basin Investigation, Central Valley Project, California.* Technical Memorandum No. D-8330-2002-10, United States Department of the Interior, Bureau of Reclamation, Technical Service Center, Seismotectonics and Geophysics Group, Denver, CO., doi.org/10.1017/9781139629010.006.

U.S. Geologic Survey. (2020). “Oklahoma Has Had a Surge of Earthquakes since 2009. Are They Due to fracking?” <https://www.usgs.gov/faqs/oklahoma-has-had-a-surge-earthquakes-2009-are-they-due-fracking?qt-news_science_products=0#qt-news_science_products>.

Ulmer, K. J., Green, R. A., and Rodriguez-Marek, A. (2020). “A Consistent Correlation between V s , SPT, and CPT Metrics for Use in Liquefaction Evaluation Procedures.” *Proceedings of Geo-Congress 2020*, American Society of Civil Engineers, Reston, VA, 132–140, doi.org/10.1061/9780784482810.015.

Whitman, R. V. (1971). “Resistance of Soil to Liquefaction and Settlement.” *Soils and Foundations*, 11(4), 59–68.

Zalachoris, G., He, J., and Rathje, E. (2020). “Earthquake Time Series from Events in Texas, Oklahoma, and Kansas.” DesignSafe-CI, doi.org/10.17603/ds2-v310-qc53.

Zalachoris, G., and Rathje, E. M. (2019). “Ground Motion Model for Small-to-Moderate Earthquakes in Texas, Oklahoma, and Kansas.” *Earthquake Spectra*, 35(1), 1–20, doi.org/10.1193/022618EQS047M.

5 Conclusion

The first objective of this research was to develop a framework for assessing liquefaction potential associated with deep wastewater injection-induced earthquakes in Oklahoma, Texas, and Kansas (OTK). Development and testing of this model are discussed in Manuscripts 1 and 2, presented in Chapters 2 and 3, respectively. The second objective of this research was to determine the minimum magnitude (M_{min}) threshold required for assessing regional liquefaction hazard for induced events in OTK and for performing probabilistic liquefaction hazard analyses (PLHA) for these events. Determination of M_{min} thresholds for both induced and tectonic events is discussed in Manuscript 3, presented in Chapter 4. Key findings of the three manuscripts include:

1. The new liquefaction triggering model presented herein can be used to evaluate liquefaction triggering potential associated with deep wastewater injection-induced earthquakes in OTK. This model incorporates new depth-stress reduction factor (r_d) and Magnitude Scaling Factor (MSF) relationships specific to induced events in OTK. The new r_d and MSF relationships can be used to compute normalized cyclic stress ratio (CSR*) in the context of the stress-based simplified procedure. The resulting CSR* can be used in conjunction with the normalized cyclic resistance ratio ($CRR_{M7.5}$) curves from Green et al. (2019) to estimate liquefaction triggering potential for induced earthquakes in OTK.
2. The r_d relationship developed herein for induced events in OTK predicts lower values of r_d than the models developed for tectonic earthquakes. This is consistent with observations by Novakovic et al. (2018) that, for larger earthquakes, induced earthquake ground motions tend to be richer in high-frequency content than tectonic earthquakes. These high frequency motions lead to less rigid soil column response and, hence, lower r_d. Magnitude (M_w), time-weighted average small-strain shear wave velocity of the upper 12 m (V_{s12}), and peak ground acceleration (a_{max}) were found to be significant predictors of r_d. Predicted r_d increases with increasing M_w and V_{s12} but decreases with increasing a_{max}.
3. The MSF relationship developed for induced events in OTK predicts lower values of MSF than relationships developed for tectonic earthquakes. This is consistent with the

observations of Boore and Thompson (2015) that ground motion duration tends to increase much more rapidly with distance in the CEUS than in the WUS. MSF for OTK was found to increase with increasing a_{max} and decrease with increasing M_w and increasing hypocentral distance (R_{hyp}). MSF in OTK exhibits scaling breaks for relatively large values of a_{max} ($a_{max} > 0.25g$) and for relatively large values of R_{hyp} ($R_{hyp} > 35$ km).

4. Liquefaction potential at three sites impacted by the 3 Sep 2016, M_w5.8 Pawnee, OK, induced earthquake was assessed using the new OTK induced seismicity-specific liquefaction triggering model, as well as several procedures commonly used to evaluate liquefaction potential for tectonic earthquakes. At most locations evaluated, predictions of liquefaction severity made using the new liquefaction triggering model were more consistent with field observations of liquefaction than predictions made using existing models. The models developed for tectonic earthquakes over-predicted the severity of liquefaction for the Pawnee earthquake. While the new model slightly under-predicted liquefaction severity at some Pawnee test sites, it generally provided accurate predictions of liquefaction severity at the Pawnee test locations.
5. Accounting for the observed differences in liquefaction triggering potential for induced and tectonic earthquakes is important when considering seismic design and policy in areas subject to induced seismicity. Because existing methods used to assess the liquefaction triggering potential of tectonic earthquakes tend to over-predict the liquefaction potential for a given induced earthquake, use of traditional liquefaction triggering models in design may lead to over-conservatism in design and increased costs required for liquefaction mitigation. It is important to note, however, that while the findings of this study show that the liquefaction potential from induced earthquakes is less than from tectonic earthquakes, the overall risk of liquefaction in areas currently experiencing liquefaction may still be higher than historic levels due to the increased rate of induced seismicity in these areas.
6. For sites capable of supporting building structures, $M_{min} = 5.0$ was sufficient to fully capture liquefaction hazard for both tectonic and induced seismic sources. For "extremely susceptible" sites that may be of relevance to other infrastructure (e.g., pipelines or levees), $M_{min} = 4.5$ is recommended when considering tectonic sources. These findings are in accord with previous recommendations regarding M_{min} for PLHA for tectonic

events. In contrast, the results from this study suggest that consideration of M_{min} as low as 4.0 may be required to fully capture the liquefaction hazard due to induced earthquakes at extremely susceptible sites in OTK. However, there has been no historical evidence of liquefaction occurring during numerous tectonic or induced events with $M_w < 4.5$ in this region. As a result, and because the use of $M_{min} < 4.5$ results in only minor changes to the estimated liquefaction hazard, $M_{min} = 4.5$ may still be sufficient for evaluating liquefaction hazard at these sites due to induced earthquakes.

Recommendations for future research include:

1. This research considered liquefaction potential from deep wastewater injection-induced earthquakes in a single case study area (i.e., OTK). As confirmed in this study, relationships for r_d and MSF vary by region and seismic source. As a result, research into liquefaction potential from induced earthquakes generated by other human activities or occurring in other regions is also needed.
2. The analysis framework used herein to develop the liquefaction triggering model for induced earthquakes in OTK can also be used to develop triggering models for tectonic earthquakes in regions different than those modeled by existing variants of the simplified procedure. This includes stable continental regions, which may not be modeled accurately by existing variants developed for active tectonic regions (e.g., California).
3. As noted in Manuscript 1, MSF for induced events in OTK was found to be lower than predicted by the Green et al. (2017) MSF relationship for tectonic events in the CEUS. As discussed in this paper, the majority of the ground motions used to develop the Green et al. (2017) CEUS model were scaled from WUS ground motions using state-of-the-art methods (McGuire et al. 2001). However, the scaling procedures used were likely focused on scaling for spectral amplitude as opposed to duration. This may explain why MSF for the Green et al. (2017) CEUS model were closer to MSF predicted by the Green et al. (2017) WUS model than to MSF for induced events in OTK. Developing a new MSF relationship for tectonic events in the CEUS based only on recorded motions may result in MSF that are more representative of durational trends in the CEUS than the WUS.

Appendix A. Contents of Appendices

Appendix B. Supplemental Figures for Manuscript #1

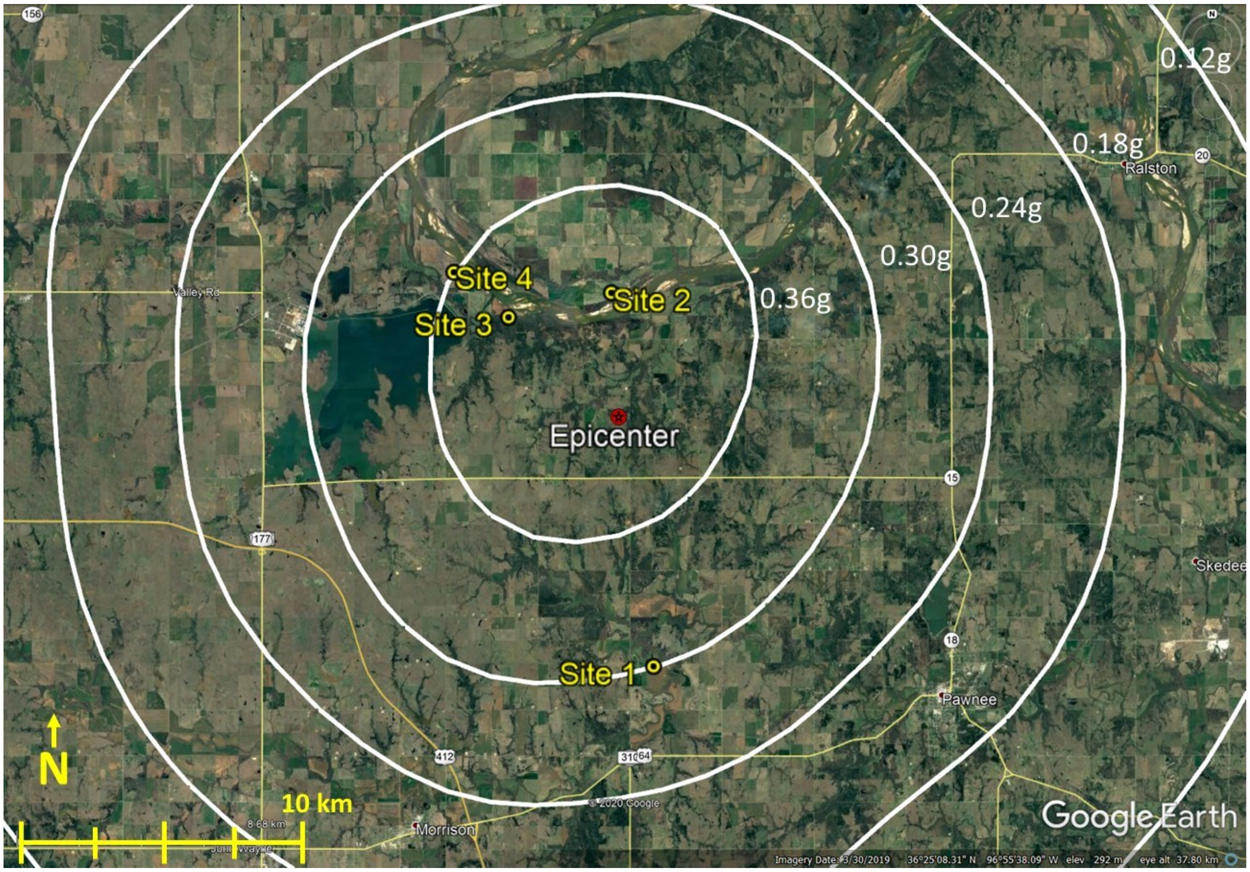

Figure B.1. USGS ShakeMap for 2016 M_w5.8 Pawnee, OK earthquake showing contours of inferred peak ground acceleration. Liquefaction Sites 1,2, 3, and 4, identified by Clayton et al. (2016) and Kolawole et al. (2017), are also indicated. Aerial imagery source: Google Earth, imagery date 3/30/2019, date accessed 10/7/2020.

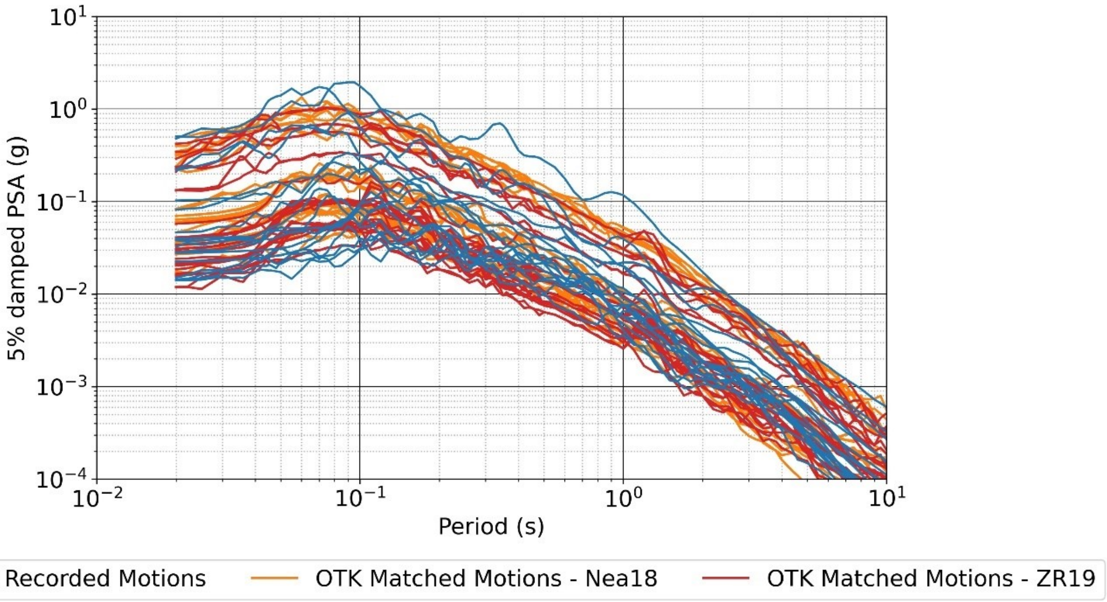

Figure B.2. Comparison of pseudo-spectral response spectra for recorded OTK ground motions and motions spectrally matched to spectra based on the Novakovic et al. (2018) [Nea18] and Zalachoris and Rathje (2019) [ZR19] GMPEs.

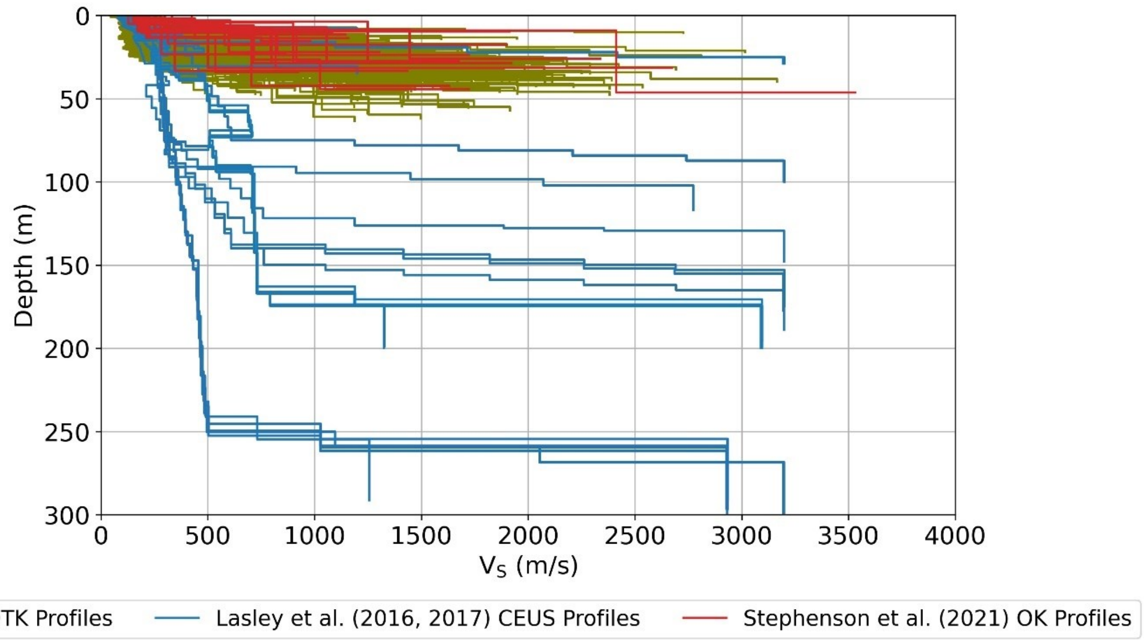

Figure B.3. Comparison of the Oklahoma, Texas, and Kansas (OTK), Lasley et al. (2016) CEUS, and Stephenson et al. (2021) V_s profiles.

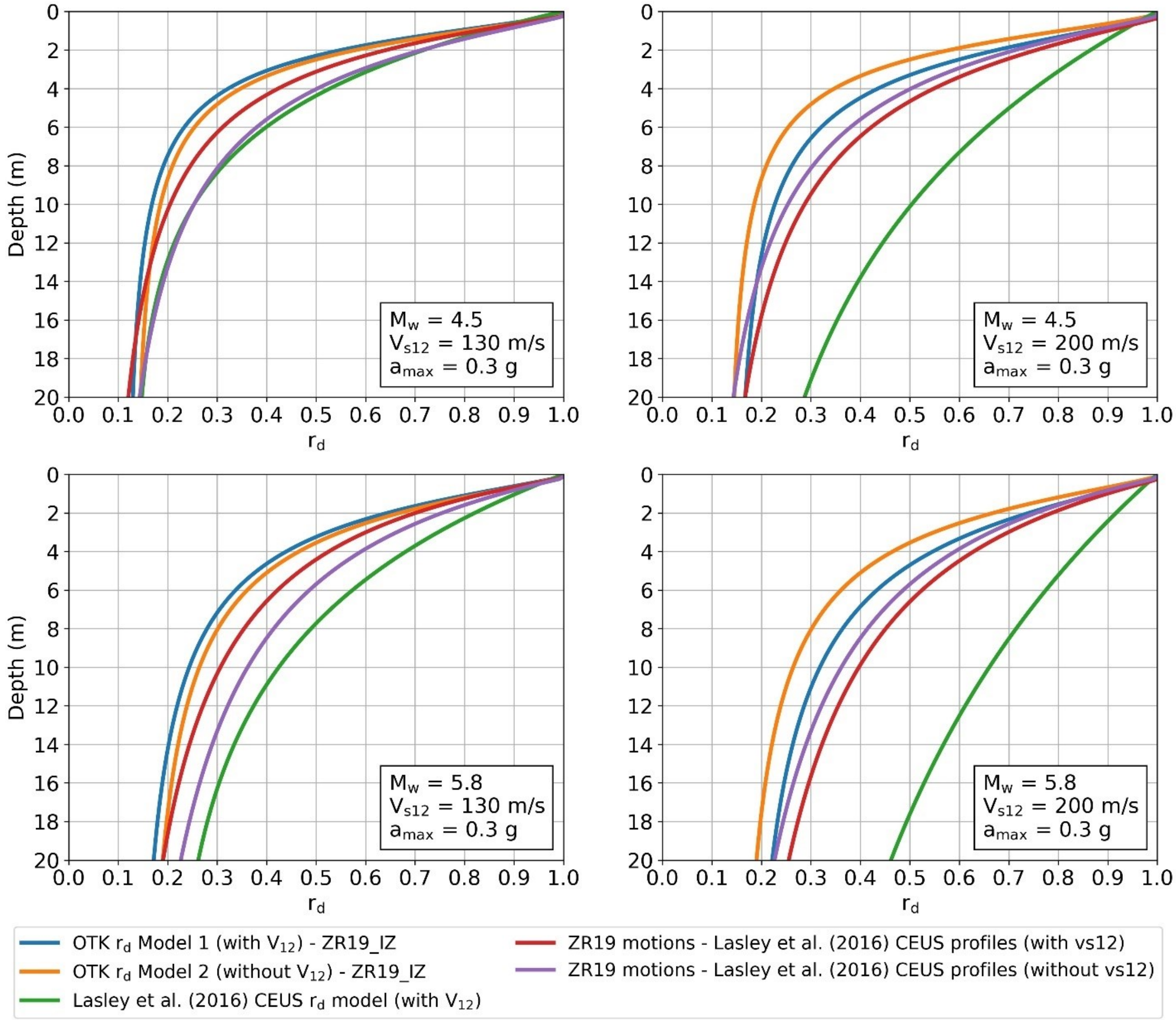

Figure B.4. Comparison of OTK r_d Models 1 and 2 to r_d models developed using the OTK ground motions and Lasley et al. (2016, 2017) site profiles. Results are shown for the ZR19_IZ ground motion dataset. The Lasley et al. (2016) CEUS r_d relationship is also shown.

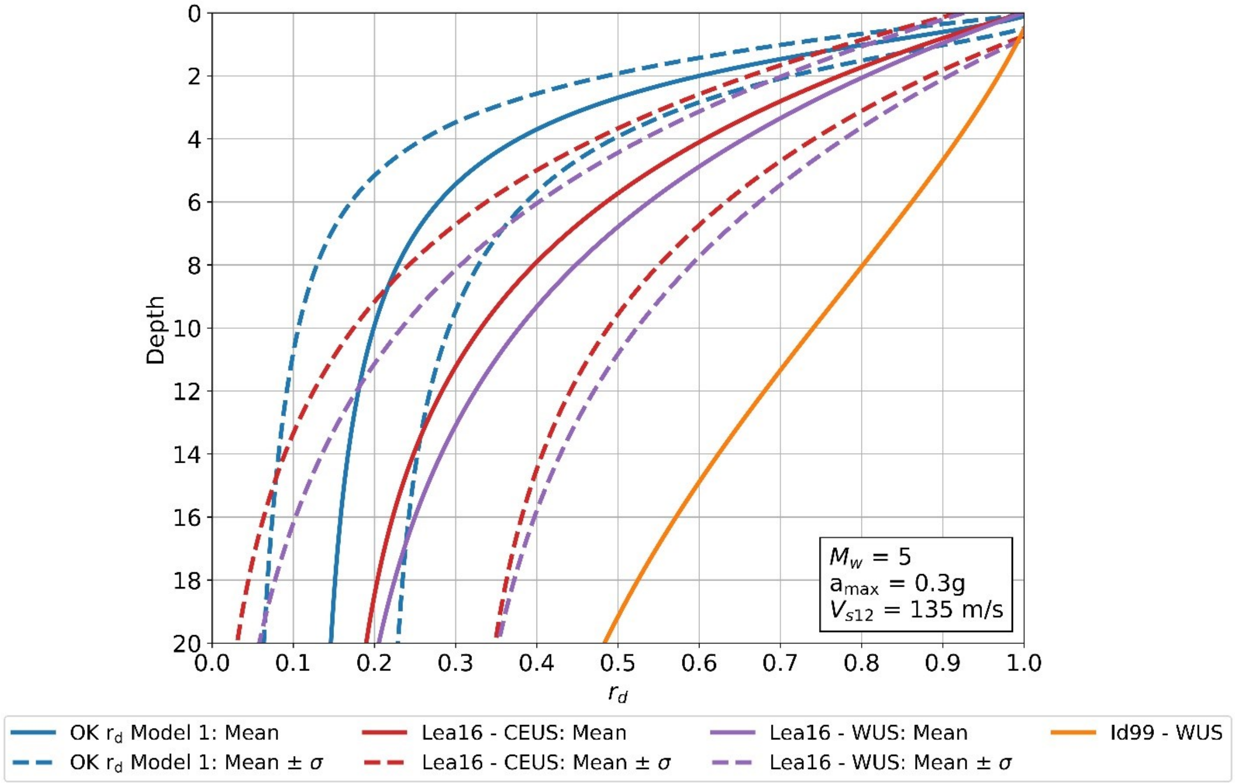

Figure B.5. Comparison of Oklahoma r_d Model 1 from the current study and the r_d relationships proposed by Lasley et al. (2016) [Lea16] for the CEUS and WUS and by Idriss (1999) [I99] for the WUS. Estimates are shown for $M_w = 5.0$, $a_{max} = 0.3g$, and $V_{s12} = 135$ m/s. Mean and mean plus/minus one standard deviation curves are shown for the OK and Lea16 models. Oklahoma model estimates are based on the ZR19_IZ dataset.

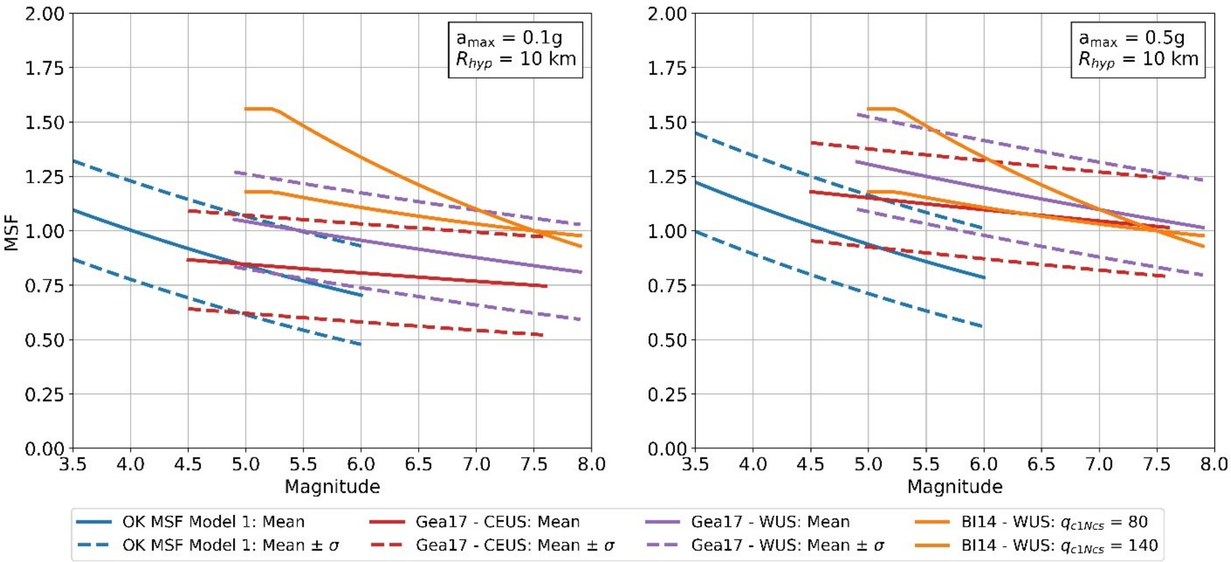

Figure B.6. Comparison of Oklahoma MSF Model 1 from the current study and the MSF relationships proposed by Green et al. (2017) [Gea17] for the CEUS and WUS and by Boulanger and Idriss (2014) [BI14] for the WUS. Estimates are shown for a_{max} = 0.1g and 0.3g, and for R_{hyp} = 10 km. Mean and mean plus/minus one standard deviation curves are shown for the OK and Gea17 models. Curves for the BI14 model are shown for q_{c1Ncs} = 80 and 140 atm. Oklahoma model estimates are based on the ZR19_IZ dataset.

Appendix C. Comparison of rd and MSF Relationships for Different Regression Datasets

The r_d and MSF relationships presented herein are developed based on the results of equivalent-linear site response analyses performed using induced ground motions and representative regional soil profiles. Separate site response analyses are performed using both the Darendeli and Stokoe (2001) and Ishibashi and Zhang (1993) shear modulus reduction and damping degradation (MRD) curves. These curves are used in site response analysis to model the nonlinear response of the soil. The results from analyses using the two different MRD curves are compared to see the effect of MRD on the resulting r_d and n_{eq} relationships. Separate site response analyses are also performed using two induced ground motion catalogs discussed herein. Both datasets include recorded ground motions from Zalachoris et al. (2020). In addition, one catalog included ground motions scaled using the Zalachoris and Rathje (2019) GMPE, and the second catalog included ground motions scaled using the Novakovic et al. (2018) GMPE. This resulted in four sets of site response analysis results developed using: (1) the Zalachoris and Rathje (2019) ground motion database with Ishibashi and Zhang (1993) MRD curves (referred to as the ZR19_IZ dataset), (2) the Zalachoris and Rathje (2019) ground motion database with Darendeli and Stokoe (2001) MRD curves (ZR19_DS dataset), (3) the Novakovic et al. (2018) ground motion database with Ishibashi and Zhang (1993) MRD curves (Nea18_IZ dataset), and (4) the Novakovic et al. (2018) ground motion database with Darendeli and Stokoe (2001) MRD curves (Nea18_DS dataset). Separate r_d, n_{eq}, and MSF relationships are developed for each dataset to account for the effects of MRD and GMPE selection on the regressed relationships.

The ZR19 GMPE predicts spectra based on rotation-angle independent geometric average of horizontal ground-motion amplitudes (RotD50) (Boore 2010), while the Nea18 GMPE predicts spectra for the geometric mean of the horizontal components of motion. However, RotD50 amplitudes are typically very similar to geometric mean amplitudes (Novakovic et al. 2018), which allows for direct comparisons between the two GMPEs.

Comparison plots for r_d Model 1 and Model 2 for the ZR19_IZ, ZR19_DS, Nea18_IZ, and Nea18_DS datasets are provided in Figure C.1. Overall trends with depth are similar for the four models, particularly relative to the Lasley et al. (2016) and Idriss (1999) models. However, predicted r_d for the ZR19 datasets tends to be higher than for the Nea18 datasets. The ZR19 estimates for the M_w, a_{max}, and V_{s12} range values shown are approximately 0-12% higher than the Nea18 estimates. The differences in estimated r_d tend to increase with M_w and depth, decrease with increasing a_{max}, and remain constant with changes in V_{s12}. Differences are also noted when comparing r_d estimates for the IZ and DS MRD datasets. For a_{max} = 0.5g, estimated r_d for the DS datasets tend to be 10-15% larger than the IZ datasets for depths less than approximately 6 m but approximately 5% smaller for depths greater than 6 m. For a_{max} = 0.1g, predictions are similar for DS and IZ at shallow depths, but estimates for the IZ datasets are 2-10% higher for depths greater than 6 m. The observed differences tend to increase with increases in M_w and decrease with increases in V_{s12}. While the impact of MRD and GMPE selection on r_d tends to be small, the additional uncertainty resulting from MRD and GMPE selection should be considered in analysis.

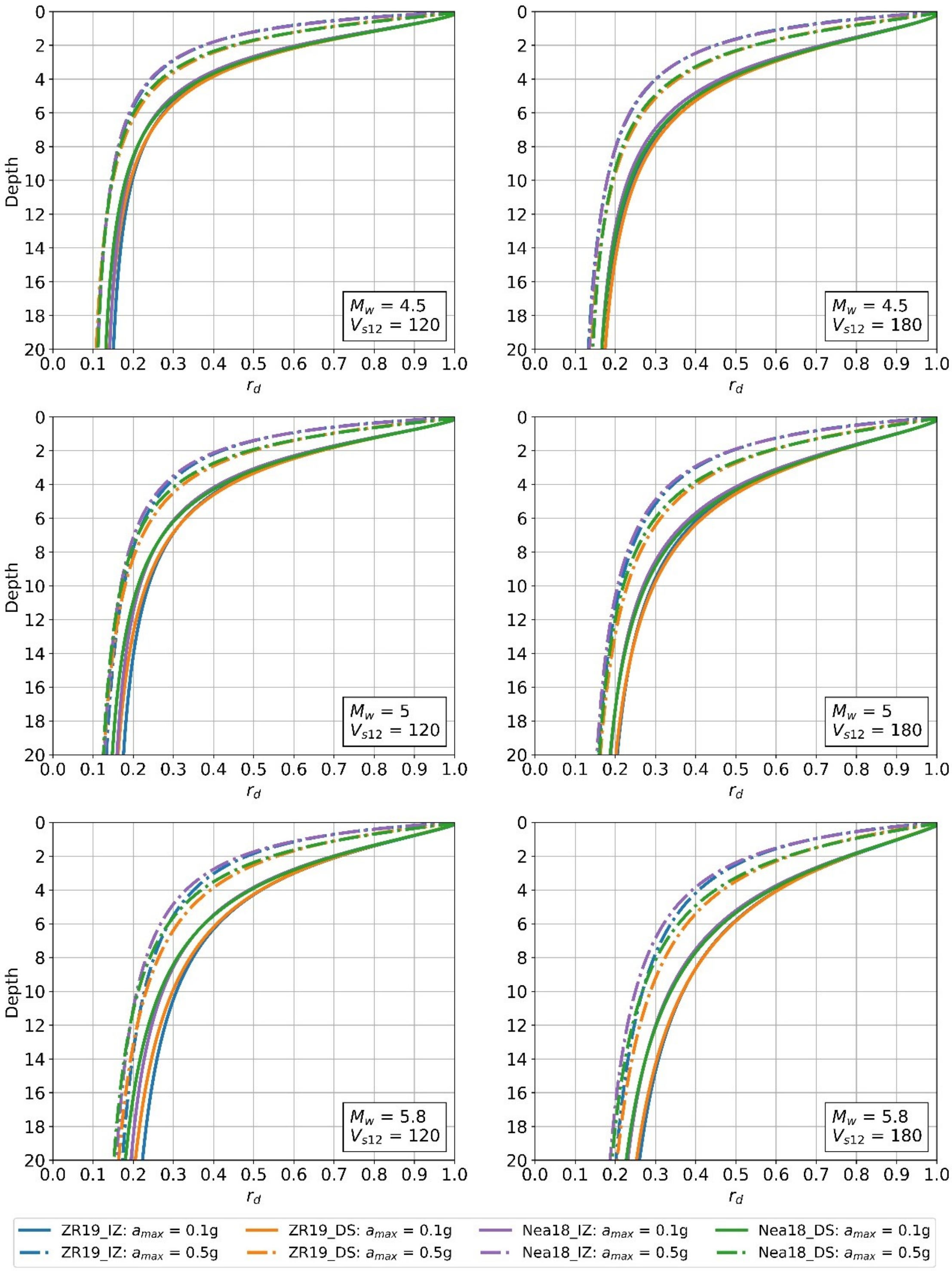

Figure C.1. Comparison of r_d Model 1 for the ZR19_IZ, ZR19_DS, Nea18_IZ, and Nea18_DS Datasets. Curves are shown for M_w = 4.5, 5.0, and 5.8; a_{max} = 0.1g and 0.5g; and V_{s12} = 120 m/s and 180 m/s.

Figure C.2 shows a comparison of the regressed MSF models for each of the four datasets used in this study. Curves are shown for R_{hyp} = 10 km and 30 km and for a_{max} = 0.1g and 0.5g. As shown in this figure, the four datasets result in very similar regressed MSF models. For MSF Model 1, the ZR19 dataset and IZ MRD curves tend to result in slightly lower MSF for $M_w \lesssim 4.5$ and slightly higher values for $M_w \gtrsim 4.5$. The maximum observed difference between the models (i.e., comparing ZR19_IZ to Nea18_DS) is approximately 7%. For Model 2, the Nea18 dataset and DS MRD result in slightly higher MSF for a_{max} = 0.5g and $M_w \lesssim 5$, with a maximum observed difference of approximately 5%. For a_{max} = 0.5g and $M_w > 5$, as well as for a_{max} = 0.1g, predictions for all four datasets are within 1-2%. The effect of MRD and GMPE selection on MSF is smaller than for r_d. However, it should still be considered when performing analyses using these MSF relationships.

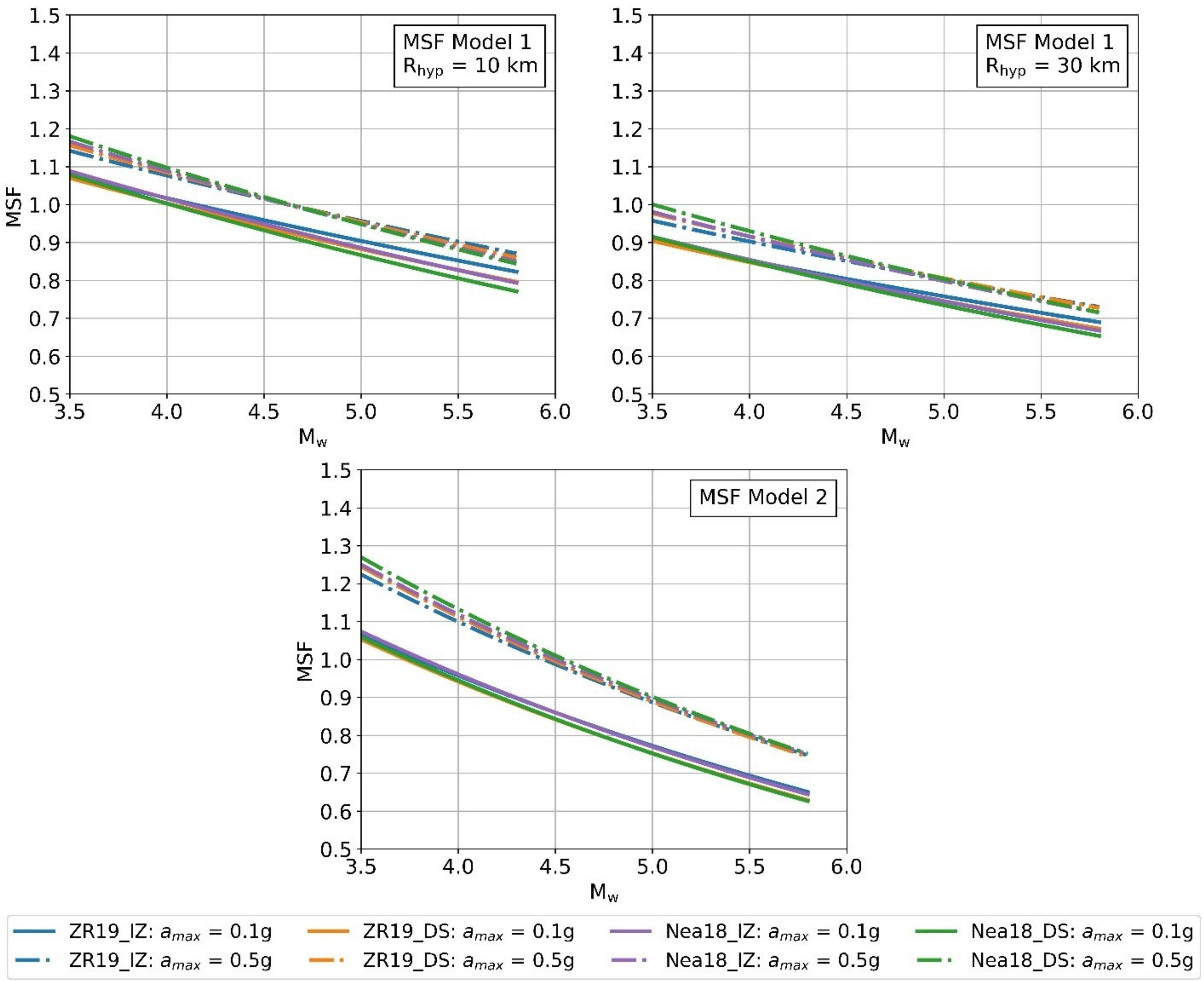

Figure C.2. Comparison of MSF models for the ZR19_IZ, ZR19_DS, Nea18_IZ, and Nea18_DS Datasets. Curves for Model 1 are shown for R_{hyp} = 10 km and 30 km. Curves for both models are shown for a_{max} = 0.1g and 0.5g.

Appendix D. Python Scripts for Induced Seismicity-Specific rd and MSF Relationships

```
# -*- coding: utf-8 -*-
"""
Created on Mon Oct 26 14:40:56 2020

@author: Tyler Quick

rd Function:
rd_OTK(depth, Mag, amax, vs12, dataset = 'ZR19_IZ', model = 1)
    Outputs = rd, tau_event_rd, tau_profile_rd, sig_0_rd, sig_total_rd

MSF Function:
MSF_OK(coefs, b, Mag, amax, vs12, vsbed, hypd, dataset, model)
    Outputs = neq, MSF, tau_event_neq, tau_profile_neq, sig_0_neq,
                 sig_total_neq, sig_total_ln_MSF


"""
import pandas as pd
import numpy as np

def rd_OTK(depth, Mag, amax, vs12, dataset = 'ZR19_IZ', model = 1):

    ### Inputs

    # depth = Depth of interest (can be an array of depths)
    # Mag = Moment magnitude (Mw)
    # amax = Peak ground acceleration (units of g)
    # vs12 = Time-weighted average shear wave velocity (Vs) of the upper 12 m
        # of the profile (m/s)
    # dataset = GMPE and MRD used to create desired dataset.
        # Options: 'ZR19_IZ', 'ZR19_DS', 'Nea18_IZ', 'Nea18_DS'
        ## GMPEs: Zalachoris and Rathje (2019) and Novakovic et al. (2018)
        ## MRDs: Darendeli and Stokoe (2001) and Ishibashi and Zhang (1993)
        ## Defaults is "ZR19_IZ"
    # model = Desired rd model
        ## Options are '1' (includes Vs12) and '2' (does not include Vs12)

    # Model Coefficients for Model 1, Model 2, and Standard Deviation Model
    coefs_model_1 = pd.DataFrame([
        ['ZR19_DS', 0.9504, 0.02106, -1.1204, 0.05544, 0.05063, 0.03463,
         -0.01387, 0.003986, -0.01211, 0.0014337, 0.2283, 0.008446, 0.09263,
         0.00718, 0.1148, 0.02984, -0.0002179, 0.00008383, -0.147, 0.004163,
         0.004663, 0.0002191, 0.01109, 0.002086, 0.0547, 0.038],
        ['Nea18_DS', 0.9843, 0.02286, -1.2094, 0.05976, 0.00191, 0.03781,
         -0.02252, 0.00445, -0.01133, 0.0014482, 0.2536, 0.009438, 0.109,
         0.00788, 0.1365, 0.03208, -0.0001848, 0.00008515, -0.1452, 0.004199,
         -0.04787, 0.002915, -1.15, 0.09958, 0.7687, 0.1314, 0.004664,
         0.0002247, 0.01421, 0.002215, 0.057, 0.0379],
        ['ZR19_IZ', 0.9514, 0.02085, -0.9855, 0.05682, 0.03472, 0.03344,
         -0.00614, 0.003882, -0.00957, 0.0013634, 0.2261, 0.008375, 0.09936,
         0.00694, 0.0672, 0.017, -0.0003672, 0.00008361, -0.1237, 0.003993,
```

```
     -0.047108, 0.002723, -0.5747, 0.05256, 0.3977, 0.0574, 0.004568,
     0.0002289, 0.0099, 0.001998, 0.055, 0.036],
    ['Nea18_IZ', 0.9693, 0.02281, -1.0643, 0.05977, -0.03643, 0.03706,
     -0.01079, 0.004339, -0.00911, 0.0013855, 0.248, 0.009193, 0.121,
     0.00789, 0.0981, 0.01862, -0.0003404, 0.00008582, -0.1228, 0.004088,
     -0.04516, 0.002719, -0.5665, 0.05083, 0.448, 0.0625, 0.004556,
     0.0002346, 0.01367, 0.002105, 0.0574, 0.0355]],
    columns = ['Dataset', 'a1', 'sig_a1', 'a2', 'sig_a2', 'a3', 'sig_a3',
               'a4', 'sig_a4', 'a5', 'sig_a5', 'a6', 'sig_a6', 'a7',
               'sig_a7', 'a8', 'sig_a8', 'a9', 'sig_a9', 'a10','sig_a10',
               'a11', 'sig_a11', 'a12', 'sig_a12', 'a13', 'sig_a13',
               'a14', 'sig_a14', 'theta_rd', 'sig_theta_rd', 'tau_event',
               'tau_profile'])

coefs_model_2 = pd.DataFrame([
    ['ZR19_DS', 0.9147, 0.01842, -0.4313, 0.04749, 0.04963, 0.03562,
     -0.01573, 0.004114,  -0.01027, 0.001406, 0.2242, 0.008863, 0.09009,
     0.00736, 0.1507, 0.03222, -0.1435, 0.004378, -0.04905, 0.002899,
     -1.0219, 0.10696, 0.7772, 0.1385, 0.00856, 0.002188, 0.0548,0.0456],
    ['Nea18_DS', 0.9545, 0.02133, -0.5251, 0.04971, 0.00539, 0.03883,
     -0.02466, 0.004746, -0.00944, 0.001452, 0.2502, 0.009666, 0.10522,
     0.00816, 0.1757, 0.03564, -0.1421, 0.004236, -0.04675, 0.003002,
     -1.0755, 0.10234, 0.8222, 0.1446, 0.01145, 0.002227, 0.0570,0.0449],
    ['ZR19_IZ', 0.8939, 0.01842, -0.3243, 0.04541, 0.02729, 0.03341,
     -0.00802, 0.004148, -0.00838, 0.001364, 0.2240, 0.008755, 0.09814,
     0.00702, 0.0853, 0.01713, -0.1218, 0.004075, -0.04671, 0.002757,
     -0.5377, 0.05543, 0.4162, 0.0605, 0.00855, 0.002181, 0.0551,0.0445],
    ['Nea18_IZ', 0.9172, 0.01989, -0.4058, 0.04927, -0.03972, 0.03740,
     -0.01321, 0.004545, -0.00806, 0.001320, 0.2462, 0.009936, 0.11846,
     0.00796, 0.1148, 0.01837, -0.1210, 0.003851, -0.04499, 0.002778,
     -0.5309, 0.05019, 0.4628, 0.0610, 0.01209, 0.002203,0.0574,0.0437]],
    columns = ['Dataset', 'b1', 'sigma_b1', 'b2', 'sigma_b2', 'b3',
               'sigma_b3', 'b4', 'sigma_b4', 'b5', 'sigma_b5', 'b6',
               'sigma_b6', 'b7', 'sigma_b7', 'b8', 'sigma_b8', 'b9',
               'sigma_b9', 'b10', 'sigma_b10', 'b11', 'sigma_b11', 'b12',
               'sigma_b12', 'theta_rd', 'sigma_theta_rd', 'tau_event',
               'tau_profile'])

coefs_stdev_all = pd.DataFrame([
    [1,'ZR19_DS',0.0537,6.0516, 0.0647, -0.3607, 1.0243, -0.9984,1.6515],
    [1,'Nea18_DS',0.0528,5.8068, 0.0682, -0.3412,1.0225, -0.9988,1.6857],
    [1,'ZR19_IZ',0.0493,6.2395, 0.0702, -0.3217, 1.0324, -0.9536,1.5548],
    [1,'Nea18_IZ',0.0498,6.0594, 0.072, -0.3126, 1.0316, -0.9598,1.561],
    [2,'ZR19_DS',0.0521,5.8598, 0.0702, -0.3411, 1.0268, -1.1561,1.5023],
    [2,'Nea18_DS',0.0529,5.7001, 0.0716, -0.3322,1.0261, -1.1574,1.5126],
    [2,'ZR19_IZ',0.0498,6.4478, 0.0687, -0.339, 1.0366, -1.1536,1.3749],
    [2,'Nea18_IZ',0.0504,6.2425, 0.0714,0.3207, 1.0364, -1.1525,1.3777]],
    columns = ['Model', 'Dataset', 'c1', 'c2', 'c3','c4','c5','c6','c7'])

# Convert depth to array if single depth is entered
if (isinstance(depth, float) or isinstance(depth, int)):
    depth = np.array([depth])

amaxbreak = 0.25 # scaling break in amax

# Import coefficients for selected model and calculate alpha, beta, gamma
if model == 1:
```

```
    coefs = coefs_model_1[coefs_model_1.Dataset.str.contains(dataset)]
    coefs_std = coefs_stdev_all[(coefs_stdev_all.Dataset == dataset)]
    coefs_std = coefs_std[coefs_std.Model == model]

    a1 = coefs['a1'].values[0]
    a2 = coefs['a2'].values[0]
    a3 = coefs['a3'].values[0]
    a4 = coefs['a4'].values[0]
    a5 = coefs['a5'].values[0]
    a6 = coefs['a6'].values[0]
    a7 = coefs['a7'].values[0]
    a8 = coefs['a8'].values[0]
    a9 = coefs['a9'].values[0]
    a10 = coefs['a10'].values[0]
    a11 = coefs['a11'].values[0]
    a12 = coefs['a12'].values[0]
    a13 = coefs['a13'].values[0]
    a14 = coefs['a14'].values[0]
    theta = coefs['theta_rd'].values[0]
    tau_event = coefs['tau_event'].values[0]
    tau_profile = coefs['tau_profile'].values[0]
    c1 = coefs_std['c1'].values[0]
    c2 = coefs_std['c2'].values[0]
    c3 = coefs_std['c3'].values[0]
    c4 = coefs_std['c4'].values[0]
    c5 = coefs_std['c5'].values[0]
    c6 = coefs_std['c6'].values[0]
    c7 = coefs_std['c7'].values[0]

    if amax <= amaxbreak:
        alpha_rd = a1 + a4*np.minimum(Mag,6.5) + a5*np.log(amax) +
                   a9*vs12
        beta_rd = a2 + a6*Mag + a10*np.log(amax) + a14*vs12
        gamma_rd = a3 + a7*Mag + a11*np.log(amax)
    elif amax > amaxbreak:
        alpha_rd = a1 + a4*np.minimum(Mag,6.5) + a5*np.log(amax) +
                   a8*np.log(amax/amaxbreak) + a9*vs12
        beta_rd = a2 + a6*Mag + a10*np.log(amax) +
                   a12*np.log(amax/amaxbreak) + a14*vs12
        gamma_rd = a3 + a7*Mag + a11*np.log(amax) +
                   a13*np.log(amax/amaxbreak)

else:
    coefs = coefs_model_2[coefs_model_2.Dataset.str.contains(dataset)]
    coefs_std = coefs_stdev_all[(coefs_stdev_all.Dataset == dataset)]
    coefs_std = coefs_std[coefs_std.Model == model]

    b1 = coefs['b1'].values[0]
    b2 = coefs['b2'].values[0]
    b3 = coefs['b3'].values[0]
    b4 = coefs['b4'].values[0]
    b5 = coefs['b5'].values[0]
    b6 = coefs['b6'].values[0]
    b7 = coefs['b7'].values[0]
    b8 = coefs['b8'].values[0]
    b9 = coefs['b9'].values[0]
    b10 = coefs['b10'].values[0]
```

```
    b11 = coefs['b11'].values[0]
    b12 = coefs['b12'].values[0]
    theta = coefs['theta_rd'].values[0]
    tau_event = coefs['tau_event'].values[0]
    tau_profile = coefs['tau_profile'].values[0]
    c1 = coefs_std['c1'].values[0]
    c2 = coefs_std['c2'].values[0]
    c3 = coefs_std['c3'].values[0]
    c4 = coefs_std['c4'].values[0]
    c5 = coefs_std['c5'].values[0]
    c6 = coefs_std['c6'].values[0]
    c7 = coefs_std['c7'].values[0]

    if amax <= amaxbreak:
        alpha_rd = b1 + b4*np.minimum(Mag,6.5) + b5*np.log(amax)
        beta_rd = b2 + b6*Mag + b9*np.log(amax)
        gamma_rd = b3 + b7*Mag + b10*np.log(amax)
    elif amax > amaxbreak:
        alpha_rd = b1 + b4*np.minimum(Mag,6.5) + b5*np.log(amax) +
                    b8*np.log(amax/amaxbreak)
        beta_rd = b2 + b6*Mag + b9*np.log(amax) +
                    b11*np.log(amax/amaxbreak)
        gamma_rd = b3 + b7*Mag + b10*np.log(amax) +
                    b12*np.log(amax/amaxbreak)

# Compute rd
rd = 1-alpha_rd/(1+np.exp(-(np.log(depth)-beta_rd)/gamma_rd))+theta
rd = np.minimum(rd, 1)

# Compute total standard deviation
sig_0_rd = np.zeros(len(depth))
tau_event_rd = np.zeros(len(depth))
tau_profile_rd = np.zeros(len(depth))

for i,val in enumerate(sig_0_rd):
    if depth[i] <= 3.5:
        sig_0_rd[i] = c5/(1+np.exp(-c7*(np.log(depth[i])-
                            c6)))*(c3/(1+np.exp(-c4*(3.5-c2)))+c1)
        tau_event_rd[i] = c5/(1+np.exp(-c7*(np.log(depth[i])-
                            c6)))*tau_event
        tau_profile_rd[i] = c5/(1+np.exp(-c7*(np.log(depth[i])-
                            c6)))*tau_profile
    else:
        sig_0_rd[i] = c3/(1+np.exp(-c4*(depth[i]-c2)))+c1
        tau_event_rd[i] = tau_event
        tau_profile_rd[i] = tau_profile

sig_total_rd = (sig_0_rd**2 + tau_event_rd**2 + tau_profile_rd**2)**0.5

#returns: rd, std dev of event random effect term, std dev of profile
           # random effect term, std dev of residual, total std dev

return rd, tau_event_rd, tau_profile_rd, sig_0_rd, sig_total_rd
```

```
def MSF_OTK(Mag, amax, hypd, b = 0.34, dataset = 'ZR19_IZ', model = 1):

    ### Inputs

    # Mag = Moment magnitude (Mw)
    # amax = Peak ground acceleration (units of g)
    # hypd = Hypocentral distance (km)
    # dataset = GMPE and MRD used to create desired dataset.
        # Options: 'ZR19_IZ', 'ZR19_DS', 'Nea18_IZ', 'Nea18_DS'
        ## GMPEs: Zalachoris and Rathje (2019) and Novakovic et al. (2018)
        ## MRDs: Darendeli and Stokoe (2001) and Ishibashi and Zhang (1993)
        ## Defaults is "ZR19_IZ"
    # model = Desired MSF model
        ## Options: '1' (includes Hypd) and '2' (does not include Hypd)

    # Model Coefficients for Model 1, Model 2, and Standard Deviation Model

    coefs_MSF_Mod1 = pd.DataFrame([
        ['ZR19_DS', -1.0483, 0.043, 0.4905, 0.00793, -0.3044, 0.00517,0.3504,
         0.0307, 0.03094, 0.000578, -0.0217, 0.000754, 0.5404, 0.1048,0.3717,
         0.6642],
        ['Nea18_DS', -0.7663, 0.0465, 0.4207, 0.00882, -0.2995, 0.00523,
         0.4023, 0.0269, 0.03146, 0.000574, -0.0222, 0.000749, 0.5238,0.1025,
         0.3725, 0.6508],
        ['ZR19_IZ', -1.1128, 0.0431, 0.5209, 0.00813, -0.3065,0.00516,0.2467,
         0.0236, 0.02952, 0.000584, -0.0203, 0.000752, 0.543, 0.1087,
         0.3682, 0.665],
        ['Nea18_IZ', -0.8634, 0.0458, 0.459, 0.0089, -0.3021, 0.00508,0.3019,
         0.0204, 0.03009, 0.000574, -0.0209, 0.000742, 0.5243, 0.1066,
         0.3691, 0.65]],
        columns = ['Dataset', 'd1', 'sigma_d1', 'd2', 'sigma_d2', 'd3',
                   'sigma_d3', 'd4', 'sigma_d4', 'd5', 'sigma_d5', 'd6',
                   'sigma_d6', 'tau_event_neq',
                   'tau_profile_neq', 'sigma_0_neq', 'sigma_ln_neq_OK'])

    coefs_MSF_Mod2 = pd.DataFrame([
        ['ZR19_DS', -2.104, 0.03901, 0.7658, 0.00616, -0.511, 0.00352,0.4642,
         0.03037, 0.5789, 0.1389, 0.3865, 0.7098],
        ['Nea18_DS', -1.9571, 0.04135, 0.733, 0.00675, -0.509,0.00354,0.5327,
         0.02712, 0.5715, 0.1368, 0.3877, 0.704],
        ['ZR19_IZ', -2.118, 0.03892, 0.7895, 0.00623, -0.5003,0.00346,0.3059,
         0.02273, 0.5781, 0.1384, 0.3819, 0.7065],
        ['Nea18_IZ', -2.0142, 0.04077, 0.7672, 0.00676, -0.4991, 0.00342,
         0.3771, 0.0202, 0.5669, 0.1364, 0.3832, 0.6978]],
        columns = ['Dataset', 'e1', 'sigma_e1', 'e2', 'sigma_e2', 'e3',
                   'sigma_e3', 'e4', 'sigma_e4', 'tau_event_neq',
                   'tau_profile_neq', 'sigma_0_neq', 'sigma_ln_neq_OK'])

    amaxbreak = 0.25
    hypdbreak = 35

    if model == 1:
        coefs = coefs_MSF_Mod1[coefs_MSF_Mod1.Dataset.str.contains(dataset)]

        d1 = coefs['d1'].values[0] # (Intercept)
        d2 = coefs['d2'].values[0] # Magnitude
        d3 = coefs['d3'].values[0] # ln(amax)
```

```
    d4 = coefs['d4'].values[0] # ln(amax/0.25)
    d5 = coefs['d5'].values[0] # Rhyp
    d6 = coefs['d6'].values[0] # Rhyp - 35 km
    tau_event_neq = coefs['tau_event_neq'].values[0]
    tau_profile_neq = coefs['tau_profile_neq'].values[0]
    sig_0_neq = coefs['sigma_0_neq'].values[0]
    sig_total_neq = coefs['sigma_ln_neq_OK'].values[0]

    if (isinstance(hypd, float) or isinstance(hypd, int)):
        if amax <= amaxbreak:
            if hypd <= hypdbreak:
                neq = np.exp(d1 + d2*Mag + d3*np.log(amax) + d5*hypd)
            else:
                neq = np.exp(d1 + d2*Mag + d3*np.log(amax) + d5*hypd +
                       d6*(hypd-hypdbreak))
        else:
            if hypd <= hypdbreak:
                neq = np.exp(d1 + d2*Mag + d3*np.log(amax) +
                       d4*np.log(amax/amaxbreak) + d5*hypd)
            else:
                neq = np.exp(d1 + d2*Mag + d3*np.log(amax) +
                       d4*np.log(amax/amaxbreak) + d5*hypd + d6*(hypd-
                       hypdbreak))

        MSF = np.minimum(2.04,(7.25/neq)**b)
    else:
        neq = np.zeros(len(hypd))
        MSF = np.zeros(len(hypd))
        for i,val in enumerate(hypd):
            if amax <= amaxbreak:
                if hypd[i] <= hypdbreak:
                    neq[i] = np.exp(d1 + d2*Mag + d3*np.log(amax) +
                              d5*hypd[i])
                else:
                    neq[i] = np.exp(d1 + d2*Mag + d3*np.log(amax) +
                              d5*hypd[i] + d6*(hypd[i]-hypdbreak))
            else:
                if hypd[i] <= hypdbreak:
                    neq[i] = np.exp(d1 + d2*Mag + d3*np.log(amax) +
                              d4*np.log(amax/amaxbreak) + d5*hypd[i])
                else:
                    neq[i] = np.exp(d1 + d2*Mag + d3*np.log(amax) +
                              d4*np.log(amax/amaxbreak) + d5*hypd[i] +
                              d6*(hypd[i]-hypdbreak))

            MSF[i] = np.minimum(2.04,(7.25/neq[i])**b)

    sig_total_ln_MSF = np.minimum(b*sig_total_neq,2.04)

else:

    coefs = coefs_MSF_Mod2[coefs_MSF_Mod2.Dataset.str.contains(dataset)]

    e1 = coefs['e1'].values[0] # (Intercept)
    e2 = coefs['e2'].values[0] # Magnitude
    e3 = coefs['e3'].values[0] # ln(amax)
    e4 = coefs['e4'].values[0] # ln(amax/0.25)
```

```
    tau_event_neq = coefs['tau_event_neq'].values[0]
    tau_profile_neq = coefs['tau_profile_neq'].values[0]
    sig_0_neq = coefs['sigma_0_neq'].values[0]
    sig_total_neq = coefs['sigma_ln_neq_OK'].values[0]

    if (isinstance(hypd, float) or isinstance(hypd, int)):
        if amax <= amaxbreak:
            neq = np.exp(e1 + e2*Mag + e3*np.log(amax))
        else:
            neq = np.exp(e1 + e2*Mag + e3*np.log(amax) +
                    e4*np.log(amax/amaxbreak))

        MSF = np.minimum(2.04,(7.25/neq)**b)
    else:
        neq = np.zeros(len(hypd))
        MSF = np.zeros(len(hypd))
        for i,val in enumerate(hypd):
            if amax <= amaxbreak:
                neq[i] = np.exp(e1 + e2*Mag + e3*np.log(amax))
            else:
                neq[i] = np.exp(e1 + e2*Mag + e3*np.log(amax) +
                          e4*np.log(amax/amaxbreak))

            MSF[i] = np.minimum(2.04,(7.25/neq[i])**b)

    sig_total_ln_MSF = np.minimum(b*sig_total_neq,2.04)

#returns: MSF, std dev of event random effect term, std dev of profile
          # random effect term, std dev of residual,
          # total std dev of neq, total std dev of MSF

return neq, MSF, tau_event_neq, tau_profile_neq, sig_0_neq,
         sig_total_neq, sig_total_ln_MSF
```

Appendix E. Supporting Documents for Liquefaction Hazard Evaluation at the Pawnee, OK Test Sites

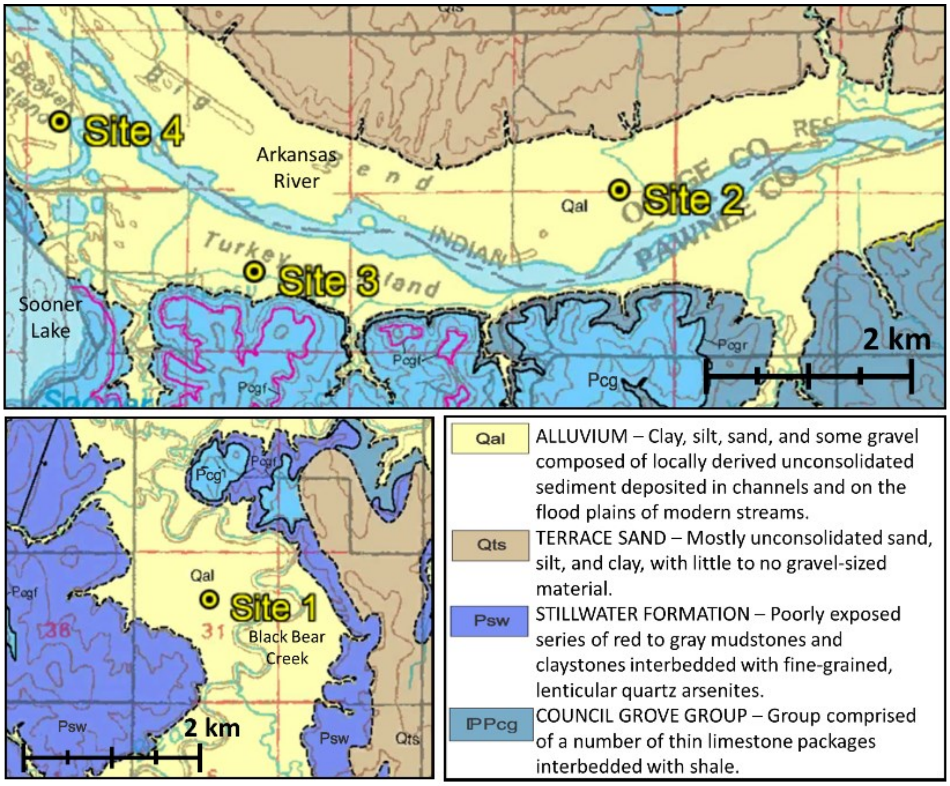

Figure E.1. Geologic maps of the Pawnee earthquake liquefaction sites. (Stanley and Chang 2016)

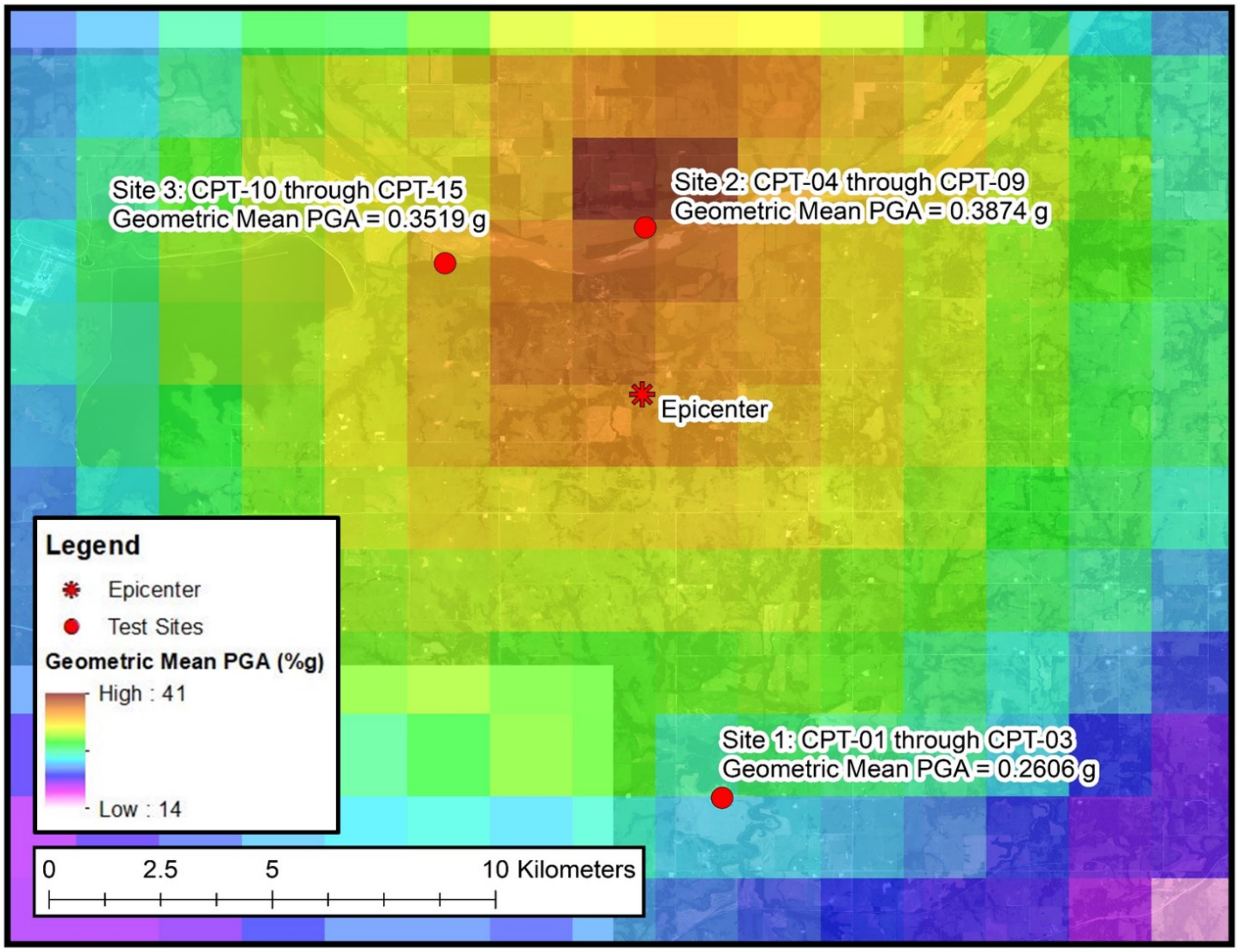

Figure E.2. Geometric Mean a_{max} for 3 Sep 2016, Pawnee, OK earthquake based on USGS ShakeMap. (USGS 2016)

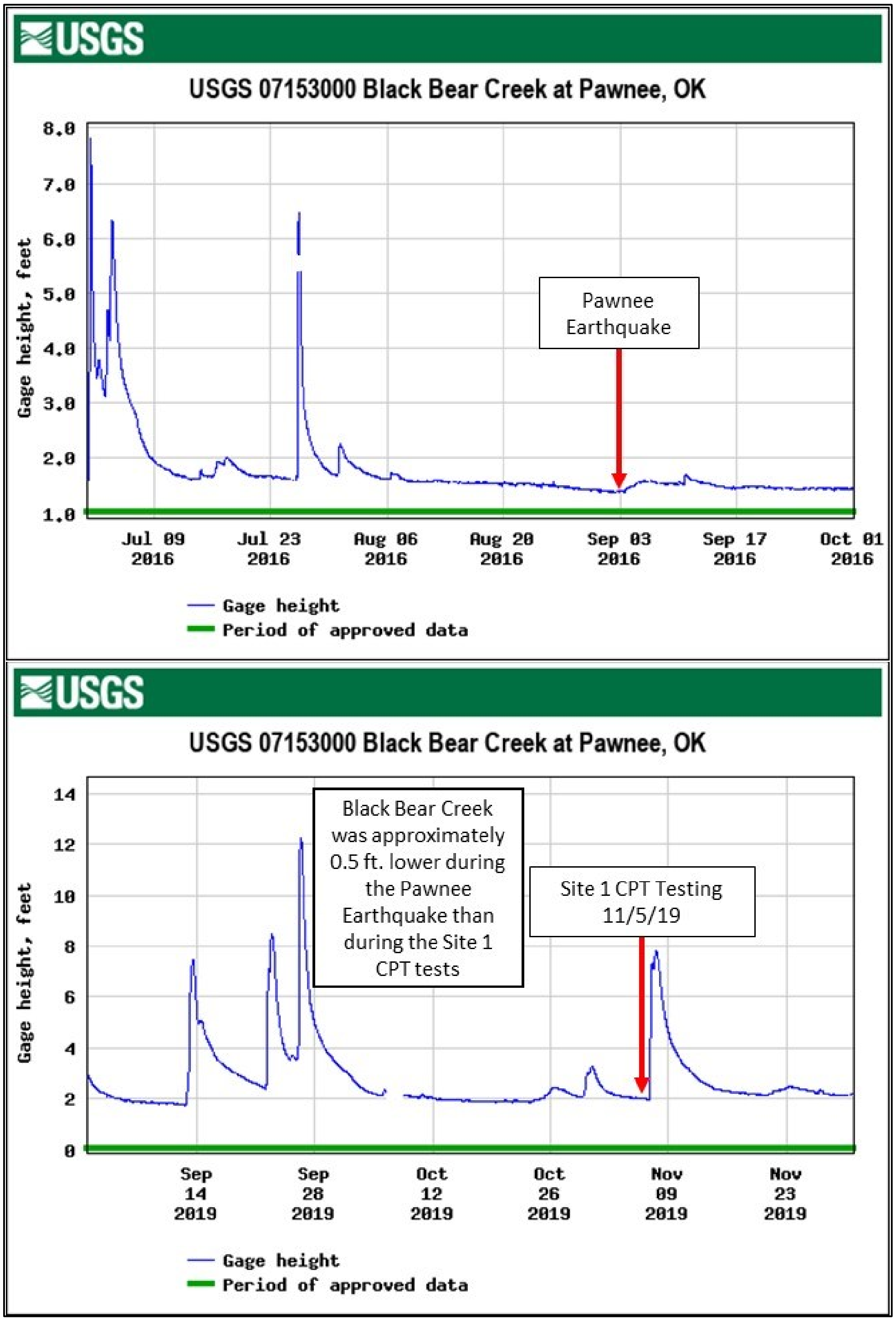

Figure E.3. Gage data for Black Bear Creek at Pawnee, OK during the 3 Sep 2016 Pawnee Earthquake and 5 Nov 2019 CPT testing at Site 1. (after U.S. Geologic Survey 2016b,c)

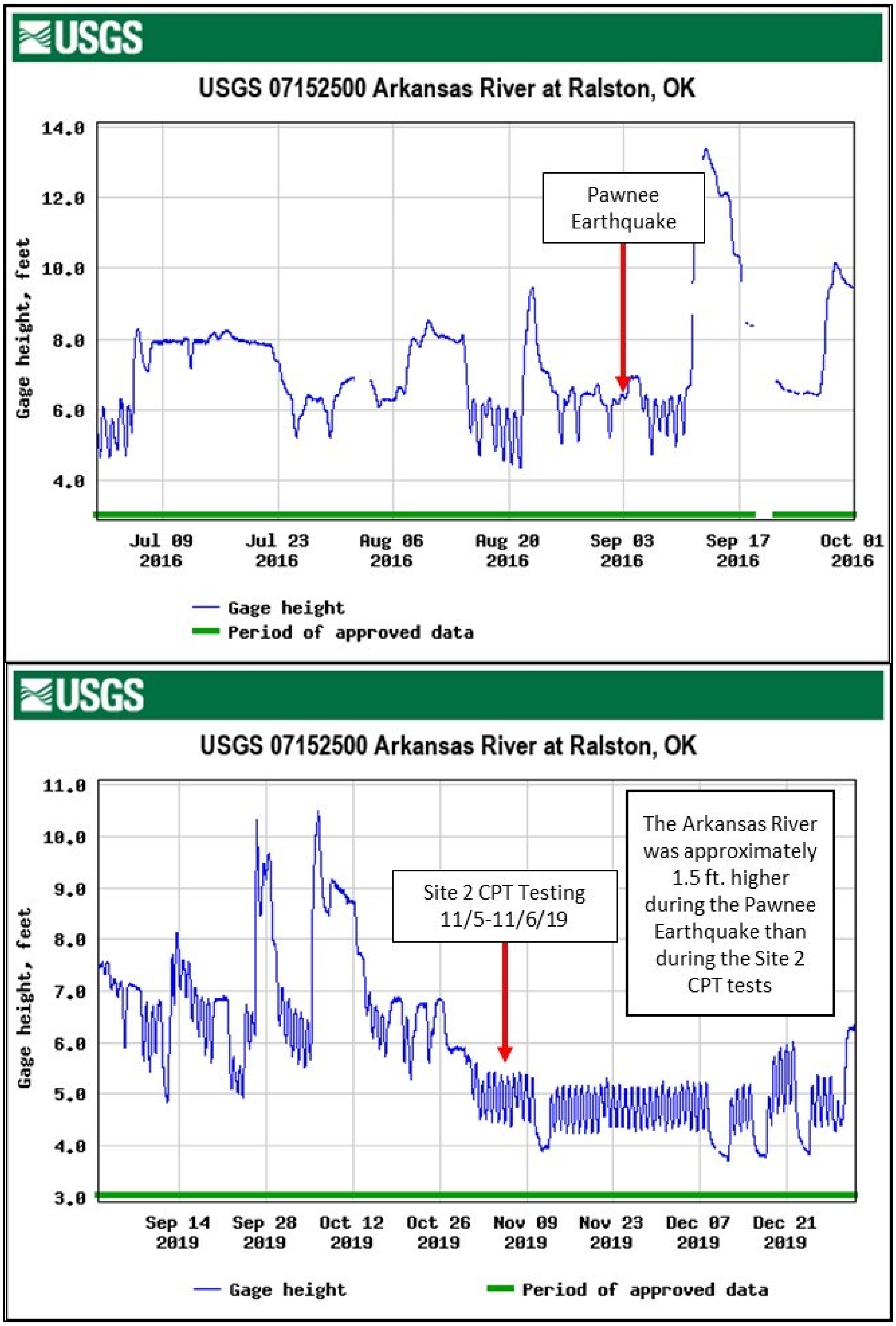

Pawnee Earthquake

Site 2 CPT Testing 11/5-11/6/19

The Arkansas River was approximately 1.5 ft. higher during the Pawnee Earthquake than during the Site 2 CPT tests

Figure E.4. Gage data for Arkansas River at Ralston, OK during the 3 Sep 2016 Pawnee Earthquake and 5-6 Nov 2019 CPT testing at Site 2. (after U.S. Geologic Survey 2016b,c)

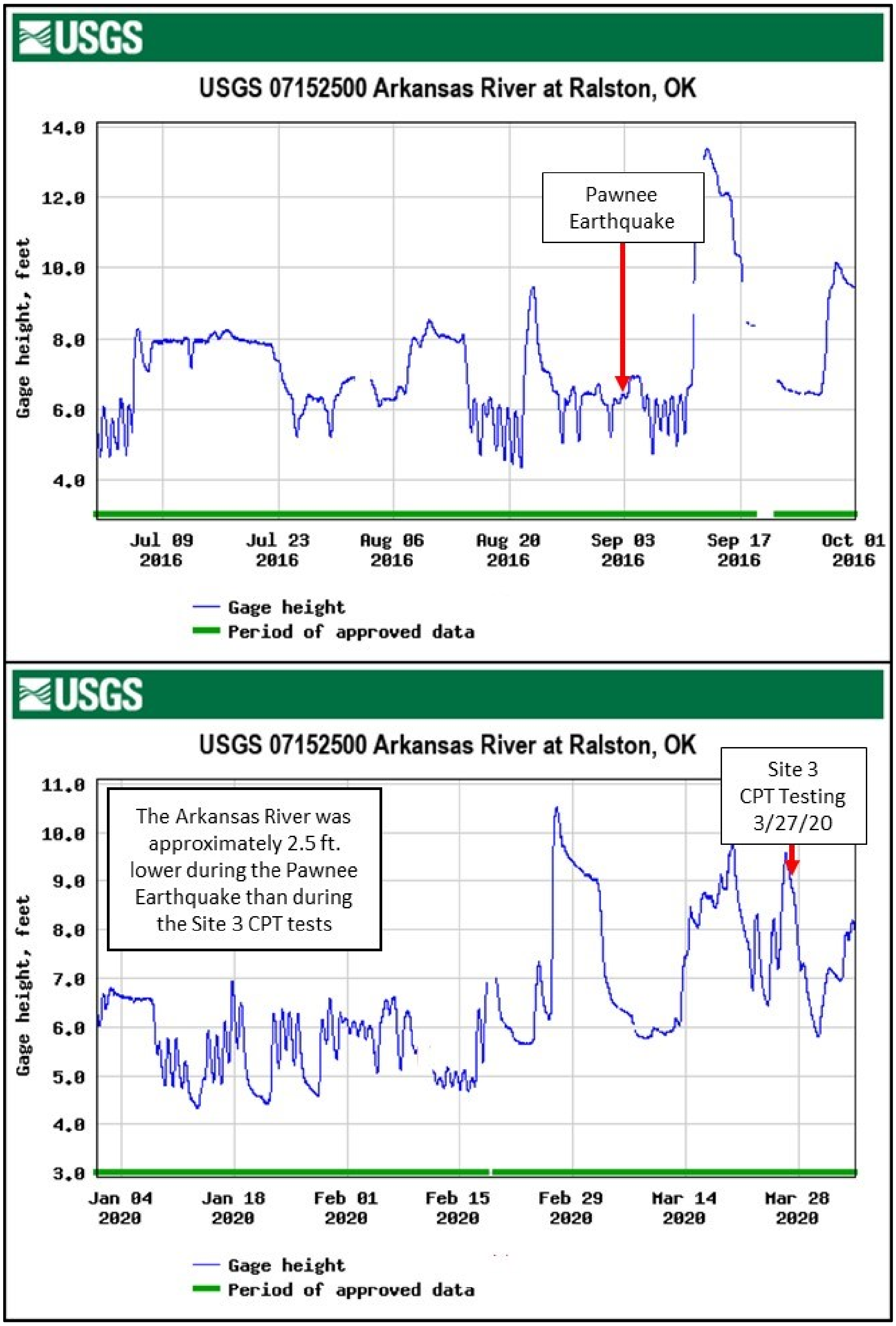

Pawnee Earthquake

The Arkansas River was approximately 2.5 ft. lower during the Pawnee Earthquake than during the Site 3 CPT tests

Site 3 CPT Testing 3/27/20

Figure E.5. Gage data for Arkansas River at Ralston, OK during the 3 Sep 2016 Pawnee Earthquake and 27 Mar 2020 CPT testing at Site 3. (after U.S. Geologic Survey 2016b,c)

Appendix F. Field and Lab Test Data from Site Characterization at all Pawnee, OK Test Sites

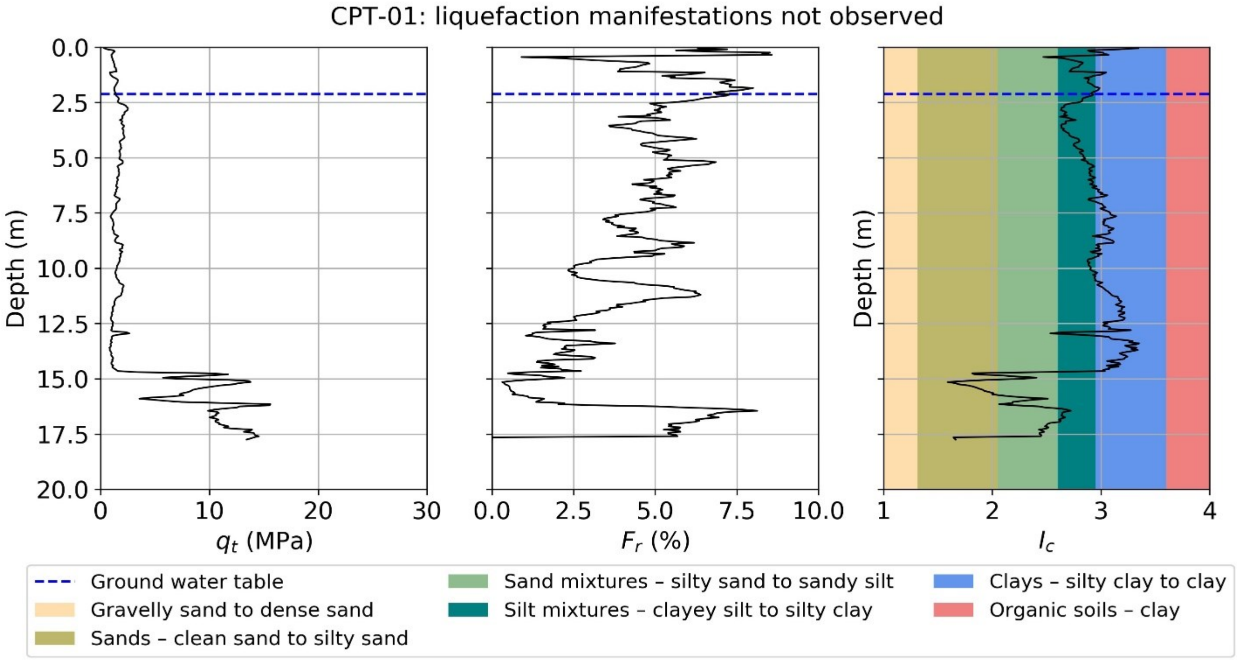

Figure F.1. CPT test results for CPT-01, Site 1.

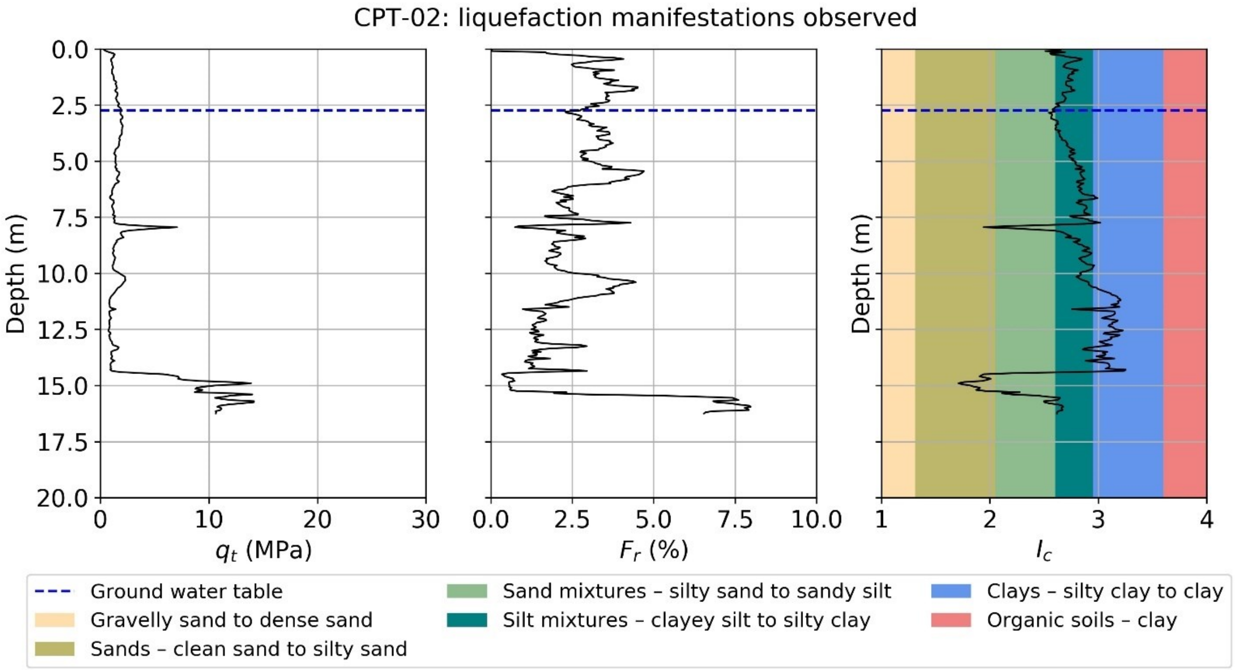

Figure F.2. CPT test results for CPT-02, Site 1.

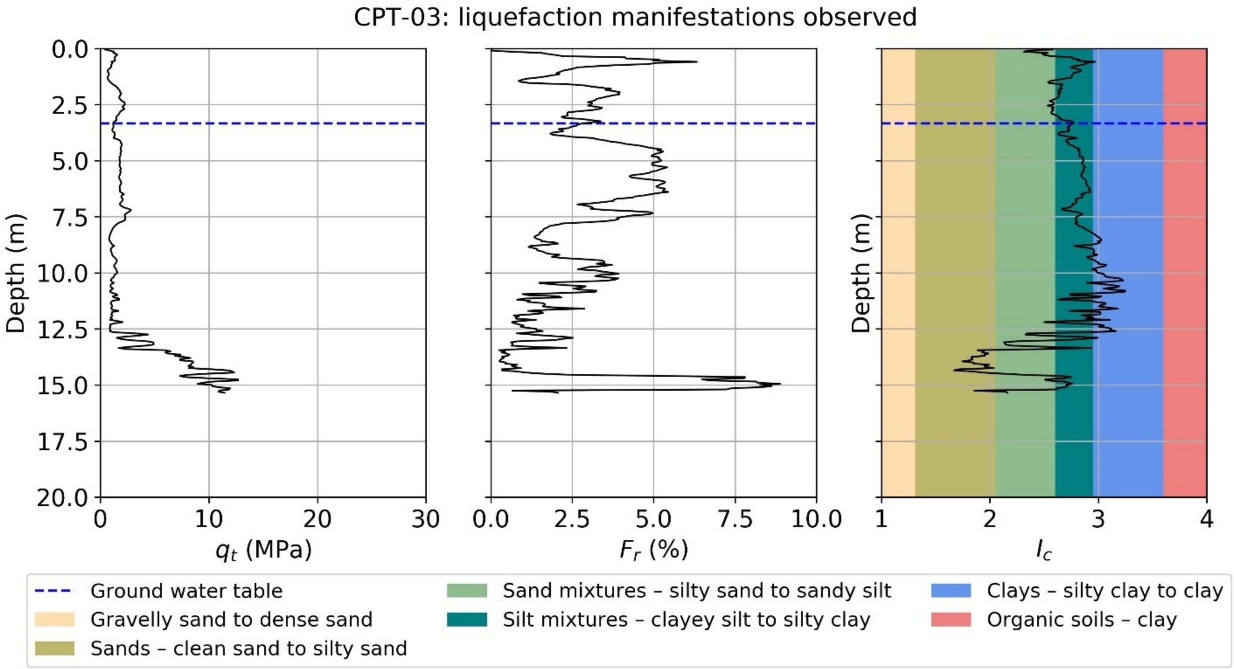

Figure F.3. CPT test results for CPT-03, Site 1.

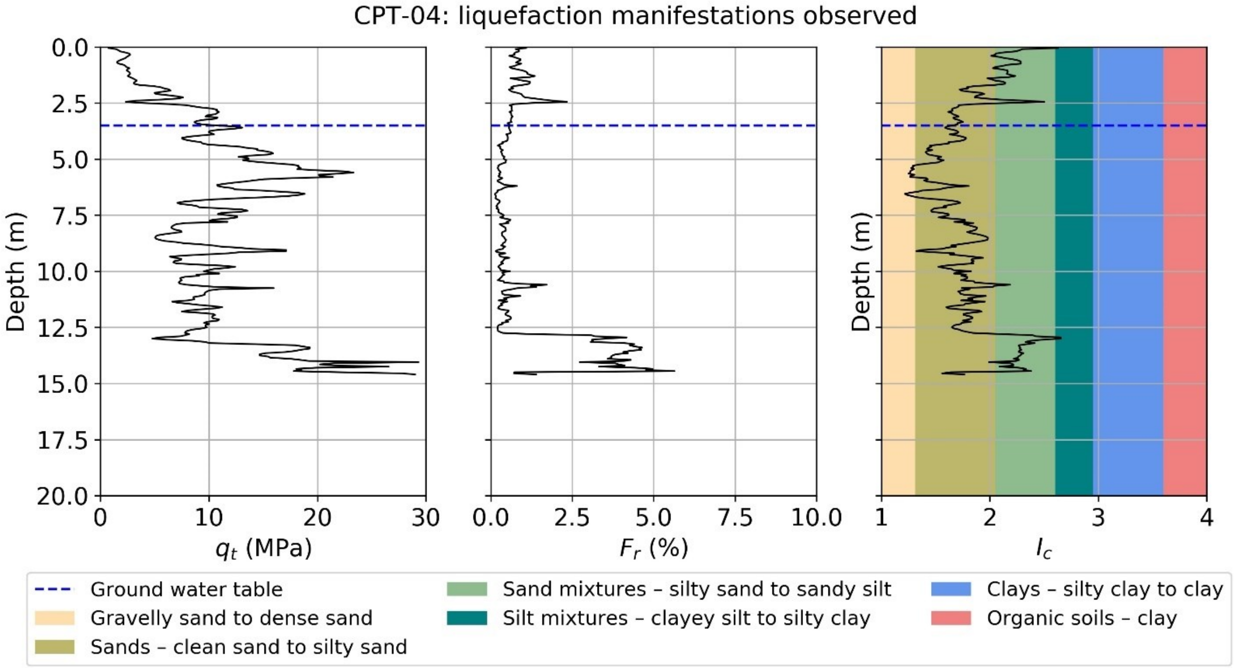

Figure F.4. CPT test results for CPT-04, Site 2.

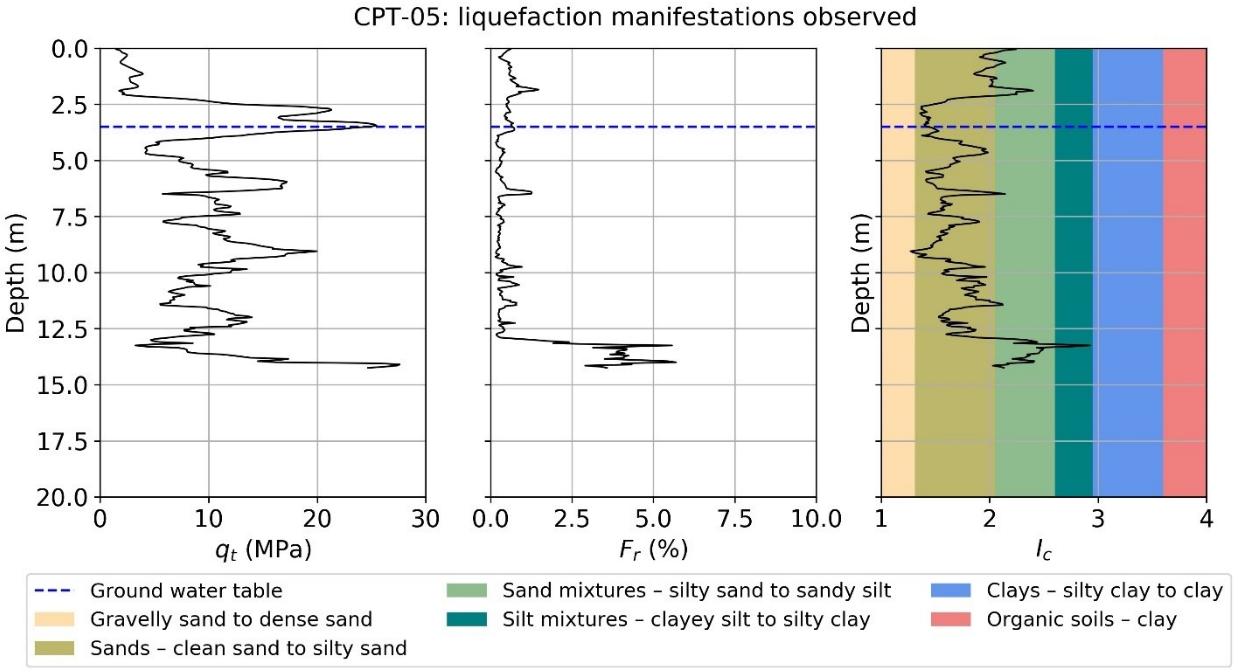

Figure F.5. CPT test results for CPT-05, Site 2.

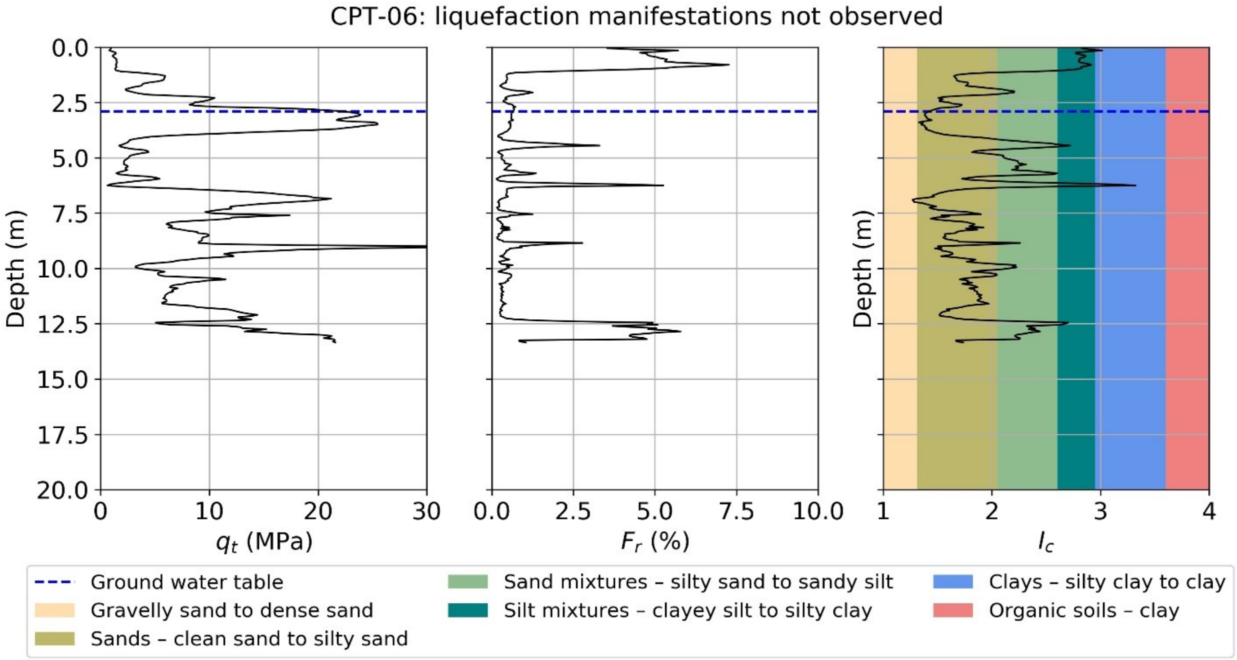

Figure F.6. CPT test results for CPT-06, Site 2.

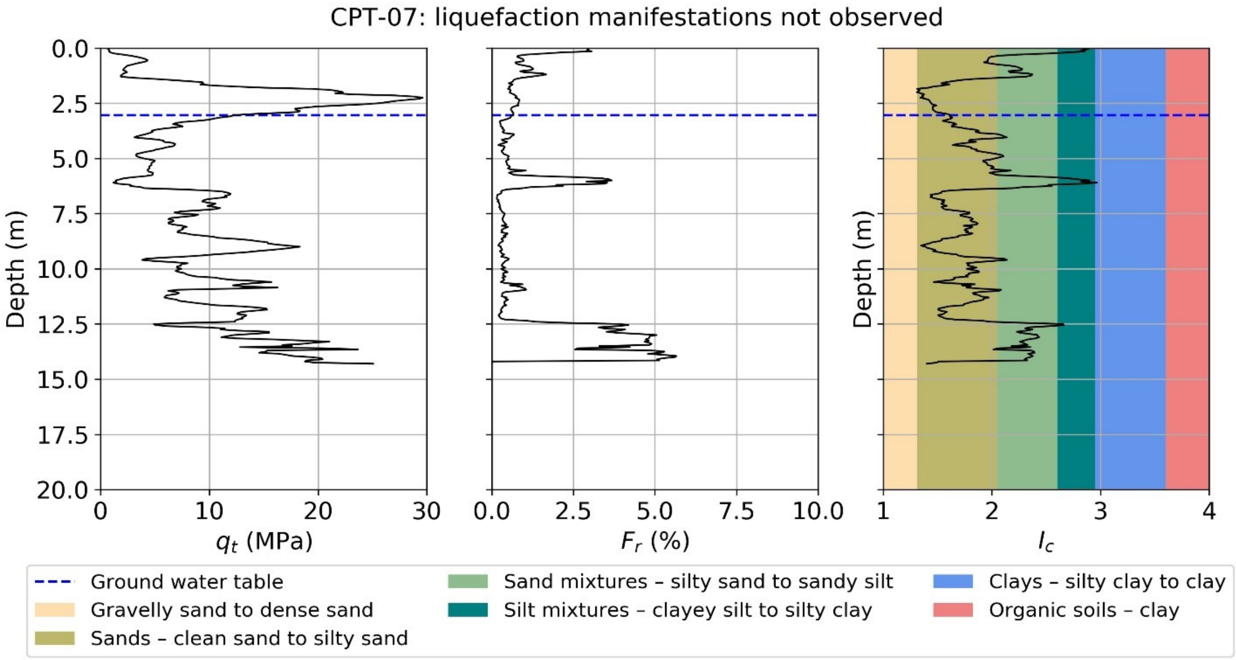

Figure F.7. CPT test results for CPT-07, Site 2.

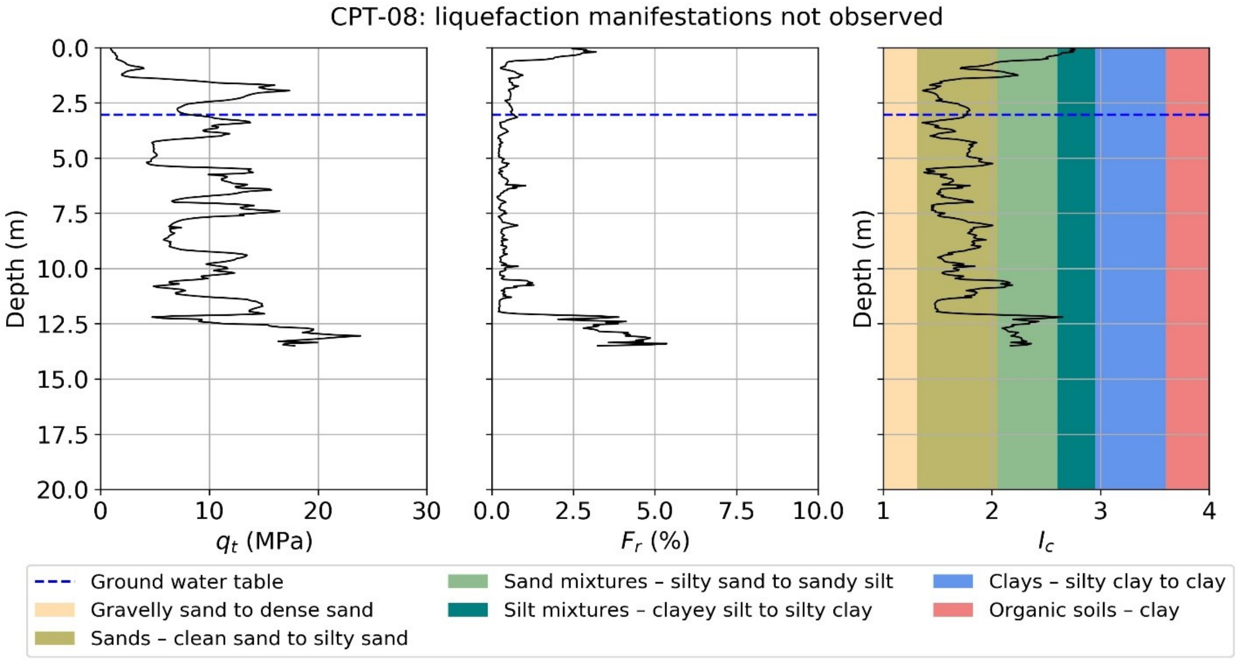

Figure F.8. CPT test results for CPT-08, Site 2.

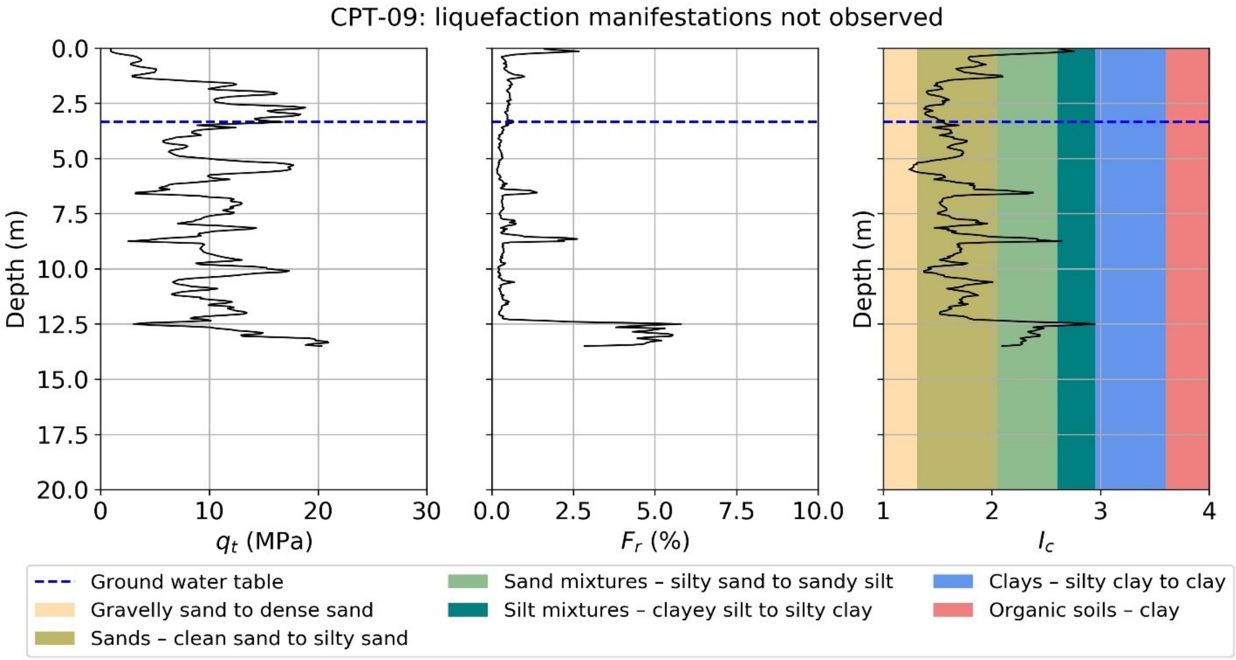

Figure F.9. CPT test results for CPT-09, Site 2.

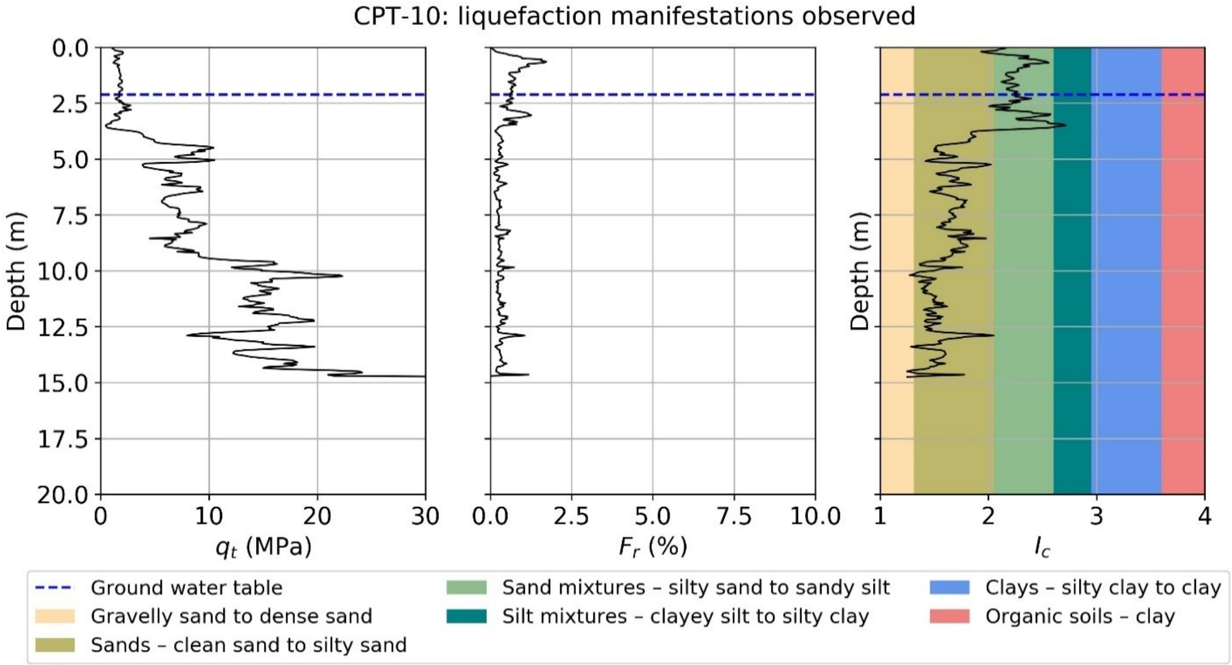

Figure F.10. CPT test results for CPT-10, Site 3.

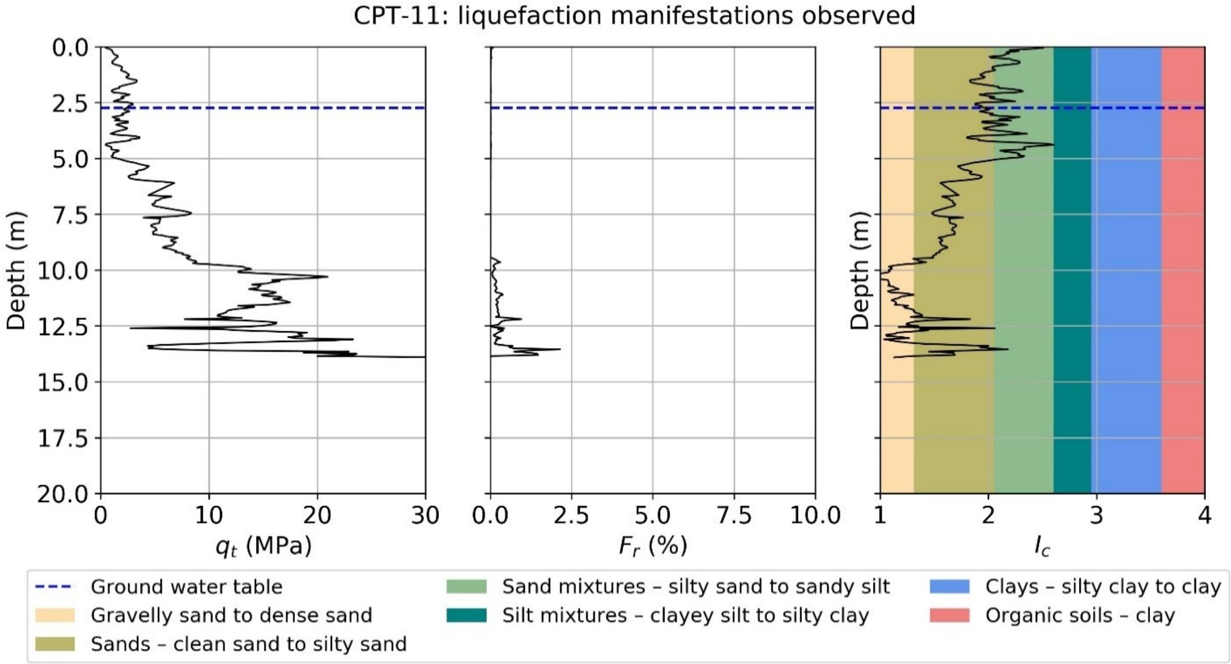

Figure F.11. CPT test results for CPT-11, Site 3.

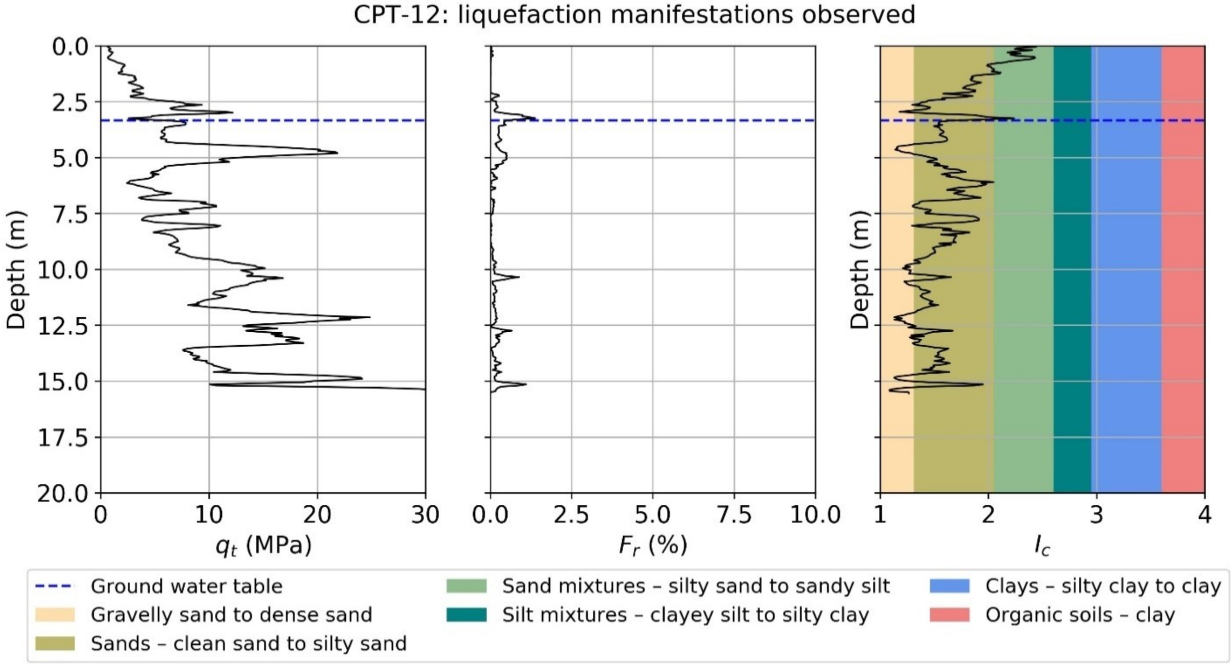

Figure F.12. CPT test results for CPT-12, Site 3.

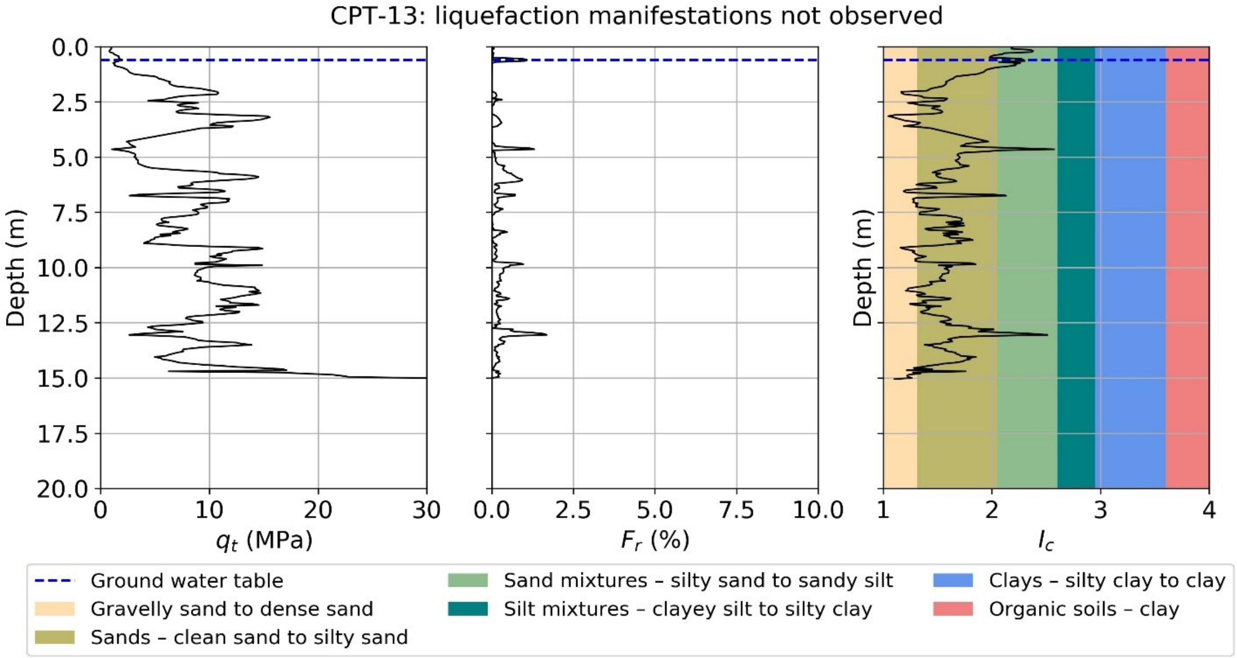

Figure F.13. CPT test results for CPT-13, Site 3.

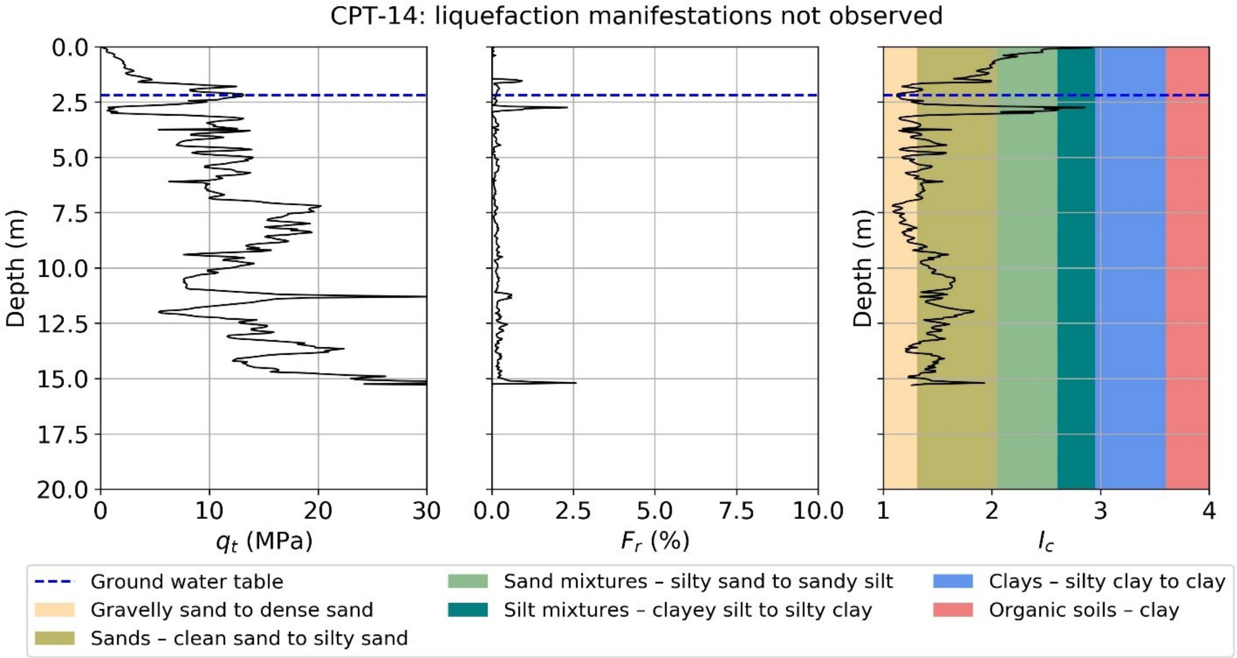

Figure F.14. CPT test results for CPT-14, Site 3.

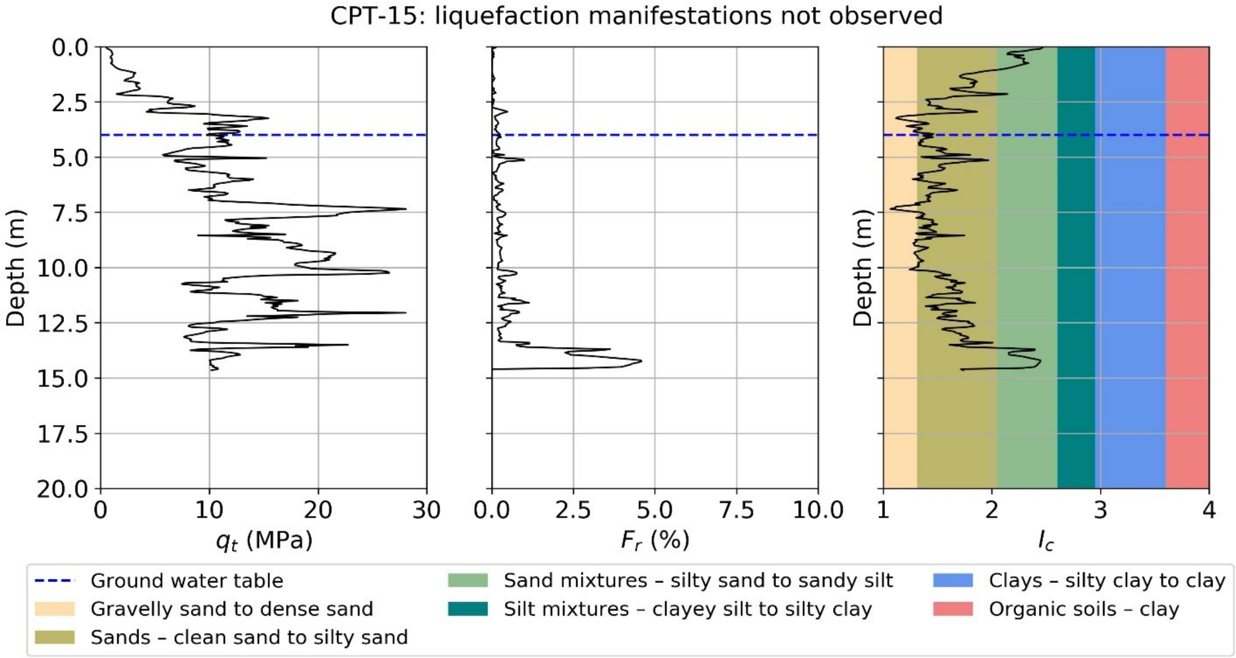

Figure F.15. CPT test results for CPT-15, Site 3.

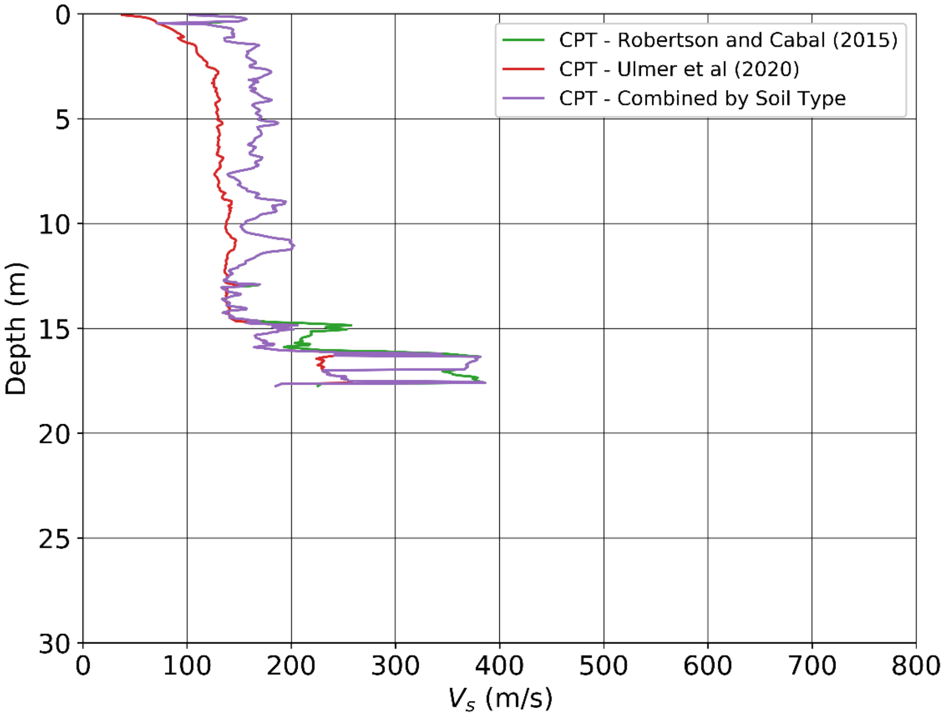

Figure F.16. V_s profiles for CPT-01, Site 1, developed using CPT correlations.

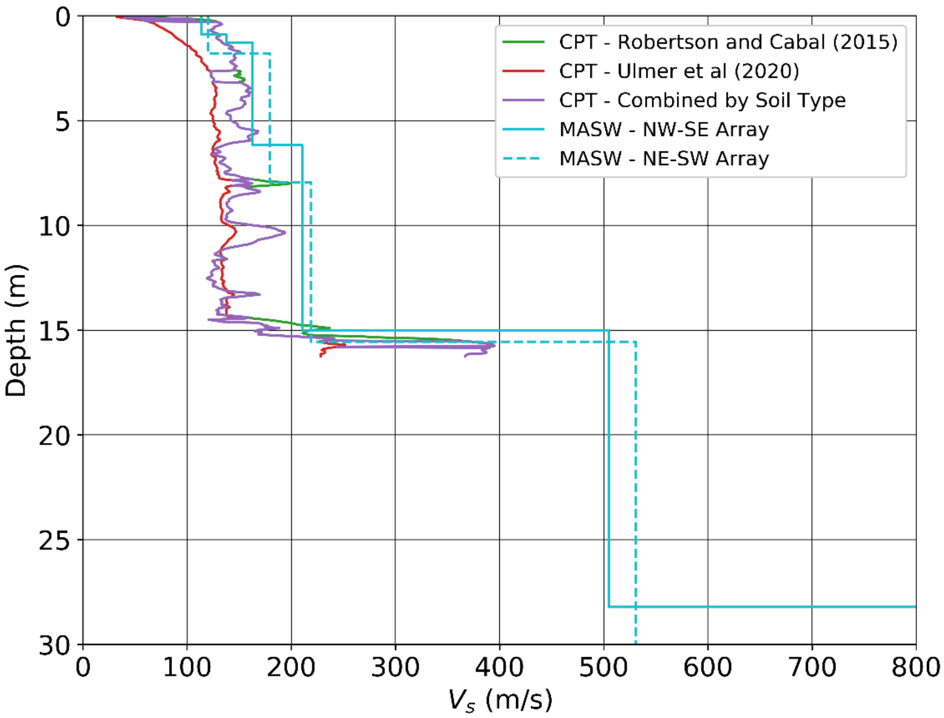

Figure F.17. V$_s$ profiles for CPT-02, Site 1, developed using CPT correlations and MASW tests.

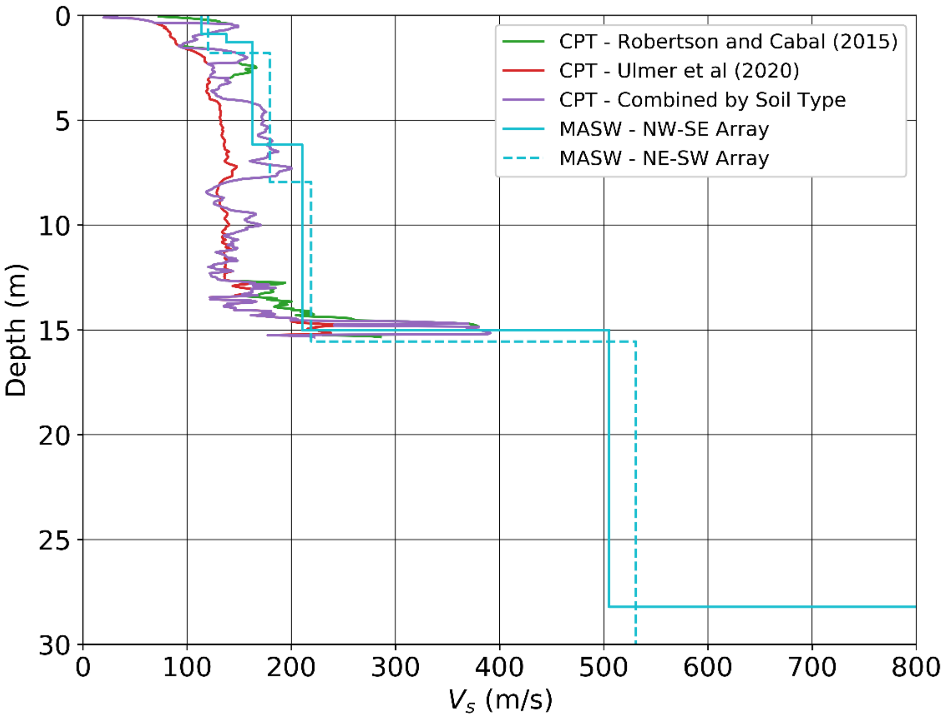

Figure F.18. V$_s$ profiles for CPT-03, Site 1, developed using CPT correlations and MASW tests. MASW results for both MASW geophone array layouts are shown.

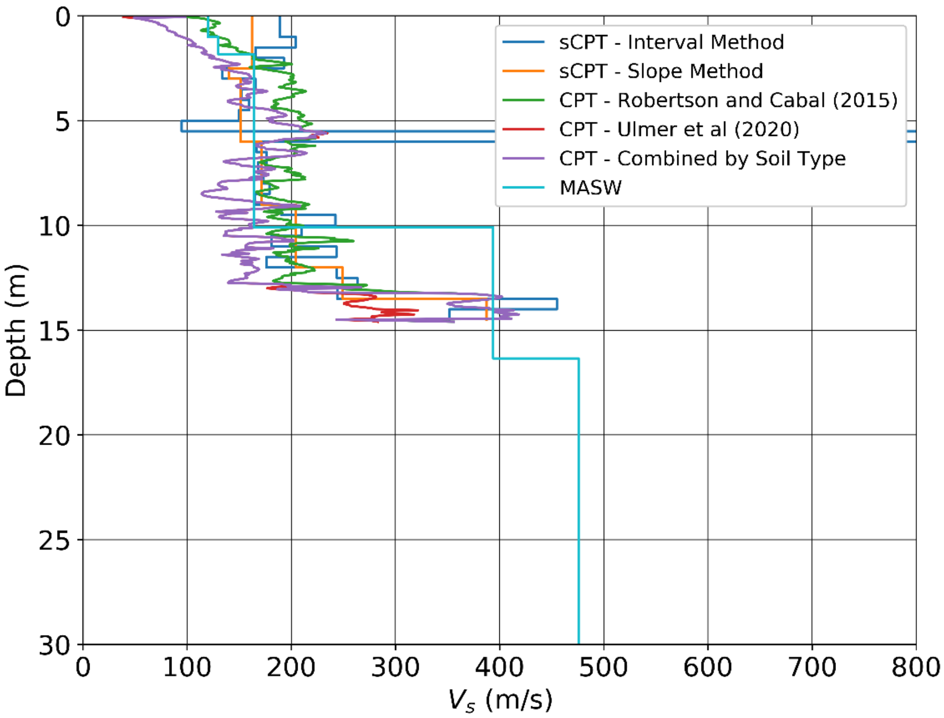

Figure F.19. V_s profiles for CPT-04, Site 2, developed using CPT correlations, sCPT tests, and MASW tests.

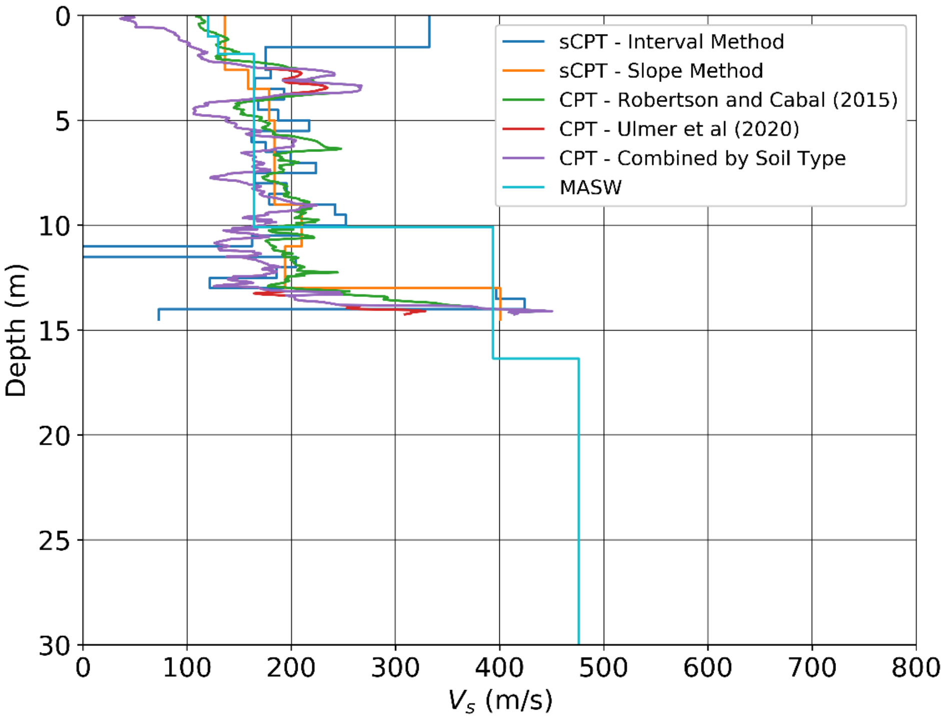

Figure F.20. V_s profiles for CPT-05, Site 2, developed using CPT correlations, sCPT tests, and MASW tests.

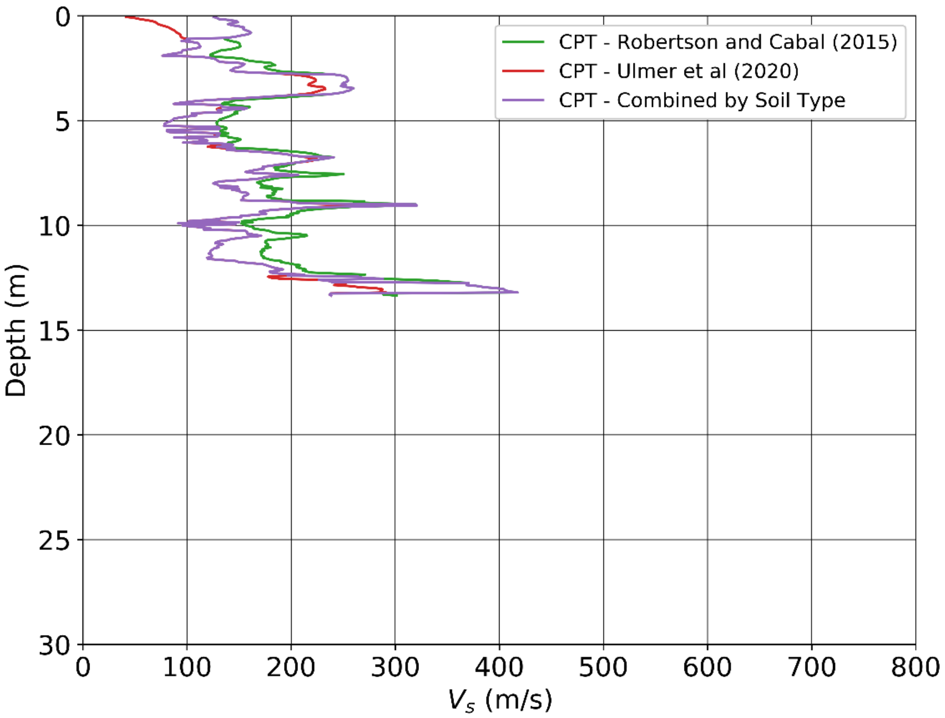

Figure F.21. V_s profiles for CPT-06, Site 2, developed using CPT correlations.

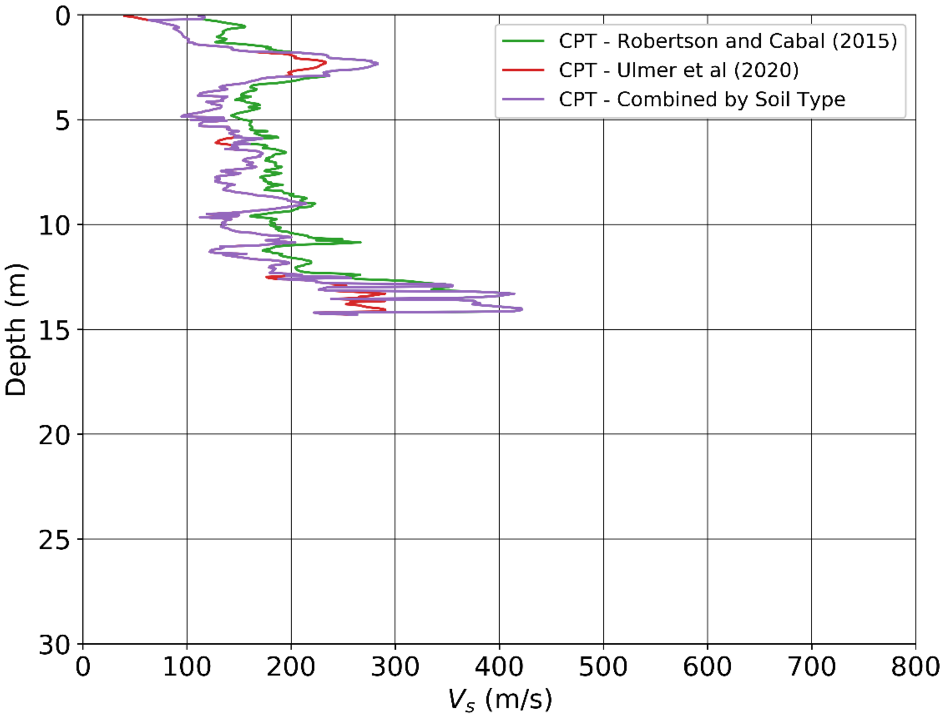

Figure F.22. V_s profiles for CPT-07, Site 2, developed using CPT correlations.

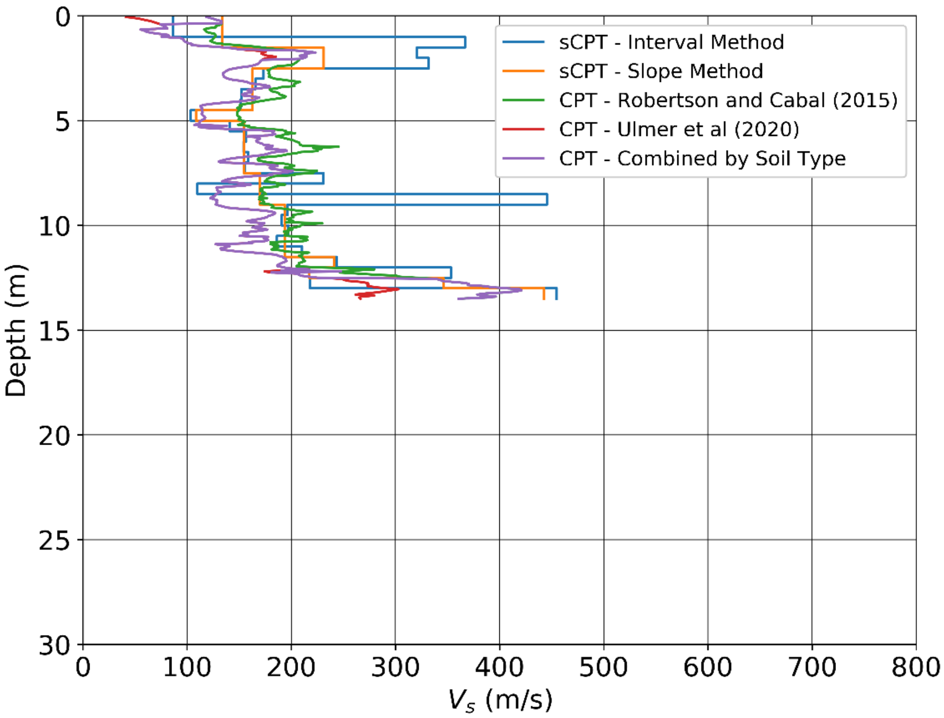

Figure F.23. V_s profiles for CPT-08, Site 2, developed using CPT correlations and sCPT tests.

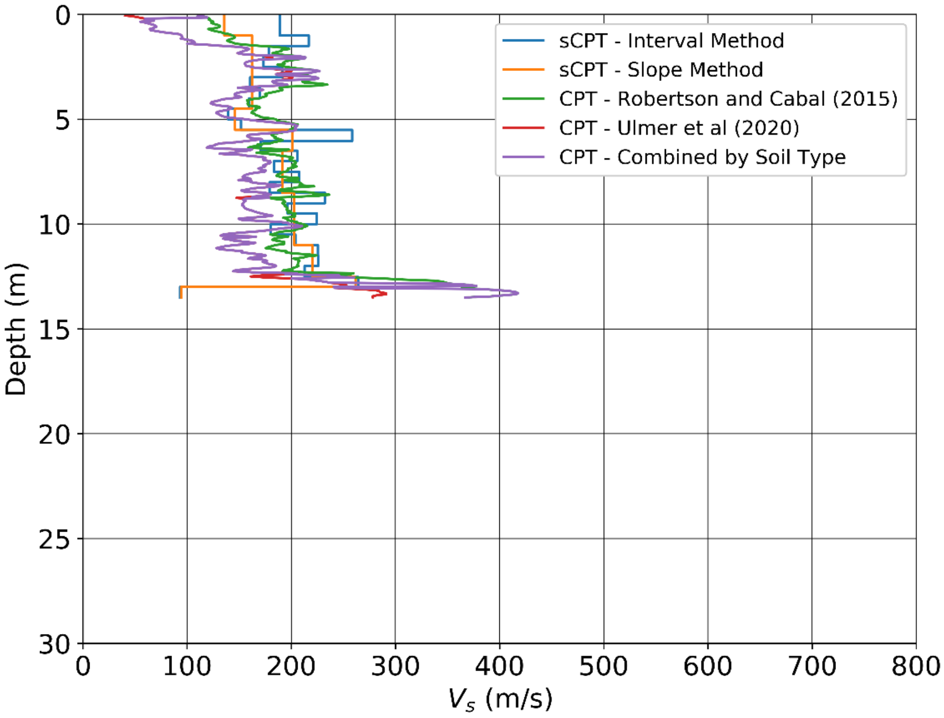

Figure F.24. V_s profiles for CPT-09, Site 2, developed using CPT correlations and sCPT tests.

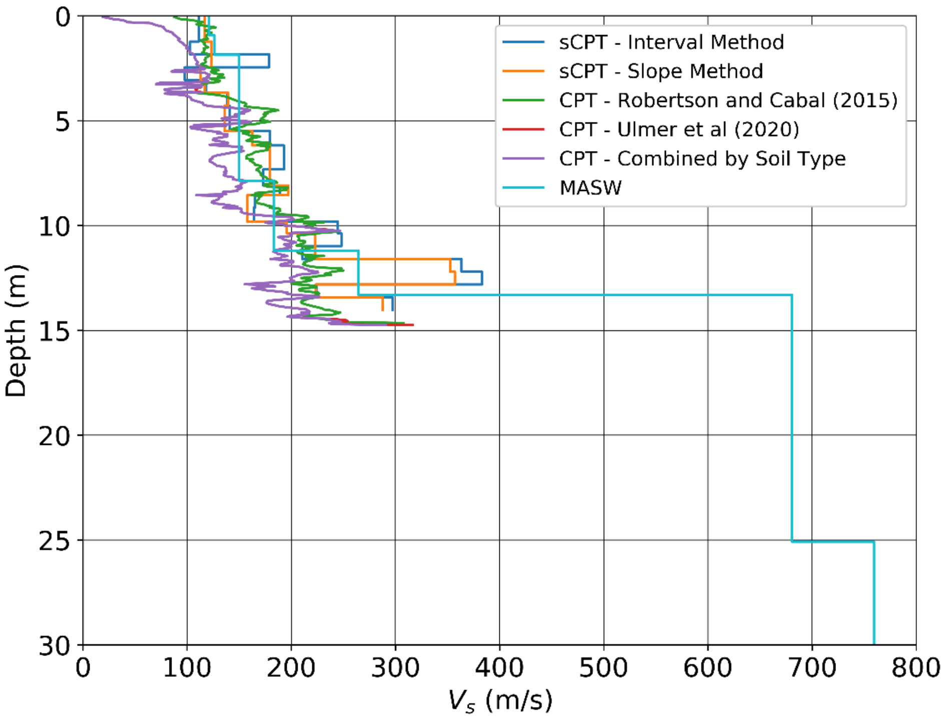

Figure F.25. V_s profiles for CPT-10, Site 3, developed using CPT correlations, sCPT tests, and MASW tests.

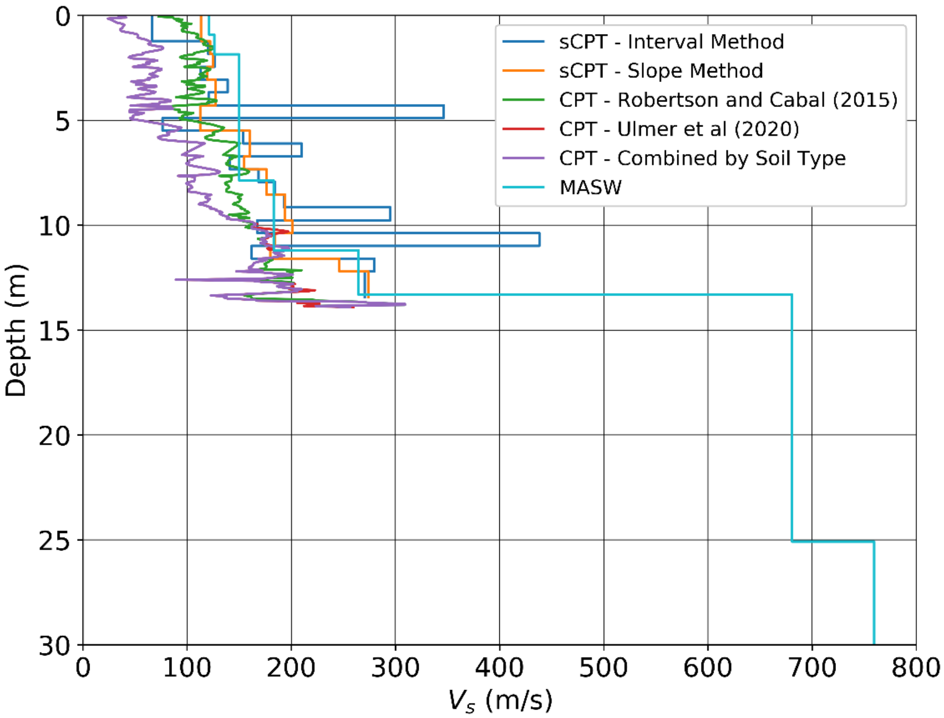

Figure F.26. V_s profiles for CPT-11, Site 3, developed using CPT correlations, sCPT tests, and MASW tests.

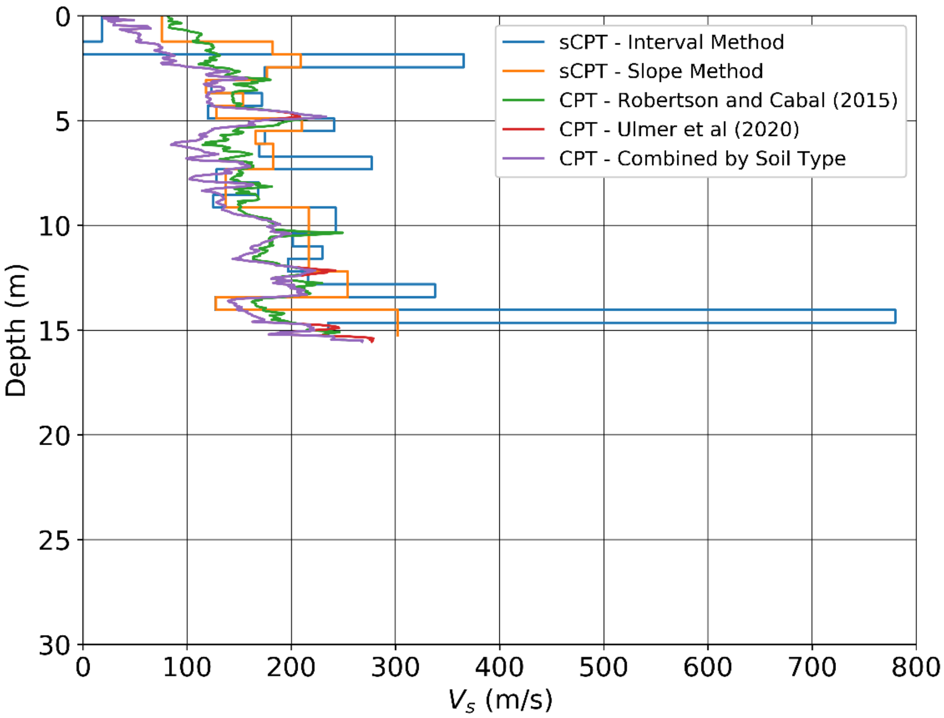

Figure F.27. V_s profiles for CPT-12, Site 3, developed using CPT correlations and sCPT tests.

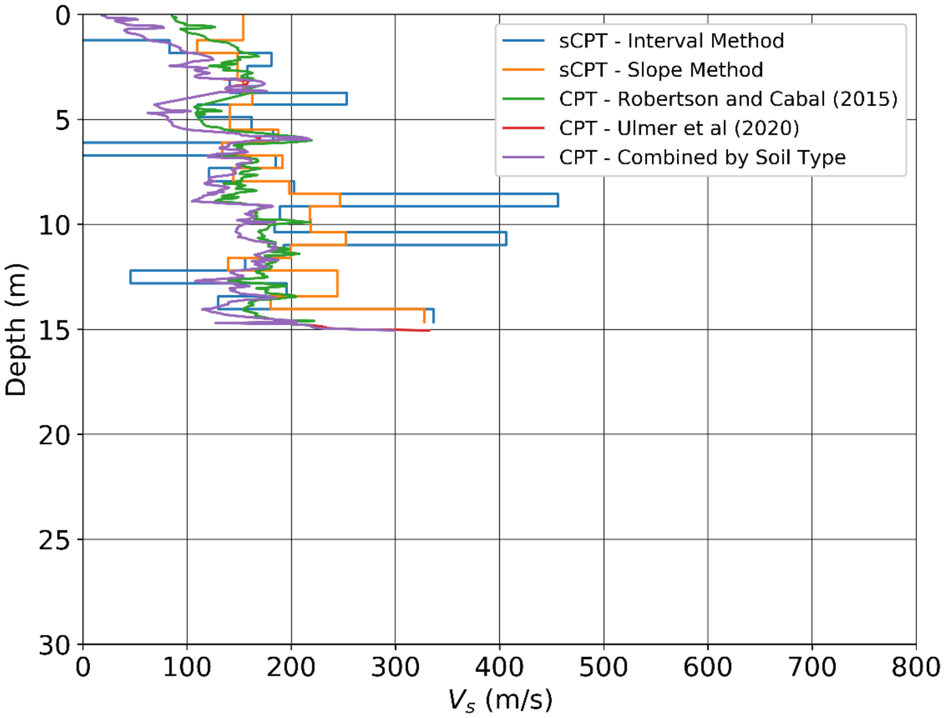

Figure F.28. V_s profiles for CPT-13, Site 3, developed using CPT correlations and sCPT tests.

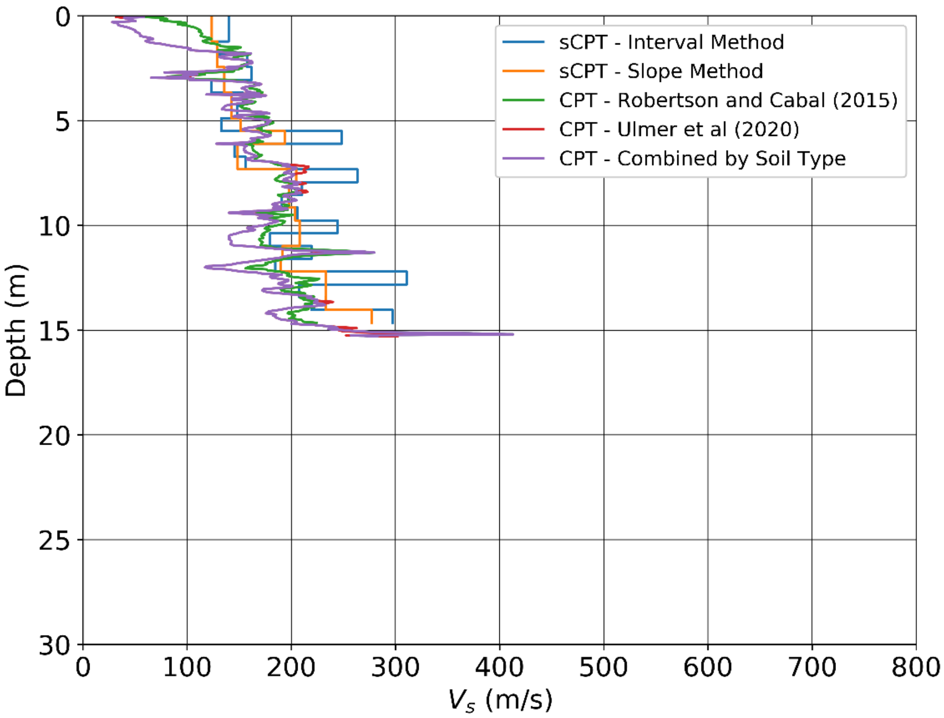

Figure F.29. V_s profiles for CPT-14, Site 3, developed using CPT correlations and sCPT tests.

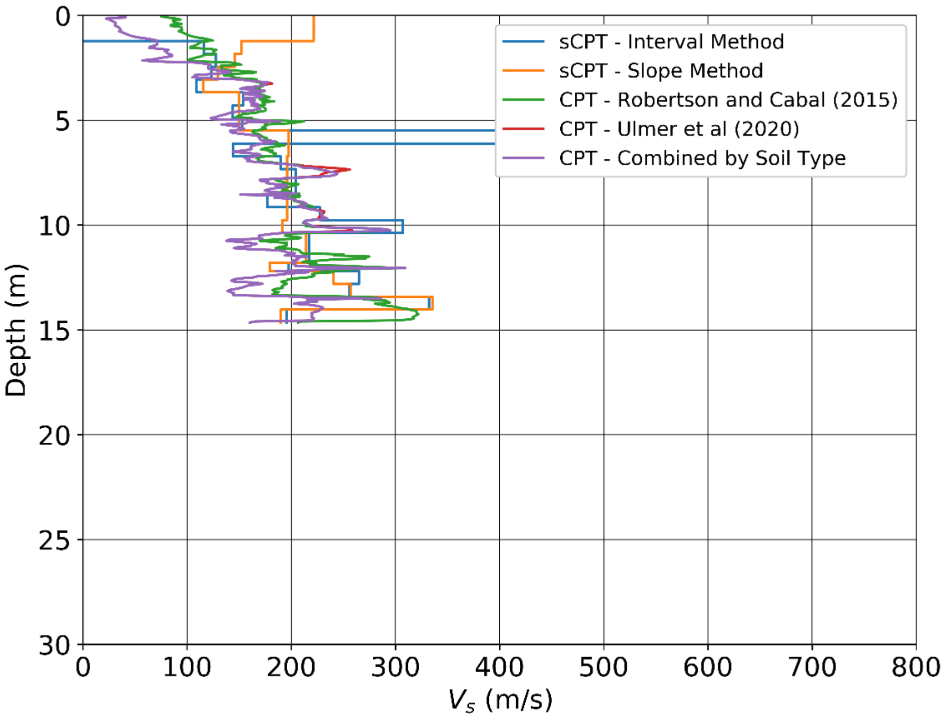

Figure F.30. V_s profiles for CPT-15, Site 3, developed using CPT correlations and sCPT tests.

A soil behavior type index (I_c) value of 2.6, the boundary between “sandy silt” and “clayey silt mixtures” based on SBT_n, is often used to screen out clay-like soils from liquefaction analyses (Robertson and Wride 1998) because they are likely not susceptible to liquefaction triggering. However, Boulanger and Idriss (2014) note that other cutoff values as high as 2.8 or as low as 2.4 may be justified based on site-specific sampling and testing. For this reason, lab tests, including particle-size analysis and Atterberg limit tests, were performed on hand auger samples taken near CPT-03 at Site 1 and CPT-05 at Site 2. Samples were taken at depths where I_c values were close to 2.6 to better assess the properties of these soils.

Samples taken from depths of approximately 1.2, 2.1, 3, and 4 m near CPT-03 at Site 1 were classified as lean clay (CL) with fines contents (FC) of 96-99%. Soils at a depth of 2.1 m had a liquid limit (LL) of 39 and plasticity index (PI) of 24, and soils at a depth of 3 m had a LL of 49 and a PI of 32. These soils are not liquefiable. These samples have $I_c > \sim 2.6$, which supports the use of $I_c = 2.6$ as a threshold for liquefaction susceptibility at Site 1. Particle-size distributions and Atterberg limits for these samples are presented in Figure F.31 and Figure F.32, respectively.

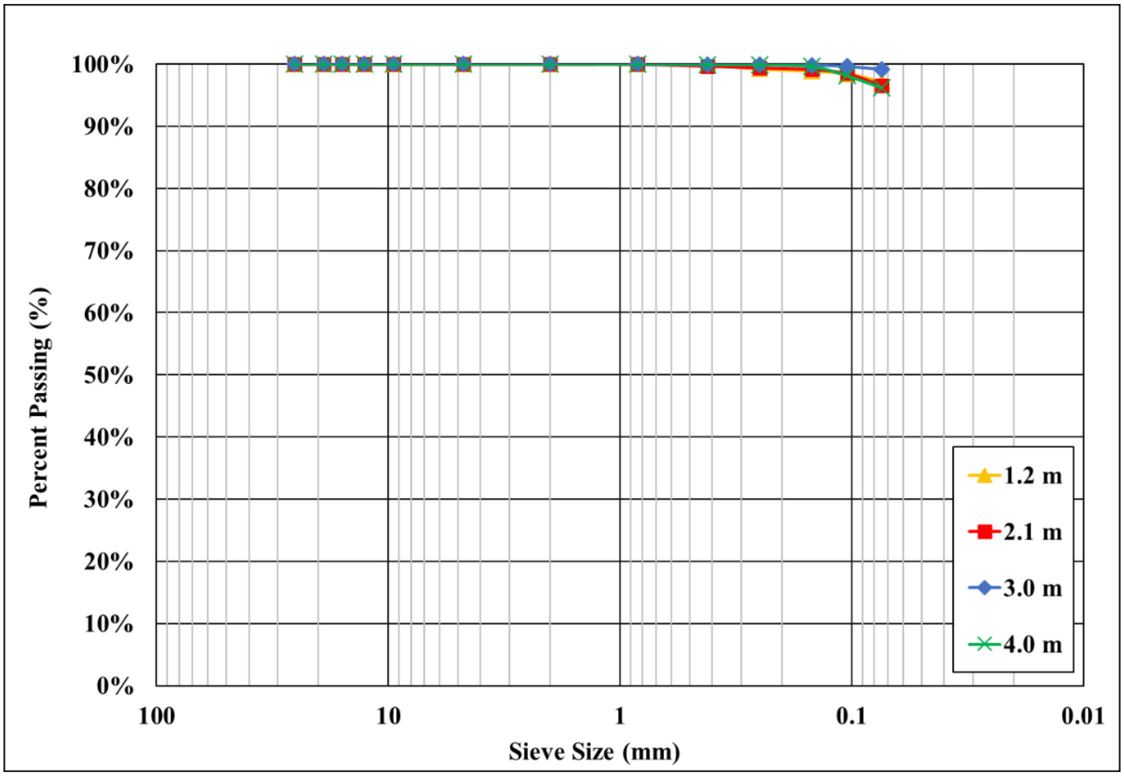

Figure F.31. Particle-size distribution for samples taken near CPT-03, Site 1. Sample depths are indicated in the legend.

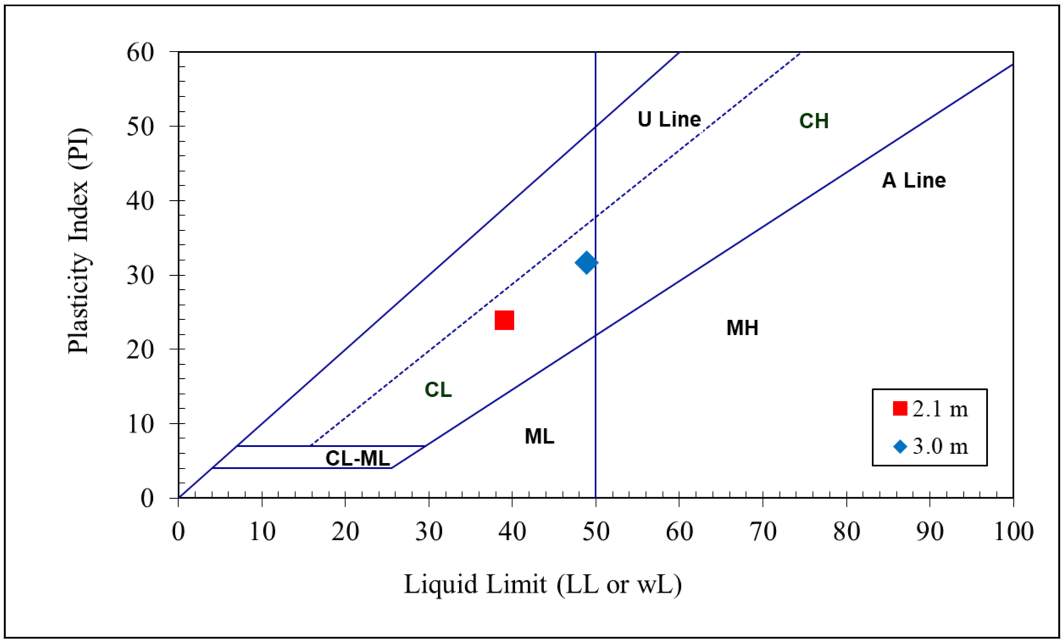

Figure F.32. Atterberg limits for soil samples taken near CPT-03, Site 1. Sample depths are indicated in the legend.

Samples taken from depths of approximately 1.2, 2.1, 3.0, and 3.7 m near CPT-05 at Site 2 were also tested. Fines content varied across the depths tested with FC of 41% at 1.2 m depth, 91% at 2.1 m depth, 2% at 3.0 m depth, and 4% at 3.7 m depth. Soils at 1.2 m were classified as silty sand (SM) with non-plastic fines. Soils at 2.1 m depth were classified as CL with LL of approximately 31 and PI of approximately 9. Soils at depths of 3.0 and 3.7 m were classified as fine, poorly graded sand (SP). Particle-size distributions and Atterberg limits for these samples are presented in Figure F.33 and Figure F.34, respectively.

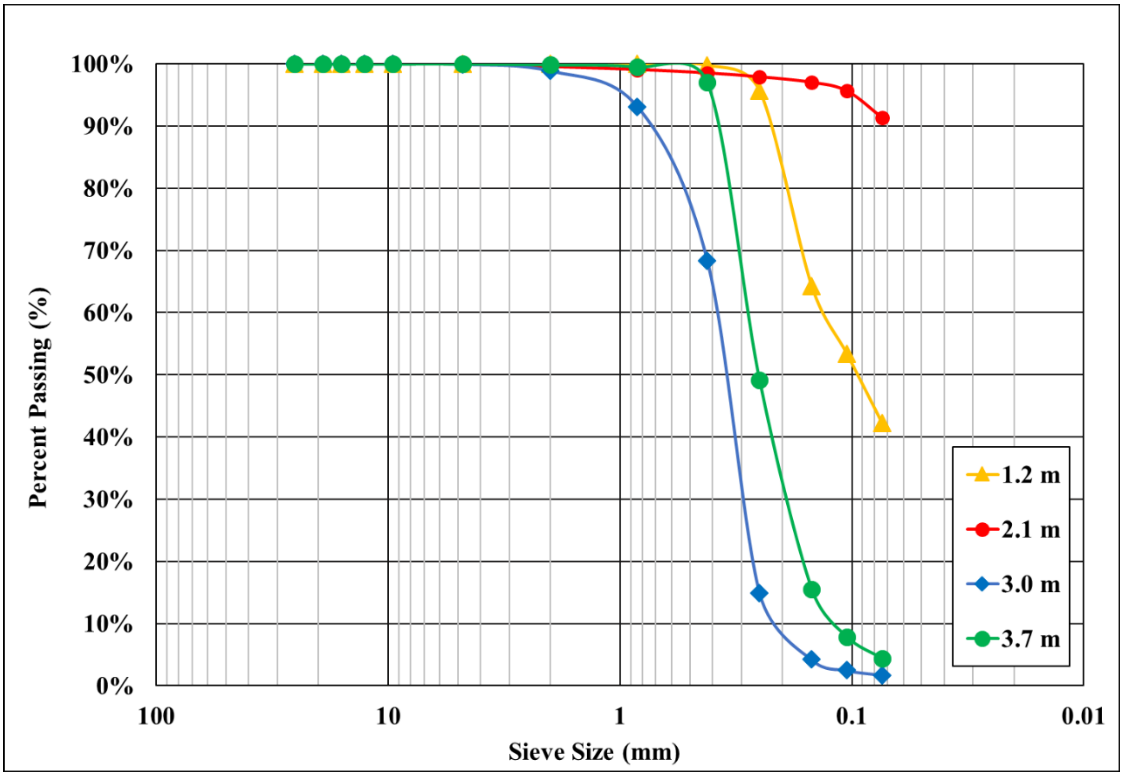

Figure F.33. Particle-size distribution for samples taken near CPT-05, Site 2. Sample depths are indicated in the legend

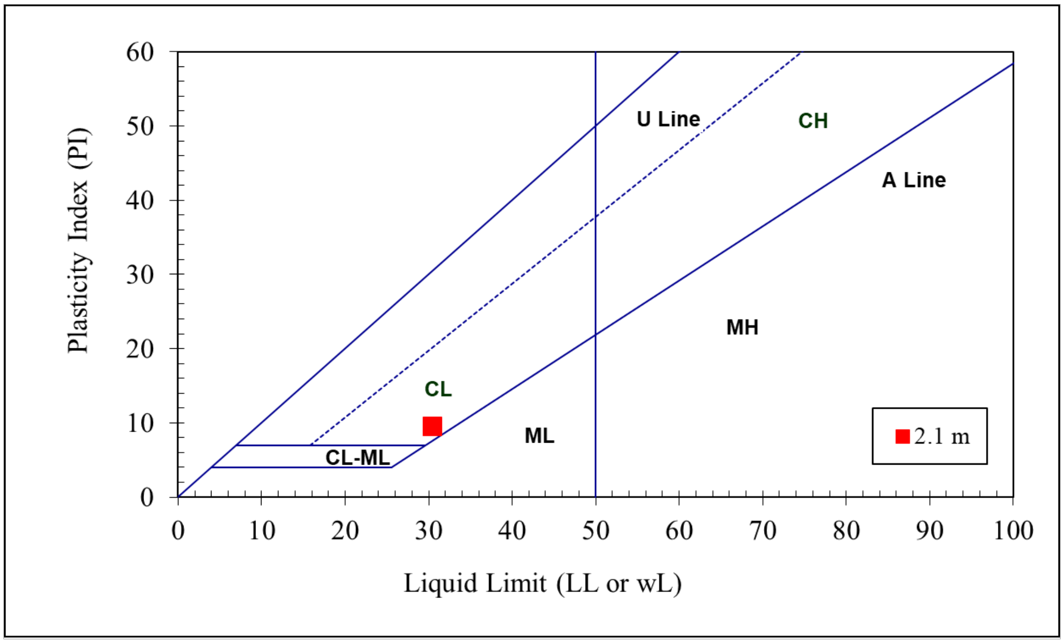

Figure F.34. Atterberg limits for the soil sample taken near CPT-05, Site 2. Sample depth is indicated in the legend.

Lab tests are reflective of the I_c profiles at CPT-04 and CPT-05, which indicate silty sand or sandy silt at depths less than approximately 1.5 m with higher I_c values between depths 2 and 2.5 m, indicating more clay-like behavior. I_c values for depths deeper than 2.5 m indicate sand-like behavior. Based on the lab test results, the soils sampled at a depth of 2.1 m are not susceptible to liquefaction while the soils sampled at depths of 1.2, 3.0, and 3.7 m would likely be susceptible to liquefaction. $I_c \approx 2.4$ for the non-susceptible soils at a depth of 2.1 m while I_c was as high as 2.3 for the liquefaction susceptible soils above this depth. These results suggest that a cutoff for liquefaction of $I_c = 2.4$ may be justified at Site 2. A sensitivity analysis was performed during liquefaction hazard assessment to test the effect of I_c cutoff on estimated liquefaction potential. This analysis found that, due to the limited presence of soil having $2.4 \leq I_c < 2.6$, the choice of I_c threshold between 2.4 to 2.6 had negligible impact on estimated risk of liquefaction at Site 2. As such, an I_c cutoff of 2.6 was used to be consistent with typical implementation of the selected liquefaction triggering models.

Although lab tests were not performed on soils from Site 3, a sensitivity analysis was completed for Site 3 using I_c thresholds ranging from 2.4 to 2.6. As with Site 2, selection of the I_c

liquefaction susceptibility threshold within this range had negligible impact on the estimated risk of liquefaction at Site 3. An I_c threshold for liquefaction susceptibility of 2.6 was also used at Site 3.

Appendix G. Profiles from Liquefaction Hazard Assessment and Model Evaluation

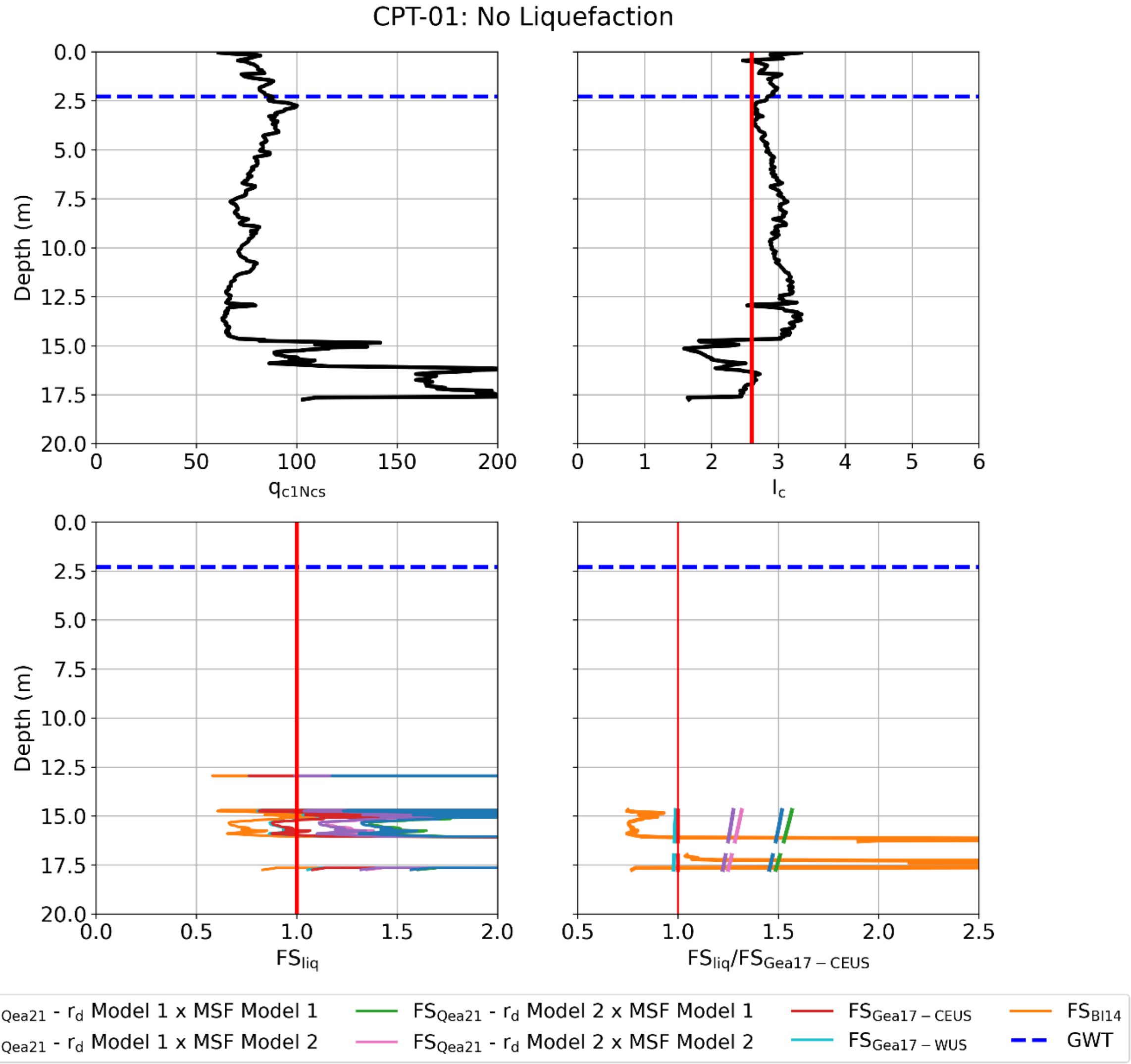

Figure G.1. Profiles of q_{c1Ncs}, I_c, FS_{liq}, and FS_{liq} normalized by FS_{liq} for the Green et al. (2017) CEUS model ($FS_{Gea17\text{-}CEUS}$) for CPT-01, Site 1 (no post-event liquefaction manifestations observed). FS_{liq} for the Qea21 model (FS_{Qea21}) is shown for the ZR19_IZ database.

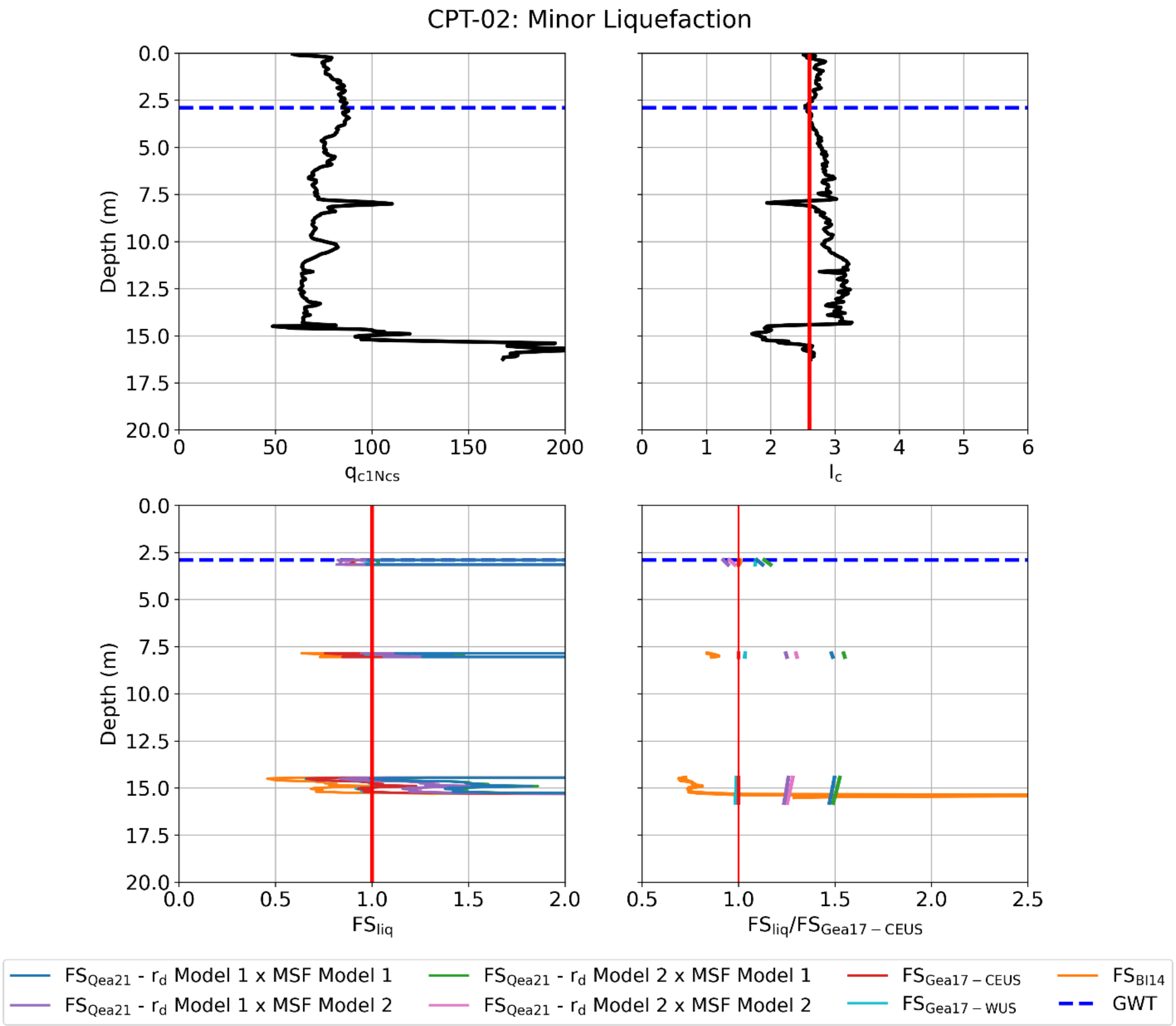

Figure G.2. Profiles of q_{c1Ncs}, I_c, FS_{liq}, and FS_{liq} normalized by FS_{liq} for the Green et al. (2017) CEUS model ($FS_{Gea17\text{-}CEUS}$) for CPT-02, Site1 (minor post-event liquefaction manifestations observed). FS_{liq} for the Qea21 model (FS_{Qea21}) is shown for the ZR19_IZ database.

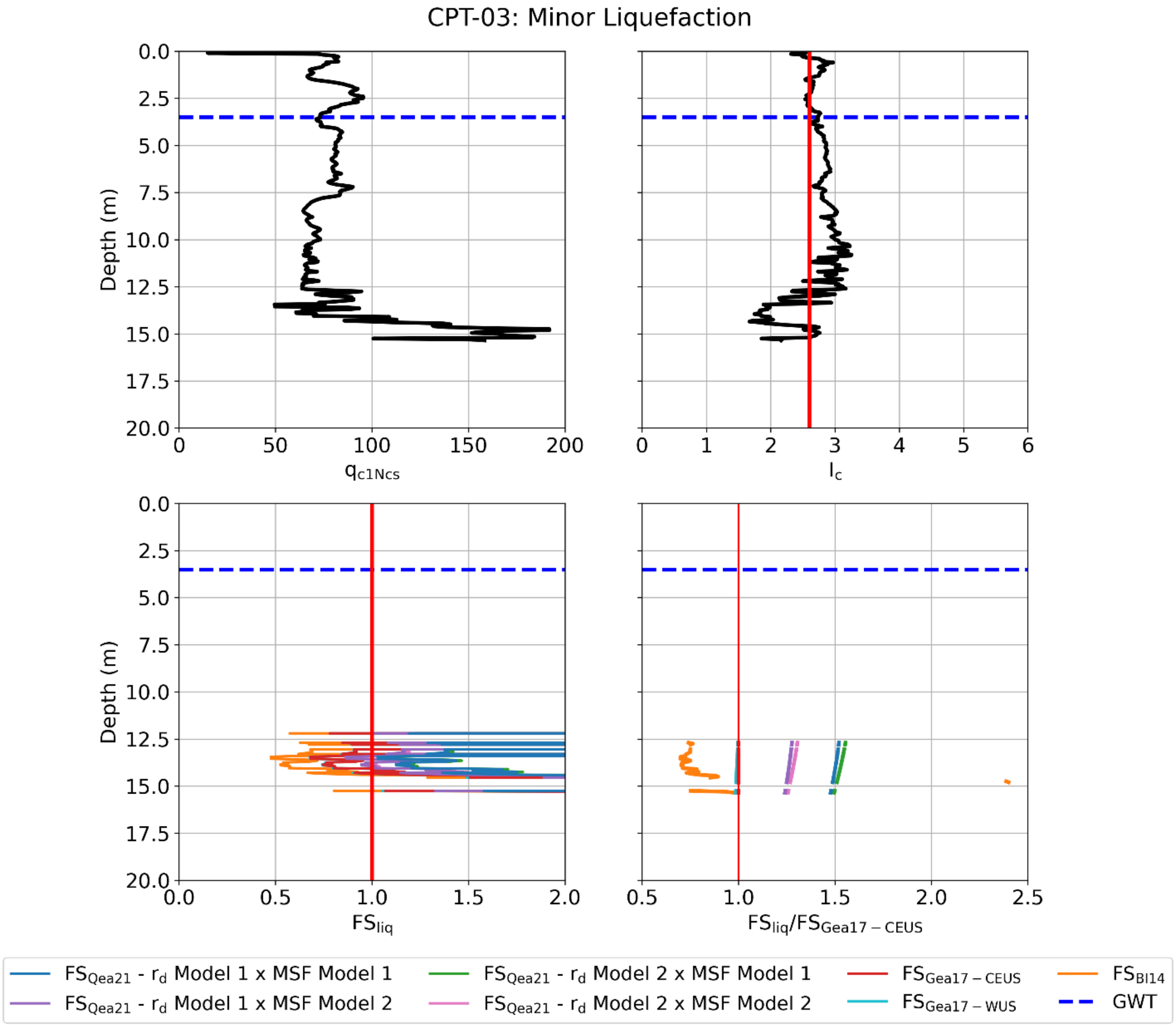

Figure G.3. Profiles of q_{c1Ncs}, I_c, FS_{liq}, and FS_{liq} normalized by FS_{liq} for the Green et al. (2017) CEUS model ($FS_{Gea17-CEUS}$) for CPT-03, Site 1 (minor post-event liquefaction manifestations observed). FS_{liq} for the Qea21 model (FS_{Qea21}) is shown for the ZR19_IZ database.

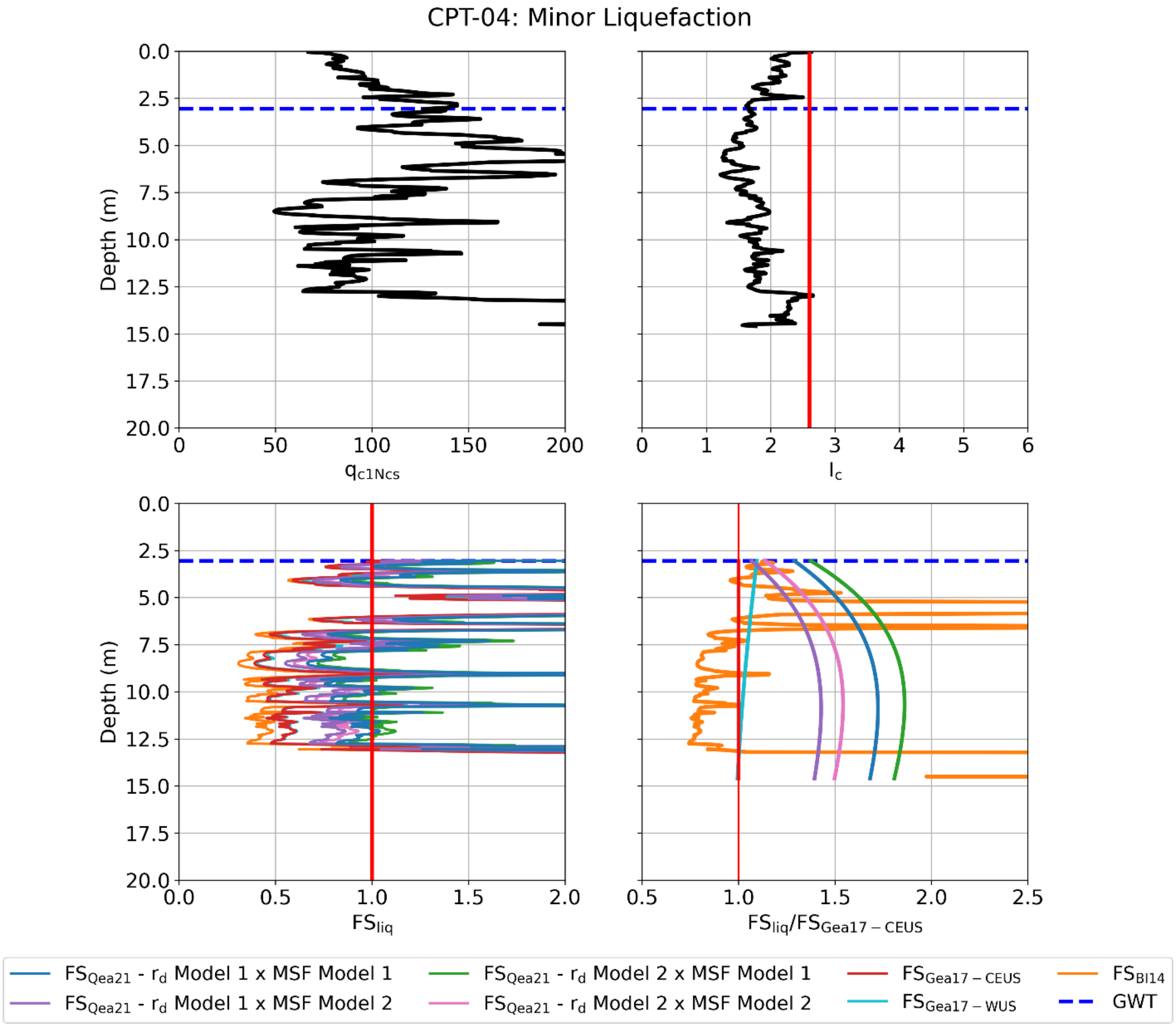

Figure G.4. Profiles of q_{c1Ncs}, I_c, FS_{liq}, and FS_{liq} normalized by FS_{liq} for the Green et al. (2017) CEUS model ($FS_{Gea17-CEUS}$) for CPT-04, Site 2 (minor post-event liquefaction manifestations observed). FS_{liq} for the Qea21 model (FS_{Qea21}) is shown for the ZR19_IZ database.

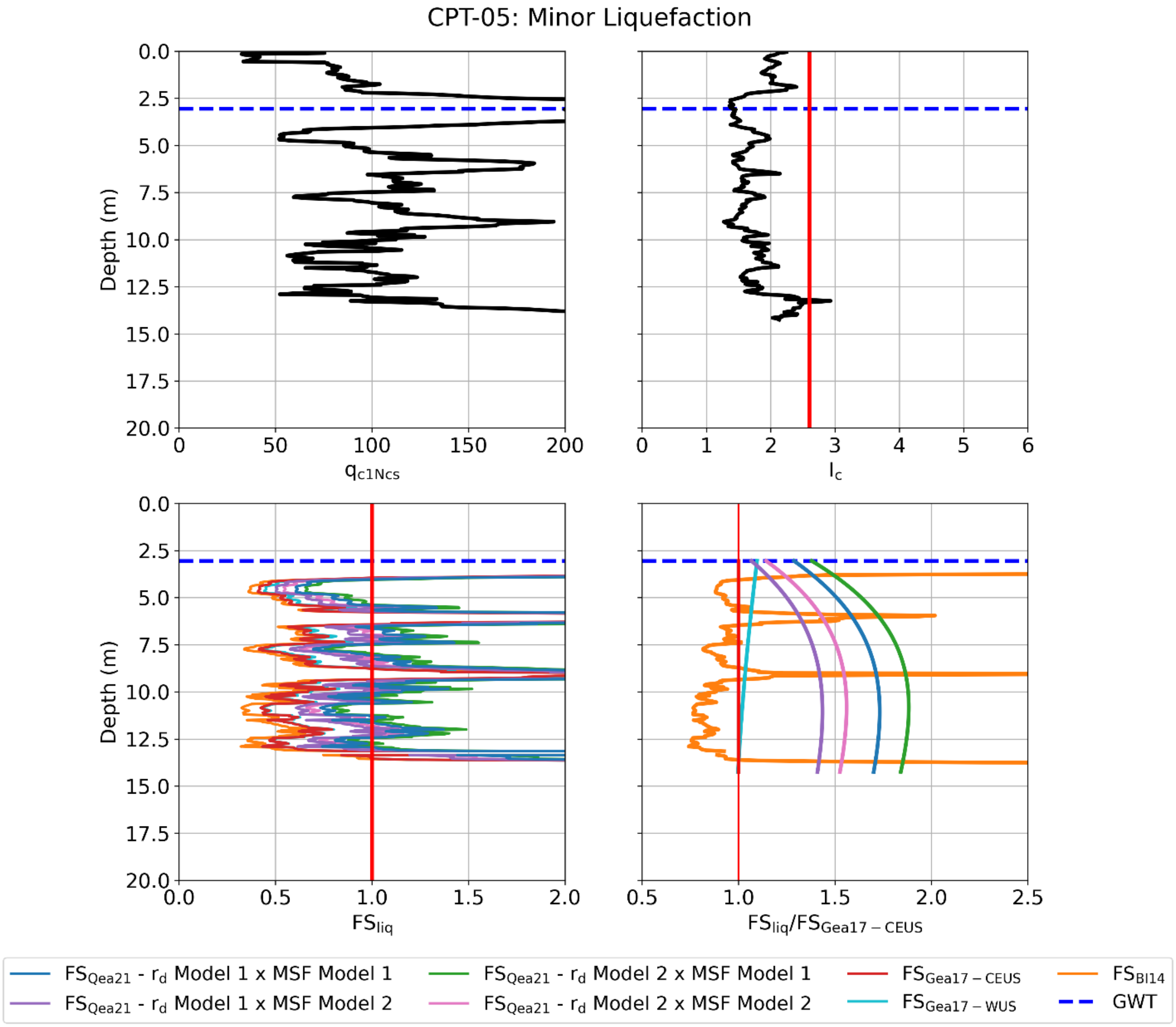

Figure G.5. Profiles of q_{c1Ncs}, I_c, FS_{liq}, and FS_{liq} normalized by FS_{liq} for the Green et al. (2017) CEUS model ($FS_{Gea17-CEUS}$) for CPT-05, Site 2 (minor post-event liquefaction manifestations observed). FS_{liq} for the Qea21 model (FS_{Qea21}) is shown for the ZR19_IZ database.

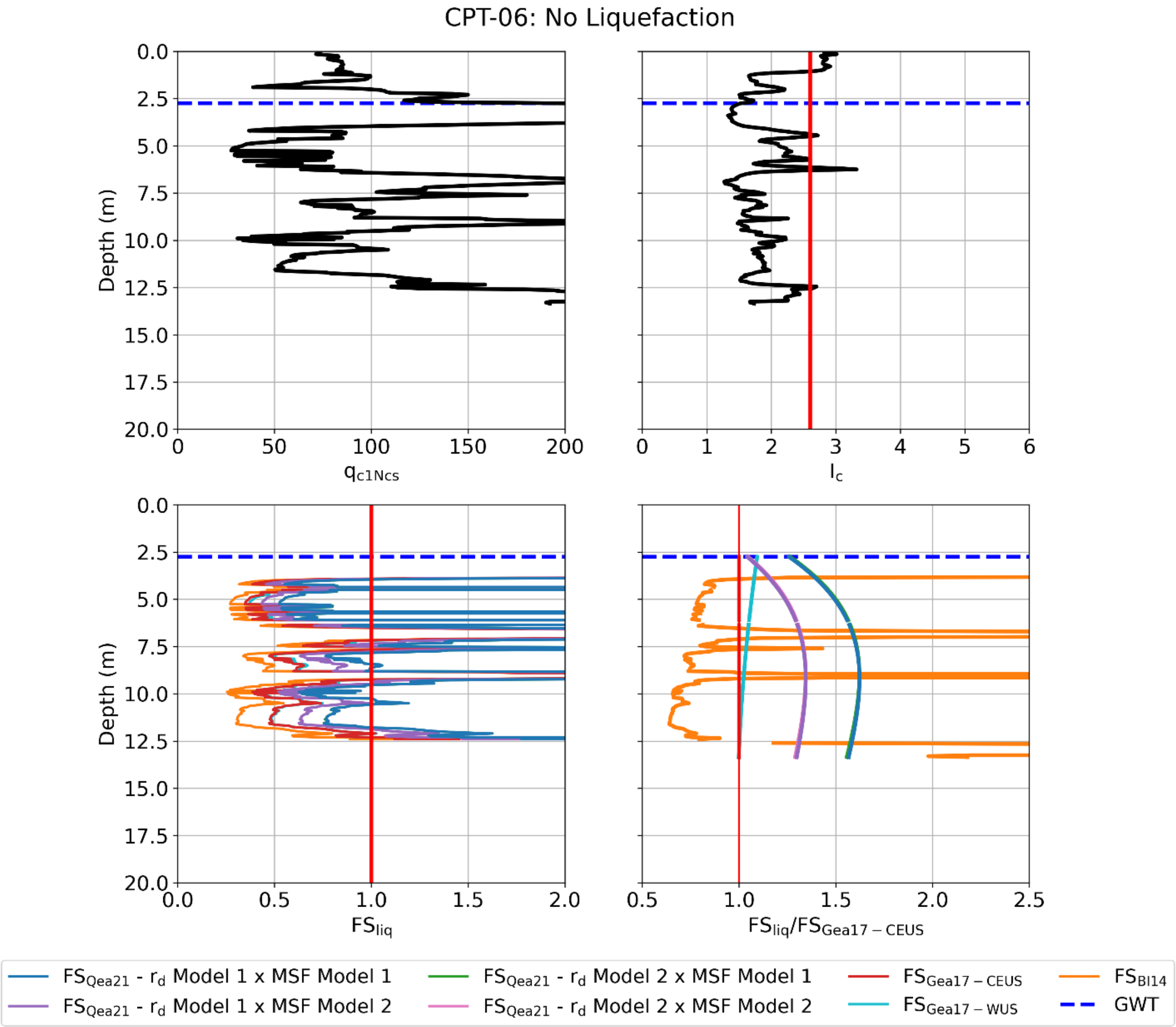

Figure G.6. Profiles of q_{c1Ncs}, I_c, FS_{liq}, and FS_{liq} normalized by FS_{liq} for the Green et al. (2017) CEUS model ($FS_{Gea17-CEUS}$) for CPT-06, Site 2 (no post-event liquefaction manifestations observed). FS_{liq} for the Qea21 model (FS_{Qea21}) is shown for the ZR19_IZ database.

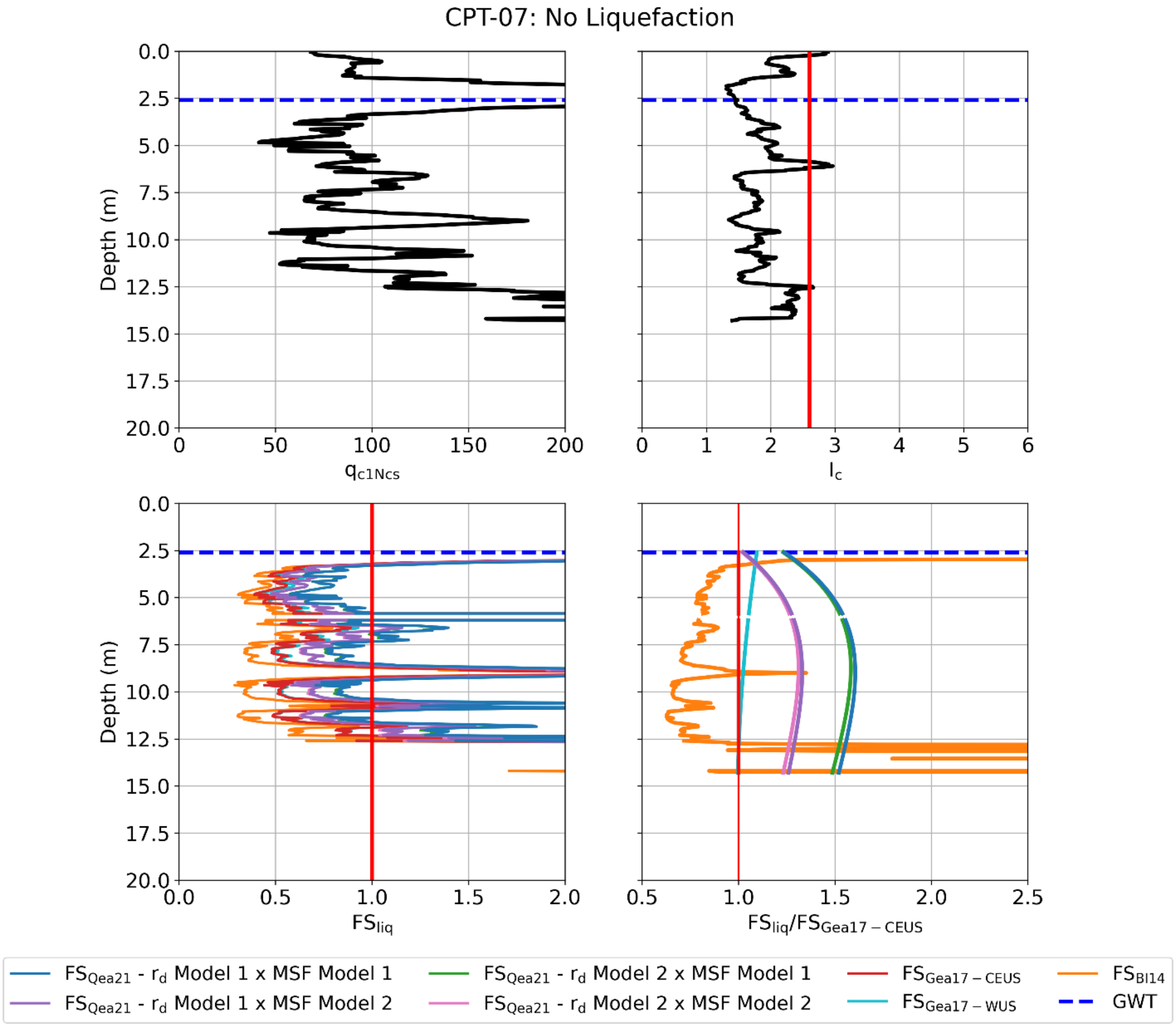

Figure G.7. Profiles of q_{c1Ncs}, I_c, FS_{liq}, and FS_{liq} normalized by FS_{liq} for the Green et al. (2017) CEUS model ($FS_{Gea17\text{-}CEUS}$) for CPT-07, Site 2 (no post-event liquefaction manifestations observed). FS_{liq} for the Qea21 model (FS_{Qea21}) is shown for the ZR19_IZ database.

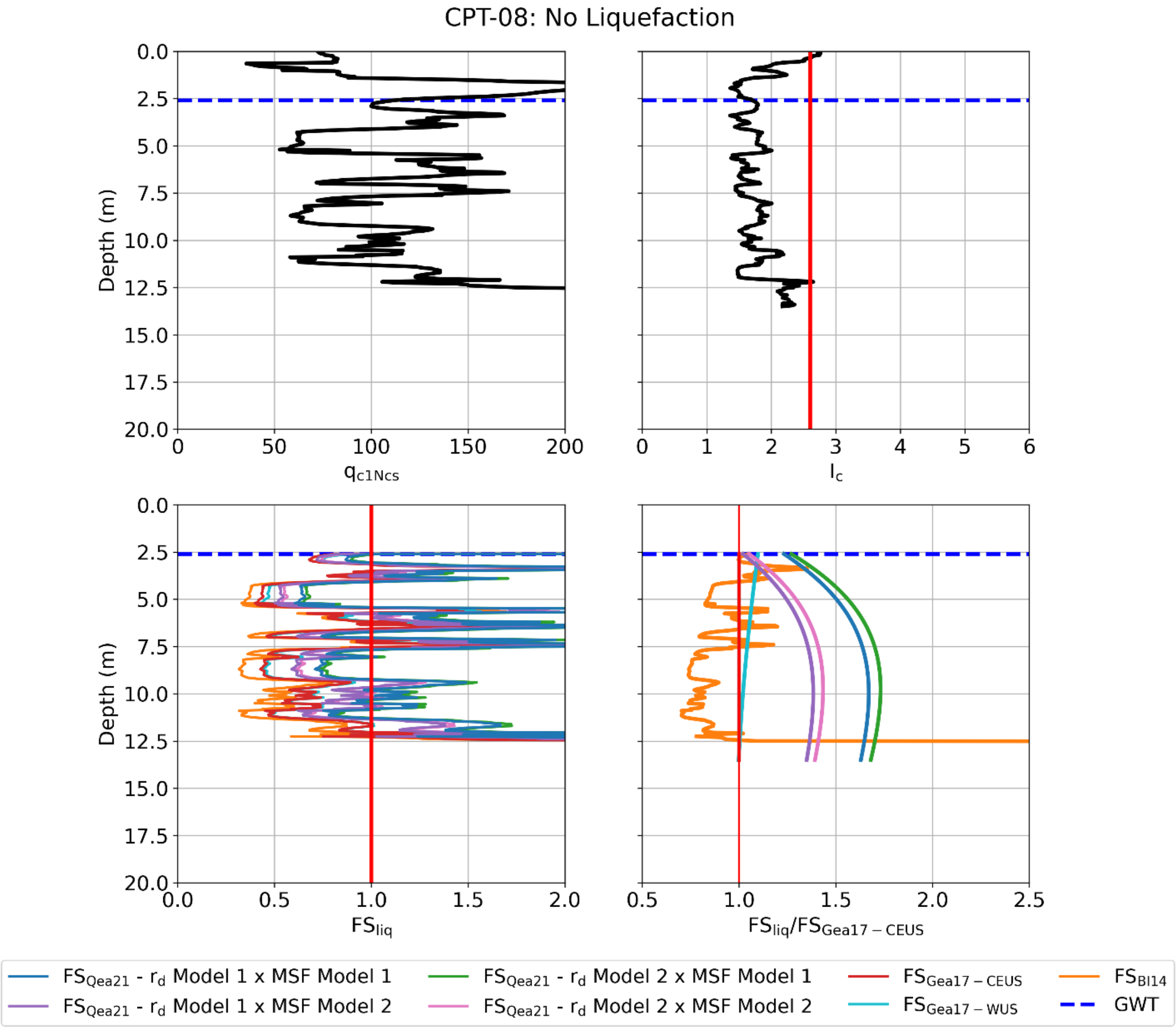

Figure G.8. Profiles of q_{c1Ncs}, I_c, FS_{liq}, and FS_{liq} normalized by FS_{liq} for the Green et al. (2017) CEUS model ($FS_{Gea17-CEUS}$) for CPT-08, Site 2 (no post-event liquefaction manifestations observed). FS_{liq} for the Qea21 model (FS_{Qea21}) is shown for the ZR19_IZ database.

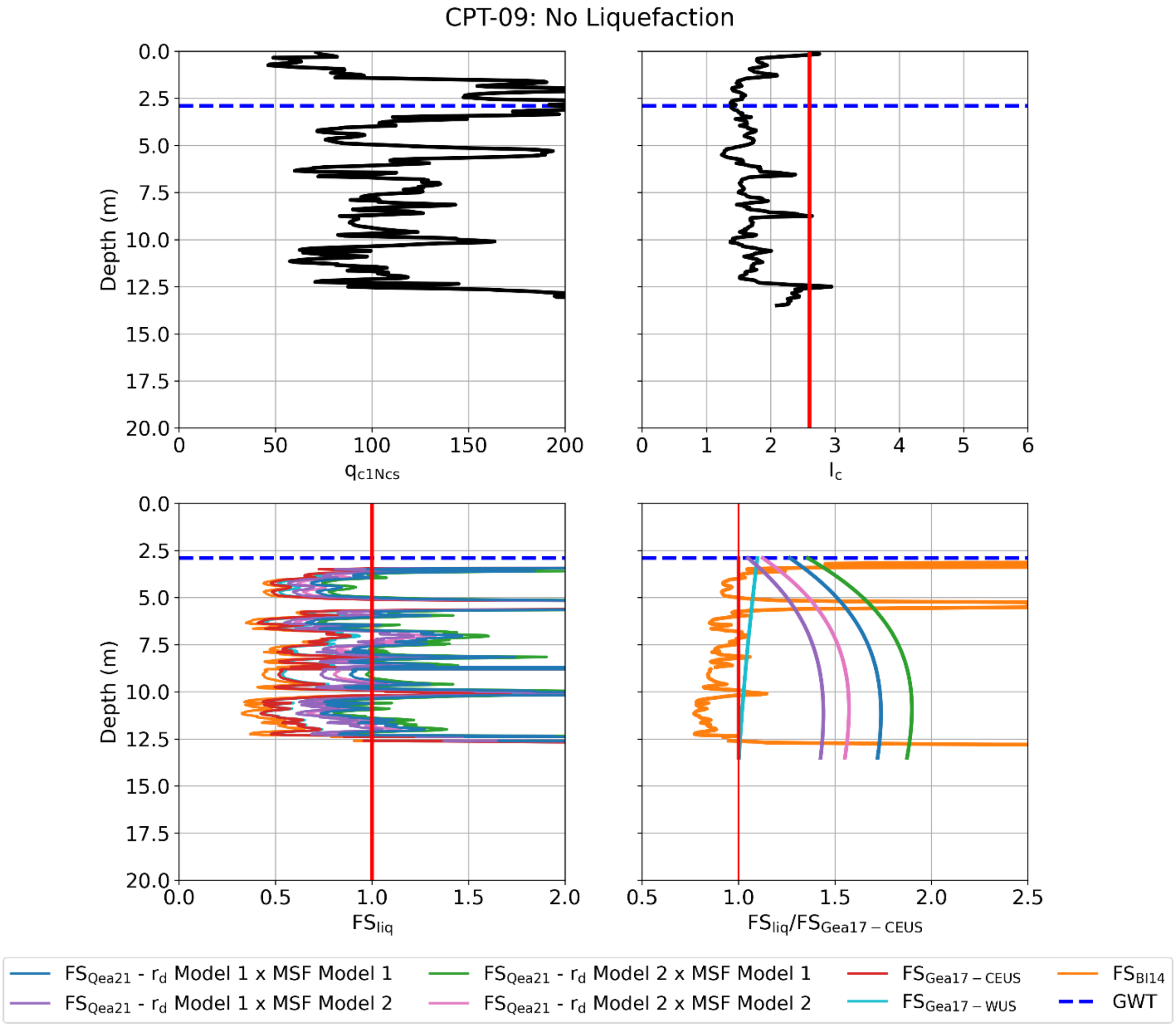

Figure G.9. Profiles of q_{c1Ncs}, I_c, FS_{liq}, and FS_{liq} normalized by FS_{liq} for the Green et al. (2017) CEUS model ($FS_{Gea17-CEUS}$) for CPT-09, Site 2 (no post-event liquefaction manifestations observed). FS_{liq} for the Qea21 model (FS_{Qea21}) is shown for the ZR19_IZ database.

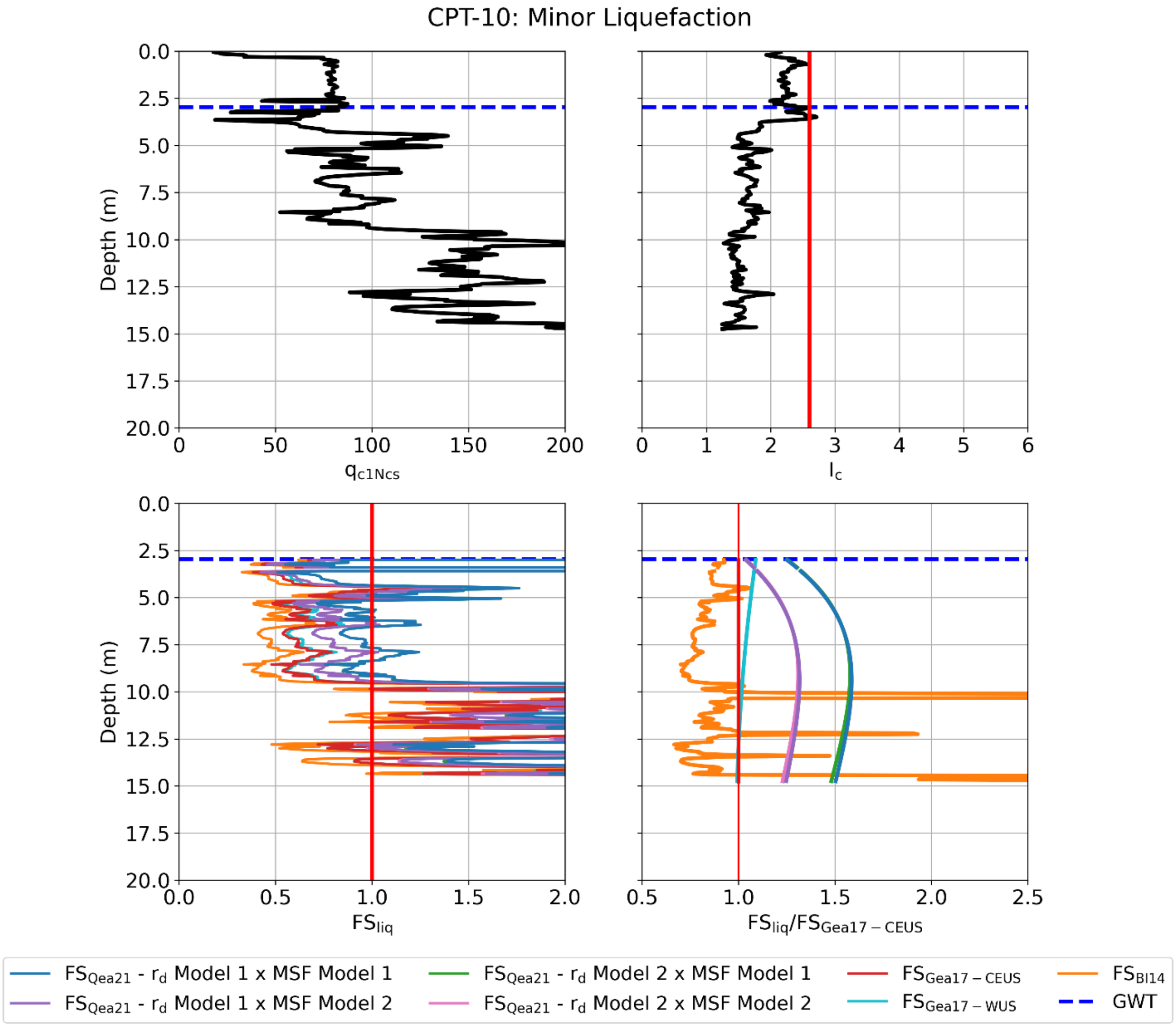

Figure G.10. Profiles of q_{c1Ncs}, I_c, FS_{liq}, and FS_{liq} normalized by FS_{liq} for the Green et al. (2017) CEUS model ($FS_{Gea17-CEUS}$) for CPT-10, Site 3 (minor post-event liquefaction manifestations observed). FS_{liq} for the Qea21 model (FS_{Qea21}) is shown for the ZR19_IZ database.

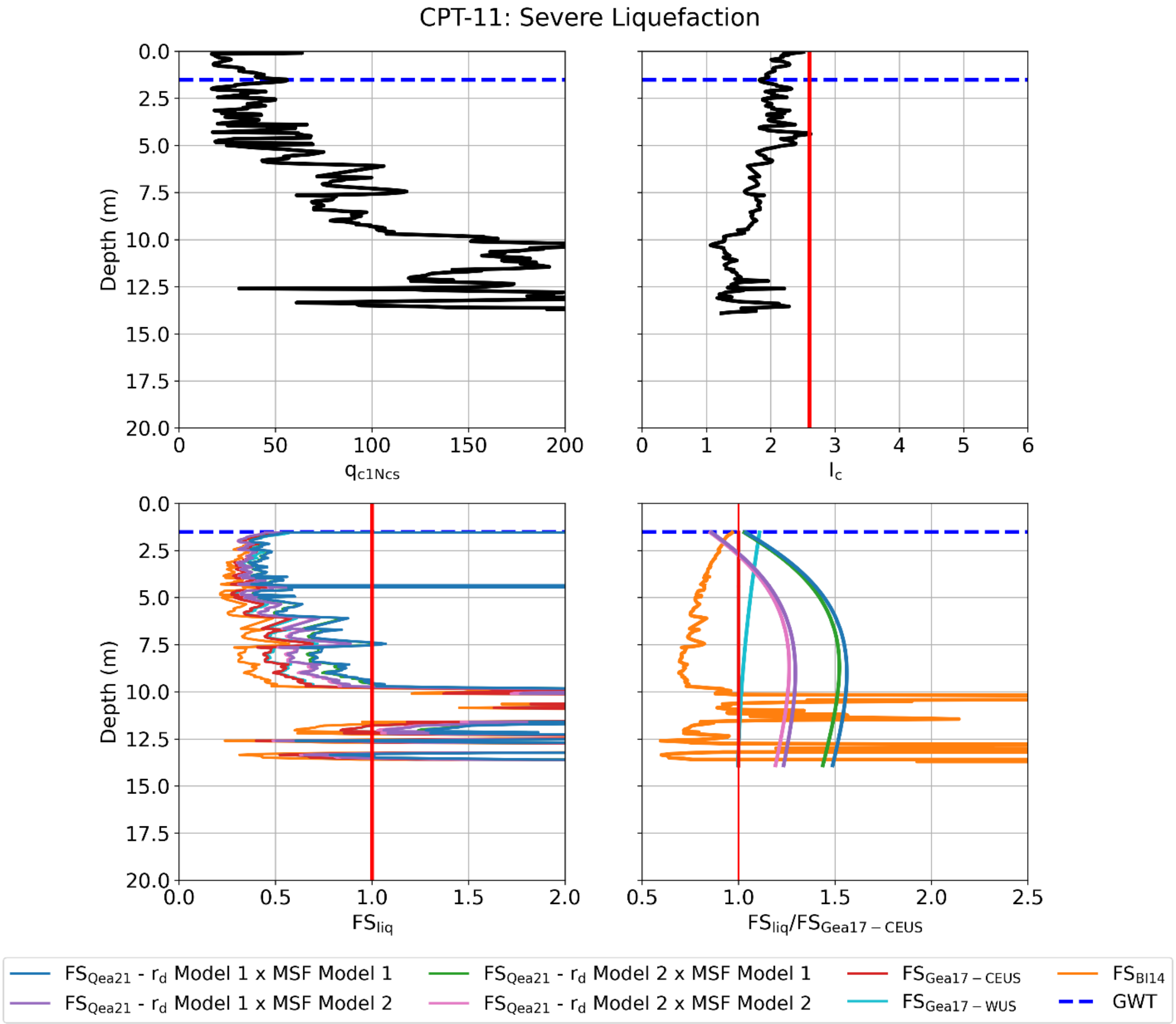

Figure G.11. Profiles of q_{c1Ncs}, I_c, FS_{liq}, and FS_{liq} normalized by FS_{liq} for the Green et al. (2017) CEUS model ($FS_{Gea17-CEUS}$) for CPT-11, Site 3 (severe post-event liquefaction manifestations observed). FS_{liq} for the Qea21 model (FS_{Qea21}) is shown for the ZR19_IZ database.

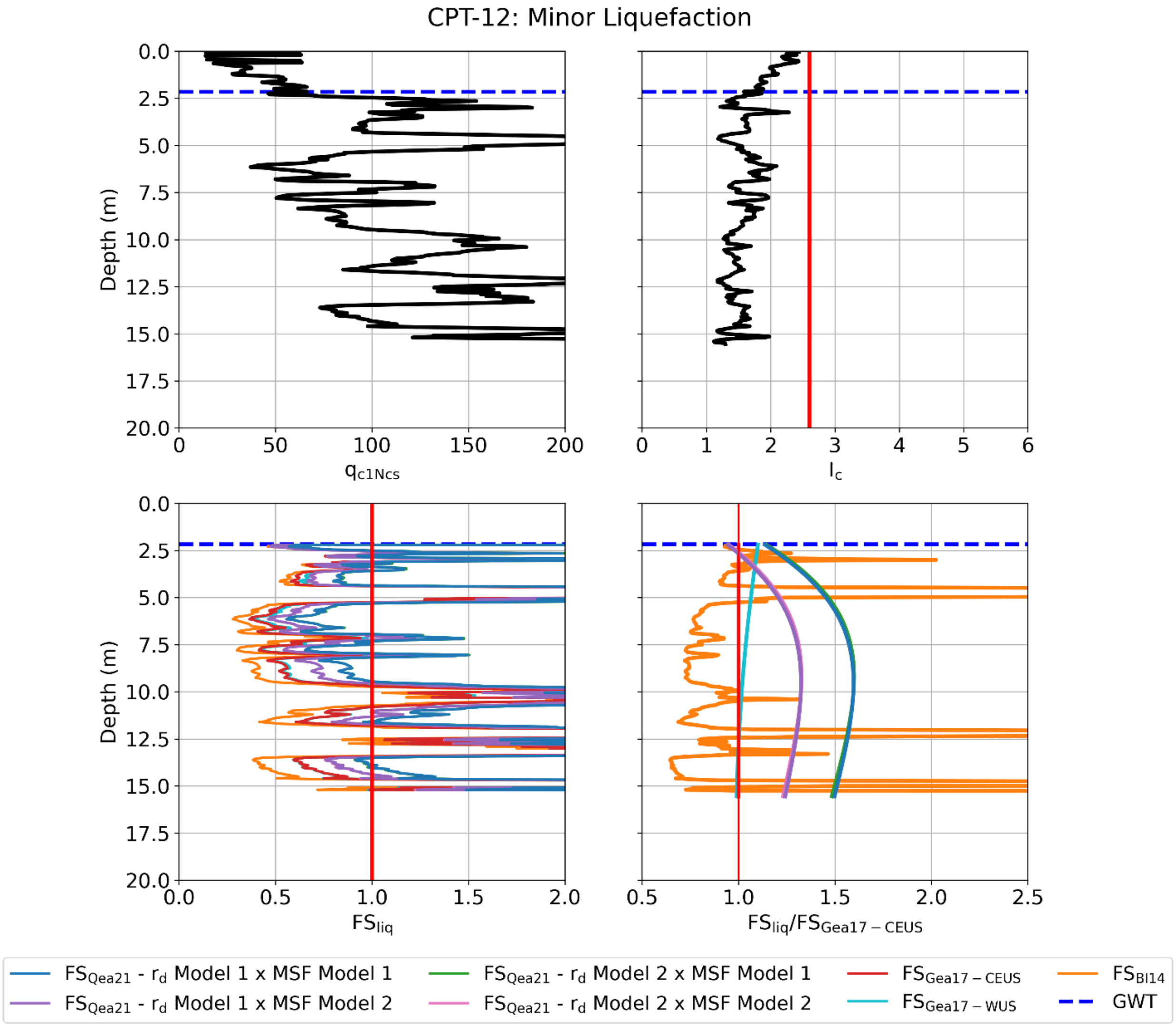

Figure G.12. Profiles of q_{c1Ncs}, I_c, FS_{liq}, and FS_{liq} normalized by FS_{liq} for the Green et al. (2017) CEUS model ($FS_{Gea17-CEUS}$) for CPT-12, Site 3 (minor post-event liquefaction manifestations observed). FS_{liq} for the Qea21 model (FS_{Qea21}) is shown for the ZR19_IZ database.

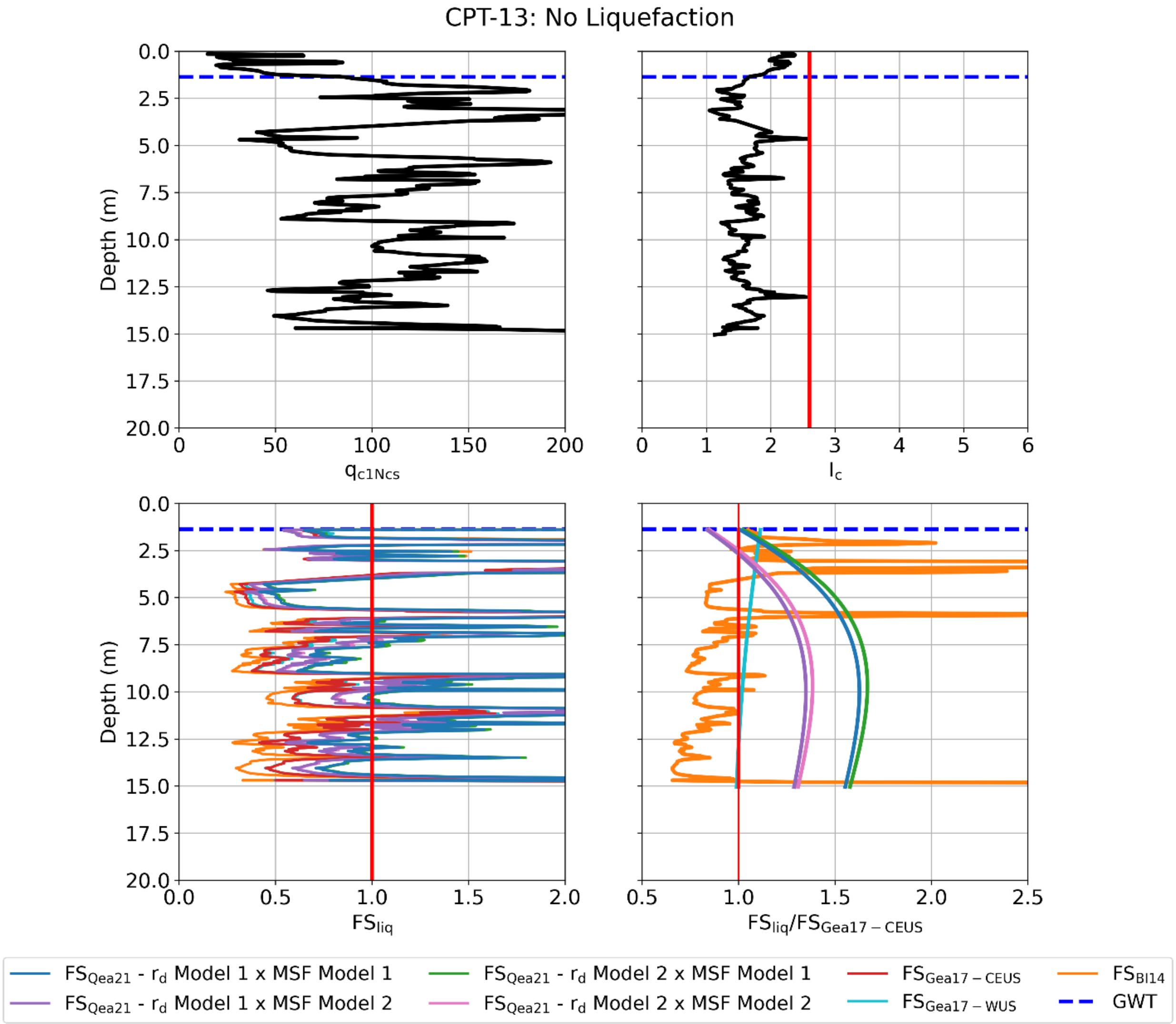

Figure G.13. Profiles of q_{c1Ncs}, I_c, FS_{liq}, and FS_{liq} normalized by FS_{liq} for the Green et al. (2017) CEUS model ($FS_{Gea17-CEUS}$) for CPT-13, Site 3 (no post-event liquefaction manifestations observed). FS_{liq} for the Qea21 model (FS_{Qea21}) is shown for the ZR19_IZ database.

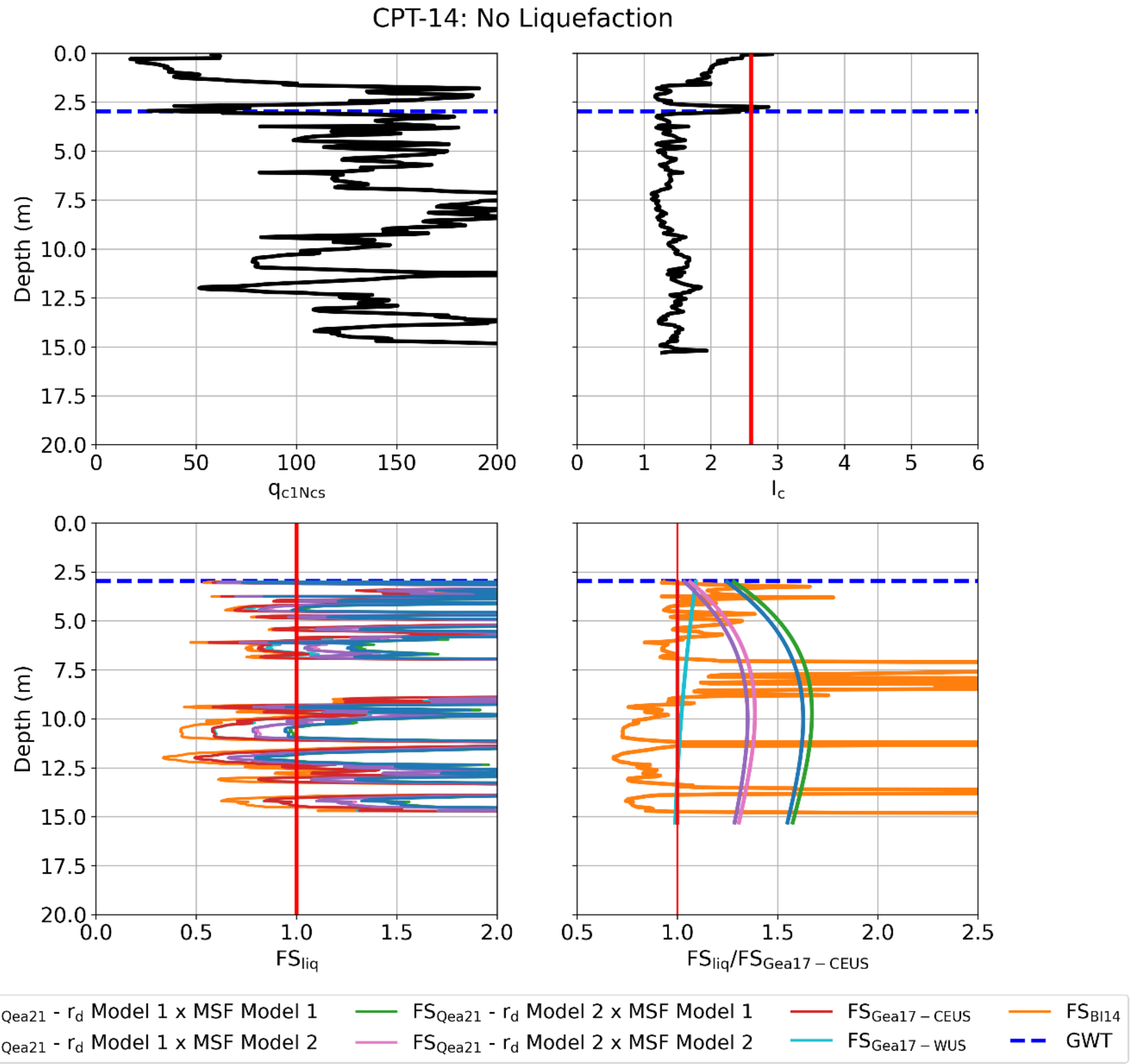

Figure G.14. Profiles of q_{c1Ncs}, I_c, FS_{liq}, and FS_{liq} normalized by FS_{liq} for the Green et al. (2017) CEUS model ($FS_{Gea17\text{-}CEUS}$) for CPT-14, Site 3 (no post-event liquefaction manifestations observed). FS_{liq} for the Qea21 model (FS_{Qea21}) is shown for the ZR19_IZ database.

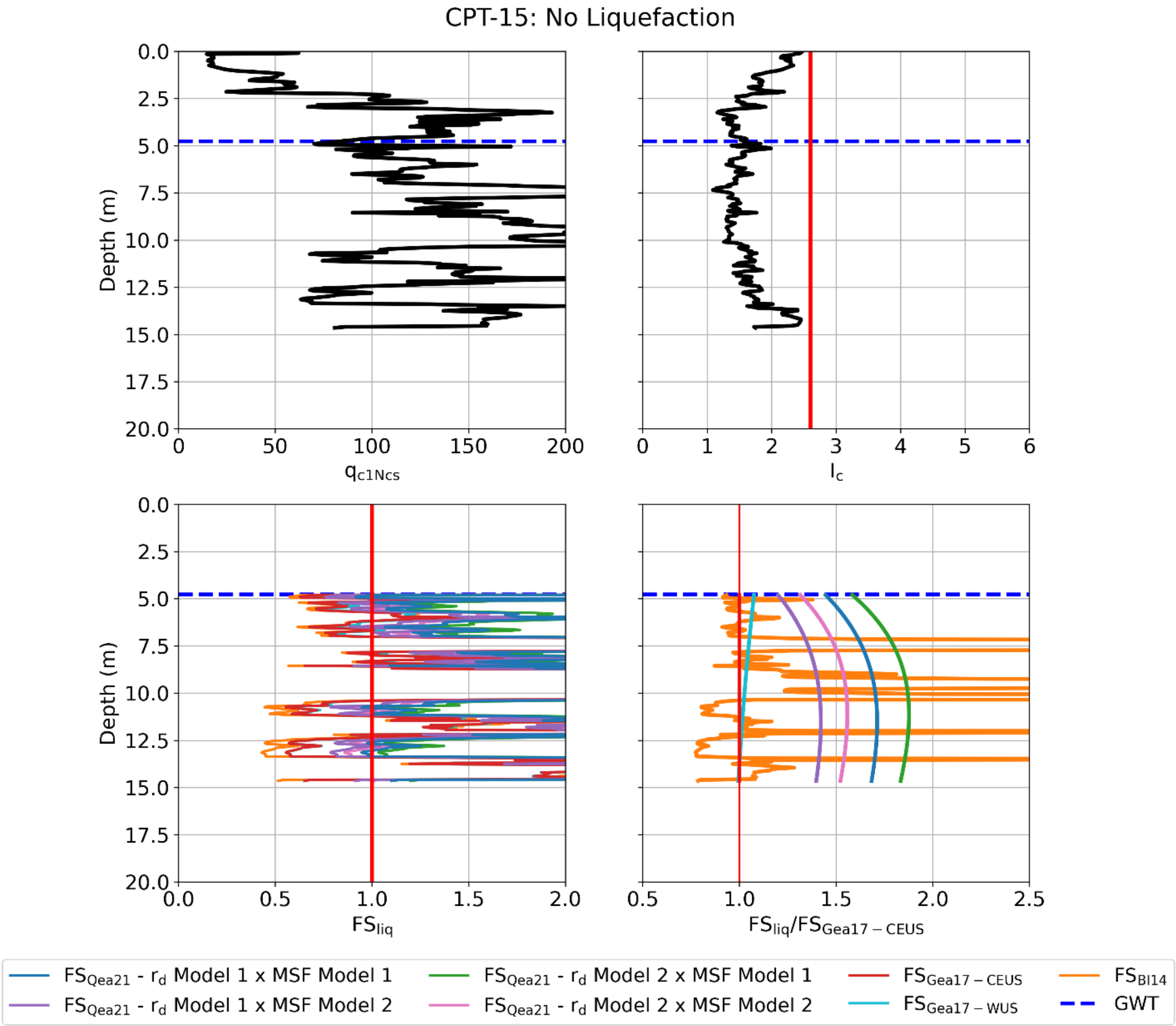

Figure G.15. Profiles of q_{c1Ncs}, I_c, FS_{liq}, and FS_{liq} normalized by FS_{liq} for the Green et al. (2017) CEUS model ($FS_{Gea17\text{-}CEUS}$) for CPT-15, Site 3 (no post-event liquefaction manifestations observed). FS_{liq} for the Qea21 model (FS_{Qea21}) is shown for the ZR19_IZ database.

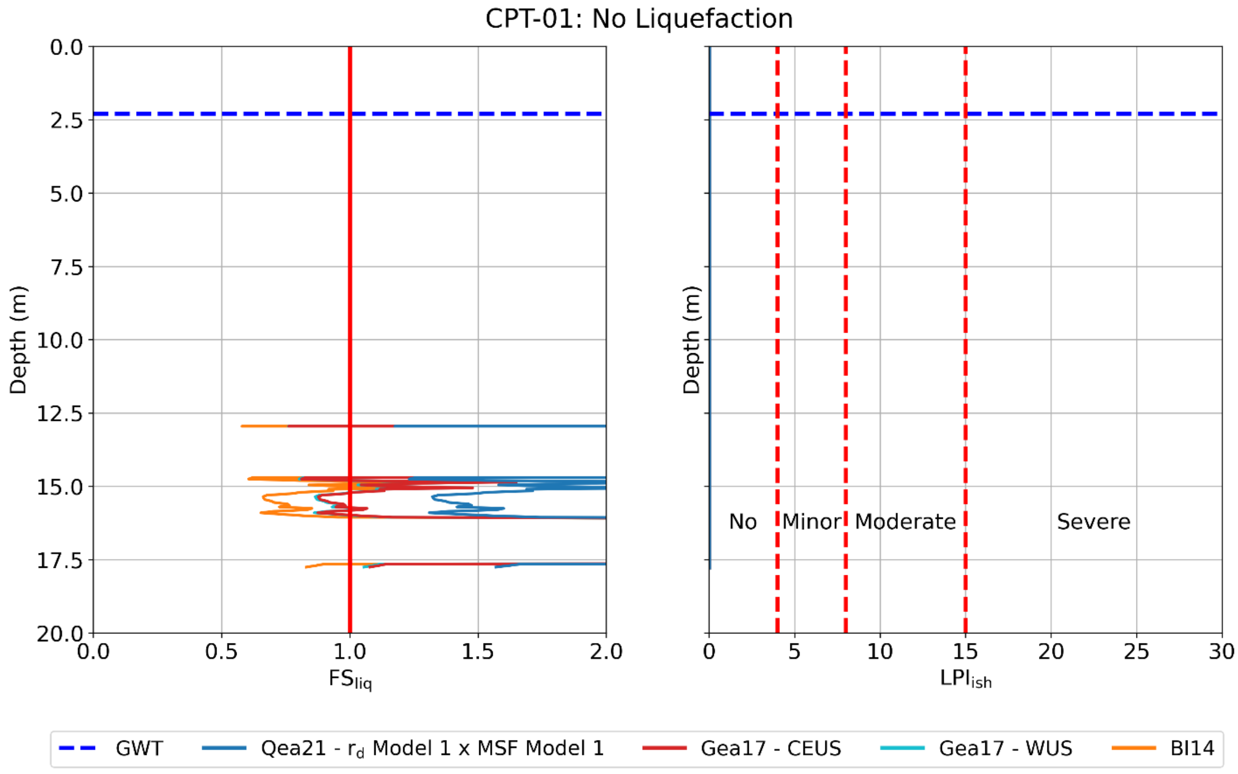

Figure G.16. FS$_{liq}$ and LPI$_{ish}$ profiles for CPT-01, Site 1. Results for the Qea21 model are shown for the ZR19_IZ database, r$_d$ Model 1, and MSF Model 1. LPI$_{ish}$ liquefaction surficial manifestation severity thresholds are also indicated.

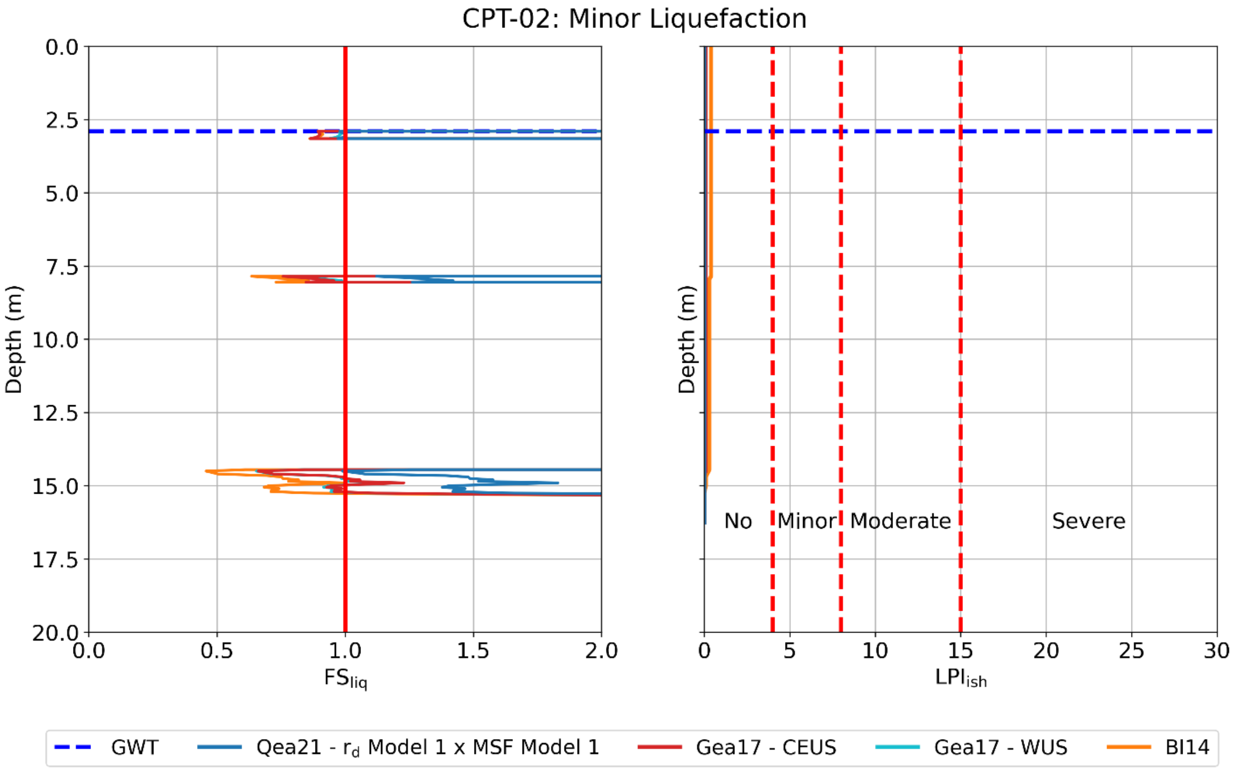

Figure G.17. FS$_{liq}$ and LPI$_{ish}$ profiles for CPT-02, Site 1. Results for the Qea21 model are shown for the ZR19_IZ database, rd model 1, and MSF model 1. LPI$_{ish}$ liquefaction surficial manifestation severity thresholds are also indicated.

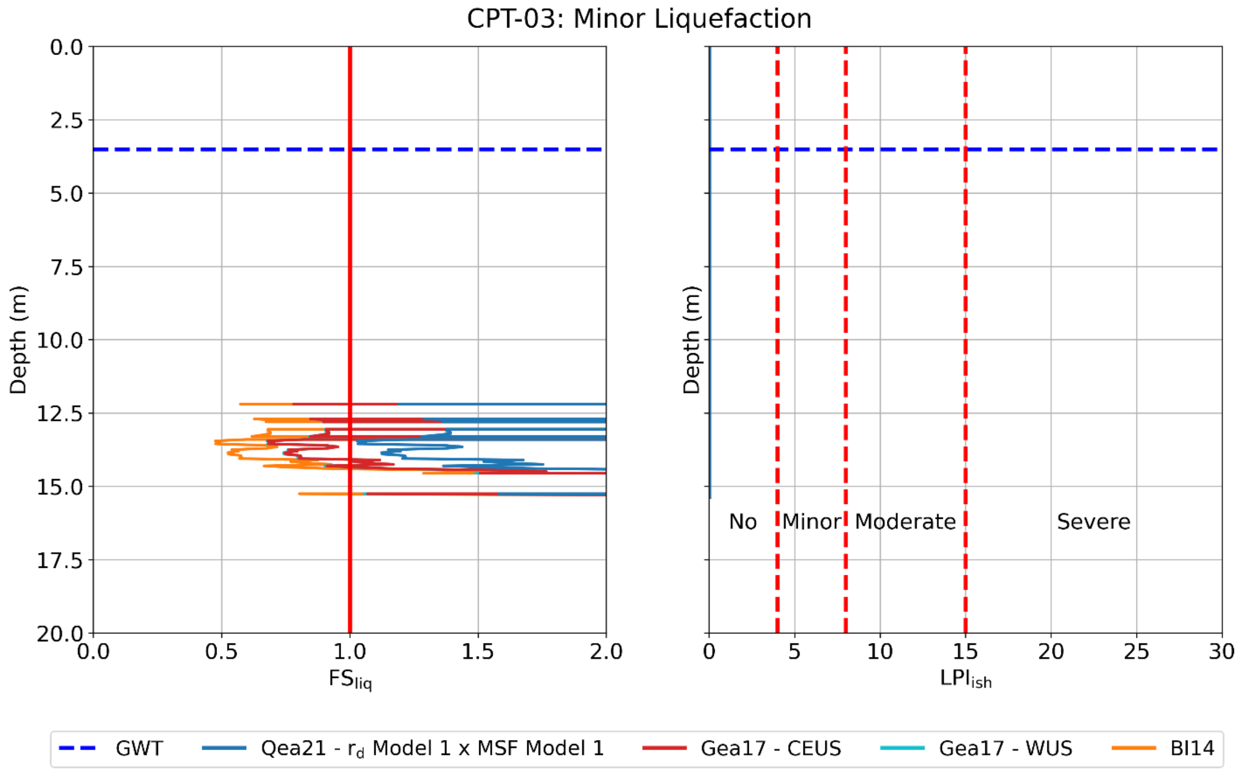

Figure G.18. FS_{liq} and LPI_{ish} profiles for CPT-03, Site 1. Results for the Qea21 model are shown for the ZR19_IZ database, r_d Model 1, and MSF Model 1. LPI_{ish} liquefaction surficial manifestation severity thresholds are also indicated.

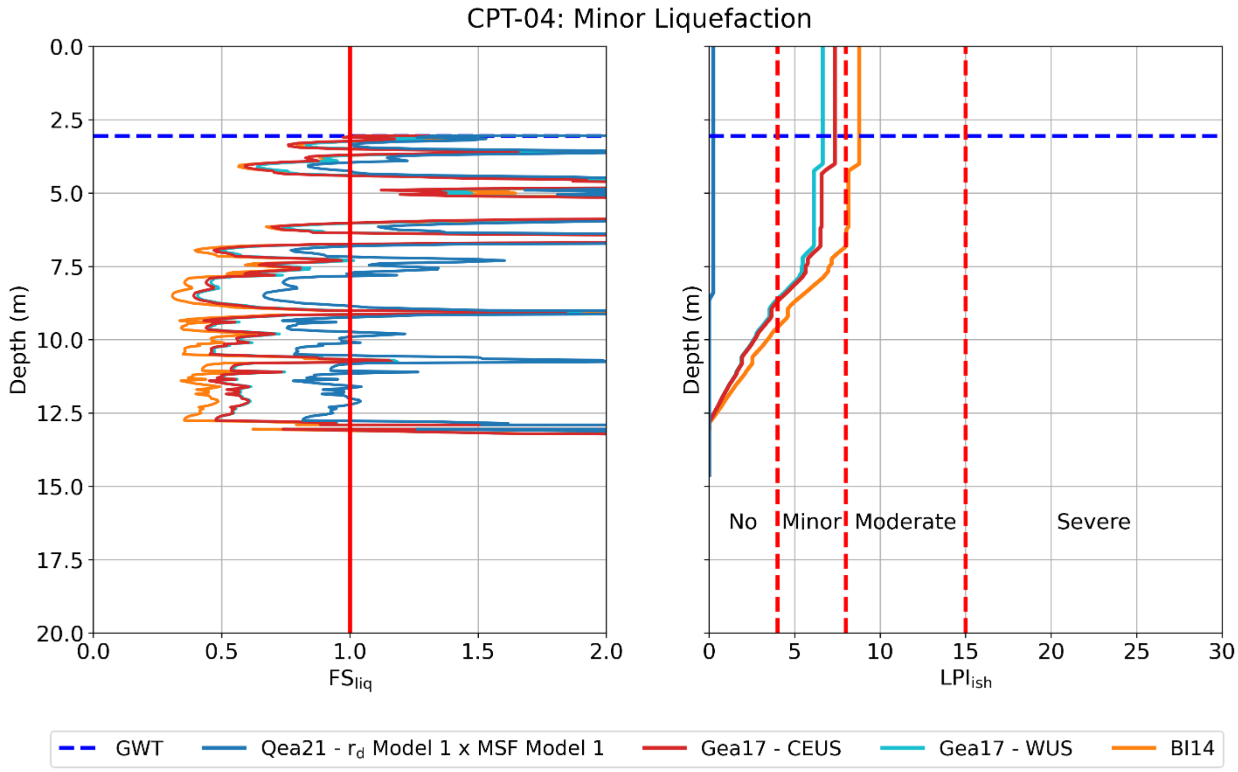

Figure G.19. FS_{liq} and LPI_{ish} profiles for CPT-04, Site 2. Results for the Qea21 model are shown for the ZR19_IZ database, r_d Model 1, and MSF Model 1. LPI_{ish} liquefaction surficial manifestation severity thresholds are also indicated.

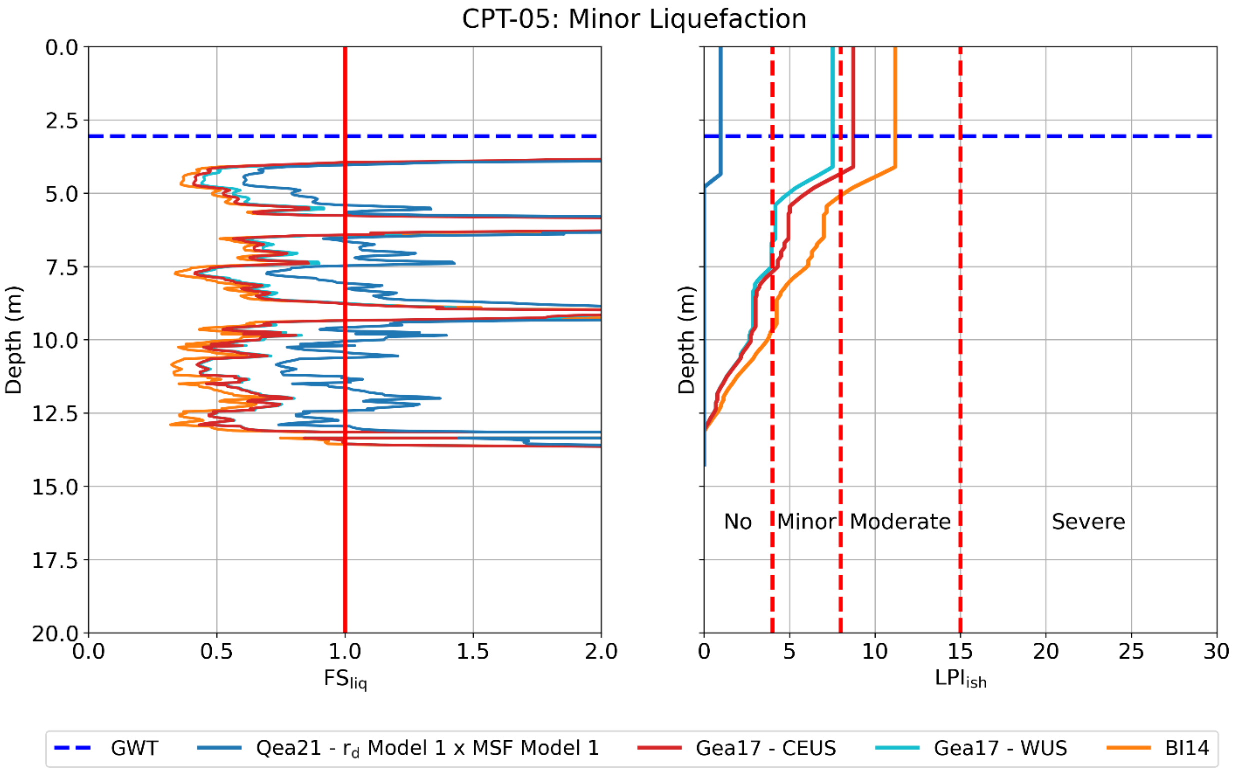

Figure G.20. FS_{liq} and LPI_{ish} profiles for CPT-05, Site 2. Results for the Qea21 model are shown for the ZR19_IZ database, r_d Model 1, and MSF Model 1. LPI_{ish} liquefaction surficial manifestation severity thresholds are also indicated.

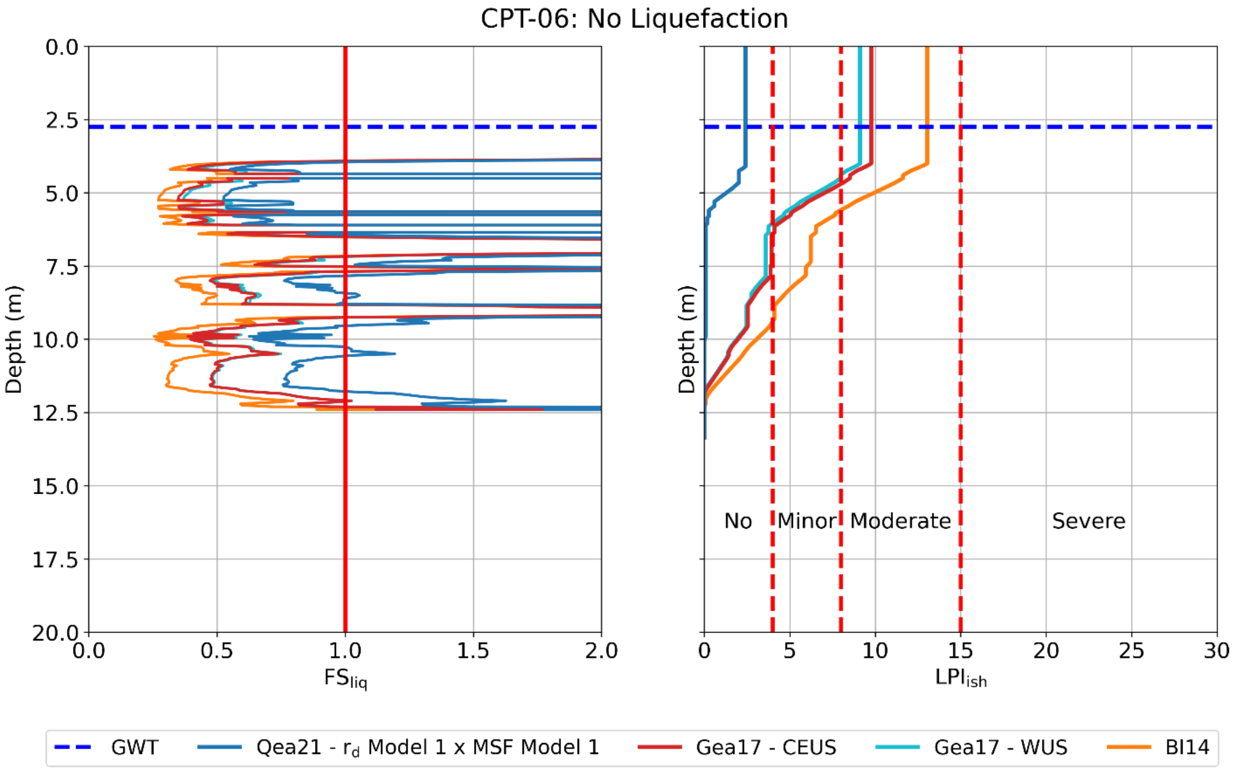

Figure G.21. FS$_{liq}$ and LPI$_{ish}$ profiles for CPT-06, Site 2. Results for the Qea21 model are shown for the ZR19_IZ database, r$_d$ Model 1, and MSF Model 1. LPI$_{ish}$ liquefaction surficial manifestation severity thresholds are also indicated.

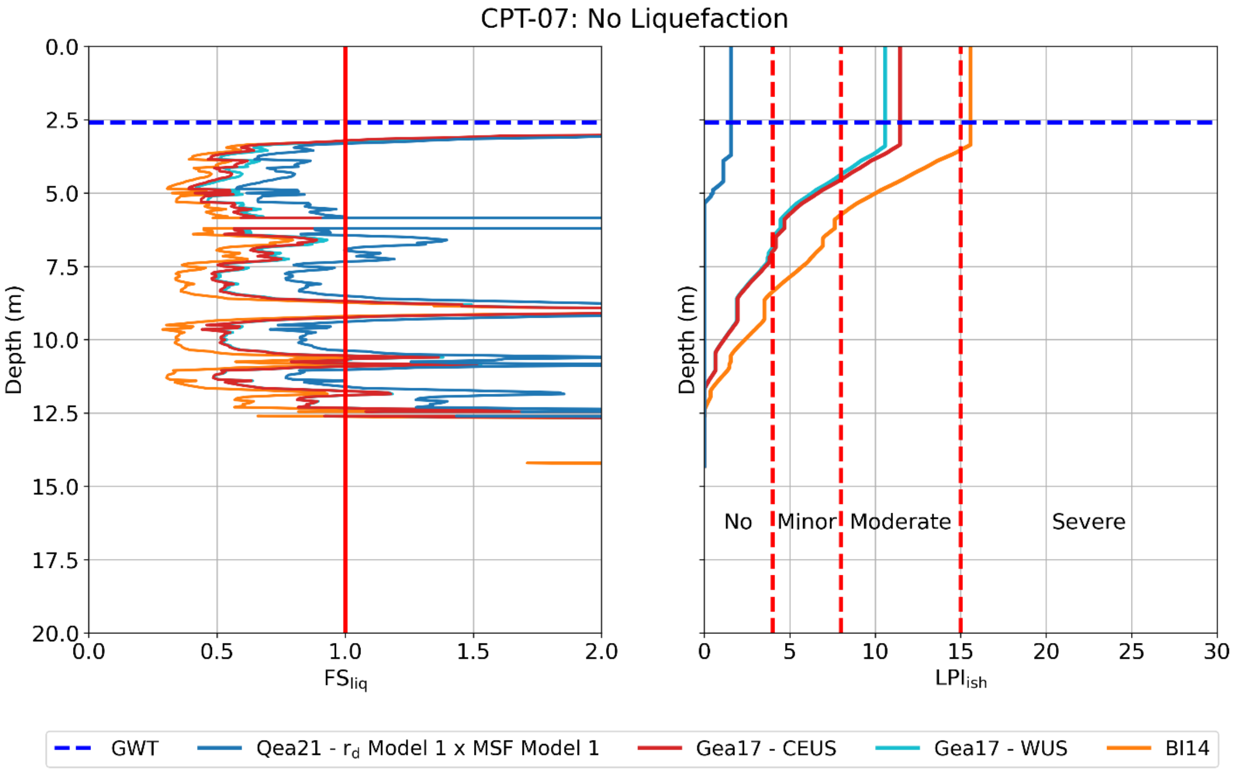

Figure G.22. FS$_{liq}$ and LPI$_{ish}$ profiles for CPT-07, Site 2. Results for the Qea21 model are shown for the ZR19_IZ database, r$_d$ Model 1, and MSF Model 1. LPI$_{ish}$ liquefaction surficial manifestation severity thresholds are also indicated.

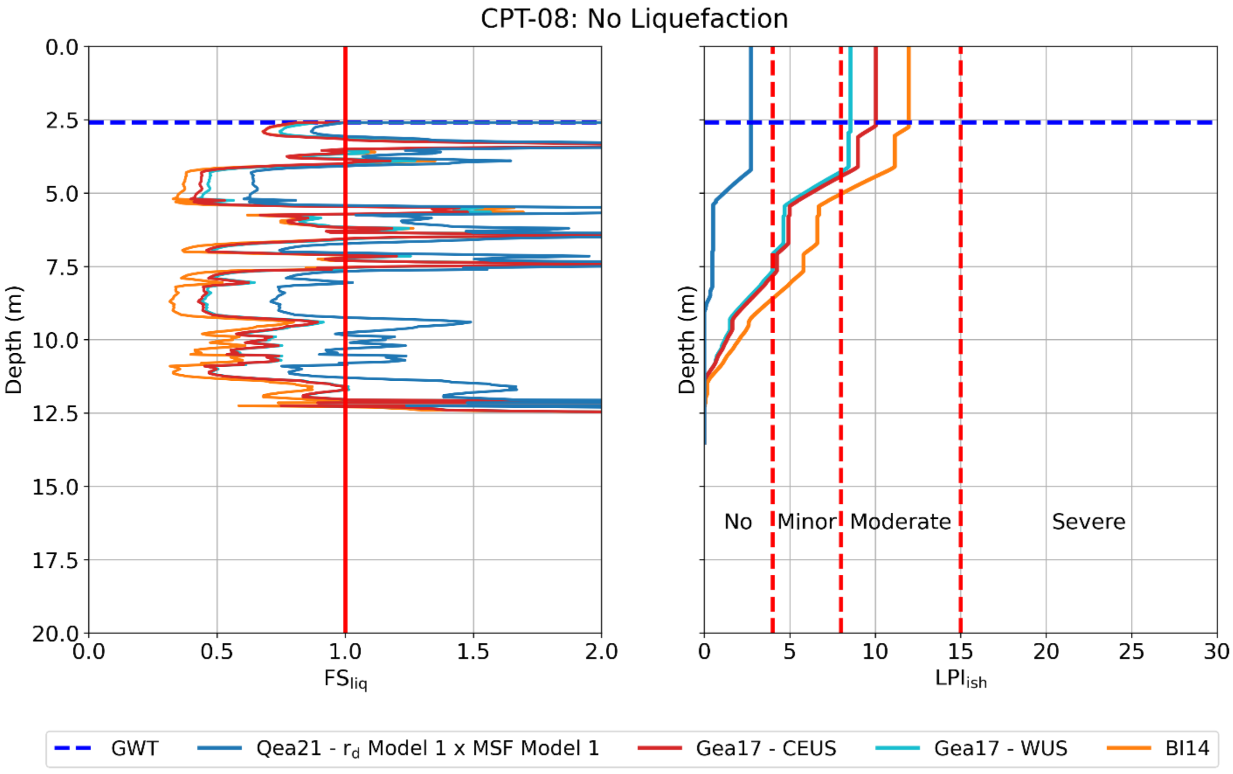

Figure G.23. FS_{liq} and LPI_{ish} profiles for CPT-08, Site 2. Results for the Qea21 model are shown for the ZR19_IZ database, r_d Model 1, and MSF Model 1. LPI_{ish} liquefaction surficial manifestation severity thresholds are also indicated.

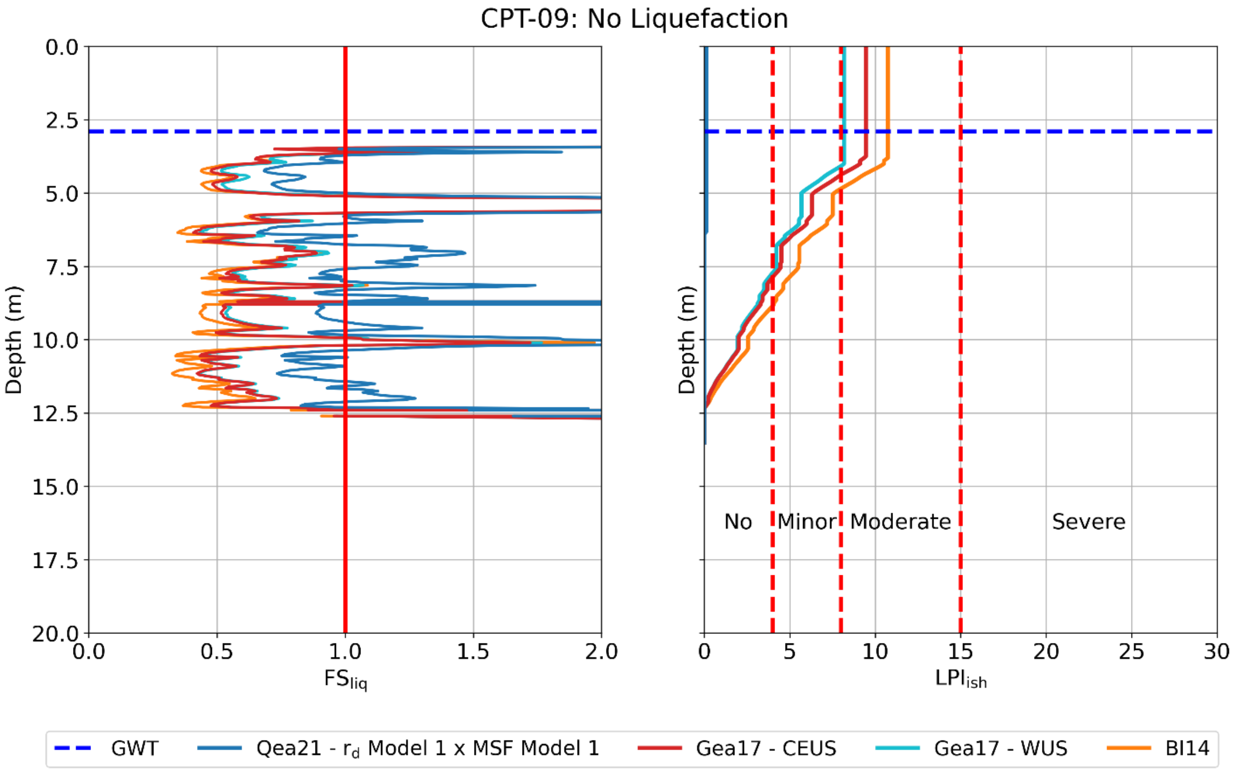

Figure G.24. FS$_{liq}$ and LPI$_{ish}$ profiles for CPT-09, Site 2. Results for the Qea21 model are shown for the ZR19_IZ database, r$_d$ Model 1, and MSF Model 1. LPI$_{ish}$ liquefaction surficial manifestation severity thresholds are also indicated.

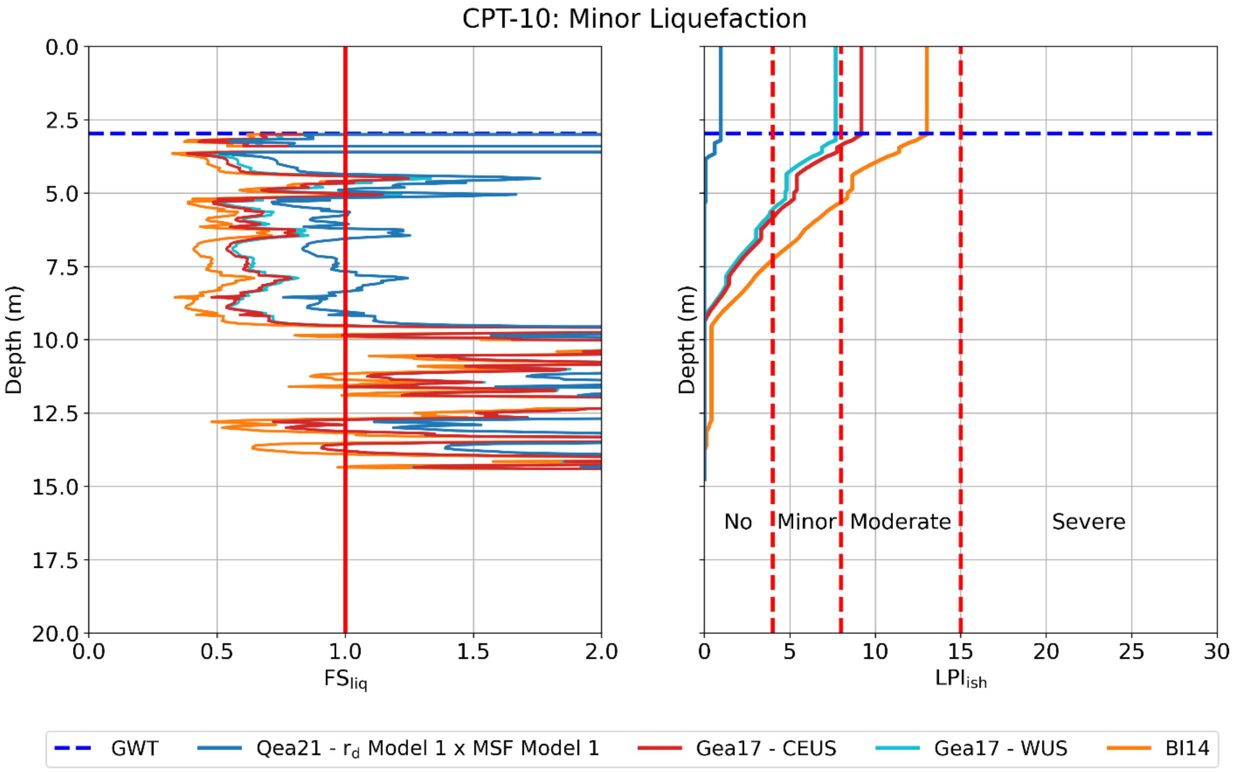

Figure G.25. FS_{liq} and LPI_{ish} profiles for CPT-10, Site 3. Results for the Qea21 model are shown for the ZR19_IZ database, r_d Model 1, and MSF Model 1. LPI_{ish} liquefaction surficial manifestation severity thresholds are also indicated.

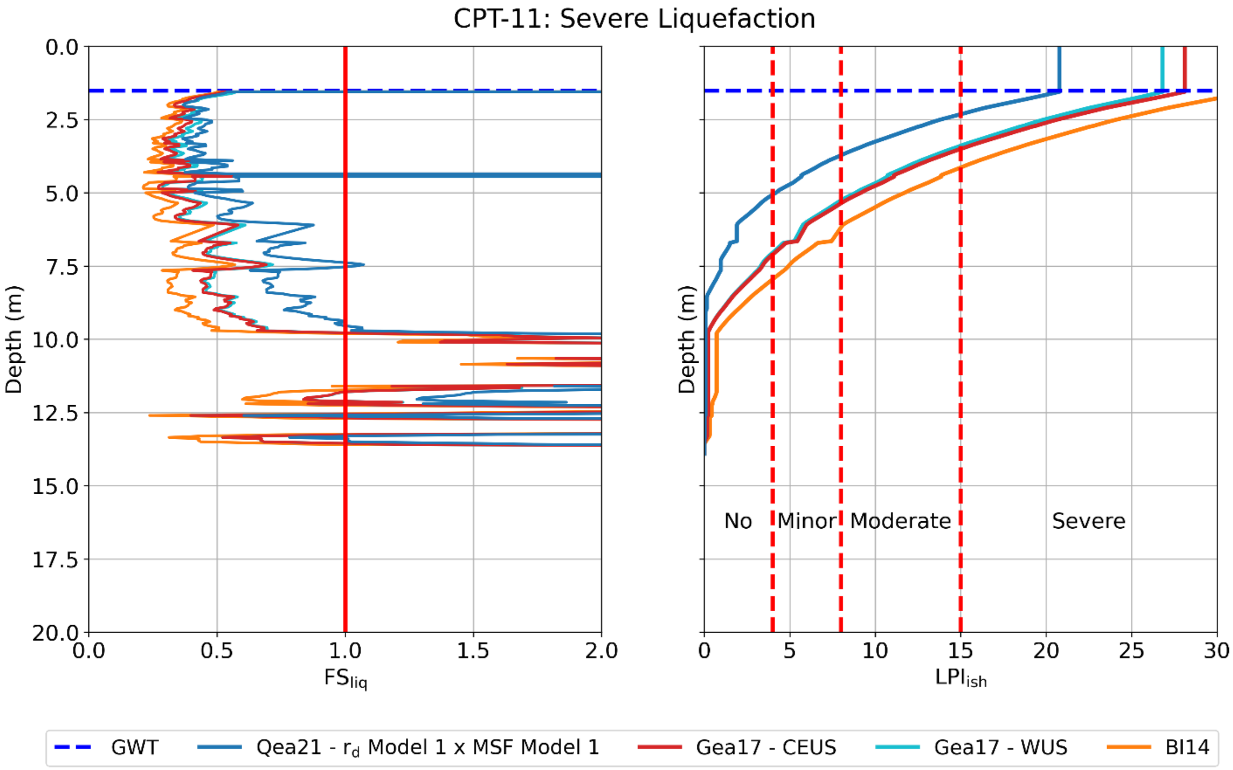

Figure G.26. FS_{liq} and LPI_{ish} profiles for CPT-11, Site 3. Results for the Qea21 model are shown for the ZR19_IZ database, r_d Model 1, and MSF Model 1. LPI_{ish} liquefaction surficial manifestation severity thresholds are also indicated.

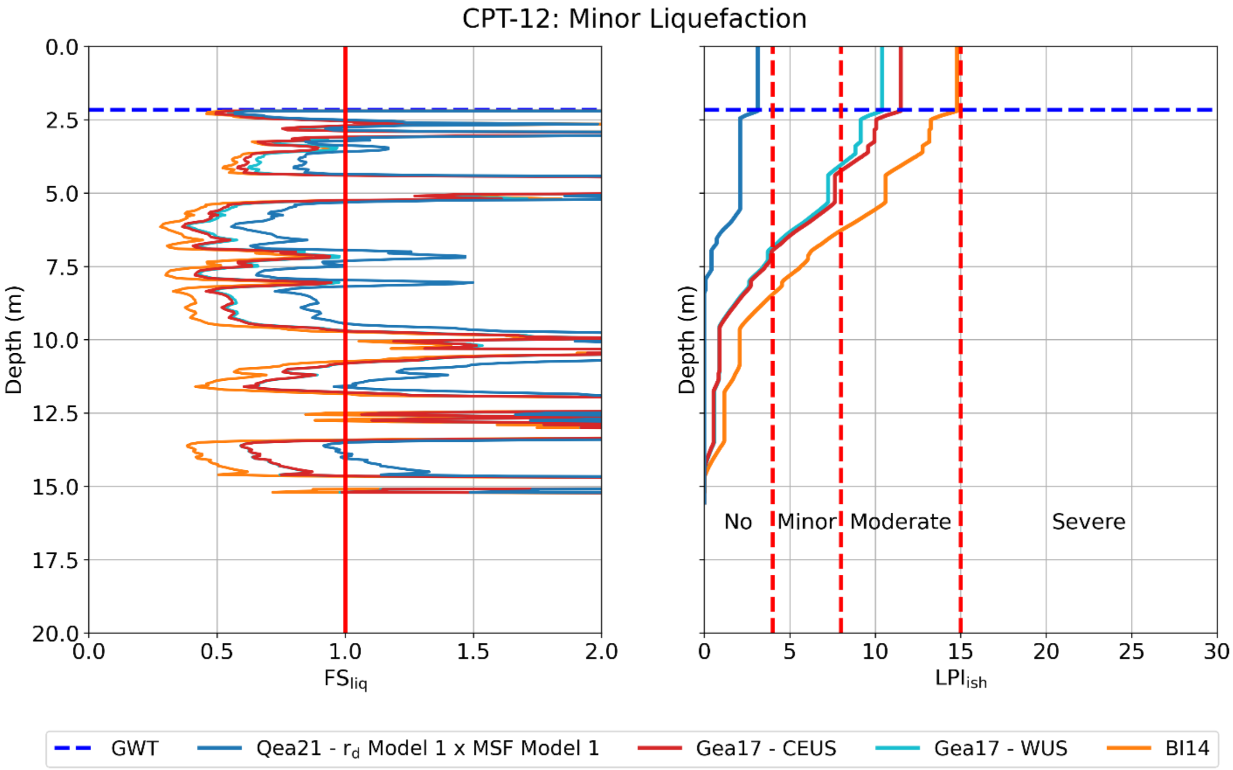

Figure G.27. FS_{liq} and LPI_{ish} profiles for CPT-12, Site 3. Results for the Qea21 model are shown for the ZR19_IZ database, r_d Model 1, and MSF Model 1. LPI_{ish} liquefaction surficial manifestation severity thresholds are also indicated.

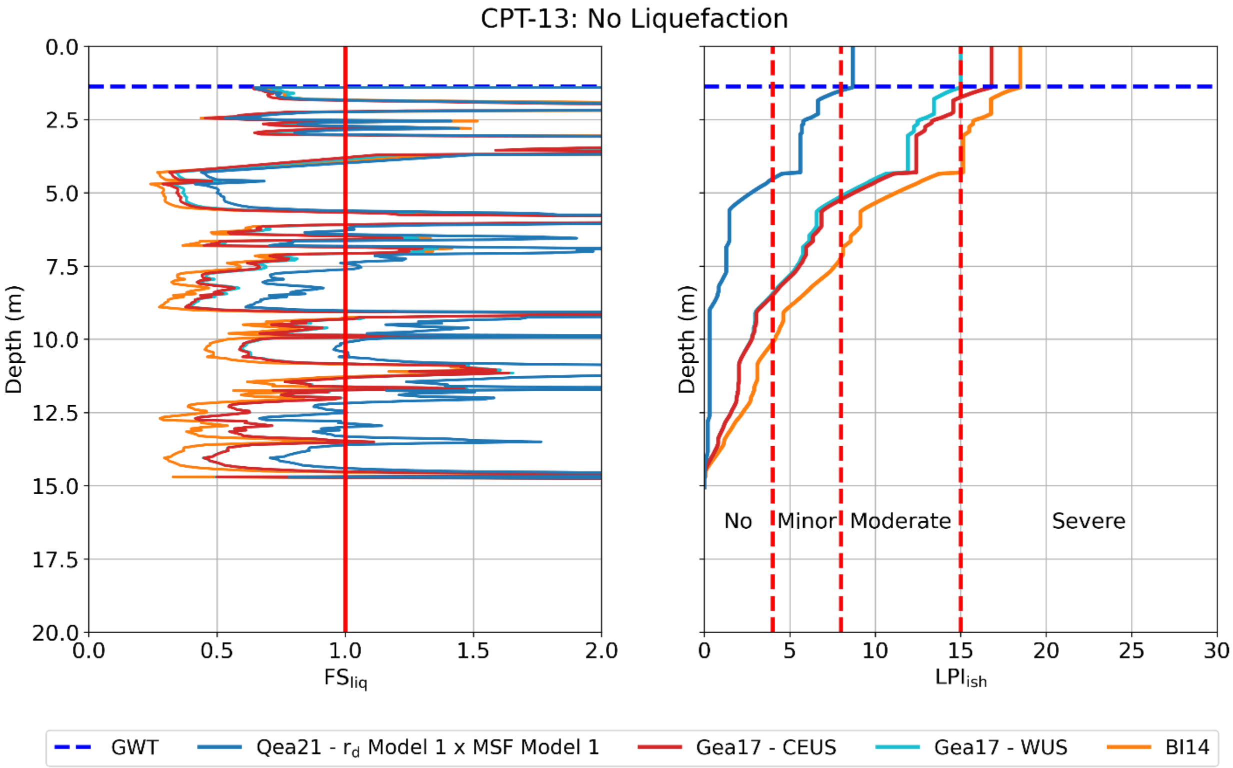

Figure G.28. FS_{liq} and LPI_{ish} profiles for CPT-13, Site 3. Results for the Qea21 model are shown for the ZR19_IZ database, r_d Model 1, and MSF Model 1. LPI_{ish} liquefaction surficial manifestation severity thresholds are also indicated.

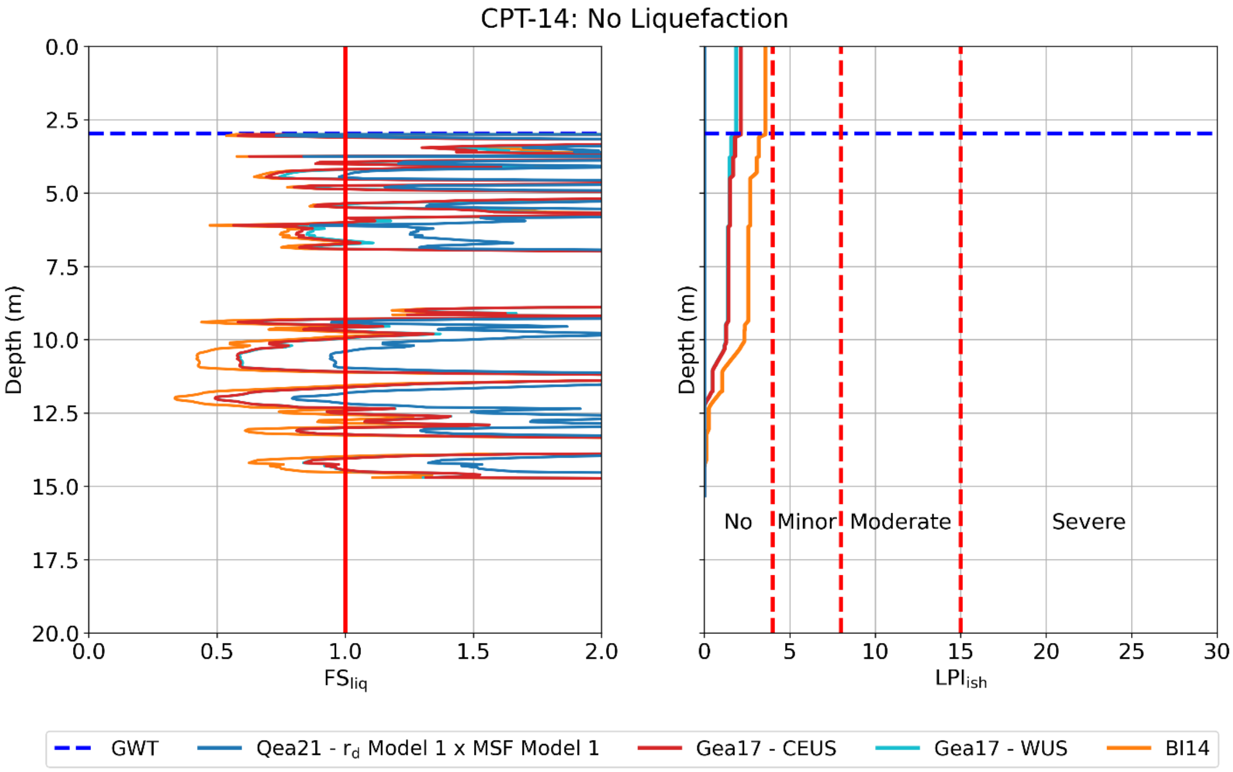

Figure G.29. FS_{liq} and LPI_{ish} profiles for CPT-14, Site 3. Results for the Qea21 model are shown for the ZR19_IZ database, r_d Model 1, and MSF Model 1. LPI_{ish} liquefaction surficial manifestation severity thresholds are also indicated.

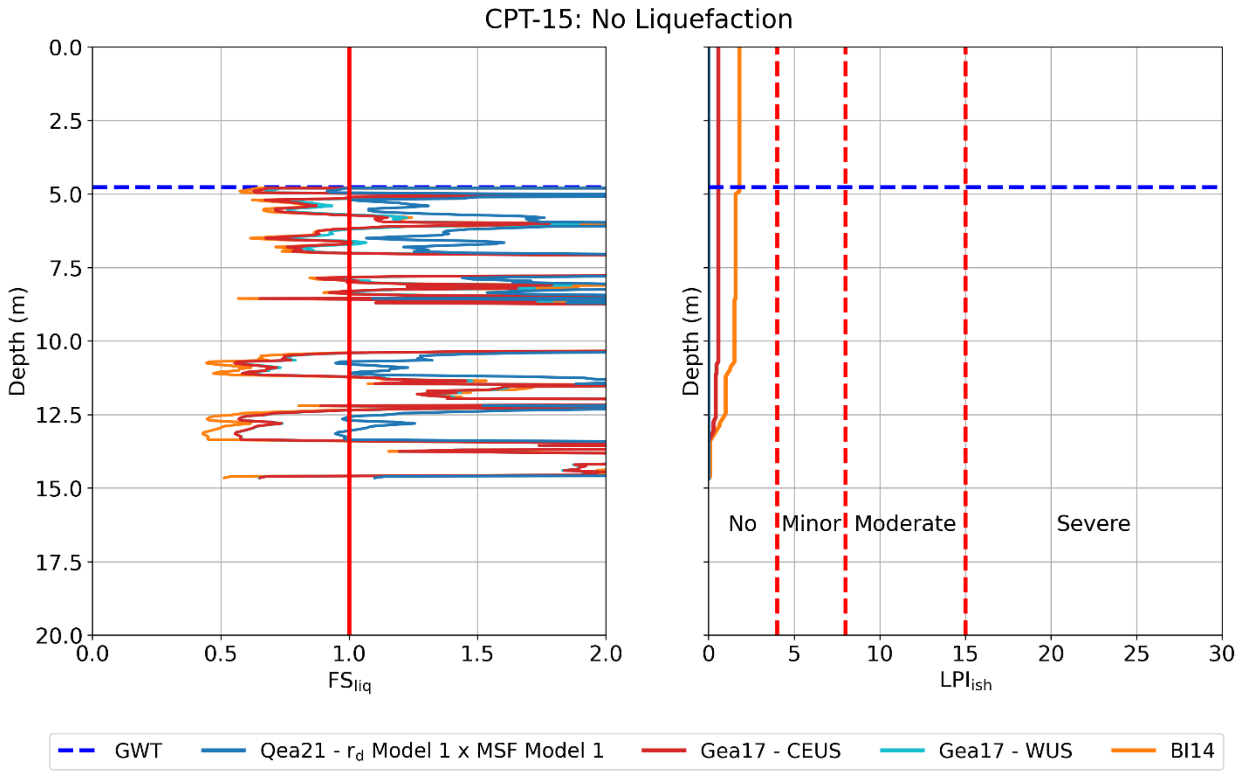

Figure G.30. FS$_{liq}$ and LPI$_{ish}$ profiles for CPT-15, Site 3. Results for the Qea21 model are shown for the ZR19_IZ database, r$_d$ Model 1, and MSF Model 1. LPI$_{ish}$ liquefaction surficial manifestation severity thresholds are also indicated.

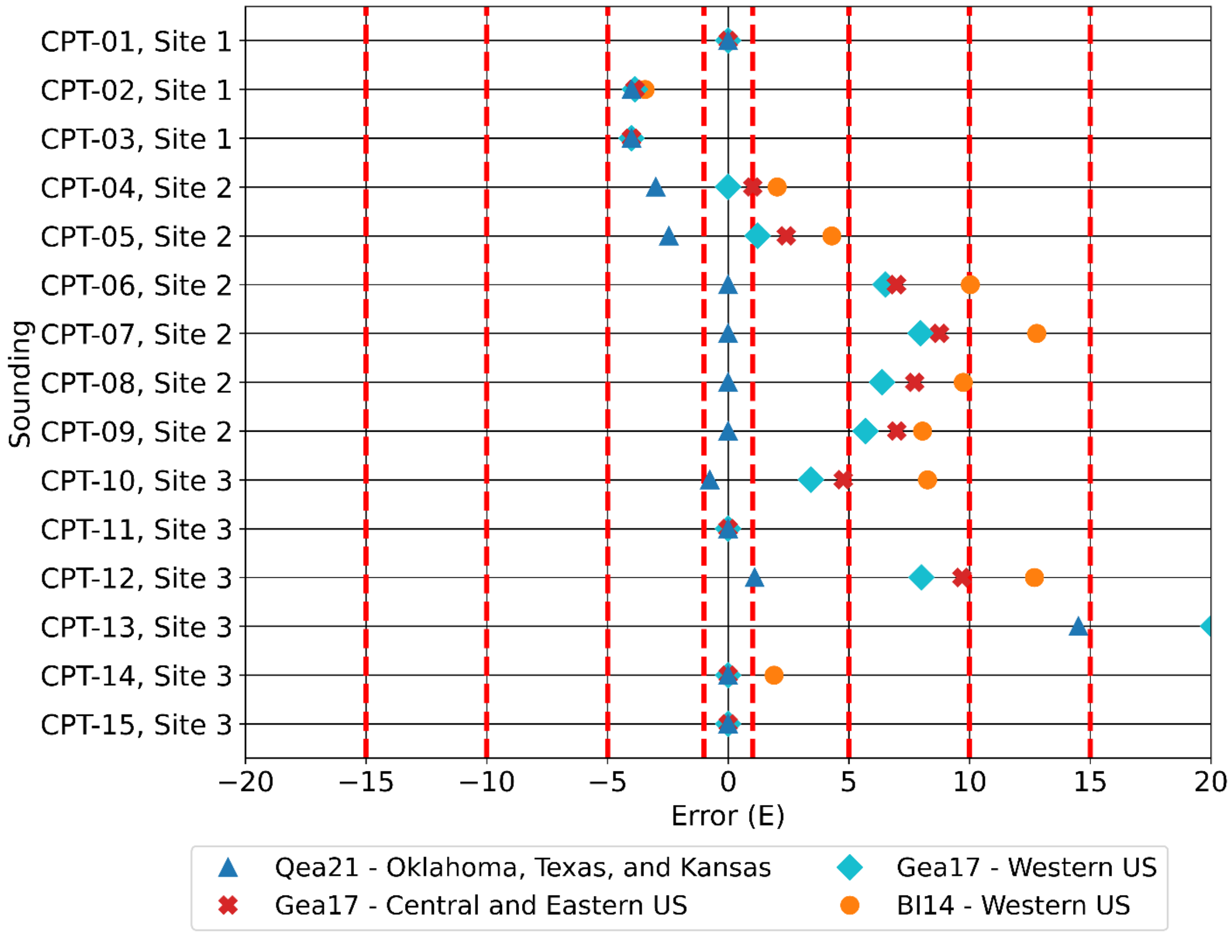

Figure G.31. LPI$_{ish}$ prediction error (*E*) for the Pawnee test sites assuming the water table is 0.5 m higher than originally estimated. Results are shown for the Quick et al. (2021) [Qea21] induced seismicity-specific model using r$_d$ Model 1, MSF Model 1, and the ZR19_IZ dataset; the Green et al. (2017) CEUS [Gea17 – CEUS] and WUS [Gea17 – WUS] models; and the Boulanger and Idriss (2014) [BI14] model. Error classification thresholds from Table 3.8 are also indicated.

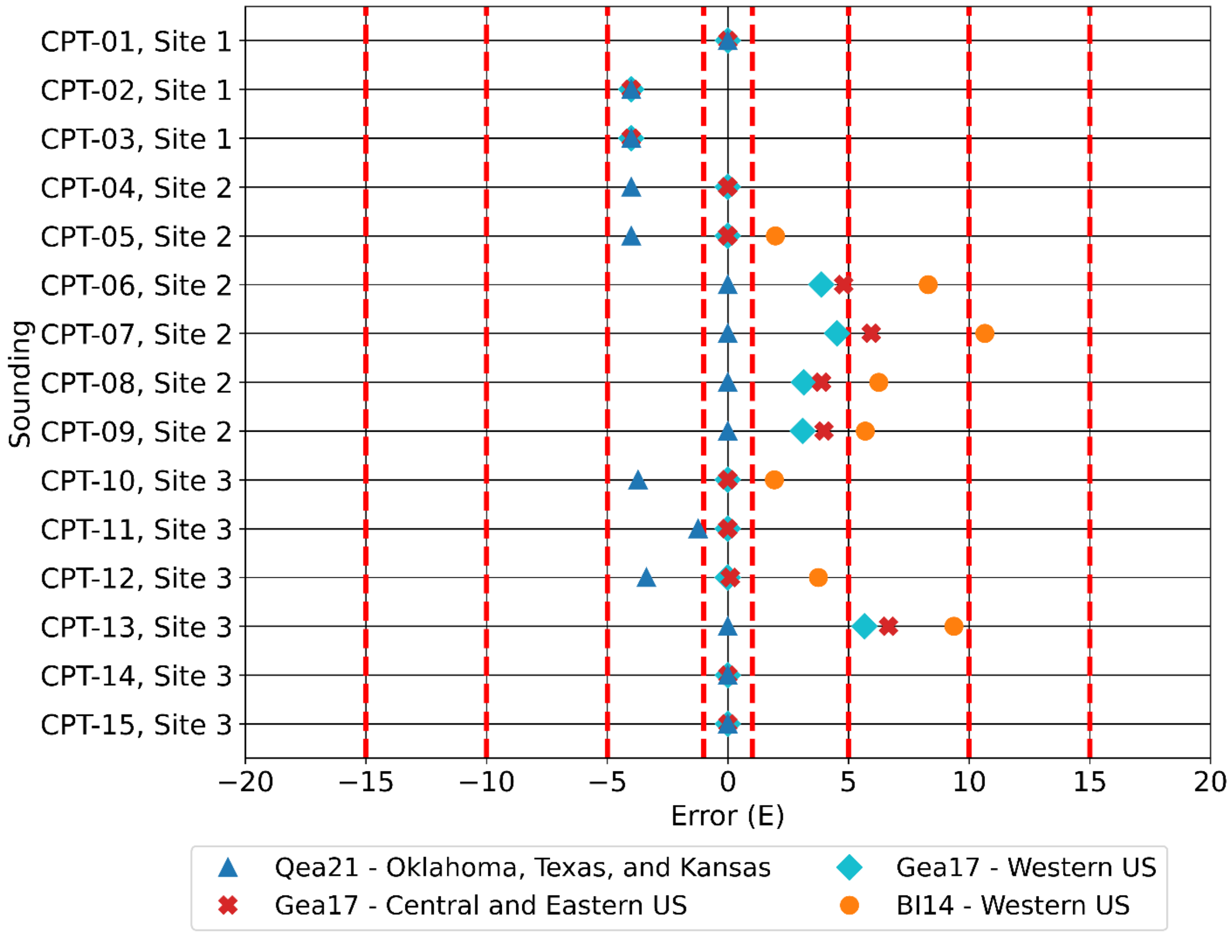

Figure G.32. LPI$_{ish}$ prediction error (*E*) for the Pawnee test sites assuming the water table is 0.5 m lower than originally estimated. Results are shown for the Quick et al. (2021) [Qea21] induced seismicity-specific model using r$_d$ Model 1, MSF Model 1, and the ZR19_IZ dataset; the Green et al. (2017) CEUS [Gea17 – CEUS] and WUS [Gea17 – WUS] models; and the Boulanger and Idriss (2014) [BI14] model. Error classification thresholds from Table 3.8 are also indicated.

Appendix H. Comparison of LPIish Predictions for the Quick et al. (2021) Liquefaction Triggering Model Based on Modulus Reduction and Damping Model, rd Model, and MSF Model

Quick et al. (2021) [Qea21] stress reduction factor (r_d) and magnitude scaling factor (MSF) relationships were developed based on the results of equivalent-linear site response analyses performed using induced ground motions and representative regional soil profiles. Separate analyses were performed using both the Darendeli and Stokoe (2001) and Ishibashi and Zhang (1993) shear modulus reduction and damping degradation (MRD) curves. These curves are used to model the nonlinear response of the soil. During Qea21 model development, separate numerical site response analyses were performed for each MRD curve to see the effect of MRD on the resulting r_d and n_{eq} relationships. As discussed in Quick et al. (2021) [Chapter 2], separate site response analyses were also performed using two induced ground motion catalogs that included (1) ground motions scaled using the Zalachoris and Rathje (2019) GMPE and (2) ground motions scaled using the Novakovic et al. (2018) GMPE. This resulted in four sets of site response analysis results developed using: (1) the Zalachoris and Rathje (2019) ground motion database with Ishibashi and Zhang (1993) MRD curves (referred to as the ZR19_IZ dataset), (2) the Zalachoris and Rathje (2019) ground motion database with Darendeli and Stokoe (2001) MRD curves (ZR19_DS dataset), (3) the Novakovic et al. (2018) ground motion database with Ishibashi and Zhang (1993) MRD curves (Nea18_IZ dataset), and (4) the Novakovic et al. (2018) ground motion database with Darendeli and Stokoe (2001) MRD curves (Nea18_DS dataset). Separate r_d, n_{eq}, and MSF relationships were developed for each dataset to account for the effects of MRD and GMPE selection on the regressed relationships.

The results for the Qea21 liquefaction triggering model presented in Chapter 3 are for the ZR19_IZ dataset. Computed LPI_{ish} values for this dataset and the other three datasets are shown in Table H.1. As shown in this table, there is some minor variation in LPI_{ish} estimates for the different datasets. In general, the computed LPI_{ish} values tend to be higher for the datasets developed using the Ishibashi and Zhang (1993) MRD curves (i.e., ZR19_IZ, Nea18_IZ) than for datasets developed using the Darendeli and Stokoe (2001) MRD curves (i.e., ZR19_DS, Nea18_DS). Additionally, datasets developed with ground motions scaled to the Novakovic et al.

(2018) GMPE (i.e., Nea18_IZ, Nea18_DS) tend to result in higher computed LPI_{ish} values than datasets developed using ground motions scaled to the Zalachoris and Rathje (2019) GMPE (i.e., ZR19_IZ, ZR19_DS). As a result, the Nea18_IZ dataset results in higher computed LPI_{ish} values while the ZR19_DS dataset results in the lowest LPI_{ish} values. The maximum observed difference between LPI_{ish} for the ZR19_DS dataset and the Nea18_IZ dataset is 3.2 (CPT-11). The difference at most locations is smaller. The choice of dataset does not impact the predicted severity category for any of the CPT sounding locations.

Table H.1. Computed LPI_{ish} value and prediction error for the Oklahoma liquefaction triggering model for all datasets.

Sounding	Site	Dataset							
		ZR19_IZ		ZR19_DS		Nea18_IZ		Nea18_DS	
		LPI_{ish}	Prediction Error	LPI_{ish}	Prediction Error	LPI_{ish}	Prediction Error	LPI_{ish}	Prediction Error
CPT-01	1	0.0	0.0	0.0	0.0	0.0	0.0	0.0	0.0
CPT-02	1	0.0	-4.0	0.0	-4.0	0.0	-4.0	0.0	-4.0
CPT-03	1	0.0	-4.0	0.0	-4.0	0.0	-4.0	0.0	-4.0
CPT-04	2	0.2	-3.8	0.0	-4.0	0.4	-3.6	0.0	-4.0
CPT-05	2	1.0	-3.0	0.0	-4.0	1.0	-3.0	0.0	-4.0
CPT-06	2	2.4	0.0	1.3	0.0	2.8	0.0	1.7	0.0
CPT-07	2	1.6	0.0	0.3	0.0	1.8	0.0	0.4	0.0
CPT-08	2	2.7	0.0	0.8	0.0	3.4	0.0	1.4	0.0
CPT-09	2	0.1	0.0	0.0	0.0	0.5	0.0	0.0	0.0
CPT-10	3	1.0	-3.0	0.6	-3.4	1.3	-2.7	0.6	-3.4
CPT-11	3	20.5	0.0	17.9	0.0	21.1	0.0	18.3	0.0
CPT-12	3	3.1	-0.9	1.6	-2.4	3.5	-0.5	2.3	-1.7
CPT-13	3	7.8	3.8	5.1	1.1	8.1	4.1	5.4	1.4
CPT-14	3	0.0	0.0	0.0	0.0	0.0	0.0	0.0	0.0
CPT-15	3	0.0	0.0	0.0	0.0	0.0	0.0	0.0	0.0

Table H.2 provides a comparison of the computed LPI_{ish} values for the Qea21 liquefaction triggering model based on different combinations of r_d Models 1 and 2 and MSF Models 1 and 2. Results are shown for the ZR19_IZ dataset. As discussed in Chapter 3, the choice of MSF model had a more significant impact on FS_{liq} than the choice of r_d model. Consequently, the choice of MSF model has a more significant impact on LPI_{ish}. MSF Model 2 results in lower MSF values due to the small R_{hyp} of the Pawnee sites. This results in a lower computed FS_{liq} and higher computed LPI_{ish} for MSF Model 2. The difference in the computed LPI_{ish} between MSF Models 1 and 2 is as high as 4.5, but is generally smaller. The choice of r_d model resulted in much smaller changes in LPI_{ish} with r_d Model 1 leading to computed LPI_{ish} up to 1.2 higher. The maximum difference between the computed LPI_{ish} values for r_d Model 1 with MSF Model 2 and LPI_{ish} values for r_d Model 2 with MSF Model 1 was 5.1. While the difference is smaller at most locations, the choice of r_d and/or MSF model results in differences in predicted liquefaction severity at some locations. This included CPT-07, CPT-08, CPT-12, and CPT-13. At CPT-07, CPT-08, and CPT-13, the use of MSF Model 2 leads to over-prediction of liquefaction severity, while at CPT-12, the larger computed LPI_{ish} values from MSF Model 2 actually match better with observed liquefaction severity. Overall, the use of r_d Model 1 and MSF Model 1 appears to provide more accurate predictions of liquefaction severity.

Table H.2. Computed LPI_{ish} values and prediction error for the Oklahoma liquefaction triggering model based on the ZR19_IZ dataset and both r_d and MSF models.

Sounding	Site	**r_d Model**							
		1		**1**		**2**		**2**	
		MSF Model							
		1		**2**		**1**		**2**	
		LPI_{ish}	Prediction Error	LPI_{ish}	Prediction Error	LPI_{ish}	Prediction Error	LPI_{ish}	Prediction Error
CPT-01	1	0.0	0.0	0.0	0.0	0.0	0.0	0.0	0.0
CPT-02	1	0.0	-4.0	0.0	-4.0	0.0	-4.0	0.0	-4.0
CPT-03	1	0.0	-4.0	0.0	-4.0	0.0	-4.0	0.0	-4.0
CPT-04	2	0.2	-3.8	2.3	-1.7	0.0	-4.0	1.1	-2.9
CPT-05	2	1.0	-3.0	2.7	-1.3	0.0	-4.0	1.8	-2.2
CPT-06	2	2.4	0.0	4.9	0.9	2.3	0.0	4.7	0.7
CPT-07	2	1.6	0.0	5.8	1.8	1.7	0.0	6.2	2.2
CPT-08	2	2.7	0.0	5.9	1.9	2.1	0.0	5.0	1.0
CPT-09	2	0.1	0.0	2.8	0.0	0.0	0.0	1.9	0.0
CPT-10	3	1.0	-3.0	4.1	0.0	0.9	-3.1	4.1	0.0
CPT-11	3	20.5	0.0	24.8	0.0	20.9	0.0	25.2	0.0
CPT-12	3	3.1	-0.9	7.8	0.0	3.1	-0.9	7.7	0.0
CPT-13	3	7.8	3.8	12.3	8.3	7.2	3.2	11.6	7.6
CPT-14	3	0.0	0.0	0.6	0.0	0.0	0.0	0.5	0.0
CPT-15	3	0.0	0.0	0.0	0.0	0.0	0.0	0.0	0.0

Appendix I. Supplemental Figures for Manuscript #3

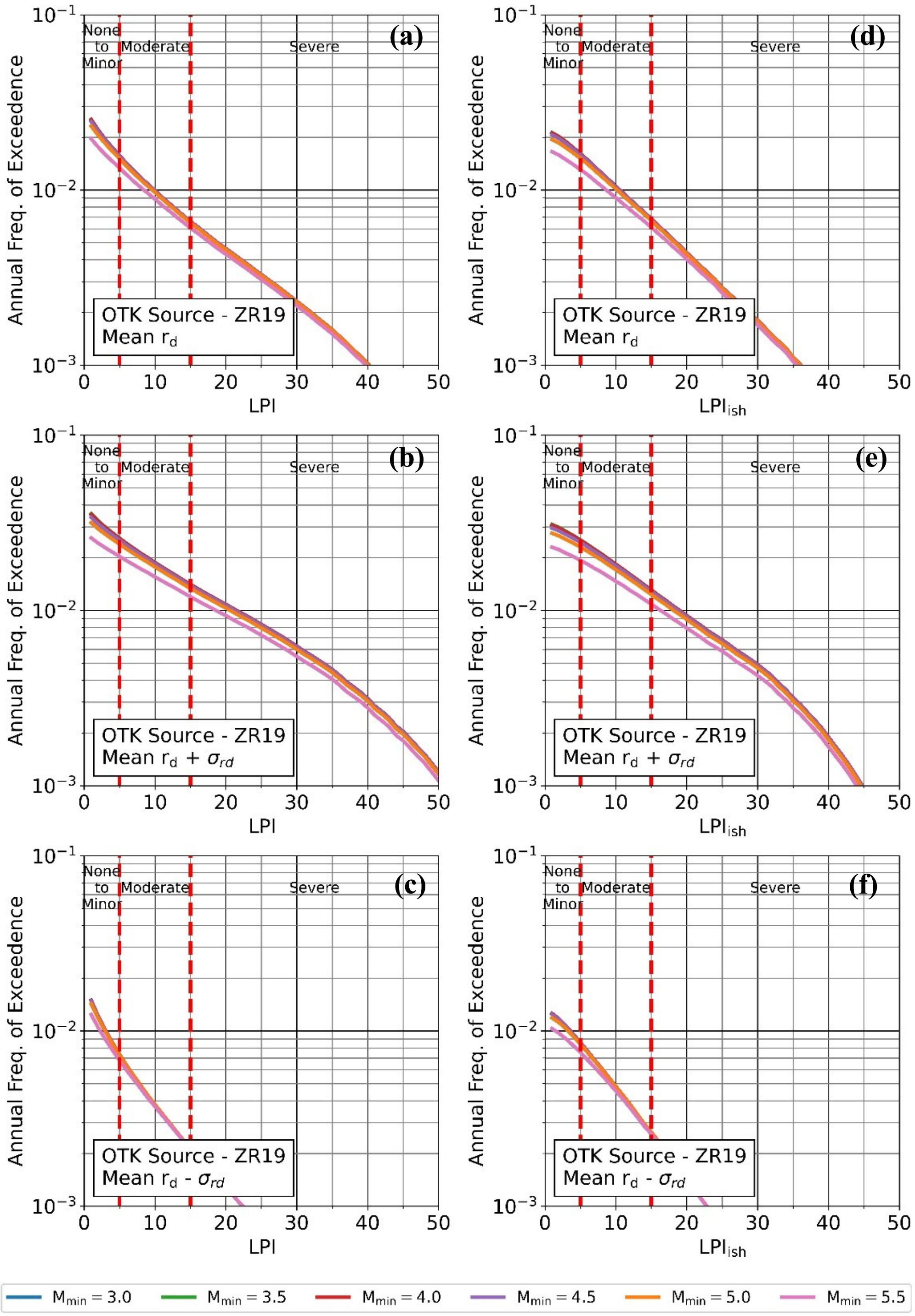

Figure I.1. AFE vs. LPI (a-c) and AFE vs. LPI_{ish} (d-f) curves for the "very susceptible" profile based on the OTK source. Results are shown based on the mean OTK r_d relationship (a, d) and based on the mean plus sigma (b, e) and mean minus sigma (c, f) r_d relationships. Curves are shown for M_{min} = 3.0 to 5.5. Iwasaki et al. (1978) surficial manifestation severity classifications are indicated.

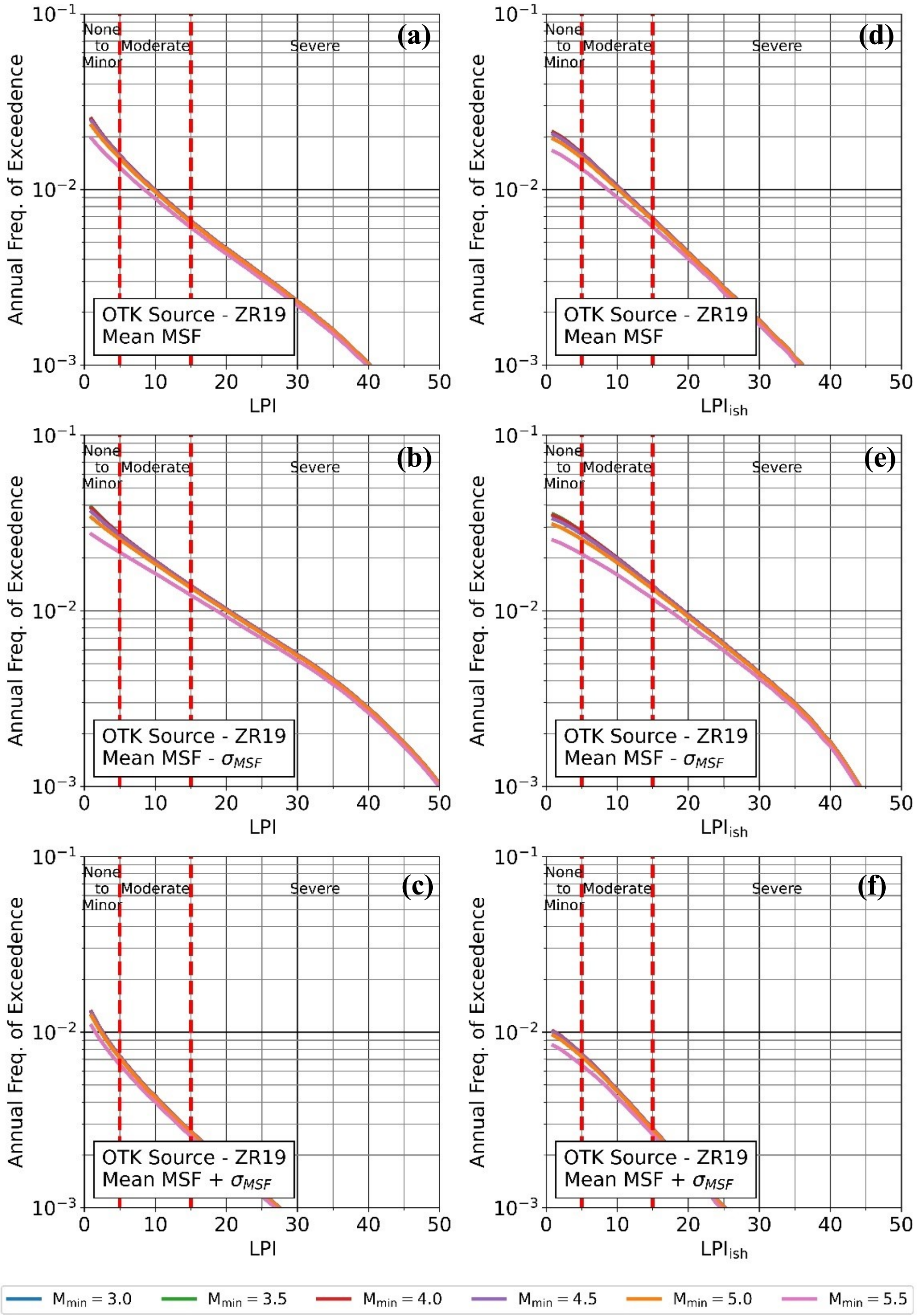

Figure I.2. AFE vs. LPI (a-c) and AFE vs. LPI$_{ish}$ (d-f) curves for the "very susceptible" profile based on the OTK source. Results are shown based on the mean OTK MSF relationship (a, d) and based on the mean plus sigma (b, e) and mean minus sigma (c, f) MSF relationships. Curves are shown for M_{min} = 3.0 to 5.5. Iwasaki et al. (1978) surficial manifestation severity classifications are indicated.

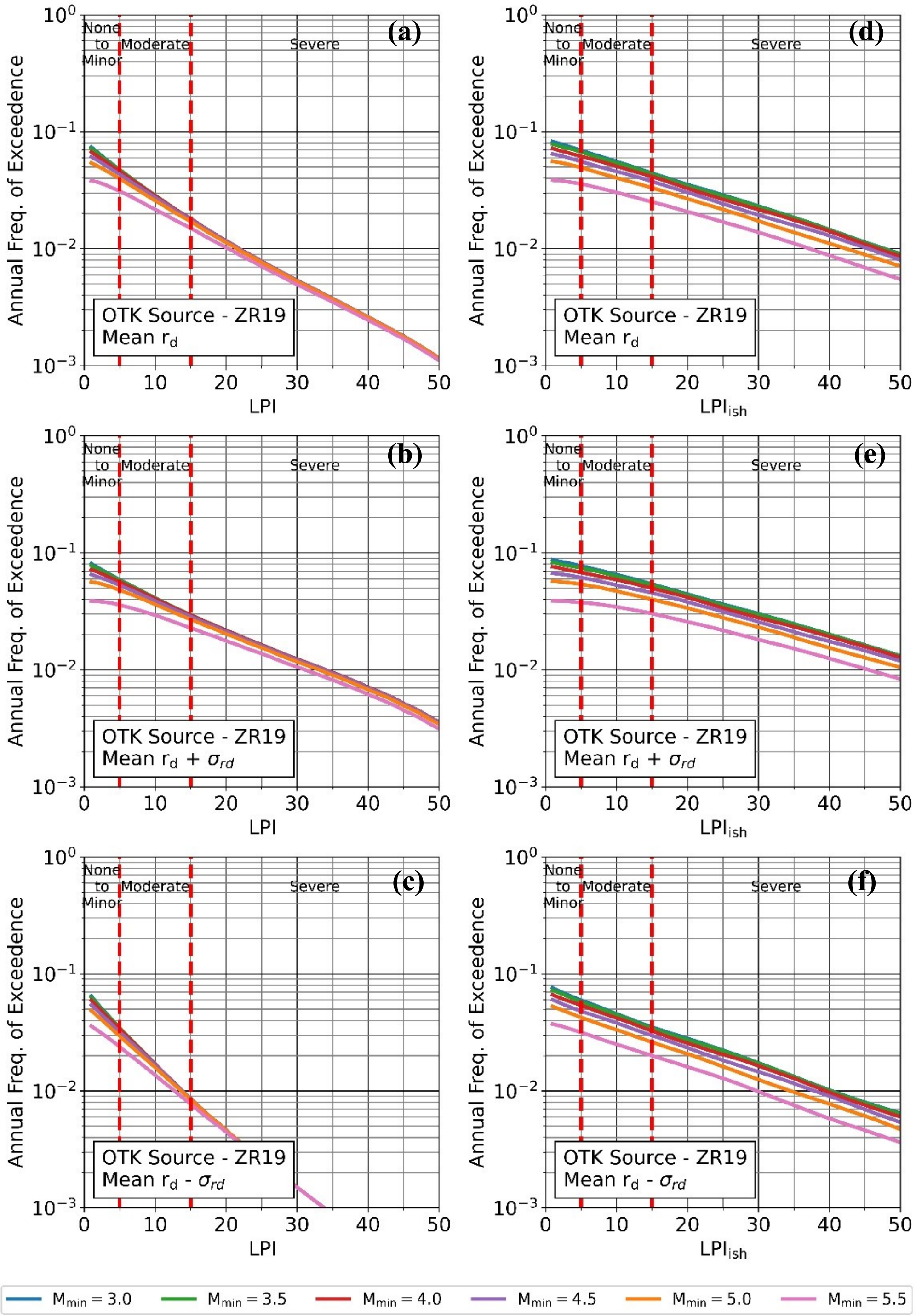

Figure I.3. AFE vs. LPI (a-c) and AFE vs. LPI_{ish} (d-f) curves for the "extremely susceptible" profile based on the OTK source. Results are shown based on the mean OTK r_d relationship (a, d) and based on the mean plus sigma (b, e) and mean minus sigma (c, f) r_d relationships. Curves are shown for M_{min} = 3.0 to 5.5. Iwasaki et al. (1978) surficial manifestation severity classifications are indicated.

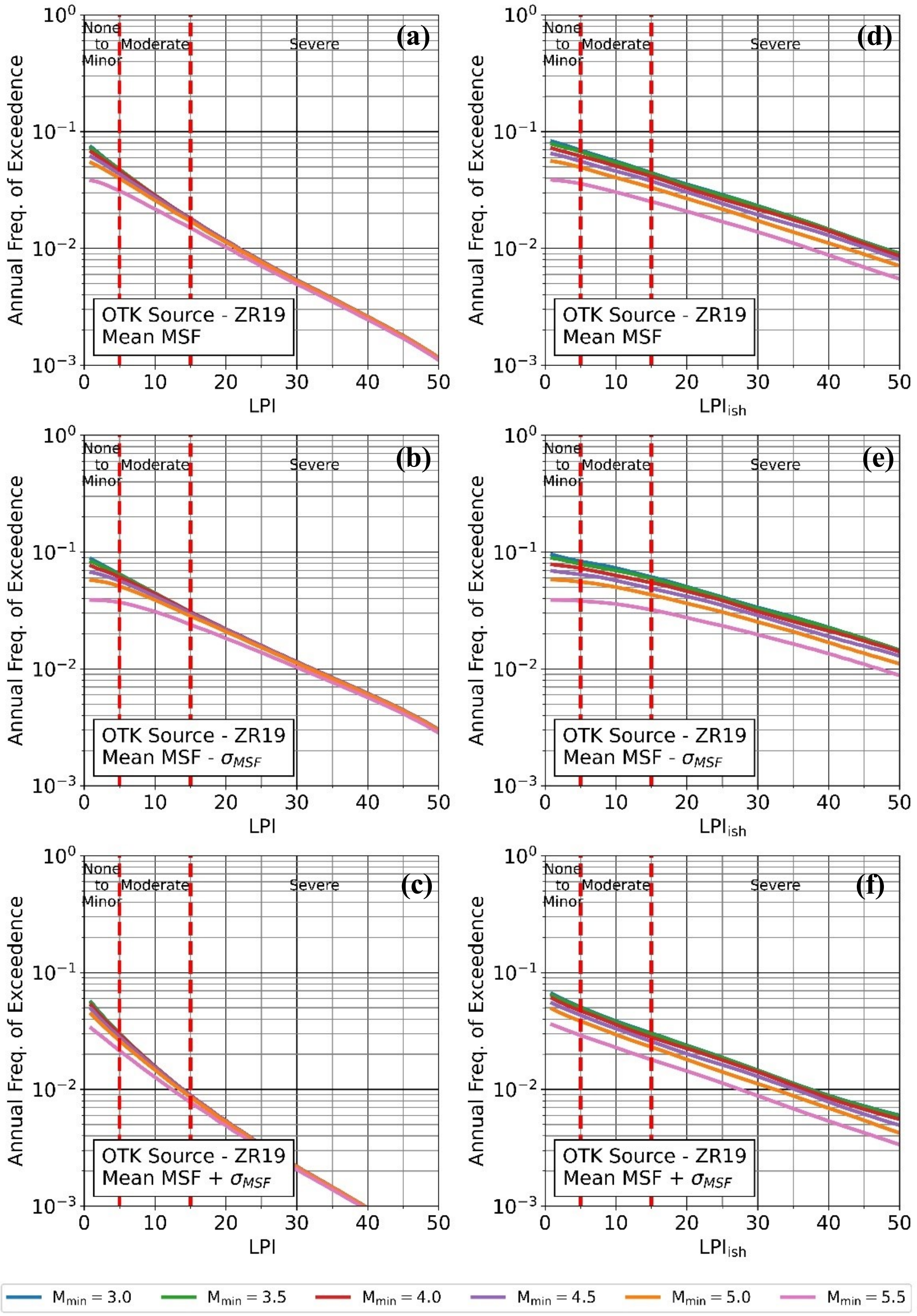

Figure I.4. AFE vs. LPI (a-c) and AFE vs. LPI$_{ish}$ (d-f) curves for the "extremely susceptible" profile based on the OTK source. Results are shown based on the mean OTK MSF relationship (a, d) and based on the mean minus sigma (b, e) and mean plus sigma (c, f) MSF relationships. Curves are shown for M_{min} = 3.0 to 5.5. Iwasaki et al. (1978) surficial manifestation severity classifications are indicated.

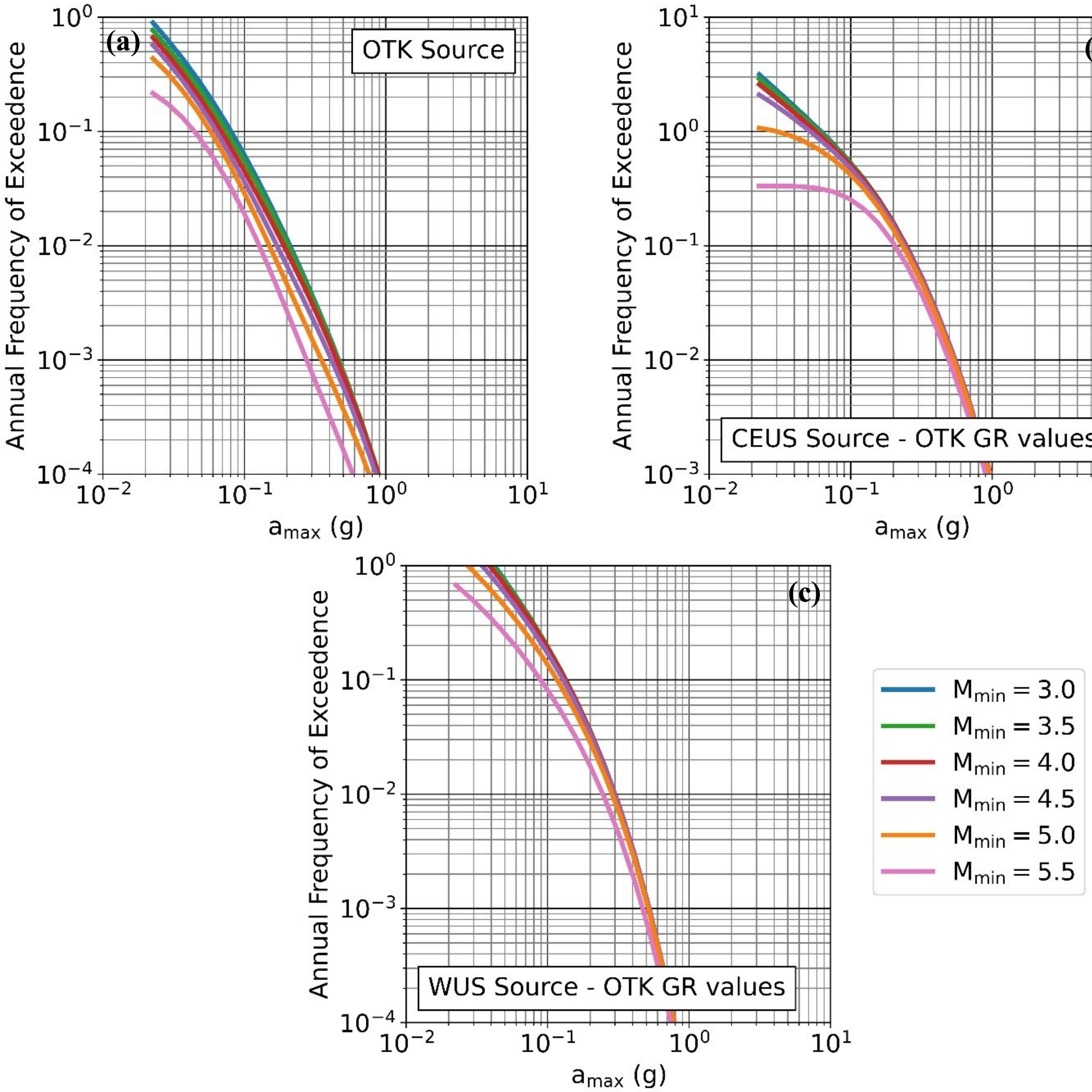

Figure I.5. AFE vs. amax curves for the OTK (a), CEUS (b), and WUS (c) sources using the OTK Gutenberg–Richter (GR) recurrence distribution parameters for all sources. Source-specific GMPEs are used. Curves are shown for Mmin = 3.0 to 5.5

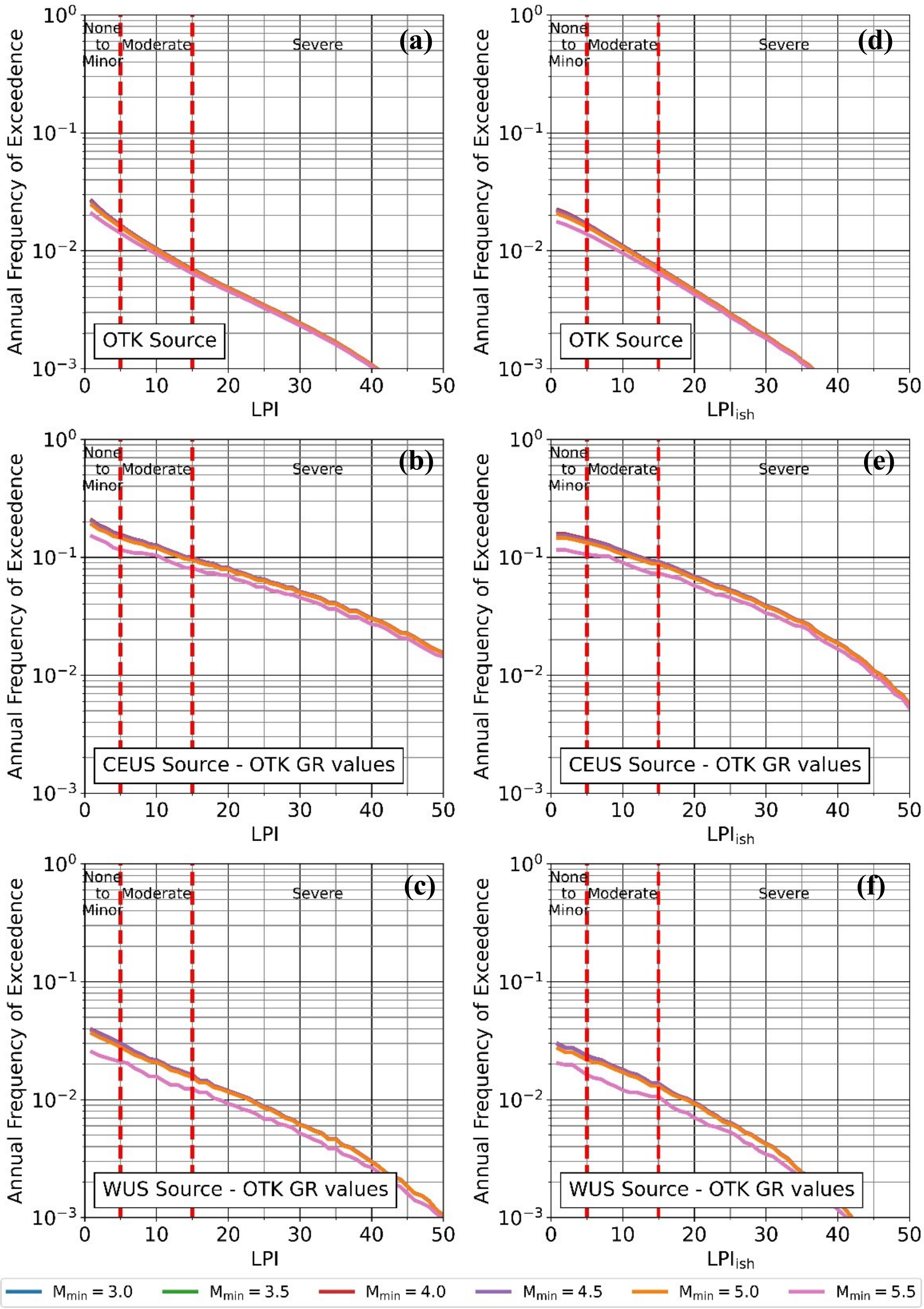

Figure I.6. AFE vs. LPI (a-c) and AFE vs. LPI_{ish} (d-f) curves for the "very susceptible" profile based on the OTK (a, b), CEUS (c, d), and WUS (e, f) sources using the OTK Gutenberg-Richter (GR) distribution for all sources. Curves are shown for M_{min} = 3.0 to 5.5. Iwasaki et al. (1978) surficial manifestation severity classifications are indicated.

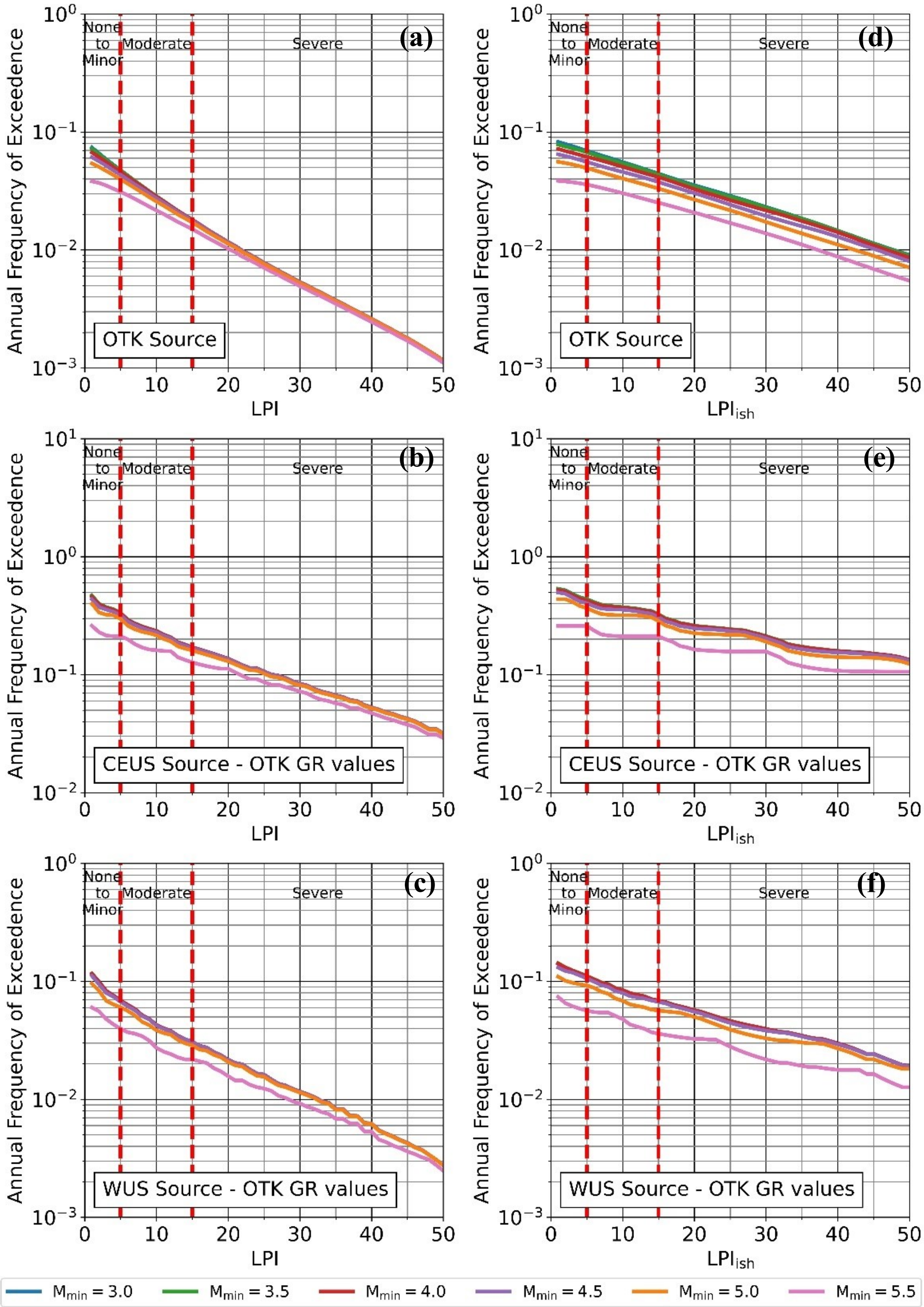

Figure I.7. AFE vs. LPI (a-c) and AFE vs. LPI$_{ish}$ (d-f) curves for the "extremely susceptible" profile based on the OTK (a, b), CEUS (c, d), and WUS (e, f) sources using the OTK Gutenberg-Richter (GR) distribution for all sources. Curves are shown for M_{min} = 3.0 to 5.5. Iwasaki et al. (1978) surficial manifestation severity classifications are indicated.

Appendix J. Conference Paper: Evaluating Liquefaction Triggering Potential at Sites Impacted by the 2016 Mw5.8 Pawnee, Oklahoma, Induced Earthquake

Evaluating Liquefaction Triggering Potential at Sites Impacted by the 2016 $M_w5.8$ Pawnee, Oklahoma, Induced Earthquake

Tyler J. Quick[1], Russell A. Green[2], Ellen M. Rathje[3], and James K. Mitchell[4]

[1]Graduate Student, Department of Civil and Environmental Engineering, Virginia Tech, Blacksburg, VA; tylerjaq@vt.edu

[2]Professor, Department of Civil and Environmental Engineering, Virginia Tech, Blacksburg, VA; rugreen@vt.edu

[3]Professor, Department of Civil, Architectural, and Environmental Engineering, University of Texas at Austin, Austin, TX; e.rathje@mail.utexas.edu

[4]University Distinguished Professor, Emeritus, Department of Civil and Environmental Engineering, Virginia Tech, Blacksburg, VA; jkm@vt.edu

ABSTRACT

Deep wastewater injection-induced seismicity has led to over a thousand $M_w>3$ earthquakes and four $M_w>5$ earthquakes in Oklahoma over the last ten years. The 3 September 2016, $M_w5.8$ Pawnee, Oklahoma, earthquake was the first induced seismic event worldwide, that the authors are aware of, where liquefaction was observed and documented, raising concerns regarding the liquefaction risk posed by future induced earthquakes. Determining the suitability of current variants of the simplified procedure for evaluating the regional liquefaction hazard caused by induced earthquakes is part of an ongoing study. A detailed site characterization campaign examining profiles where liquefaction was and was not observed following the 2016 $M_w5.8$ Pawnee, Oklahoma, earthquake is part of this study. The purpose of this paper is to present an overview of the sites targeted as part of this testing, a summary of preliminary results from the site characterization campaign, and a description of planned future testing.

INTRODUCTION

The stress-based “simplified” liquefaction evaluation procedure (Whitman 1971; Seed and Idriss 1971) is the most widely used approach to evaluate liquefaction potential worldwide. However, the procedure is semi-empirical, with the empirical aspects of it derived from data from moderate-sized tectonic earthquakes in active shallow-crustal tectonic regimes (e.g., California, Japan, and New Zealand). As a result, the suitability of the procedure for evaluating the liquefaction hazard due to induced seismicity in stable continental tectonic regimes is questionable. Although the ability of soil to resist liquefaction triggering (i.e., $CRR_{M7.5}$) is assumed to be an inherent property of the in-situ soil conditions, the ground motions from induced earthquakes may have different characteristics than those from natural tectonic earthquakes (e.g., Bommer et al. 2016; Zalachoris and Rathje 2019). Also, the geologic profiles/soil deposits in areas in the US experiencing the highest rate of induced seismicity (e.g., Oklahoma) differ from those used to develop the empirical aspects of the simplified procedure. Accordingly, and in combination with the smaller magnitudes of induced earthquakes, it is uncertain whether the depth-stress reduction factor (r_d) and Magnitude Scaling Factor (MSF) relationships inherent to existing simplified liquefaction evaluation procedures for estimating normalized Cyclic Stress Ratio (CSR*) are suitable for use with induced earthquakes because both r_d, which accounts for the non-rigid response of the soil profiles to shaking, and MSF, which accounts for durational effects of shaking on liquefaction triggering, are affected by ground motion and soil profile characteristics.

This is illustrated in Figure J.1, which shows, as a function of depth (z), the ratio of FS_{WUS}, the factor of safety against liquefaction triggering (FS) for shallow crustal tectonic events in active tectonic regions (e.g., western US), to FS_{Gron}, the FS for induced earthquakes due to natural gas production in the Groningen region of the Netherlands, both computed using the simplified procedures developed by Green et al. (2019a; b). As shown in this figure, for a peak ground acceleration (a_{max}) of 0.15g occurring during events having moment magnitudes (M_w) of 5 and 6.5, the predicted FS for the induced earthquakes in Groningen is lower, and considerably so at some depths, than it is for tectonic events. However, as a_{max} increases to 0.4 g (again for $M_w = 5$ and 6.5 events) this trend is less pronounced and the predicted FS for induced earthquakes is actually greater than that for tectonic events for a depth range of ~5 to 17 m.

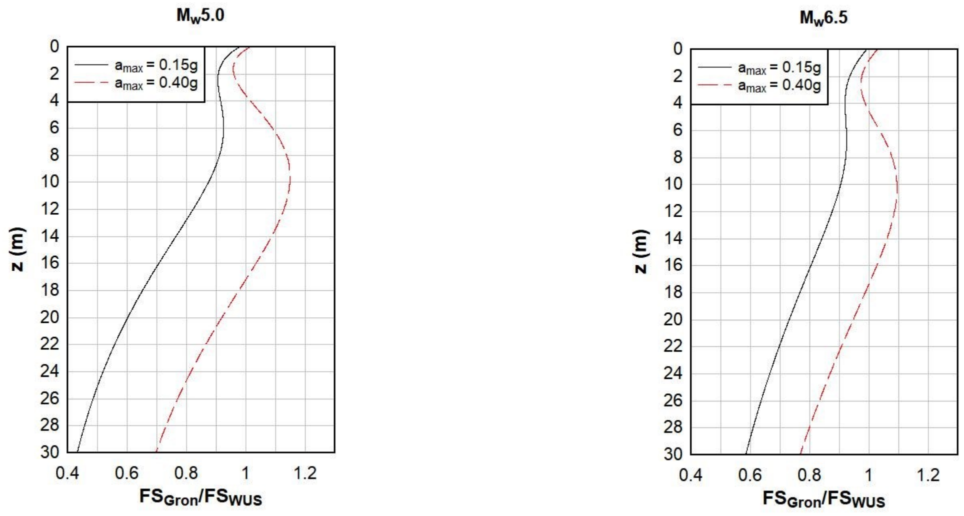

(a) (b)

Figure J.1. Ratio of the predicted FS for induced earthquakes in the Groningen region of the Netherlands and shallow crustal tectonic events (Green et al. 2019a; b): (a) M_w5.0, a_{max} = 0.15g & 0.4g; and (b) M_w6.5, a_{max} = 0.15g & 0.4g.

Although most earthquakes induced by wastewater injection in Oklahoma have been small, there have been four M_w5+ events, with the largest being the 2016 M_w5.8 Pawnee earthquake. These events have resulted in some structural damage (Clayton et al. 2016), but overall economic consequences have been limited because the earthquake epicenters were located in rural areas. However, significant damages potentially could occur if additional M_w5+ earthquakes were to occur in more populated or more vulnerable areas. The dramatic increase in the number of seismic events due to induced seismicity, even when the events are limited in size, increases the overall seismic risk in the affected areas. This includes the risk due to liquefaction, with the Pawnee earthquake being the first induced seismic event worldwide, that the authors are aware of, where liquefaction has been observed and documented. As a result, a procedure is needed to be able to accurately evaluate liquefaction triggering potential due to induced seismicity in Oklahoma due to deep wastewater injection. Note that although the Green et al. (2019b) variant of the simplified liquefaction evaluation procedure was specifically developed for induced earthquakes, the predominant source mechanism of Groningen earthquakes is normal faulting having focal depths of ~3 km; in contrast, the fault mechanism for the larger induced events in Oklahoma have been predominately strike-slip and have focal depths of ~5 km. Accordingly, and due to differences in the geologic profiles/soil deposits in Oklahoma versus Groningen, the procedure developed to evaluate liquefaction triggering due to induced earthquakes in Groningen cannot necessarily be used to evaluate liquefaction triggering due to induced earthquakes in Oklahoma.

Determining the suitability of current variants of the simplified procedure for evaluating the regional liquefaction hazard caused by induced earthquakes in Oklahoma, Texas, and Kansas is part of an ongoing study. A detailed site characterization campaign to examine profiles where effects of liquefaction were and were not observed following the Pawnee earthquake is part of this study. The purpose of this paper is to present an overview of the sites targeted for testing, a summary of the preliminary results from the site characterization campaign, and a description of planned future testing.

BACKGROUND

Anthropogenic sources of seismicity include activities such as fracking, oil and gas extraction, wastewater injection, carbon capture and storage, and reservoir filling. These activities induce changes in pore pressures and stresses in fault zones, which can lead to fault rupture (Ellsworth 2013; Foulger et al. 2018). These ruptures can lead to the release of both induced stresses and pre-existing tectonic stresses. Thus, the seismic energy released during induced events can be significantly larger than that due to the induced stress changes themselves (McGarr et al. 2002). This led Mitchell and Green (2017) to distinguish between “triggered” anthropogenic earthquakes, which primarily release pre-existing tectonic stresses, and “induced” anthropogenic earthquakes, which release primarily induced stresses. In practice, it is difficult to distinguish between the two, and both are generally referred to as “induced” earthquakes (Foulger et al. 2018), which is the convention used herein. Several studies have indicated that most faults in the crust are nearly critically stressed, which suggests that even minor changes to pore pressure, confining stress, or shear stress induced by human activity can lead to fault rupture (Foulger et al. 2018). Induced earthquakes often have shallow focal depths (~5 km in Oklahoma), which can lead to larger near-source ground motion intensity than would be estimated for similarly-sized tectonic events (Zalachoris and Rathje 2019).

Deep wastewater injection has led to a significant increase in seismicity in areas where oil and gas production and wastewater injection are prevalent such as Oklahoma, Kansas, and Texas.

Although recent regulation enacted to limit wastewater injection volumes in Oklahoma has led to reductions in regional seismicity, over 300 M3+ earthquakes occurred in 2017, which is still 300 times the natural tectonic rate of about one M3+ earthquakes per year in the state (Langenbruch and Zoback 2016; Oklahoma Office of the Secretary of Energy & Environment 2019). This dramatic increase in seismicity is of particular concern because it is occurring primarily in historically aseismic areas where building codes and construction methods have not traditionally accounted for higher levels of seismicity. This means that infrastructure in these areas may be more susceptible to damage caused by ground shaking. Additionally, although the number of M3+ earthquakes has been decreasing since 2015, some of the largest events, including the 2016 M_w5.8 Pawnee, OK earthquake, have occurred since that time.

LIQUEFACTION DURING THE PAWNEE OKLAHOMA EARTHQUAKE

The epicenter of the 3 September 2016, M_w5.8 Pawnee, Oklahoma, earthquake, was located about 15 km northwest of Pawnee, OK. The event was the strongest recorded earthquake in Oklahoma history and is one of the largest recorded earthquakes in the CEUS in the last 70 years (Tiwari and Rathje 2018). The U.S. Geological Survey (USGS) ShakeMap of a_{max} for the Pawnee event is shown in Figure J.2 (USGS 2016a). Inferred a_{max} values were as high as 0.36g within 5 km of the earthquake epicenter, decreasing to less than 0.06g at a distance of approximately 40 km.

Post-earthquake reconnaissance conducted by Clayton et al. (2016) and Kolawole et al. (2017) identified four sites where liquefaction manifestations were observed, shown in Figure J.2 as Sites 1 through 4. Site 1 lies along Black Bear Creek, a tributary of The Arkansas River, while Sites 2 through 4 are located within the floodway of the Arkansas River. Liquefaction manifestations observed included sand boils, cracking with sand ejecta, and possible lateral spreading. Examples of the liquefaction manifestations at each site are shown in Figure J.3. Conversations with landowners in the affected areas indicated that there were additional sites where liquefaction was observed but not documented. While these additional sites are not included in the present study, they are evidence that liquefaction was more widespread than suggested by initial post-earthquake reconnaissance.

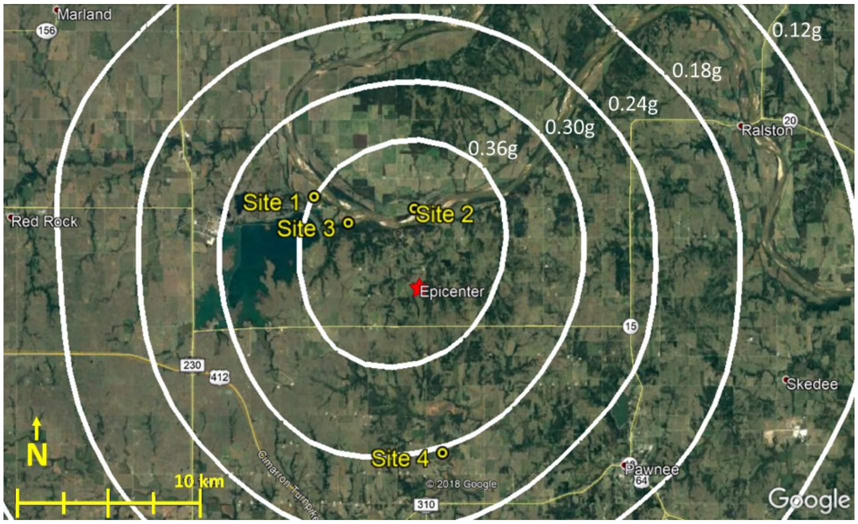

Figure J.2. USGS ShakeMap for 2016 M_w5.8 Pawnee, OK earthquake showing contours of inferred peak ground acceleration. Liquefaction Sites 1,2, 3, and 4, identified by Clayton et al. (2016) and Kolawole et al. (2017), are also indicated.

SITE INVESTIGATION

The Pawnee earthquake provides an opportunity to determine the suitability of current variants of the simplified procedure for evaluating the regional liquefaction hazard caused by induced earthquakes in Oklahoma, Texas, and Kansas. To this end, a detailed site characterization campaign is being conducted to examine soil profiles at sites where liquefaction was and was not observed following the Pawnee earthquake. A preliminary site investigation was conducted in January 2019. The primary purpose of the preliminary investigation was to gather existing information on the liquefaction sites and accurately determine areas where liquefaction features were and were not observed at these sites in order to select locations for full site characterization.

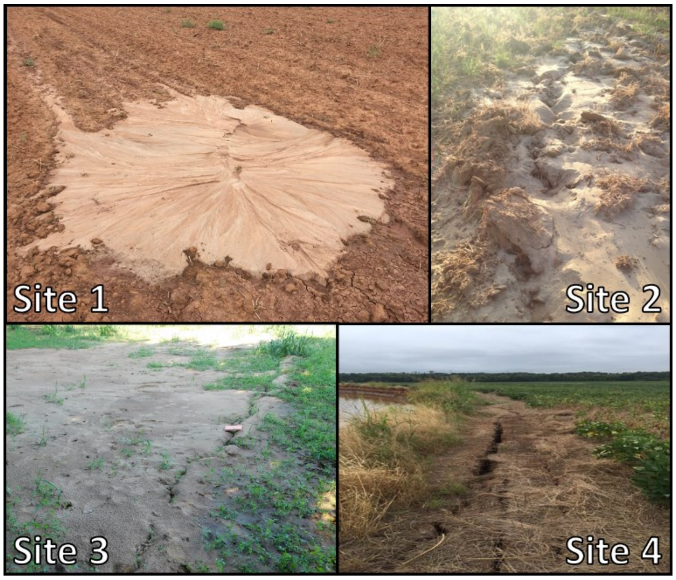

Figure J.3. Photos of liquefaction taken following the 2016 Pawnee, OK earthquake (photos from Site 1, 2, and 4 courtesy Dan Ripley, Rick Rice, and Martin Williams, respectively; photo from Site 3 is from Kolawole et al. 2017).

USGS geologic maps for the four Pawnee liquefaction sites are shown in Figure J.4 (Stanley and Chang 2016). All four sites are located in alluvial zones, which the USGS describes as consisting of sand, silt, clay, and gravel with maximum thicknesses along major streams ranging from 9 to 24 m and along minor streams ranging from 0 to 18 m (USGS 2019). Groundwater depth during the January 2019 site investigation was estimated at 1 m at Site 1, 2 m at Sites 2 and 4, and 1 to 2 m at Site 3 based on river/stream levels adjacent to the sites. Groundwater depths during the 2016 Pawnee event were estimated by comparing river gage heights during the earthquake with those during the January 2019 site investigation (USGS 2016b; c). Based on these comparisons, groundwater depth during the Pawnee earthquake was estimated at 2 m for Site 1, 2.5 m for Sites 2 and 4, and 1.5 to 2.5 m for Site 3. Shear wave velocity information was not available for any of the sites, but values of the time-weighted shear wave velocities of the upper 30 m of the profiles (V_{S30}) reported by Zalachoris et al. (2017) for alluvial sites within 35 km of the liquefaction sites ranged from 362 m/s to 580 m/s. For each of the Pawnee test sites, areas where liquefaction features were and were not observed were confirmed during the preliminary investigation using photos and anecdotal evidence provided during interviews with the property owners, as well as information from the Clayton et al. (2016) and Kolawole et al. (2017) reports.

A preliminary estimate of the liquefaction hazard at the test sites due to the Pawnee earthquake was made using the method presented by Baise and Rashidian (2018). This method estimates probability of liquefaction and liquefaction spatial extent (LSE), the percent of a given area covered by surface manifestations of liquefaction, based on peak ground velocity (PGV), V_{S30}, mean annual precipitation, closest distance to water, and water table depth. PGV was estimated based on the USGS ShakeMap (USGS 2016a), and precipitation data were taken from National Oceanic and Atmospheric Administration (NOAA) Station USC00346940 (NOAA 2019). Inputs and results for each site are shown in Table J.1. As shown in the table, the predicted probability of liquefaction at the four sites based on geologic proxies is ~26%, corresponding to an LSE of ~2%. For Sites 2 and 4, 2% is generally a reasonable estimate based on the estimated extent of liquefaction observations at these sites; however, it may be low for Sites 1 and 3 where liquefaction was more extensive. Similar estimates of probability of liquefaction and LSE would be expected for similar, nearby sites along the Arkansas River and Black Bear Creek depending on site-specific soil conditions. This agrees with observations made by local landowners that liquefaction occurred at other sites in the area, aside from those formally documented in Clayton et al. (2016) and Kolawole et al. (2017). Additionally, Clayton et al. (2016) noted that thick vegetation and low population density, made it difficult to determine the full extent of damages due to the Pawnee event. As a result, liquefaction may have occurred at nearby sites and gone unnoticed or unreported.

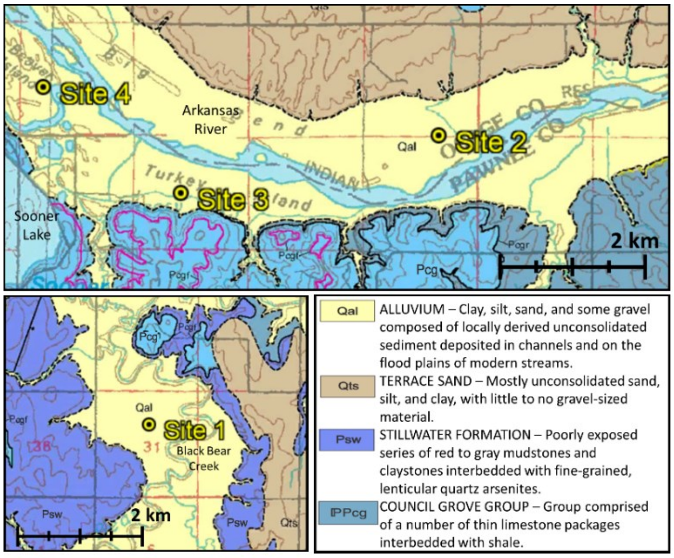

Figure J.4. Geologic maps of Pawnee earthquake liquefaction sites (Stanley and Chang 2016).

Table J.1. Liquefaction Hazard Estimates based on Baise and Rashidian (2018)

Site	Peak Ground Velocity (cm/s)	V_{s30} (m/s)	Mean Annual Precipitation (mm)	Closest Distance to Water (km)	Water Table Depth (m)	Probability of Liquefaction	Liquefaction Spatial Extent (%)
1	20	360	1021	0.15	2	0.262	2.11
2	25	360	1021	0.3	2.5	0.268	2.28
3	20	360	1021	0.11	1.5	0.267	2.26
4	20	360	1021	0	2.5	0.265	2.20

In addition to general site reconnaissance, Horizontal to Vertical Spectral Ratio (HVSR) tests were conducted at each site as part of the preliminary site investigation. HVSR test results will be used to constrain the small-strain shear wave velocity (V_S) models determined from subsequent Multichannel Analysis of Shear Wave (MASW) data inversions (Yust et al. 2018). The MASW and HVSR data will provide insights into the site response characteristics of the soil profiles, which in turn will provide insights into the appropriateness of existing r_d and MSF relationships for evaluating liquefaction triggering. HVSR tests were conducted following the guidelines provided by the SESAME project (Bard 2004) using ambient vibrations recorded at each site using a three-component broadband seismometer.

HVSR analysis was performed using the Geopsy software package. An example plot showing the results for Site 2 is shown in Figure J.5 with the peak frequency of the average H/V curve plus or minus one standard deviation highlighted. The peak frequency corresponds to the fundamental frequency of the site. The fundamental frequency at the three sites (Sites 2, 3, and 4) along the Arkansas River was approximately 3 Hz, while it was 0.86 Hz at Site 1, located along Black Bear Creek. This may be an indication of differences in alluvium thickness along the Arkansas River versus along Black Bear Creek, where a shallower depth to bedrock would lead to a stiffer site and higher fundamental frequency and vice-versa.

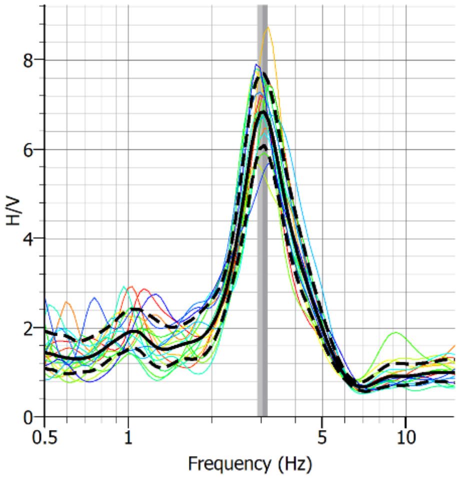

Figure J.5. HVSR results for the Site 2. Peak frequency +/- one standard deviation is shown.

PLANNED FUTURE TESTING

Future testing planned for Fall 2019 will involve detailed characterization of sites identified during the preliminary investigation. Testing will include Cone Penetration Tests (CPT), MASW tests, and hand auger sampling. CPT test results will be used to characterize the soil profile and evaluate the liquefaction potential of each test location using current CPT-based variants of the simplified liquefaction evaluation procedure (e.g., Green et al. 2019a; b). MASW tests, as well as seismic soundings performed with the CPT, will be used to develop shear wave velocity profiles for each site for use in numerical site response models. Both liquefaction and no-liquefaction test locations have been selected for testing. Liquefaction test locations were selected based on the liquefaction areas identified during the preliminary site investigation. No-liquefaction test locations were selected at the same sites, so as to be near the liquefaction test locations and in areas where conditions were likely favorable for liquefaction (e.g., low elevation areas, inside river bends) but where liquefaction manifestations were not observed during the Pawnee event. The selected test locations are shown in Figure J.6. Predictions of liquefaction potential made for each test location using current variants of the simplified liquefaction evaluation procedure will be compared to actual observations of liquefaction to evaluate the effectiveness of these methods for predicting liquefaction potential due to induced earthquakes.

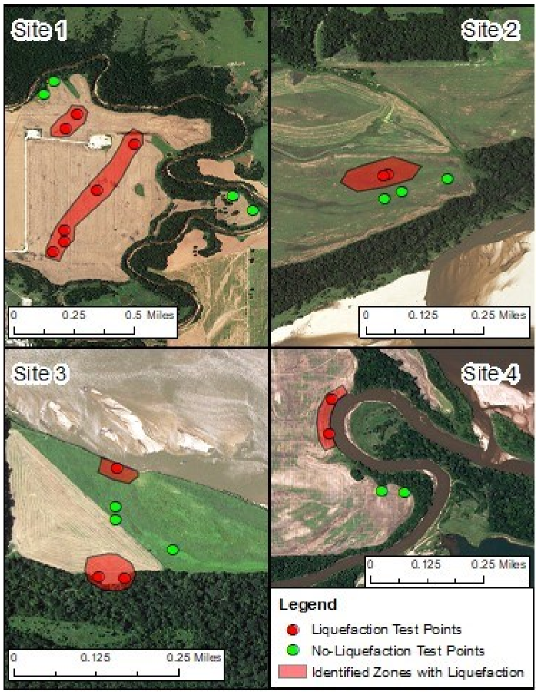

Figure J.6. Identified liquefaction areas and proposed test locations for future testing.

CONCLUSION

Induced seismicity resulting from oil and gas production wastewater injection has led to over a thousand $M_w>3$ earthquakes in Oklahoma over the last ten years, including four $M_w>5$ earthquakes (Oklahoma Office of the Secretary of Energy & Environment 2019). The $M_w5.8$ 2016 Pawnee, OK earthquake was the first induced seismic event worldwide, that the authors are aware of, where liquefaction has been observed and documented. The liquefaction observed during the Pawnee earthquake occurred in a rural area and did not significantly impact infrastructure; however, it raises concerns regarding damages that may occur if future induced events led to liquefaction in more vulnerable areas.

Given the potential differences in the characteristics of shaking of induced versus tectonic earthquakes (e.g., Bommer et al. 2016; Zalachoris and Rathje 2019) and potential regional differences in soil profiles, it is uncertain whether existing variants of the semi-empirical simplified liquefaction evaluation procedure for tectonic earthquakes can be used to accurately assess the liquefaction hazard of the region. Determining the suitability of current variants of the simplified procedure for evaluating the regional liquefaction hazard caused by induced earthquakes is part of an ongoing study, which includes a detailed site characterization campaign to examine profiles where effects of liquefaction were and were not observed following the Pawnee event.

Preliminary investigations have been conducted at four sites where liquefaction was observed during the Pawnee earthquake to gather existing information on the sites and accurately determine areas where liquefaction features were and were not observed. Geologic and hydrologic data were used to estimate probability of liquefaction and the spatial extent of liquefaction at each site during the Pawnee event based on Baise and Rashidian (2018). Estimates of liquefaction spatial extent appear reasonable for Sites 2 and 4 but may be low for Sites 1 and 3 where liquefaction was more extensive. HVSR tests were also conducted using ambient vibrations recorded at each site.

Further testing at the identified sites, including CPT and MASW tests, is planned for later this year (2019). Data from the full site investigation will be used to determine liquefaction potential of the selected sites based on current variants of the simplified procedure. Results will be compared with field observations of liquefaction to evaluate the effectiveness of these methods for determining liquefaction potential of induced earthquakes.

ACKNOWLEDGEMENTS

This study is based on work supported in part by the USGS grant G18AP00094 and U.S. National Science Foundation (NSF) grants CMMI-1030564, CMMI-1435494, CMMI-1724575, and CMMI-1825189. The authors gratefully acknowledge this support. However, any opinions, findings, and conclusions expressed in this paper are those of the authors and do not necessarily reflect the views of the USGS or NSF. The authors also acknowledge and thank Dr. Clint Wood from the University of Arkansas for the use of his HVSR equipment and Dr. Brett Maurer from the University of Washington for his review of this paper.

REFERENCES

Baise, L.G., and Rashidian, V. (2018). “A Geospatial Approach to Liquefaction Assessment for Rapid Response and Loss Estimation.” *Geotechnical Earthquake Engineering and Soil Dynamics V*, GSP 291, ASCE, VA, 1–10.

Bard, P. (2004). “Guidelines for the implementation of the H/V spectral ratio technique on ambient vibrations: Measurements, processing and interpretation.” SESAME European Research Project, WP12—Deliverable D23.12, 1–62.

Bommer, J. J., Dost, B., Edwards, B., Stafford, P. J., van Elk, J., Doornhof, D., and Ntinalexis, M. (2016). “Developing an application-specific ground-motion model for induced seismicity.” *Bulletin of the Seismological Society of America*, 106(1), 158–173.

Clayton, P., Zalachoris, G., Rathje, E., Bheemasetti, T., Caballero, S., Yu, X., and Bennett, S. (2016). “The geotechnical aspects of the September 3, 2016 M5.8 Pawnee, Oklahoma earthquake.” Geotechnical Extreme Events Reconnaissance Association, <http://www.geerassociation.org/> (Sep. 15, 2019).

Ellsworth, W. L. (2013). “Injection-induced earthquakes.” *Science*, 341(6142), 1–8.

Foulger, G. R., Wilson, M. P., Gluyas, J. G., Julian, B. R., and Davies, R. J. (2018). “Global review of human-induced earthquakes.” *Earth-Science Reviews*, 178, 438–514.

Green, R.A., Bommer, J.J., Rodriguez-Marek, A., Maurer, B., Stafford, P., Edwards, B., Kruiver, P.P., de Lange, G., and van Elk, J. (2019a). “Addressing Limitations in Existing ‘Simplified’ Liquefaction Triggering Evaluation Procedures: Application to Induced Seismicity in the Groningen Gas Field.” *Bulletin of Earthquake Engineering*, 17, 4539–4557.

Green, R.A., Bommer, J.J., Stafford, P.J., Maurer, B.W., Kruiver, P.P., Edwards, B., Rodriguez-Marek, A., de Lange, G., Oates, S.J., Storck, T., Omidi, P., Bourne, S.J., and van Elk, J. (2019b). “Liquefaction Hazard of the Groningen Region of the Netherlands due to Induced Seismicity.” *Journal of Geotechnical and Geoenvironmental Engineering*, (*in review*).

Kolawole, F., Atekwana, E. A., and Ismail, A. (2017). “Near-surface electrical resistivity investigation of coseismic liquefaction-induced ground deformation associated with the 2016 M_w 5.8 Pawnee, Oklahoma, earthquake.” *Seismological Research Letters*, 88(4), 1017–1023.

McGarr, A., Simpson, D., and Seeber, L. (2002). “Case histories of induced and triggered seismicity.” *International Geophysics*, 81(A), 647–661.

Mitchell, J. K., and Green, R. A. (2017). “Some induced seismicity considerations in geo-energy resource development.” *Geomechanics for Energy and the Environment*, 10, 3–11.

NOAA (2019). “Normals Annual/Seasonal Station Details: PAWNEE, OK US, GHCND:USC00346940.” <https://www.ncdc.noaa.gov/cdo-web/datasets/normal_ann/stations/GHCND:USC00346940/detail> (Sep. 10, 2019).

Oklahoma Office of the Secretary of Energy & Environment. (2019). “Earthquakes in Oklahoma: What We Know.” <https://earthquakes.ok.gov/what-we-know/> (Jun. 20, 2019).

Seed, H. B., and Idriss, I. M. (1971). “Simplified procedure for evaluating soil liquefaction potential.” *Journal of the Soil Mechanics and Foundations Division*, 97(9), 1249–1273.

Stanley, T. M., and Chang, J. M. (2016). Geologic Map of the Keystone Lake 30x60-Minute Quadrangle, Creek, Noble, Osage, Pawnee, Payne, Osage, Tulsa, and Washington Counties, Oklahoma: Oklahoma Geologic Survey OGQ-92, Oklahoma Geol. Surv., Norman, OK

Tiwari, A., and Rathje, E. M. (2018). “Engineering characteristics of earthquake motions from the Pawnee and Cushing Earthquakes in Oklahoma.” *Geotechnical Earthquake Engineering and Soil Dynamics V*, GSP 291, ASCE, Reston, VA, 378–386.

USGS (2016a). “ShakeMap for M 5.8 – 14 km NW of Pawnee, Oklahoma.” <https://earthquake.usgs.gov/earthquakes/eventpage/us10006jxs/executive> (Jun. 19, 2019).

USGS (2016b). “National Water Information System data available on the World Wide Web (USGS Water Data for the Nation): USGS 07153000 Black Bear Creek at Pawnee, OK.” <https://waterdata.usgs.gov/nwis/uv?site_no=07153000> (Jul. 4, 2019).

USGS (2016c). “National Water Information System data available on the World Wide Web (USGS Water Data for the Nation): USGS 07152500 Arkansas River at Ralston, OK.” <https://waterdata.usgs.gov/ok/nwis/uv/?site_no=07152500&PARAmeter_cd=00065,00060> (Jul. 4, 2019).

USGS (2019). “Oklahoma Alluvium.” <https://mrdata.usgs.gov/geology/state/sgmc-unit.php?unit=OKQal%3B0> (Jul. 2, 2019).

Whitman, R. V. (1971). “Resistance of Soil to Liquefaction and Settlement.” *Soils and Foundations*, 11(4), 59–68.

Yust, M. B. S., Cox, B. R., and Cheng, T. (2018). “Epistemic Uncertainty in Vs Profiles and Vs30 Values Derived from Joint Consideration of Surface Wave and H/V Data at the FW07 TexNet Station.” *Geotechnical Earthquake Engineering and Soil Dynamics V*, GSP 291, ASCE, Reston, VA, 387–399.

Zalachoris, G., Rathje, E. M., and Paine, J. G. (2017). "V_{S30} characterization of Texas, Oklahoma, and Kansas using the p-wave seismogram method." *Earthquake Spectra*, 33(3), 943–961.

Zalachoris, G., and Rathje, E. M. (2019). "Ground Motion Model for Small-to-Moderate Earthquakes in Texas, Oklahoma, and Kansas." *Earthquake Spectra*, 35(1), 1–20.